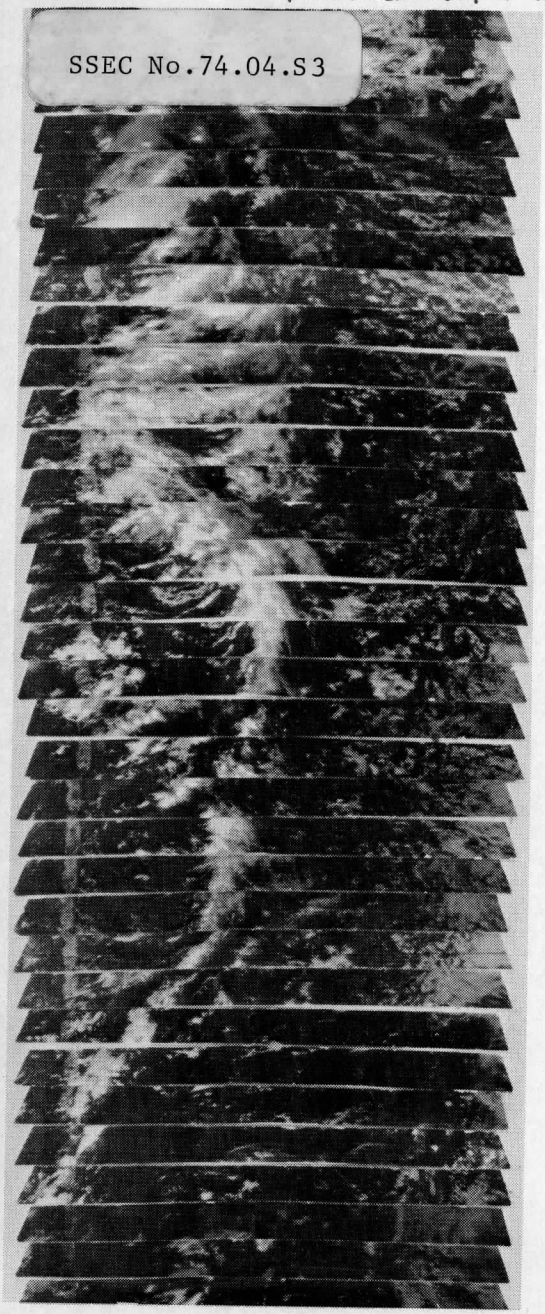

Annual Report 1973

NG – 26 – 72

Space Science and
Engineering Center

University of
Wisconsin – Madison

STUDIES OF THE ATMOSPHERE USING AEROSPACE PROBES

COVER DESCRIPTION

ATS-III satellite images, brightness enhanced to emphasize convective cores, were cut into strips 5 degrees of latitude wide (25°-30°N lat.) extending from 90°W longitude to 20°W. The strips, arranged in chronological sequence, cover the period from 3 May to 28 July 1969, and all were taken at about local noon. The sequence shown on the cover includes an interesting case of a cloud band originally resulting from a cold front moving eastward which is transformed into a cloud cluster moving westward in association with a surface low pressure trough. Further details are contained in the paper by D. N. Sikdar and D. P. Wylie.

STUDIES OF THE ATMOSPHERE

USING AEROSPACE PROBES

1973

STUDIES OF THE ATMOSPHERE

USING AEROSPACE PROBES

1973

Annual Report, NOAA Grant NG-26-72

The research reported in this document has been supported by the National Oceanic and Atmospheric Administration

April 1974

Published for the
Space Science and Engineering Center
by the
University of Wisconsin Press

Published 1974

The University of Wisconsin Press

Box 1379, Madison, Wisconsin 53701

The University of Wisconsin Press, Ltd.

70 Great Russell Street, London

First printing

Printed in the United States of America

ISBN 0-299-97054-X

Correspondence concerning editorial matters should be addressed to

Space Science and Engineering Center

University of Wisconsin

1225 West Dayton Street

Madison, Wisconsin 53706

Orders for copies of this report should be addressed to

The University of Wisconsin Press

CONTENTS

PREFACE

The number of papers included in this report is large and represents, to some extent, the continuing trend toward investigation of more specific problems rather than general areas of interest. This trend appears to result from increasing application of satellite images in operational meteorology.

The seven papers starting with Dr. Parent's summary constitute an attempt to predict the residual errors in positional accuracy inherent to the SMS/GOES satellite system design. The results of this related series of studies substantially confirms that, provided the satellite system operates reasonably close to design specifications, the SMS/GOES system will produce extremely valuable data from which accurate cloud motion information will be obtained. We look forward to continuing our studies with the greater effectiveness which SMS/GOES data will permit.

I would like to express my sincere appreciation for the cooperation and assistance provided to the authors by the numerous members of SSEC and other sections of the University which have made their work possible. I am happy to acknowledge the contributions to satellite meteorology made by the authors, and we all are grateful to NOAA for sponsoring this work.

Verner E. Suomi
Principal Investigator

TEMPORAL CLOUD STATISTICS OVER THE TROPICAL ATLANTIC AND PACIFIC DURING SUMMER AND WINTER

John A. Young and D. N. Sikdar

ABSTRACT

Time series of satellite-observed cloud amount over the tropical Atlantic and Pacific oceans, from 140°E to 0°W, are studied in terms of geographical and seasonal differences. The behavior at each location is presented by temporal statistics. These include the mean, standard deviation, and normalized band spectra. The degree of coupling along latitude circles is expressed in terms of coherency magnitudes. Coherency phase distribution summaries give information on the associated scales and apparent speeds of propagation. The Atlantic and Pacific statistics are contrasted in terms of zonal oceanic averages and full geographical variations for summer and winter seasons.

It is found that mean coverage in the northern summer is greater in the east-Pacific and Atlantic regions . The central Pacific shows greater relative variability. The coherent low frequency fluctuations show minimum power levels near the equator in both domains, with the greatest coherency magnitudes found near the central Pacific ITCZ. Winter patterns of mean and transient activity levels are similar to those of the summer in the central Pacific. However, seasonal similarities are less in the Atlantic, where the transient levels show indistinct geographical distributions in winter. Curiously, the coherency magnitudes show better organization of space-time fluctuations in the winter in both domains. Coherent ITCZ behavior is evident at most longitudes except those with the highest frequencies. Propagation directions and apparent wavelengths in the two domains are most similar in winter. Their summer differences are due to ill-defined or opposing senses at some frequencies.

1. INTRODUCTION

This is the fourth in a series of papers using satellite cloud data to quantitatively document the space-time behavior of tropical cloud systems. The focus has been on the synoptic-scale properties of cloud amount, which appears to provide a more stable measure of cloud activity than does brightness data on smaller scales. The temporal behavior has been expressed mainly in a spectral framework, so that the characteristics can be categorized according to time scale. The first paper (Sikdar, Young and Suomi, 1972, henceforth referred to

as paper "A") showed geographical variations over the tropical Pacific during the summer of 1967 for fluctuation periods shorter than 20 days. Attention was focused primarily on the intensity of transient activity (using time spectra) and east-west propagation lifetimes and speeds (using coherencies taken from cross-spectra). In a subsequent paper (Young and Sikdar, 1973), zonal propagation was exhibited. Here we used the more flexible tool of band-pass time filtering. Finally, Heinricy and Young (1974, appearing in this volume) have studied the longer-term statistical behavior of clouds over the eastern tropical Atlantic and western Africa. This research emphasized the long-period changes in cloud amount and in the modulation envelope of its short-period cluster-like fluctuations.

The primary goals of this work are to extend the documentation of geographical variations (begun in paper A for the Pacific summer) to the Atlantic, and to document the winter and the summer regime in both regions. The basic procedures are identical to those described in paper A, since those statistical measures are of a summary nature and facilitate comparison. The cloud amount data were obtained from ESSA III mosaics for rectangular sectors (10° longitude by 5° latitude) in the two primary domains. As in paper A, the "Pacific" domain is defined as extending over the central Pacific, from 140°E to 120°W. The "Atlantic" domain extends from 120°W to 0°W and includes the eastern Pacific and the tropical Atlantic. The 6-month "winter" season (Northern hemisphere) is defined as extending from September 1, 1967 to February 28, 1968 for both domains. The 6-month "summer" season for the Atlantic domain is March 1, 1967 to August 31, 1967; the "summer" statistics published in paper A extended from April 1, 1967 to July 31, 1967.

Section 2 provides a basic comparison of latitudinal structures for the Atlantic and Pacific domains in the summer. Section 3 exhibits the full geographical variations for the summer Atlantic. Winter spectral data for both domains are shown in section 4, while the zonal propagation (coherency phase) statistics are summarized for both seasons and domains in section 5.

2. SUMMER COMPARISON OF ZONAL AVERAGES: ATLANTIC VS. PACIFIC

A broad summary of contrasts between the Atlantic and Pacific domains is displayed by the zonal means of the statistics for the summer season, varying with latitude only. To minimize distortions by continental data, the zonal means were calculated as longitudinal averages over oceanic sectors only. Figure 1 shows the latitudinal distributions of the simplest statistics. The transient activity, as evidenced by the standard deviation field labeled "RMS", is rather uniform. There is a slight maximum near the northern ITCZ in both domains. The mean values exceed the RMS values, with maxima near the ITCZ and minima near, or somewhat to the south of the equator. The mean values are significantly higher in the Atlantic, to the extent that the relative variability of the Atlantic is comparatively small. Both the Atlantic and the Pacific show less persistence (greater relative variability) near the equator and greater persistence near the ITCZ.

Turning to the normalized spectral data, we consider the 4 frequency bands discussed in paper A covering periods from 2 to 20 days. The bands will be referred to as: very high frequencies (2.0-2.9 day periods), high frequencies (2.9-5.5 day periods), medium frequencies (5.5-8.6 day periods), and low frequencies (8.6-20.0 day periods). The corresponding band widths are not identical to each other, being .16, .16, .06, and .07 cpd, respectively. As a result, direct comparison of variance levels should be made after reducing the spectral estimates of the two higher frequency bands by the multiplicative factor of approximately 0.4. Figure 2 (a) summarizes the spectral levels obtained in paper A by latitude and frequency. We see that the high frequencies dominate the very high frequencies and that they are most prominent within 10° of the equator. The lower frequencies show a minimum near the equator and a maximum near 15°. The Atlantic results (Figure 2 (b)) are similar, although the contrast between high and low frequencies is smaller at the equator.

The space-time organization of the cloud fluctuations can be studied in terms of cross-spectra of the cloud amount time series for two adjacent sectors on the same latitude circle. Large "noise" factors and short disturbance lifetimes are marked by small coupling and reduced coherency magnitudes. These features are a part of all coherencies, but Figure 3 shows that the lower frequency bands nevertheless exhibit significant coherencies. The higher frequencies possess weak magnitudes, especially in the Atlantic. But this characteristic is probably over-emphasized by the uneven frequency band width. The high values at long periods reinforce the intuitive idea that long-period systems are organized on large spatial scales. However, it is interesting to note that the high frequency band possesses a distinct maximum in the Pacific ITCZ (Figure 3 (a)) in contrast to its absence in the Atlantic (Figure 3(b)). This suggests that 4-day pulsations of the ITCZ are more distinct in the Pacific during the summer. In addition, the low frequencies are more coherent in the Pacific than in the Atlantic.

3. SUMMER: ATLANTIC DOMAIN

The previous section demonstrated several basic similarities in latitudinal distributions of temporal cloud statistics of the Atlantic and the Pacific in summer. Because the Atlantic domain includes the continent of South America and the Pacific domain includes the edge of the Asian monsoonal circulation (Krishnamurti, 1971), it is expected that significant differences arise when longitudinal variations are allowed. The differences are examined in this section, in terms of statistical patterns, for the Atlantic summer regime. The statistical fields are not expected to match exactly at 120°W.

Figure 4 (upper) shows that the mean cloud amount maxima are found near the northern ITCZ at all longitudes and along a meridional band extending down the west coast of South America. The maximum value in excess of 0.60 is the largest in either the Atlantic or Pacific. Aside from the north-south band, an extensive "dry zone" is

apparent in the Southern Hemisphere, especially over the Atlantic, with cloud amount values slightly larger than the dry zone of the central Pacific. The minimum associated with the Sahara regime over Africa is also pronounced. The transient activity (lower diagram: the RMS of deviations from the mean) has a magnitude range of 12-26% with a distinct maximum extending into the eastern Pacific, mainly to the north of the equator. Maxima are also found near the Atlantic-African ITCZ and central South America. The relative variability tends to be small where the RMS values are small. High values are confined to small parts of the dry zones on the eastern portion of the domain.

Figure 5 shows the normalized power spectra for summer. The patterns are somewhat smoother than those of Figure 7 in paper A, partly a result of the improved statistical reliability associated with the 50% longer data record. Typical ranges of power in each frequency band are similar to those of the Pacific domain. In the lowest frequency band, the equatorial minimum is especially pronounced over South America. Higher (30%) values most closely approach the equator to the southeast of this region. To some extent, the highest frequencies vary in an inverse manner. A well defined maximum is found over equatorial South America. This extends eastward to the vicinity of the equator and the ITCZ latitudes in the eastern part of the domain. The high frequency band (periods of 2.9-5.5 days) contributes strongly at most locations in the tropics with maxima near the equator in the west and at 15°N in the east.

Maps of local coherency magnitude for interior adjacent sectors on a latitude circle are shown in Figure 6. As in the Pacific, the values are generally high, with a few minima in evidence at scattered locations. The pronounced equatorial minimum is probably due to irregular interruptions of the more persistent stratiform cloudiness in that area. The pattern for medium frequencies does not possess the distinct ITCZ maximum which characterizes the central Pacific. This band contains the highest frequency, with significant coherencies, in the planned GATE region (centered near 8°N, 23°W). Maps for the highest frequency bands possess only minor coherency maxima, with strong minima near equatorial South America.

Additional study was made of the statistics of the brightest, most active energetic clouds. These data were considered less reliable; only the primary features will be noted here. The mean and standard deviation fields showed the largest values near the equator, extending to the vicinity of the planned GATE location. The spectra showed maximum levels at periods between two and five days in the GATE area, with corresponding coherencies of marginally significant magnitudes.

4. WINTER: ATLANTIC AND PACIFIC DOMAINS

The preceding sections have provided a comparison of the Atlantic and Pacific domains for the summer months. In this section, statistics are presented for both domains in the winter season. The following figures allow comparison of seasonal differences within and between the two domains.

Figure 7 (a), taken with Figure 4 of paper A, shows that the seasonal differences of mean and transient cloud amount are surprisingly small in the central Pacific, with the northern ITCZ and southern cloud band distinct. Mean values are typically higher by about 10% in fractional area coverage. As in summer, the winter persistence (as defined by the relative variability) is at maximum in northeastern regions. A minimum is associated with the southern dry zone.

Mean winter patterns in the Atlantic (Figure 7 (b)) show the northern ITCZ and the southern dry zone to be less distinct; mean values are higher nearly everywhere else, except the Sahara. The deviation RMS pattern is very indistinct. However, the relative variability shows strongly persistent characteristscs at most locations, except coastal Africa. Contrasting the Atlantic with the Pacific during winter, we see that the mean and transient Pacific features remain more distinct than those of the Atlantic.

Without examining details, the relative spectral levels retain similar patterns between summer (paper A) and winter in the Pacific (Figure 8 (a)). The low frequencies are again at a minimum near the equator with a strong maximum at 15°-20°S. The high frequencies (2.9-5.5 day periods) are thus at a maximum near and to the north of the equator. Seasonal differences in the Atlantic are somewhat more apparent. Comparing Figures 5 and 8 (b), we see that the dominance of the high frequency band is less in the winter. In this season, the very high frequencies shift their maximum to oceanic equatorial locations. The low frequency patterns of both seasons have much in common, the equatorial minimum being most clear. Comparing the two domains during winter (Figures 8 (a) and 8 (b)), we see that the low frequency pattern is patchier in the Atlantic. The high frequency band is dominant over a larger area of the Atlantic than of the Pacific, especially in the Southern Hemisphere. The very high frequencies possess maximum relative contributions near the equator in both domains.

Examining the winter coherency magnitudes (Figures 9 (a) and 9 (b)), we find a well-defined axis of coherent activity extending along the ITCZ latitudes of both oceans at low and medium frequencies. This feature is actually clearer in the winter picture than in the summer, particularly in the Atlantic (compare this with Figure 6 and Figure 8 of paper A). The higher frequency bands of the Pacific show smaller coherency magnitudes in winter, but, again, there seems to be a well-defined maximum axis near the ITCZ. In the Atlantic winter, these

frequency bands are generally less coherent. However, periods in the band 2.9-5.5 days show maxima in the vicinity of the oceanic ITCZ. Taken as a whole, it appears that identifiable transient longitudinal coupling of cloud systems is characteristic of the Pacific ITCZ in both seasons, but that a well defined "duct" occurs in the Atlantic only during winter.

5. ZONAL PROPAGATION SUMMARIES

As discussed in paper A, the phase of "significant" coherencies (magnitudes greater than 0.5) gives information on time delays between cloud patterns in adjacent sectors. For simply propagating waves progressing in one direction, this information further implies an apparent longitudinal wavelength and speed of propagation, fluctuations in the "zonal ITCZ" corresponding to a very long wavelength. The phase indications are less clear when more than one type of fluctuation influences a region, or when a "standing" oscillation occurs.

It is clear from the results of Young and Sikdar (1973) that the characteristics of propagating systems are somewhat intermittent and irregular. As a consequence, even the "significant" phase estimates for a given frequency band are scattered (see Figures 9-11 in paper A), and comparisons of different seasons or domains are complicated. To emphasize the basic features of each such distribution, an additional screening procedure was applied. The purpose of the procedure was to represent each phase distribution by zero, one, or two points at each latitude and frequency band. Zero points were assigned if the distribution was widely scattered, or if there were just a few significant points. A single point was used to characterize a typical unimodal distribution, even if the distribution possessed many members or was broad. (Most such distributions contained 80% of the points within a phase interval of 60° width. Thus, a broad distribution, spread over both positive and negative phases, would yield a representative point estimate of small phase. This implied a planetary wave scale considerably greater than that of most individual members of the distribution.) In cases where the distribution was fundamentally bimodal, the representation consisted of two points. The results of this procedure are shown for the three lowest frequency bands discussed in paper A. The distributions are summarized for latitudes ranging from 25°S to 25°N. Latitudes taken from paper A, which range from 20°S to 20°N, are omitted.

Figure 10 (a) shows the phase summary for the 4-day cloud fluctuations. During the summer, the Pacific experiences only westward propagation near the equator. The Atlantic experiences mixed propagation directions in the Northern Hemisphere, with no well-defined propagation in much of the Southern Hemisphere. During the winter season, the Pacific propagation characteristics are quite similar to those of the summer. In contrast, the Atlantic winter propagation resembles the latitudinal distribution of the Pacific winter. Both domains experience longer wavelengths of westward propagation in winter.

The remaining lower frequencies are dominated in both domains and seasons by longer apparent wavelengths, as seen for the 7-day periods in Figure 10 (b). In the summer season, these fluctuations show westward propagation in the Northern Hemisphere and near the equator. The winter pattern is broadly similar to this in both domains, with the exception of the eastward propagation at 25°N.

The lowest frequencies (8.6-20.0 day periods,Figure 10 (c)) show a winter distribution in both domains and a summer Atlantic distribution similar to the 7-day band in winter. The Pacific summer distribution is more complicated due to the presence of two propagation modes in the vicinity of the equator at low latitudes. Of these, the westward propagating mode resembles that found in the Atlantic domain and in the winter season. However, the eastward moving mode stands out clearly as a significant smaller-scale feature.

6. CONCLUDING REMARKS

The results of this work, taken in the context of the Pacific summer calculations of paper A, provide a more complete view of the gross statistical behavior of the time varying cloud systems over the tropical Atlantic and Pacific. We note the similarities of zonally averaged statistics for the two domains during summer and conclude that maximum differences arise with respect to longitudinal variations, especially during winter. In the central Pacific, the winter patterns of cloud activity resemble those of the summer. This is less true of the Atlantic domain. The ITCZ fluctuations are marked by axes of maximum coherency, more distinct in winter than in summer. The associated phase difference distributions are centered at long apparent wavelengths and are most similar for the two domains during winter.

The best prospects for future extensions of this type of study would seem to lie in two main areas. First, there could be an examination of the remaining portion of the tropical belt (0°-140°E) This would complete the global statistical picture during both seasons. Such a study is currently underway. Second, the utilization of longer data periods would allow for study of inter-annual variations and for more reliable estimates of "normal" tropical cloud activity patterns during all seasons. In this case, it seems that the best results would be obtained by using a combination of spectrally-oriented statistical procedures of particular value would be a combination of the techniques used in these four papers and the eigenvector schemes of Wallace and Dickinson (1972).

ACKNOWLEDGMENTS

Portions of this research were reported in 1971 at the Seventh Technical Conference on Hurricanes and Tropical Meteorology at Barbados, West Indies. This research was sponsored by NOAA under Grants 1-36036 and NG-26-72.

REFERENCES

Gruber, A., 1972: Fluctuations in the Position of the ITCZ in the Atlantic and Pacific Oceans, J. Atmos. Sci., 29, 193-197.

Heinricy, D. J. and J. A. Young, 1974: Long-Term Variations in High and Low Frequency Cloud Activity over the East Atlantic-West Africa Region. Submitted to Monthly Weather Review.

Krishnamurti, T. N., 1971: Observational Study of the Tropical Upper Tropospheric Motion Field During the Northern Hemisphere Summer. J. Appl. Meteor., 10, pp. 1066-1096.

Sikdar, D. N., J. A. Young, and V. E. Suomi, 1972: Time-Spectral Characteristics of Large-Scale Cloud Systems in the Tropical Pacific. J. Atmos. Sci., 29, 229-239.

Wallace, J. M., and R. E. Dickinson, 1972: Empirical Orthogonal Representation of Time Series in the Frequency Domain. Part I: Theoretical Considerations. J. Appl. Meteor., 11, pp. 887-892.

Winston, Jay S., 1971: The Annual Course of Zonal Mean Albedo as Derived from ESSA III and V Digitalized Picture Data. Monthly Weather Review, 99, 818-827.

Young, J. A., and D. N. Sikdar, 1973: A Filtered View of Fluctuating Cloud Patterns in the Tropical Pacific. J. Atmos. Sci., 30, 392-407.

FIGURE LEGENDS

Figure 1. Zonal averages of gross cloud area statistics over oceanic portions of the "Atlantic" (thin line) and "Pacific" (thick line) domains for northern summer 1967. "RMS" refers to root-mean-square of the deviation from the mean.

Figure 2. Frequency-latitude diagrams of zonally averaged normalized power spectra of cloud amounts for oceanic sectors. Data is for summer season for (a) Pacific and (b) Atlantic domains. Analysis is made from data for uneven frequency bands plotted near periods 2.5, 4, 7, and 12 days. Units are percentage contribution to the total variance in periods between 2 and 20 days. Shading indicates contributions greater than 25%.

Figure 3. Frequency-latitude diagrams of zonally averaged local cloud amount coherency magnitudes for adjacent oceanic sectors. Data is for summer season for (a) Pacific and (b) Atlantic. Magnitude at each point is determined from mean "vector" coherencies involving the 2 adjacent sectors at the same latitude. Analysis is from plotted values near periods 2.5, 4 7, and 12 days. Shading denotes values in excess of 0.40.

Figure 4. Gross cloud amount statistics over the Atlantic domain during summer. "RMS" refers to root-mean-square of the deviation from the mean. Units are percent coverage, with solid line contour interval of 10%. Thin lines are coasts. Upper: shading denotes mean coverage in excess of 40% (note that the value was 30% in paper A). Lower: heavy (light) shading represents areas of transient (persistent) activity where rms deviation amounts are larger (smaller) than 1.0 (0.5) times the mean amount. Compare to Figure 4 in paper A.

Figure 5. Spatial distributions of normalized power spectral cloud cover amounts for summer in the Atlantic domain for separate frequency bands. Units for each band are percentage contribution to total variance in all periods less than 20 days. Solid line contour interval is 10%. Shading denotes contributions in excess of 25%. Compare to Figure 7 in paper A.

Figure 6. Spatial distribution of local cloud cover coherency magnitude for separate frequency bands from Atlantic summer data. Magnitude at each point is determined from mean "vector" coherencies involving the 2 adjacent sectors at the same latitude. Values are averages for regions with dimensions of 20° longitude, 10° latitude. Shading denotes values in excess of 0.4. The contour interval is 0.1. Compare to Figure 8 in paper A.

Figure 7 (a). Gross cloud amount statistics over the Pacific domain during winter. "RMS" refers to root-mean-square of the deviation from the mean. Units are percent coverage, with solid

line contour interval of 10%. Thin lines are coasts. Upper: shading denotes mean coverage in excess of 40%. Lower: heavy (light) shading represents areas of transient (persistent) activity where rms deviation amounts are larger (smaller) than 1.0 (0.5) times the mean amount. Compare to Figure 4 preceding and Figure 4 in paper A.

Figure 7 (b). Gross cloud amount statistics over the Atlantic during winter. Remainder of legend is same as Figure 7 (a).

Figure 8 (a). Spatial distributions of normalized power spectral cloud cover amounts for winter in the Pacific domain for separate frequency bands. Units for each band are percentage contribution to total variance in all periods less than 20 days. Solid line contour interval is 10%. Shading denotes contributions in excess of 25%. Compare to Figure 5 preceding and to Figure 7 in paper A.

Figure 8(b). Spatial distributions of normalized power spectral cloud cover amounts for winter in the Atlantic domain for separate frequency bands. Remainder of legend is same as Figure 8 (a).

Figure 9 (a). Spatial distribution of local cloud cover coherency magnitude for separate frequency bands from Pacific winter data. Magnitude at each point is determined from mean "vector" coherencies involving the 2 adjacent sectors at the same latitude. Values are averages for regions with dimensions of 20° longitude, 10° latitude. Shading denotes values in excess of 0.4. The contour interval is 0.1. Compare to Figure 6 preceding and to Figure 8 of paper A.

Figure 9 (b). Spatial distribution of local cloud cover coherency magnitude for separate frequency bands from Atlantic winter data. Remainder of legend is same as Figure 9 (a).

Figure 10 (a). Summary of representative points for coherency phase distributions, apparent zonal wavelengths and propagation speeds for periods in the range 2.9-5.5 days for both seasons and both domains. Coherency data is taken from "significant" phase distributions for zonally adjacent observational sectors at each latitude.

Figure 10 (b). Summary of representative points for coherency phase distributions as in Figure 10 (a), except for periods of 5.5-8.6 days.

Figure 10 (c). Summary of representative points for coherency phase distributions as in Figure 10 (a), except for periods of 8.6-20.0 days.

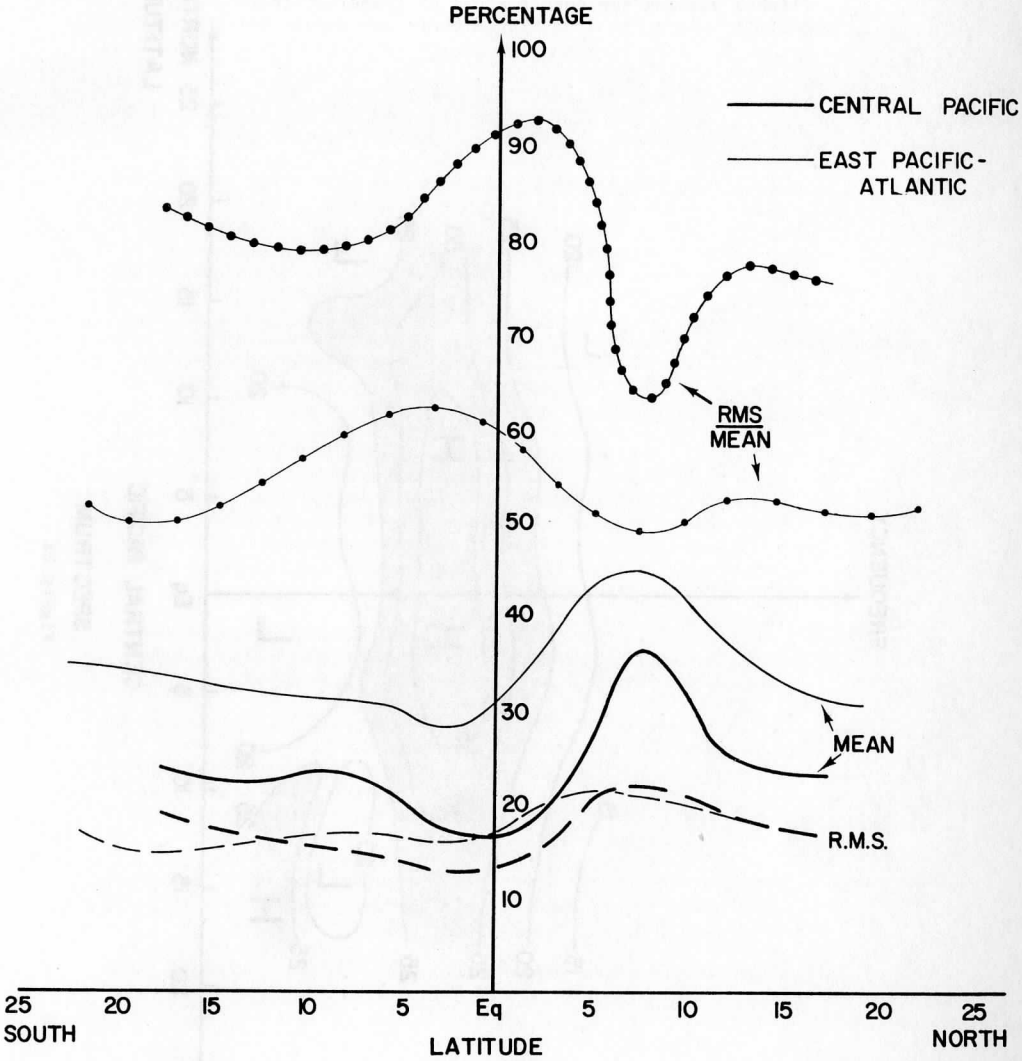
PERCENTAGE
100
90
80
70
60
50
40
30
20
10
CENTRAL PACIFIC
EAST PACIFIC-
ATLANTIC
RMS
MEAN
MEAN
R.M.S.
25
20
15
10
5
Eq
5
10
15
20
25
SOUTH
LATITUDE
NORTH

Figure 1

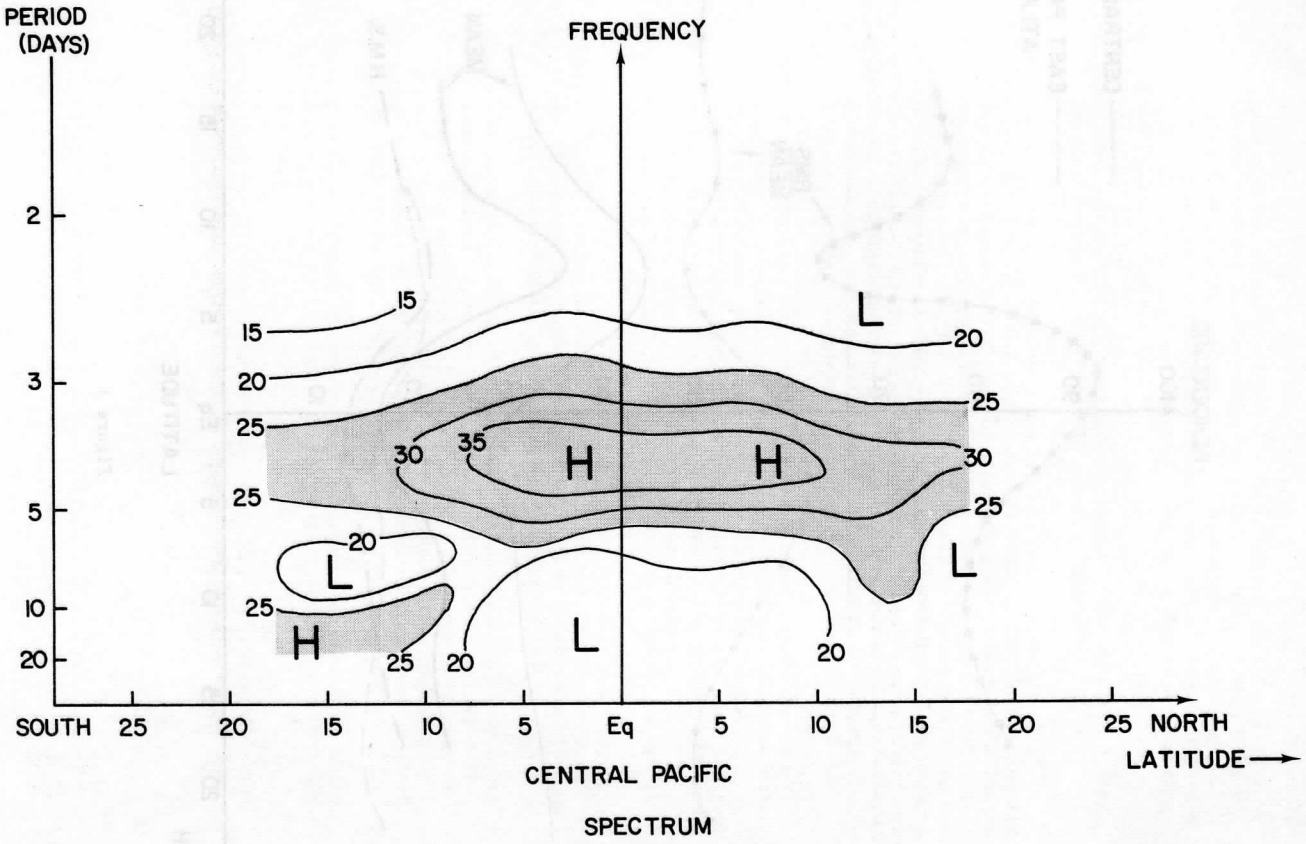
PERIOD
(DAYS)
FREQUENCY
2
3
5
10
20
15
15
20
25
30
35
H
H
L
L
L
L
20
25
30
25
20
25
25
20
SOUTH 25 20 15 10 5 Eq 5 10 15 20 25 NORTH
LATITUDE
CENTRAL PACIFIC
SPECTRUM

Figure 2a

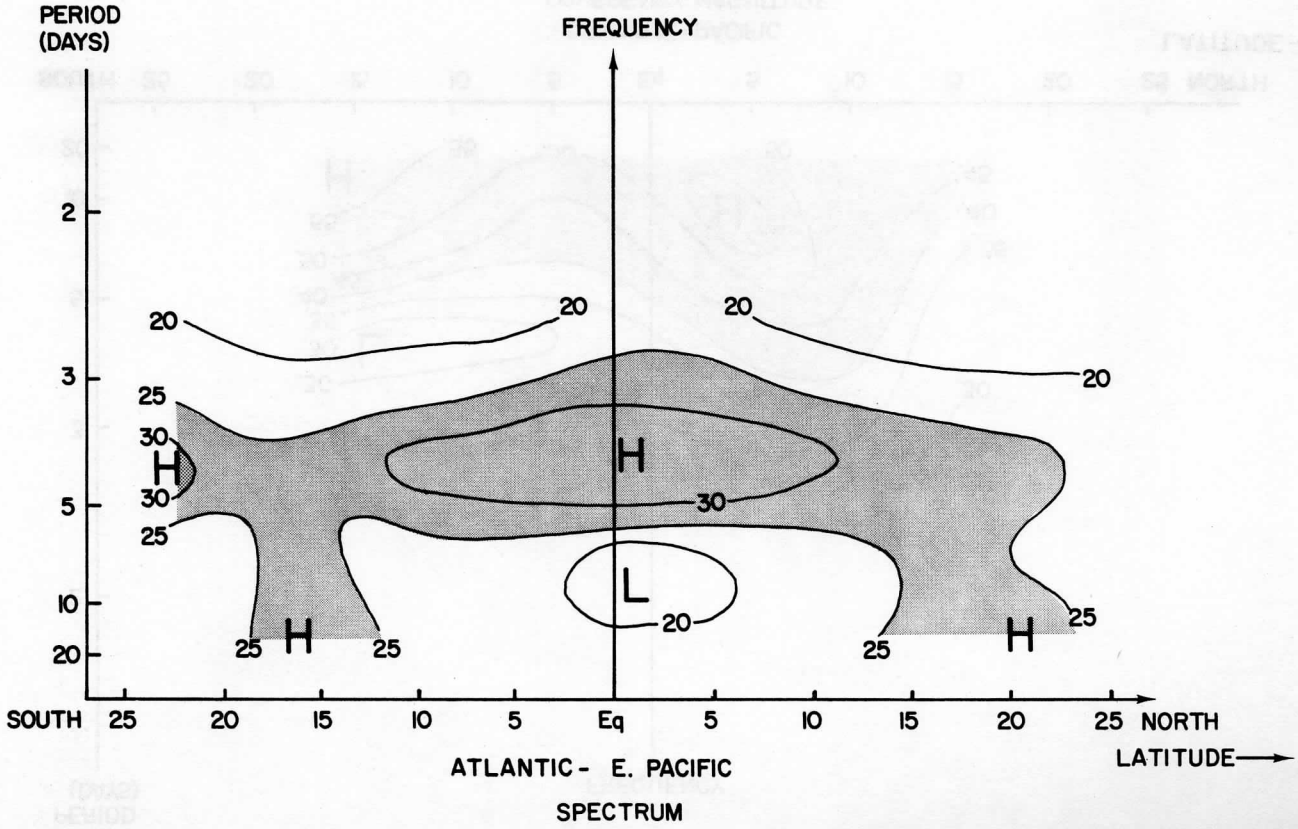
PERIOD
(DAYS)
FREQUENCY
2
3
5
10
20
20
20
20
20
25
30
H
30
25
H
30
L
20
25
H
25
25
H
25
SOUTH 25 20 15 10 5 Eq 5 10 15 20 25 NORTH
LATITUDE
ATLANTIC - E. PACIFIC
SPECTRUM

Figure 2b

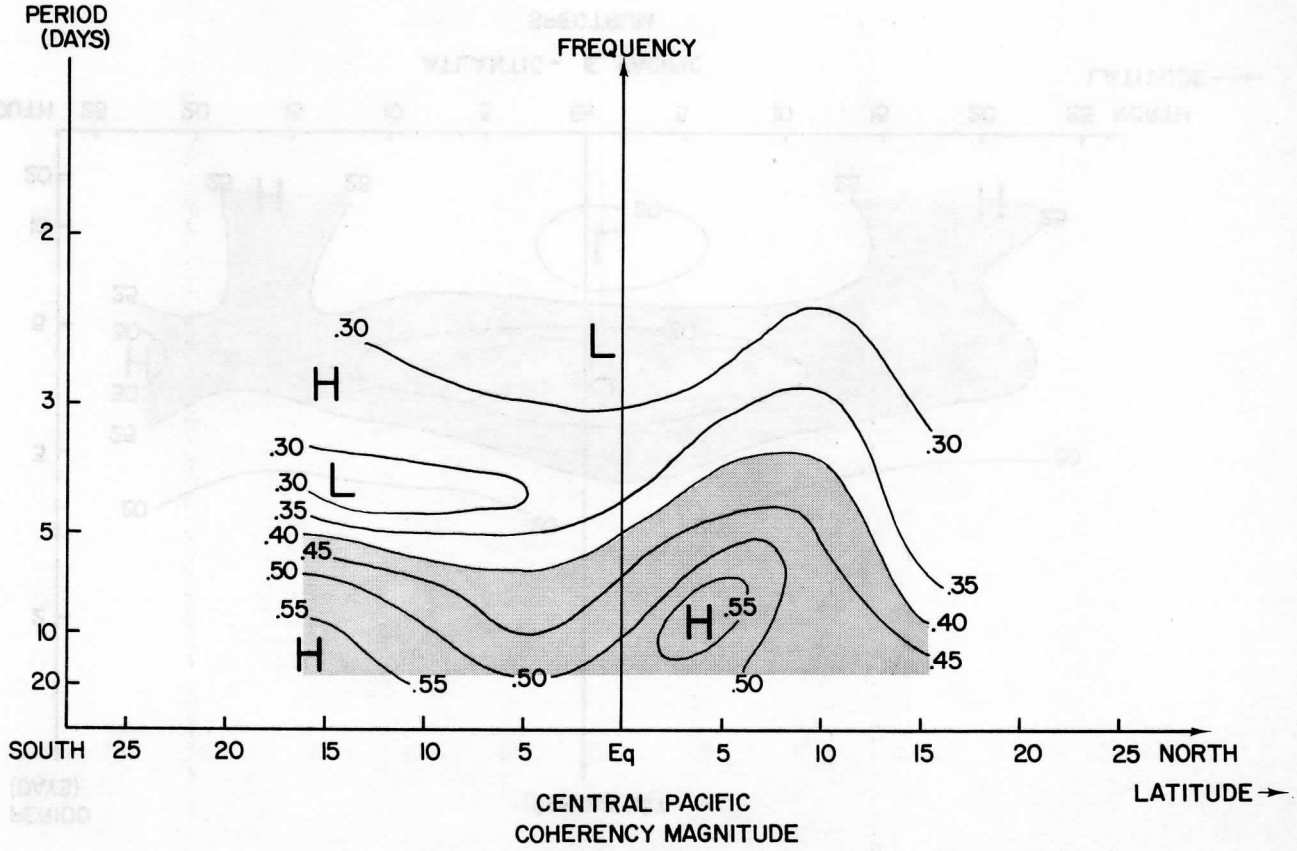
PERIOD
(DAYS)
FREQUENCY
2
3
5
10
20
.30
L
H
.30
.30
L
.35
.40
.45
.50
.55
H
.55
.50
.30
.35
.40
.45
H
.55
.50
SOUTH 25 20 15 10 5 Eq 5 10 15 20 25 NORTH
LATITUDE
CENTRAL PACIFIC
COHERENCY MAGNITUDE

Figure 3a

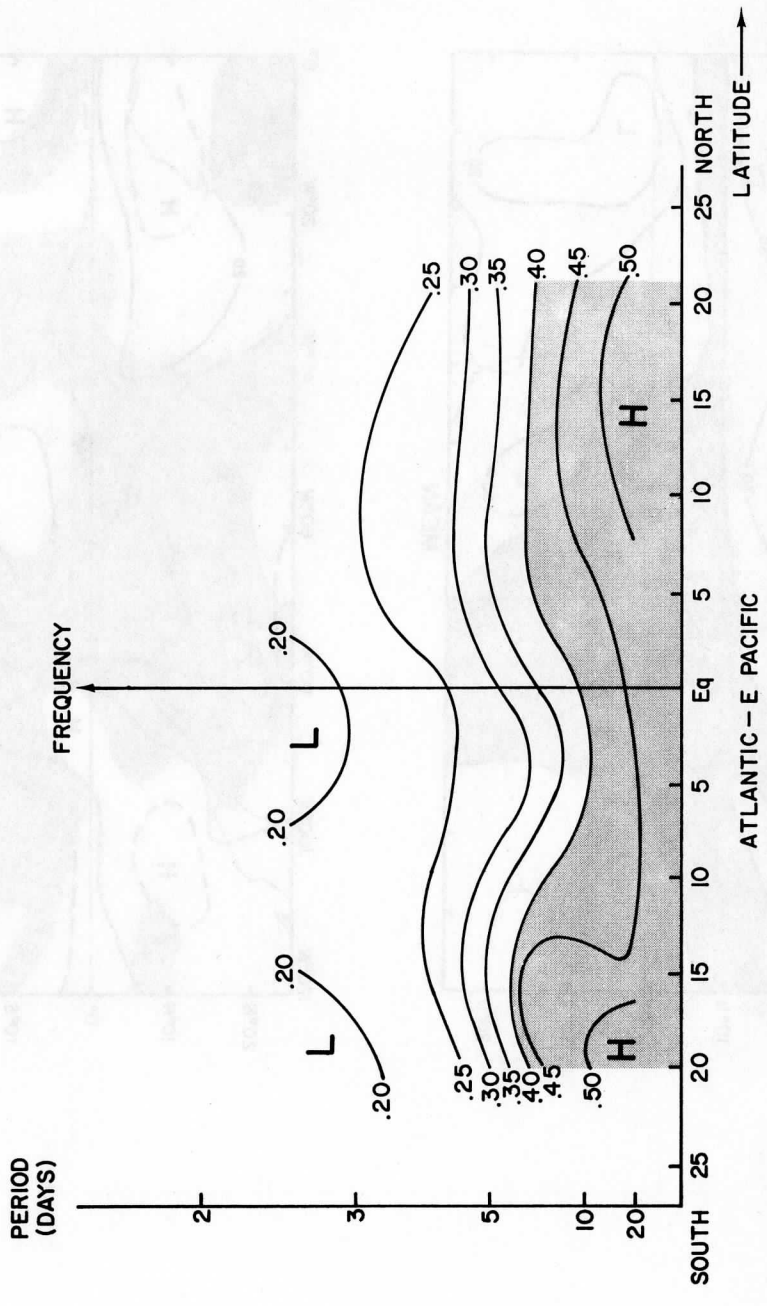
PERIOD (DAYS)
2
3
5
10
20
FREQUENCY
SOUTH 25 20 15 10 5 Eq 5 10 15 20 25 NORTH
LATITUDE
ATLANTIC – E PACIFIC
COHERENCY MAGNITUDE
L
.20
.20
L
.20
.20
H
.25
.30
.35
.40
.45
.50
.25
.30
.35
.40
.45
.50

Figure 3b

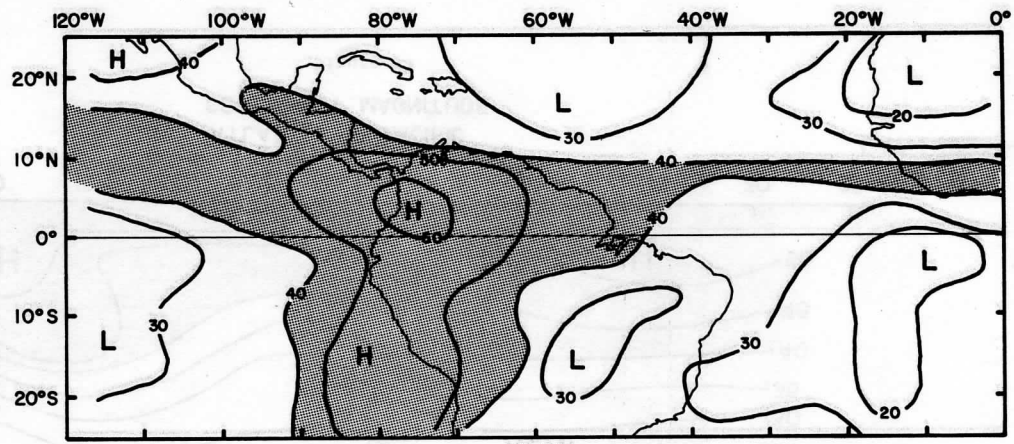
120°W
100°W
80°W
60°W
40°W
20°W
0°
20°N
10°N
0°
10°S
20°S
H
L
30
40
MEAN

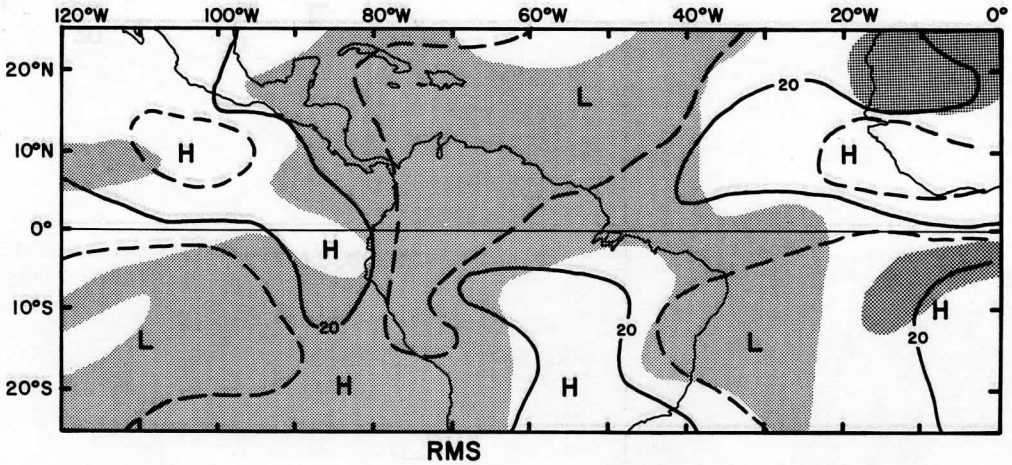
120°W
100°W
80°W
60°W
40°W
20°W
0°
20°N
10°N
0°
10°S
20°S
H
L
20
RMS

Figure 4

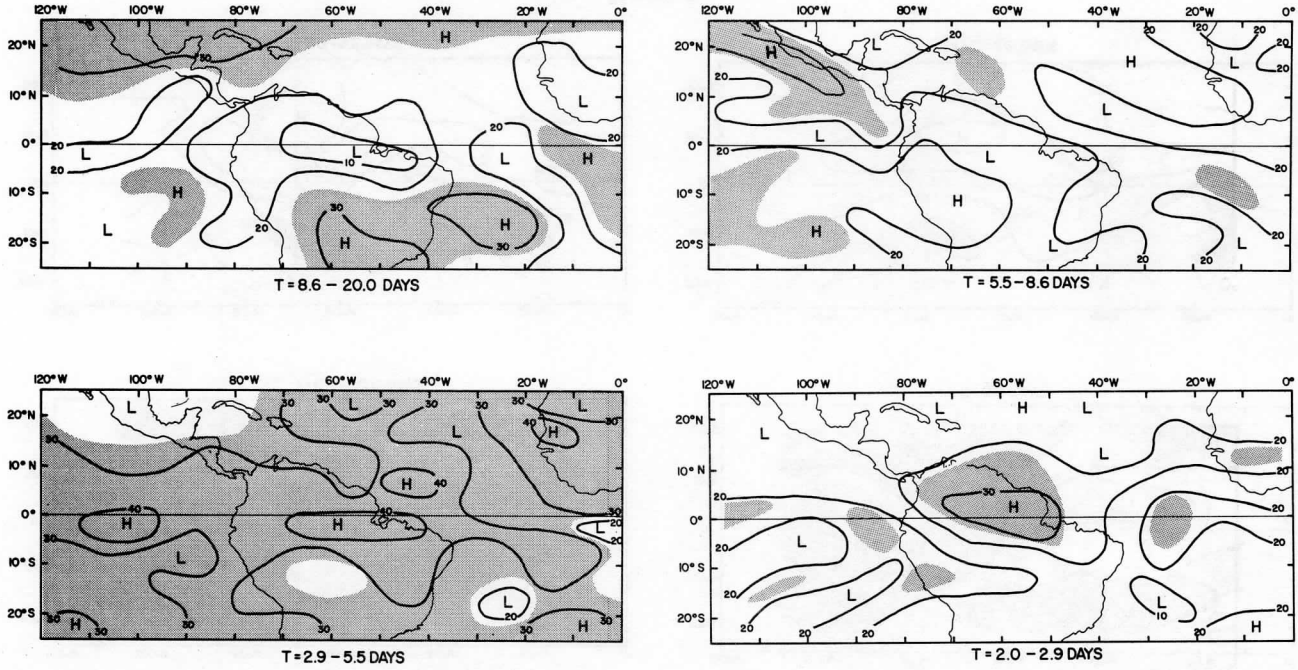
120°W
100°W
80°W
60°W
40°W
20°W
0°
20°N
10°N
0°
10°S
20°S
T = 8.6 – 20.0 DAYS
T = 5.5 – 8.6 DAYS
T = 2.9 – 5.5 DAYS
T = 2.0 – 2.9 DAYS

Figure 5

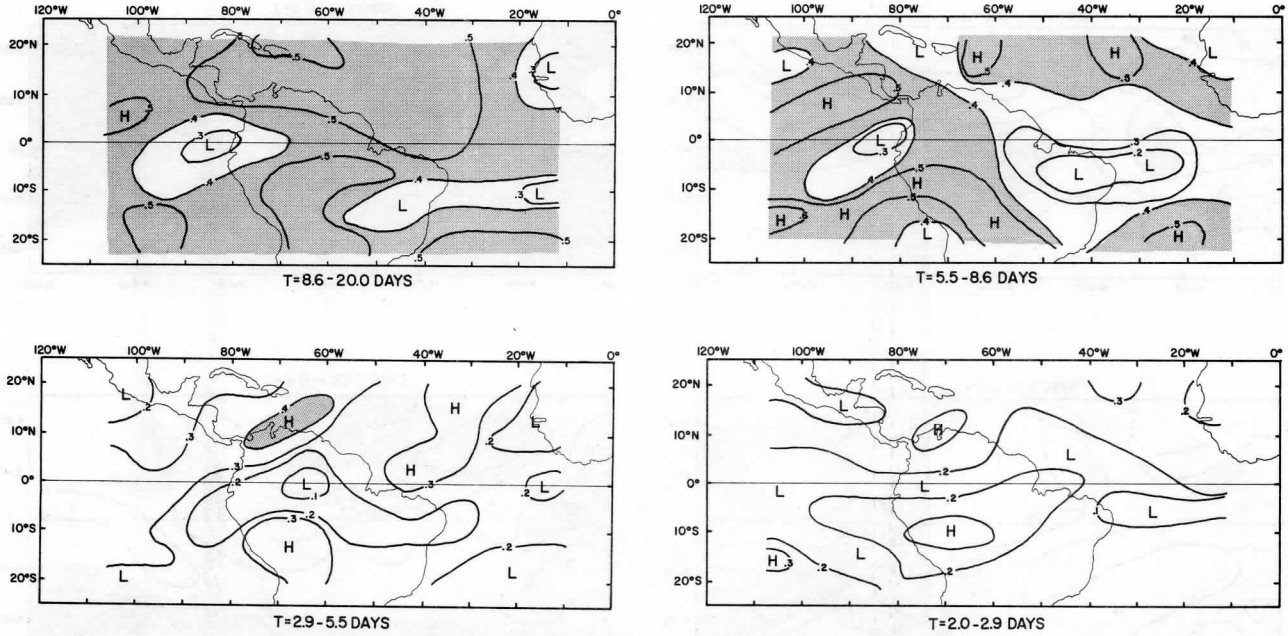
120°W
100°W
80°W
60°W
40°W
20°W
0°
20°N
10°N
0°
10°S
20°S
T=8.6-20.0 DAYS
T=5.5-8.6 DAYS
T=2.9-5.5 DAYS
T=2.0-2.9 DAYS

Figure 6

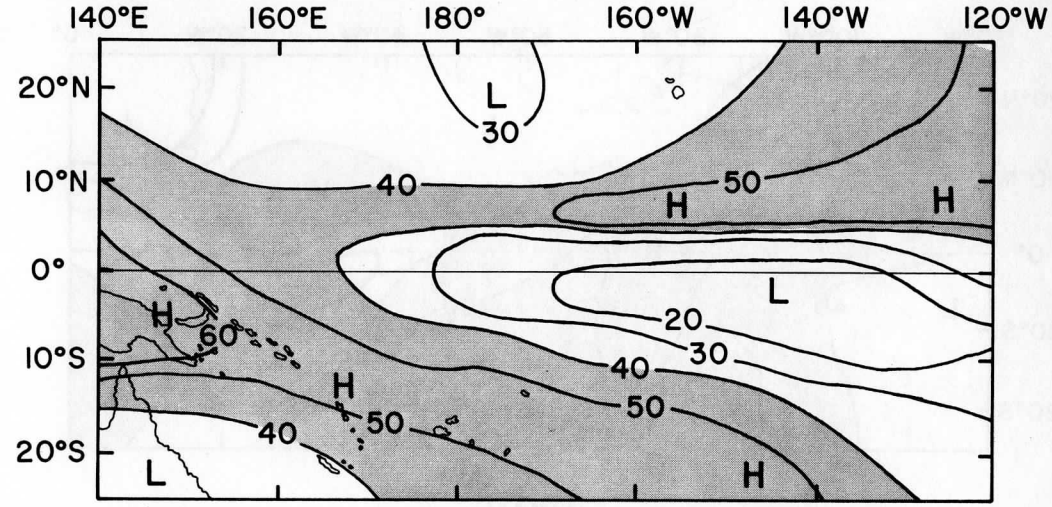

MEAN

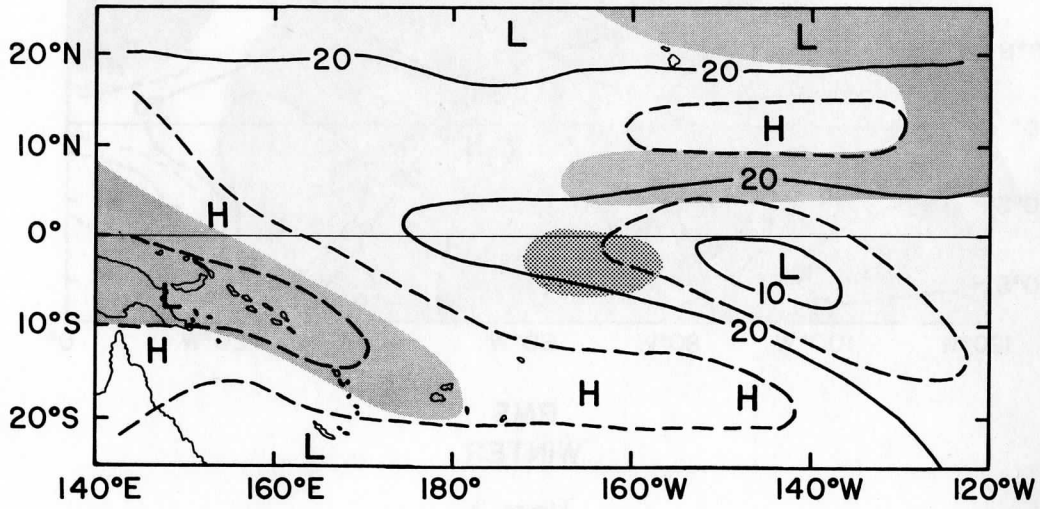

RMS

WINTER

Figure 7a

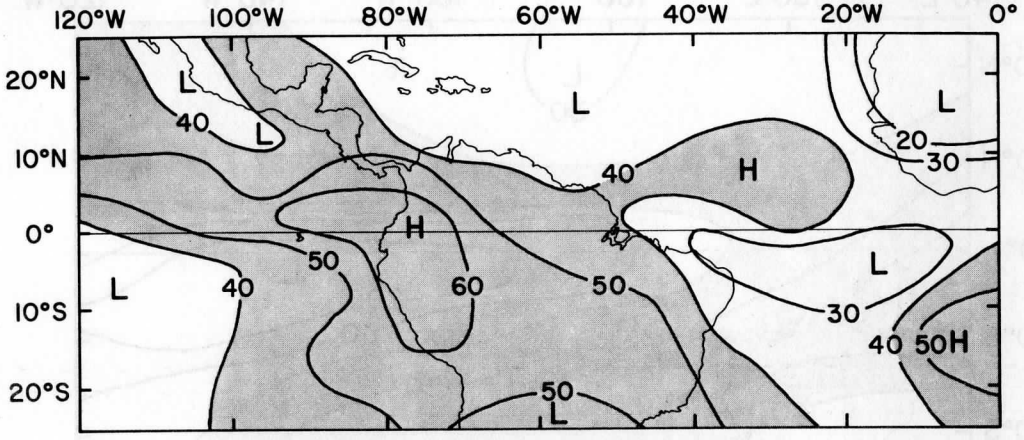

MEAN

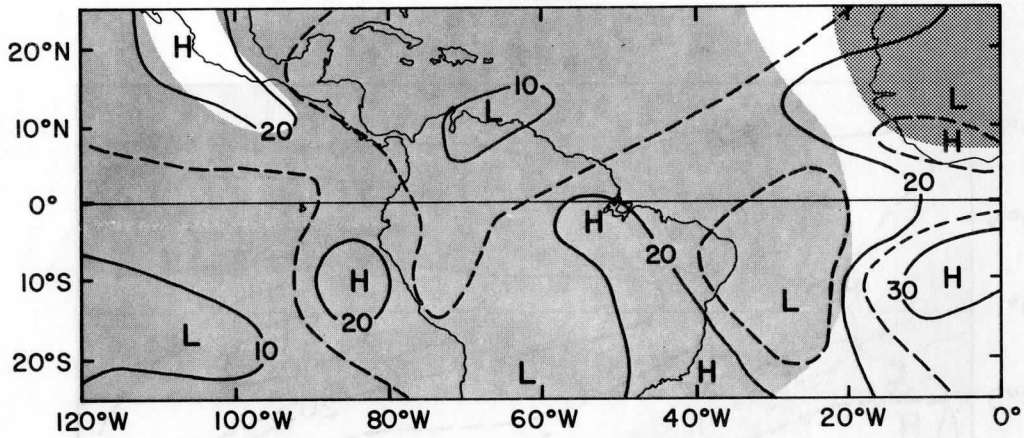

RMS
WINTER

Figure 7b

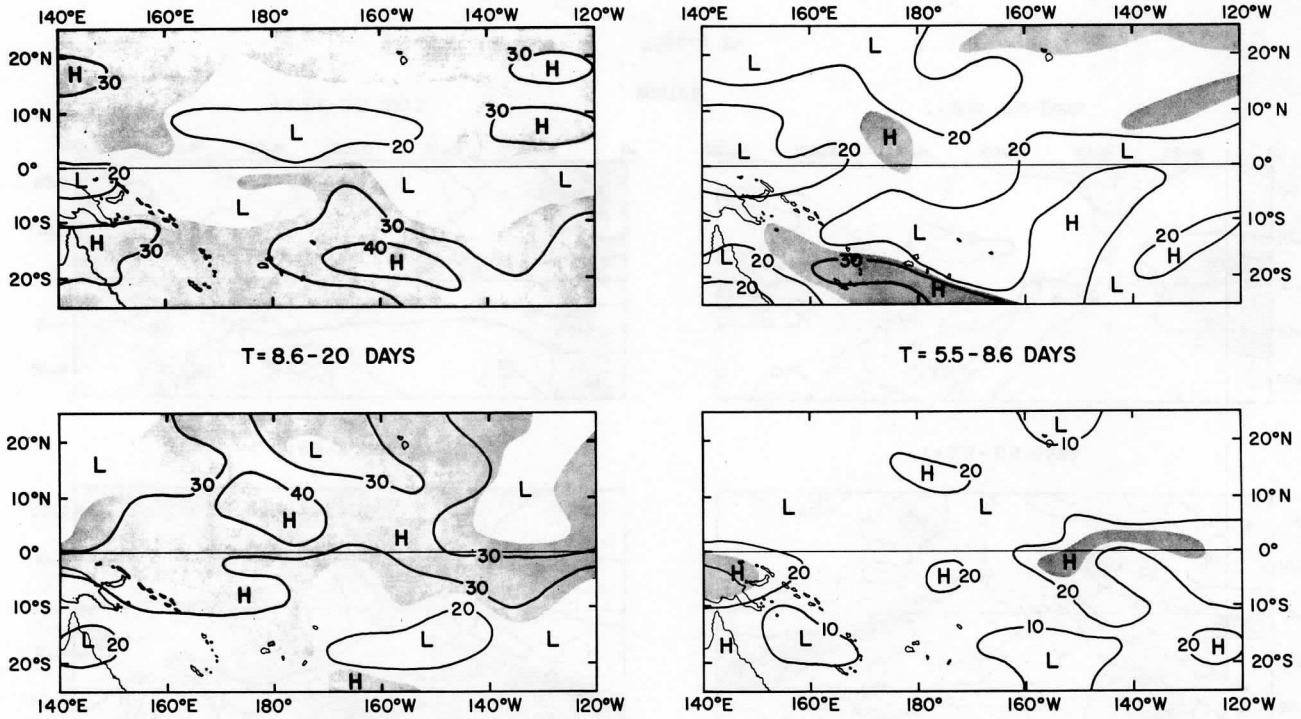
140°E
160°E
180°
160°W
140°W
120°W
20°N
10°N
0°
10°S
20°S
T= 8.6-20 DAYS
T = 5.5-8.6 DAYS
T=2.9-5.5 DAYS
T=2.0-2.9 DAYS
WINTER

Figure 8a

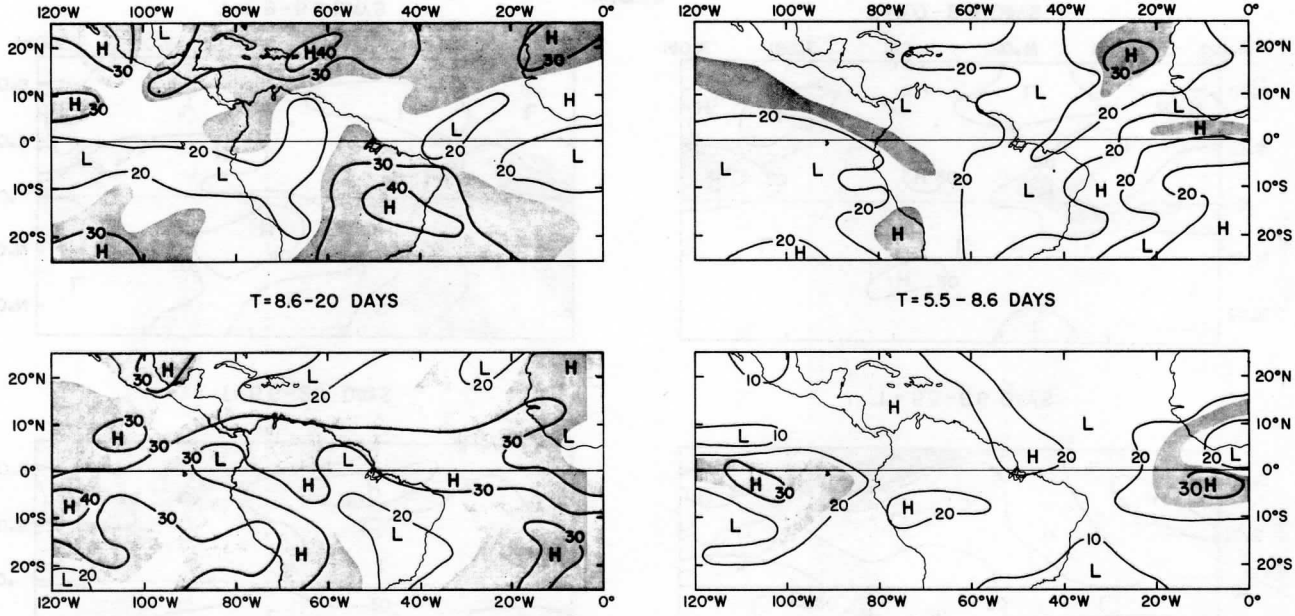
120°W
100°W
80°W
60°W
40°W
20°W
0°
20°N
10°N
0°
10°S
20°S
T=8.6-20 DAYS
T=5.5-8.6 DAYS
T=2.9-5.5 DAYS
T=2.0-2.9 DAYS
WINTER

Figure 8b

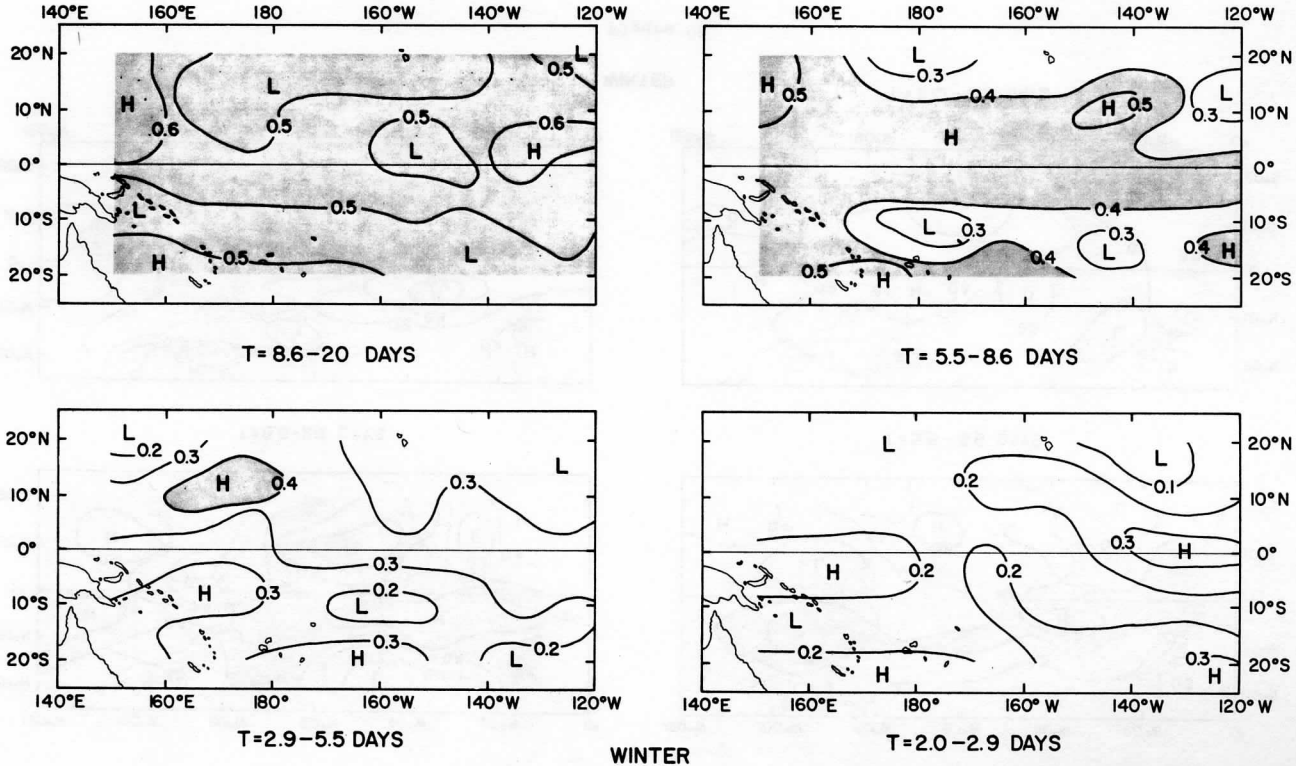
140°E
160°E
180
160°W
140°W
120°W
20°N
10°N
0°
10°S
20°S
H
L
0.6
0.5
T= 8.6–20 DAYS
T= 5.5–8.6 DAYS
T=2.9–5.5 DAYS
T=2.0–2.9 DAYS
WINTER

Figure 9a

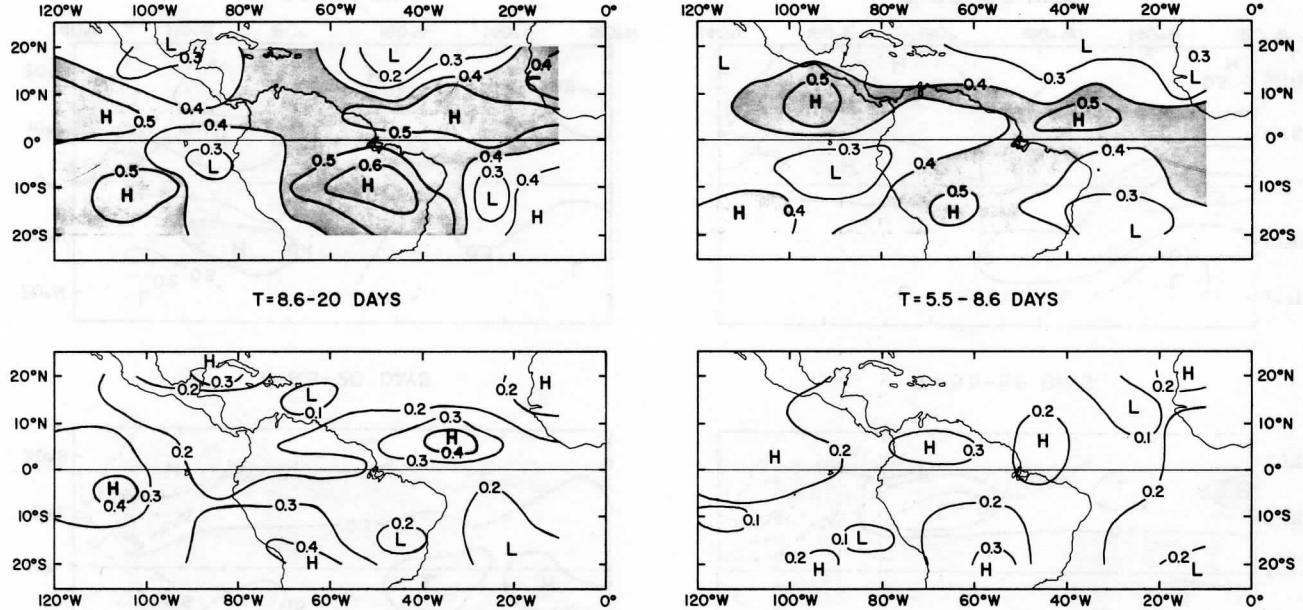
120°W 100°W 80°W 60°W 40°W 20°W 0°
20°N 10°N 0° 10°S 20°S
T=8.6-20 DAYS
T=5.5-8.6 DAYS
T=2.9-5.5 DAYS
T=2.0-2.9 DAYS
WINTER

Figure 9b

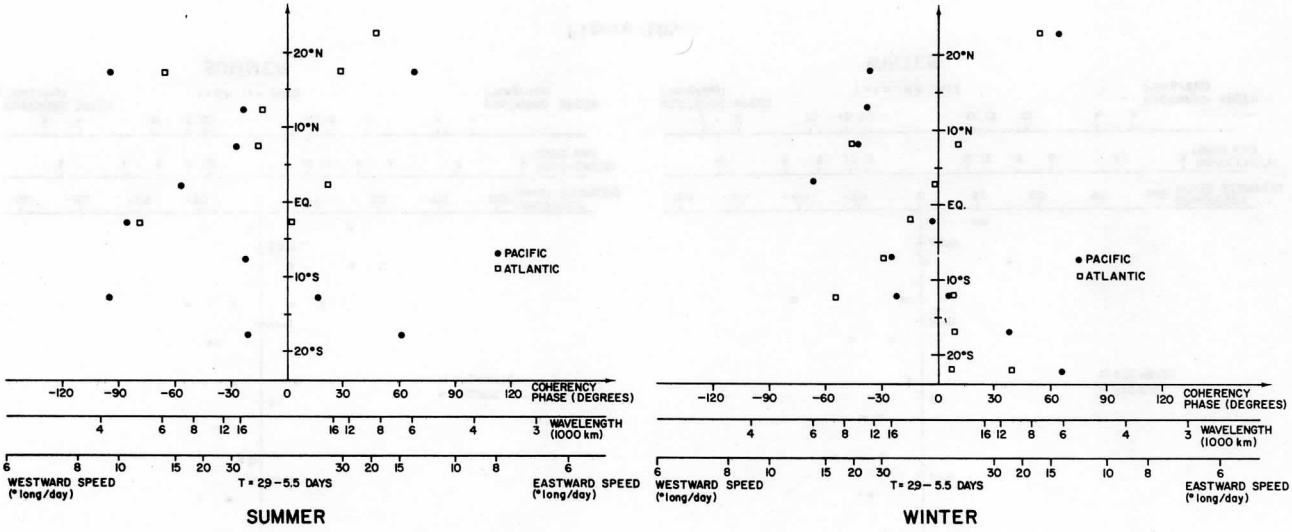
20°N
10°N
EQ.
10°S
20°S
PACIFIC
ATLANTIC
-120 -90 -60 -30 0 30 60 90 120
COHERENCY PHASE (DEGREES)
4 6 8 12 16 16 12 8 6 4 3
WAVELENGTH (1000 km)
6 8 10 15 20 30 30 20 15 10 8 6
WESTWARD SPEED (° long/day)
T = 29 – 5.5 DAYS
EASTWARD SPEED (° long/day)
SUMMER
WINTER

Figure 10a

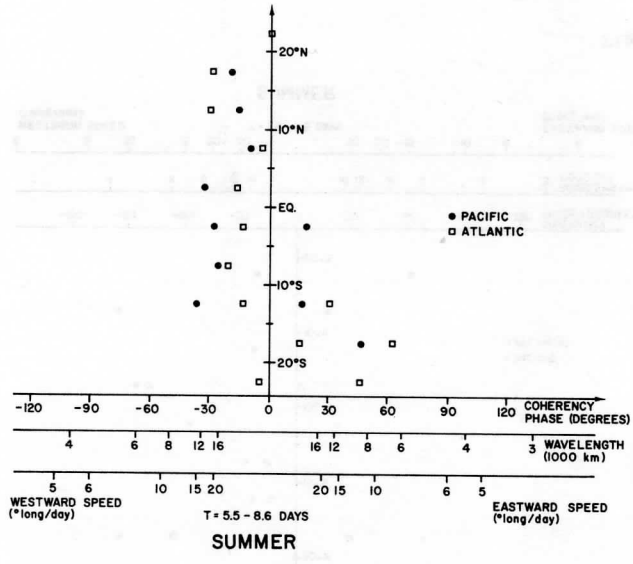
20°N
10°N
EQ.
10°S
20°S
● PACIFIC
□ ATLANTIC
-120 -90 -60 -30 0 30 60 90 120 COHERENCY PHASE (DEGREES)
4 6 8 12 16 16 12 8 6 4 3 WAVELENGTH (1000 km)
5 6 10 15 20 20 15 10 6 5
WESTWARD SPEED (°long/day)
T = 5.5 - 8.6 DAYS
EASTWARD SPEED (°long/day)
SUMMER

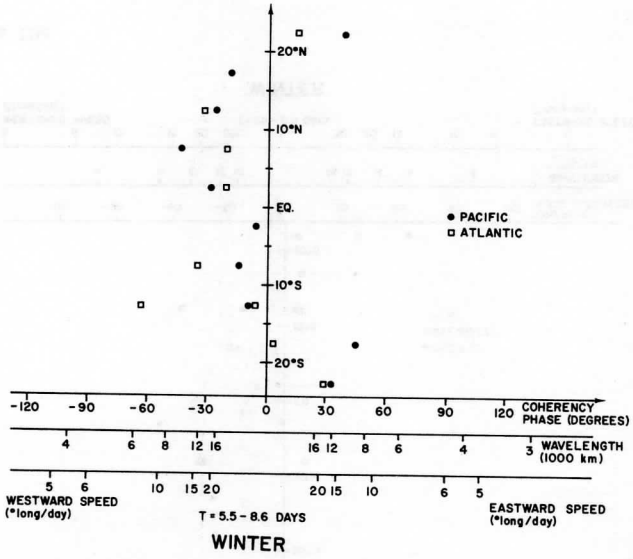
20°N
10°N
EQ.
10°S
20°S
● PACIFIC
□ ATLANTIC
-120 -90 -60 -30 0 30 60 90 120 COHERENCY PHASE (DEGREES)
4 6 8 12 16 16 12 8 6 4 3 WAVELENGTH (1000 km)
5 6 10 15 20 20 15 10 6 5
WESTWARD SPEED (°long/day)
T = 5.5 - 8.6 DAYS
EASTWARD SPEED (°long/day)
WINTER

Figure 10b

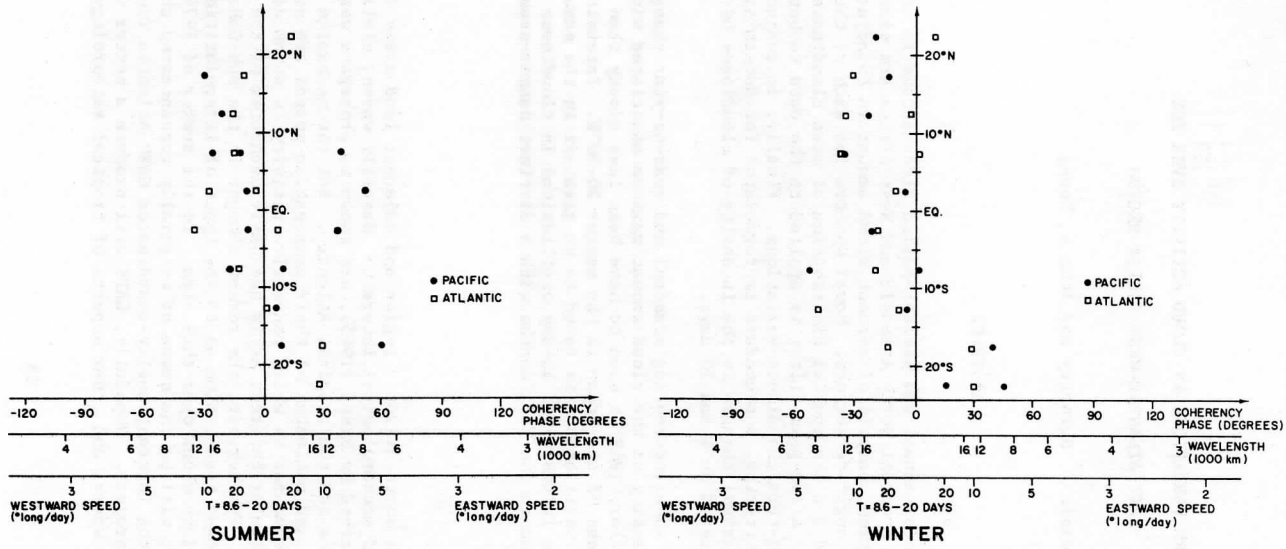
20°N
10°N
EQ.
10°S
20°S
PACIFIC
ATLANTIC
-120 -90 -60 -30 0 30 60 90 120 COHERENCY PHASE (DEGREES)
4 6 8 12 16 16 12 8 6 4 3 WAVELENGTH (1000 km)
3 5 10 20 20 10 5 3 2
WESTWARD SPEED (°long/day)
T=8.6-20 DAYS
EASTWARD SPEED (°long/day)
SUMMER
WINTER

Figure 10c

LONG-TERM VARIATIONS IN CLOUD ACTIVITY OVER THE EAST ATLANTIC-WEST AFRICA REGION

Dennis J. Heinricy and John A. Young

ABSTRACT

Seasonal, inter-annual and shorter-period fluctuations in cloudiness over the eastern tropical North Atlantic and West Africa are examined by means of time series analysis of percent cloud amount in 15 adjacent 5° latitude by 10° longitude sectors. Power spectra for each of the time series are presented and the spatial distribution of mean cloudiness amounts is investigated. A low-pass filter is applied to the data to better characterize long-term cloudiness variations. Finally, in conjunction with band-pass filtering, a procedure is formulated for determining seasonal and inter-annual changes in the intensity of cloudiness oscillations with periods centered on 4 and 10 days.

The results show interesting seasonal and year-to-year changes in the location and intensity of the cloud amount maximum associated with the ITCZ. In particular, 1969 is seen to have been less cloudy than usual over large portions of the ocean in the sector 20-30°W. Intensity of 4-day cloudiness oscillations is found to be greatest in the summer and fall months. The intensity of 10-day oscillations in cloudiness is seen to reach a maximum in the fall months with a distinct summer-season minimum.

INTRODUCTION

The tropical North Atlantic region and adjacent land areas in Africa have long been of meteorological interest. Easterly waves, similar to those first described by Riehl (1945), are known to propagate westward across West Africa and the tropical Atlantic. But the mechanics of their origin and decay and estimates of their propagation speeds are subject to wide debate. The manner in which convective activity is enhanced by these waves is of particular interest as is the basic mechanism of the convective activity itself. Furthermore, the recent drought in the sub-Sahara region has prompted renewed speculation as to the types of irregularities which might be expected to occur over this area. In the summer of 1974 the tropical Atlantic will be the scene of especially concentrated observation and research in the internationally-coordinated GARP Atlantic Tropical Experiment (GATE) project. Hopefully, GATE will produce a better understanding of easterly waves, and other aspects of tropical meteorology.

The GATE project will relieve in part one of the greatest hindrances to research in the tropical Atlantic, the lack of observational data. The problem of data paucity in the tropics has already been alleviated by the use of the meteorological satellites. Thanks to these satellites, the tropics are now continuously monitored from above, a tremendous advantage in a region possessing few meteorological observing stations.

Satellite photographs and the patterns of cloudiness which they exhibit have greatly stimulated research efforts in this field. In a recent study Wallace (1971) found that cloud brightness, as observed from satellite data, was a much better indicator of disturbed weather in the tropics than such standard meteorological variables as wind, pressure, temperature, and relative humidity. The data sets for the research to be described in this paper consist of once per day measurements from satellite photographs of percentage cloud amount in prescribed areas. This parameter is closely related to cloud brightness. Because the area used in this study is partially over land, percentage cloud amount seems preferable to cloud brightness, since over land areas high brightness values do not always indicate disturbed weather. Furthermore, brightness quality does not remain uniform because of changes in the satellite gain.

The anticipation of the GATE project has encouraged increased interest in the tropical North Atlantic as a research area. Until recently, many of the research teams actively involved in tropical research had concentrated their efforts on the Pacific area. In the Pacific, freedom from continental effects is more closely approximated and some semblance of a synoptic observation network exists.

A. Review of Literature

Most of the recent studies have employed, in one form or another, the technique of spectrum analysis of time series, the meteorological variable consisting of wind, temperature, relative humidity, and more recently, cloudiness amount (Sikdar, Young, and Suomi, 1972). While the conclusions reported in these studies varied considerably in detail, almost all investigators found a predominant wave period of from 4-5 days (Riehl, 1954; Rosenthal, 1960; Yanai et. al., 1968; Wallace and Chang, 1969; Nitta, 1970; and Sikdar et. al., 1972). These 4-5 day oscillations have usually been associated with the classical easterly waves. Waves with periods of 10 days and longer have also been reported, in particular by Wallace and Chang (1969), Yanai and Maruyama (1966), and Nitta (1970).

Other techniques have been developed as a supplement or alternative to spectrum analysis. Wallace (1972) used empirical orthogonal functions to represent time series in the frequency domain to help clarify and distinguish the types of waves found in the tropics. Young and Sikdar (1973) used latitude-time and longitude-time diagrams of filtered cloud patterns to help clarify regions of transient and persistent activity and to indicate the direction of cloud system propagation.

Comparatively less attention has been given to longer period oscillations, i.e., seasonal and inter-annual variations. Hubert (1969) noted some year-to-year variations in the ITCZ of the eastern Pacific. Also, Wallace and Chang (1969) took note of the change in intensity of the 4-day oscillation between two successive years. Beginning with the 1967

season, Simpson and his colleagues at the National Hurricane Center in Miami, Florida have been conducting a yearly census of Atlantic tropical disturbances. Simpson's study classifies the various systems in regard to their origin, propagation, and decay. Oort (1973) conducted another Atlantic study. He used satellite brightness data to compare summer season inter-annual variations over the GATE area. He found that day-to-day variations are quite large and that July and August show the highest brightness values. Of course, as already noted, an inherent problem in using brightness values over land areas is that cloudless desert areas can appear as bright as many cloud systems. Thus patterns of brightness can sometimes be misleading.

B. Statement of Research Objective

The purposes of this study are twofold. First, an attempt will be made to expand upon the type of information presented by Oort's study. In this attempt, inter-annual and seasonal changes in convective activity over the tropical Atlantic and West Africa will be examined. Whereas Oort's study dealt with the summer months only, this study will deal with a continuous data-set over a 4-year period, thus providing more information on an intra-annual scale. The second aspect of this study, closely related to the first, will treat in more detail the problem touched upon by Wallace and Chang in 1969. This is the question of the seasonal and inter-annual variability of cloudiness oscillations with periods in the range of 3-5 days and in the approximate range of 8 to 15 days. Previous studies treated the problem of phase propagation, but did not specifically treat amplitude changes in variations of a given frequency with respect to time.

In conjunction with the above, mean cloudiness amounts will be examined as will the power spectra for the 15 time series. The spectra provide some justification for the choice of particular frequency bands for more intensive study. In the following section, the method of data acquisition will be described as will the spectrum analysis and other statistical techniques used in this study. The mean cloudiness amounts and the power spectra obtained will be presented and discussed in Section 3. In Section 4, the low period cloudiness variations will be analyzed. And, in Section 5, the seasonal and inter-annual changes in the intensity of the 4-day and 10-day cloudiness oscillations will be analyzed and discussed. Section 6 will summarize the results of the study.

II. DATA ACQUISITION AND STATISTICAL TECHNIQUES EMPLOYED

The data used in this study consists of 15 sets of percentage cloud amount in adjacent 5° latitude by 10° longitude sectors over the eastern tropical North Atlantic and West Africa. Figure 1 shows the precise geographical location of the study area. The coast of Africa is indicated as is the region in which the GATE B-array will be located. The data was obtained from once-daily satellite photograph mosaics, representing output from the ESSA 3, 5, 7, and 9 satellites and ITOS 1. Beginning at March 1, 1967, the 15 data sets each extend over a 4-year interval.

A. Measurement Technique

The method used to obtain the measurements involved a super-imposed grid divided into percentage segments. Two estimates were made and the average used. Areas which appeared dull grey to the eye, corresponding to the lowest 30% on the brightness scale, were excluded. This procedure is assumed to have minimized the effect of scattered cloudiness, such as trade cumuli. Comparisons with planimeter measurements have shown that the technique is accurate to within several percent. Greater accuracy was not necessary because this study was basically concerned with relative variations rather than with absolute percentage amounts. However, within the error limits, it is likely that useful information about the absolute percentage amounts is also to be obtained from this data.

Missing data was supplied by linear interpolation when single days were missing. In several instances of longer data gaps, ATS III photographs were used in the place of the missing ESSA mosaics. An early afternoon pass was used in each case.

Because only one observation was obtained per day, this study gave no information concerning diurnal variations in cloudiness. That a diurnal variation in cloudiness does exist should not diminish the usefulness of this data-set. All observations were made at the same time each day, effectively eliminating any diurnal effects on the variations observed.

There are limitations to these data sets. Several sudden changes, known to have occurred in the satellite cameras' video amplifier chain and the associated brightness response, had a tendency to introduce false discontinuities into the data-set. These may, to some extent, be reflected in the computed spectra. In addition, changes are known to have occurred in the brightness response of the Vidicon camera system aboard the ESSA satellites. These were due to temperature changes, unequal illumination of the scan area, the problem of residual images, and other contaminating features. Described in detail by Schwalb and Gross (1969), the reader seriously interested in the relative importance of these problems is directed to their study. To attempt a precise documentation of these effects was unfortunately beyond the scope of this study. Suomi (1973) has pointed out that a small-amplitude two-day period (three days for ESSA 5) variation in brightness values occurred simply because of the orbital characteristics. Thus, one must be careful in interpreting observed features and must not attempt to read into the results more information than they contain.

Despite these limitations, the data used in this study has value. The quantity measured in this study, areal cloud amount, is somewhat affected by brightness changes, However, the error introduced is less than that contained within the brightness values themselves. Thus, the gross features observed in this data analysis should be valid. In light of the often poor brightness quality, the small element of subjectivity in the measurement technique as used in this study would seem an advantage. The computer-produced brightness values allow for no value judgments, whereas the trained human eye can often make these judgments as required for areal measurements. In further defense of the technique used, Young and Sikdar (1973), Chang (1970), and others found that individual cloud systems are usually identifiable from measurements of cloud amount. And Simpson (1968) found that waves in the wind field are accompanied by cor-

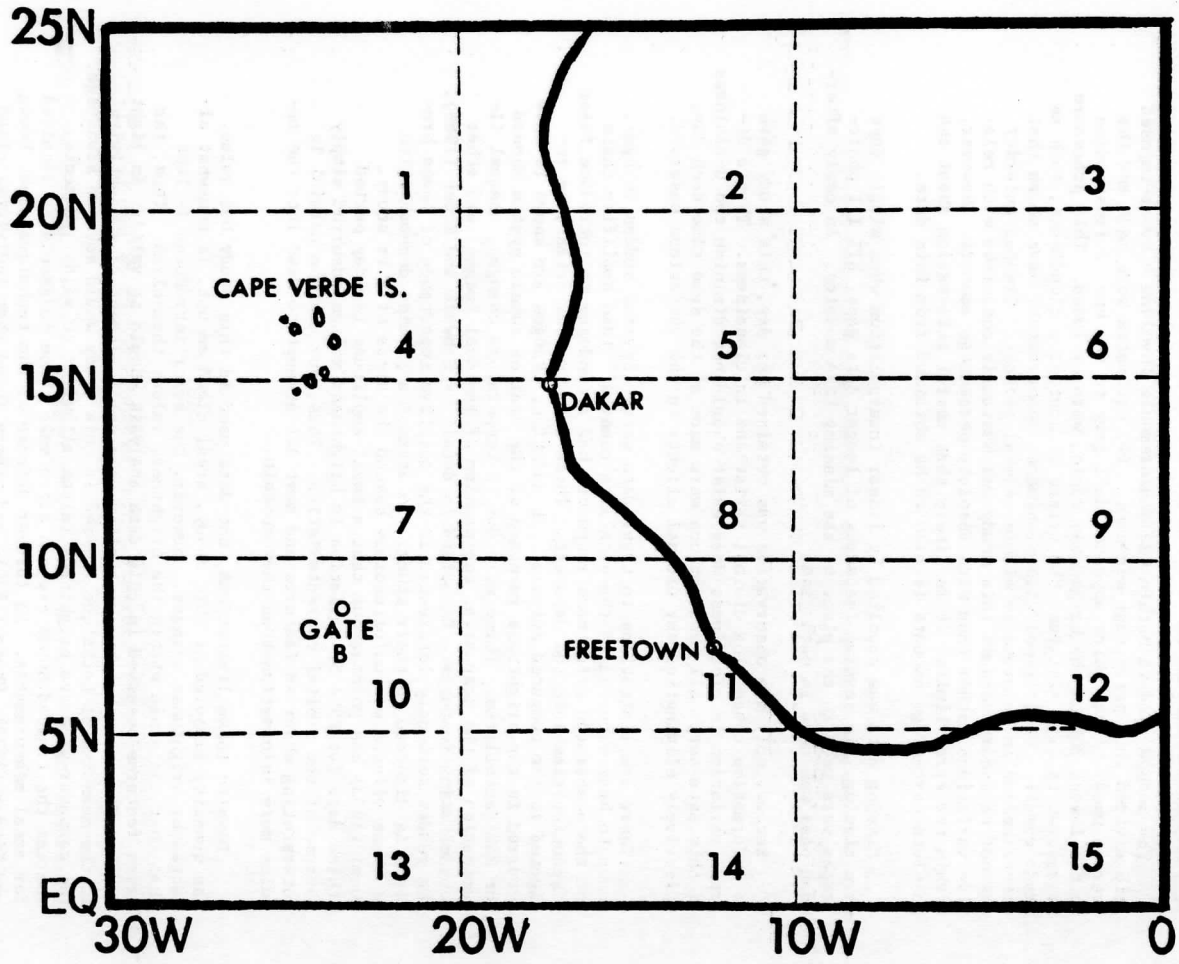

Fig. 1. Geographical location of study area. The 15 zones for which time series of percentage cloud amount were prepared are indicated by the dashed lines.

responding cloudiness variations. Thus, it is reasonable to assume that useful conclusions may be drawn from this data analysis.

B. Approach Used in Analyzing and Transforming Data

Like many of the recent studies described, this study uses the spectrum analysis technique as a starting approach. One of the most important advantages of the spectrum analysis technique is its ability to digest large quantities of data into a single graphical presentation. As used in this study, spectrum analysis is a statistical procedure which determines the frequency distribution of the variance of a time series over a prescribed frequency interval.

Spectral studies such as this cannot be used to infer the properties of extended time series because of the limited data sample. The spectra as computed can be assumed to be valid representations for only the time period under study, in this case, the four year period from March, 1967 to February, 1971. Julian (1971) and Wallace (1971) note that it is thus appropriate to label this use of spectrum analysis as diagnostic rather than statistical. Nevertheless, spectrum analysis does provide some measure of objectivity in the results obtained. It is often a preferred alternative to the case-study approach, which is entirely subjective in its selection of a particular disturbance for study.

The spectrum displays the frequency distribution of variance over a prescribed frequency range, most commonly from f = 0 to the Nyquist frequency. This is given by Equation 2.1 in cycles per day.

$$f_N = \frac{1}{2\Delta t} \qquad (2.1)$$

The Nyquist, or "folding frequency," is the highest frequency resolvable for a given time increment. The time increment, Δt, between successive observations in this study equals 1 day. Thus, f_N in this study equals 0.5 cpd. That is, the shortest period resolvable is two days.

The choice of the number of frequency bands for which spectral estimates are made, referred to as the number of "lags", is somewhat arbitrary. Resolution, or the ability to pinpoint peaks in power in a given frequency band, increases with the number of lags. However, the number of degrees of freedom, a measure of the statistical reliability of the results, decreases with increasing number of lags. Equation 2.2 (Panofsky and Brier, 1965) indicates how the number of degrees of freedom is determined.

$$\text{degrees of freedom} = \frac{2N-m/2}{m} \qquad (2.2)$$

where N = # of data points

m = # of lags

There is no simple rule to follow, although it is generally agreed that m should not be more than 10 or 15% of N.

Numerous computer programs for spectrum analysis are available. Most utilize techniques outlined by Blackman and Tukey (1957) and are quite expensive to use when a large number of data points is present. The method used in this study, the "Fast Fourier Transform," employs a different set of algorithms. However, it produces results essentially identical to other methods in much less computer time, as proven by Cooley, et. al., 1965.

The basic steps involved in the computation of the spectral estimates are the following:

(1) The trend is removed from the time series by least squares fitting of a straight line to the data and subtraction to obtain residuals.

(2) Zeroes are appended to the end of the data to extend N to an exact power of 2.

(3) The time series is subjected to a Fourier transform to obtain the complex Fourier coefficients.

(4) The real and imaginary parts of the Fourier coefficients are squared and summed over the number of bands desired and normalized to obtain the raw spectral estimate.

(5) The hanning procedure (Blackman and Tukey, 1957) is used to smooth the raw estimates.

(6) The results are normalized by dividing each estimate by the spectral frequency interval.

The power spectra computed for the original time series were dominated by a very strong annual periodicity, making it difficult to compare and assess the importance of higher frequency oscillations. To alleviate this problem, and following standard procedure, the data were subjected to a high-pass filter. This was a Gaussian filter with a standard deviation of 16.7 days and, after truncation, a total of 69 weights. This filter acted to severely attenuate power at periods greater than 50 days and thus served to better enable an analysis and comparison of higher-frequency periodicities in cloudiness amount. The response function for this filter is shown in Figure 2. The spectra obtained from the procedure just described will be presented and discussed in Section 3.

To provide insight into the strong annual and seasonal variation of cloudiness, a low-pass filter was applied to the original data sets. This filter was a 23-point normalized Gaussian weighting function with a standard deviation of 5.0 days. The effect of this filter was to severely attenuate power at frequencies less than 20 days. The response function for this filter is also shown in Figure 2.

Because of the wealth of documentation (Riehl, 1954; Wallace, 1971) attesting to the significance of periods around 4-5 and 10 days, filter functions for frequency bands centered at .1 cpd and .25 cpd (10 days and 4 days) were applied to the data sets. It is assumed that such filters might be useful in the isolation of fluctuations in cloud cluster activity and in the ITCZ. Because of the variation of exact periodicities report-

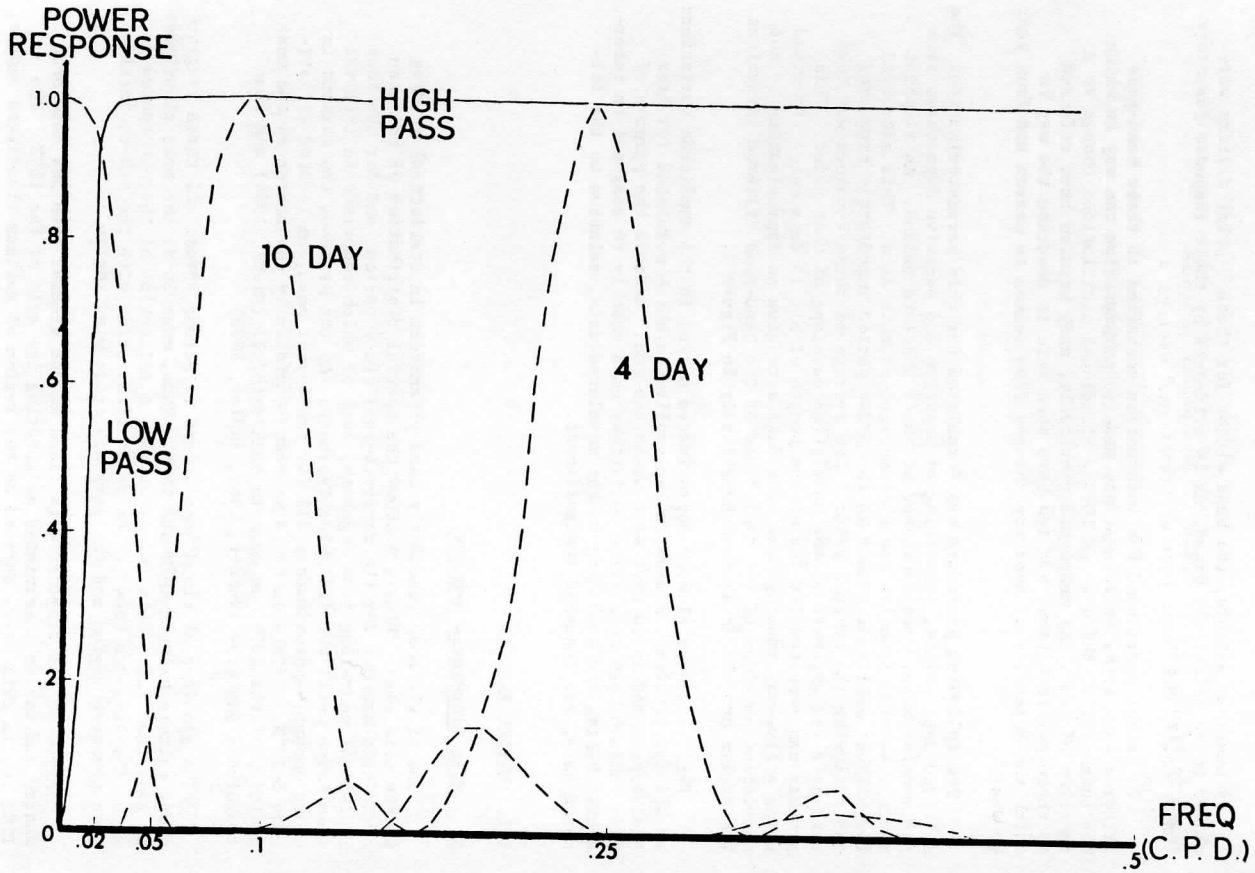

Fig. 2. Spectral response functions for the filters used in this study.

by numerous authors, the band widths for these 7-point filters were chosen to be relatively broad, as is evidenced by their response functions shown in Figure 2.

To better understand the information contained in these band-pass filtered data sets, an attempt was made to parameterize the way in which the intensity of these 4 and 10-day cloudiness oscillations change as a function of time. As mentioned previously, many studies have referred to these periodicities, but few have been able to describe the way in which the intensity of activity changes from season to season and from year to year.

The following procedure was formulated for this parameterization. The filtered data points, consisting of positive and negative departures from the running mean, were converted to their absolute values. An 11-point moving, sorting function was then applied to this data. This extracted the highest amplitude values in the 5-day period immediately preceding and following the central point. The average of these 2 values was then used as a raw estimate of the modulation envelope of that point. This process was repeated for the entire length of all 15 data sets. Smoothed using a five-day running mean, the data sets give an approximation to the modulation envelope of the amplitudes of the band-pass filtered variations. The entire process is shown schematically in Figure 3.

This procedure closely approximated maxima in the amplitude variations at all frequencies. Minima in the amplitudes which persisted for less than approximately 10 days were de-emphasized. Because the purpose of this endeavor was to examine variations on a monthly to seasonal to inter-annual basis, the small lag in the modulated data, relative to the filtered data, was rendered insignificant.

III. INITIAL RESULTS

A. Mean Cloudiness Amounts

One of the most frequently used parameters in statistical studies is the time mean. Figure 4 shows the spatial distribution of the mean cloudiness amounts for the entire 4-year study period, and for the four individual year-long time segments, each of which comprises an interval from March until the following February. As can be seen, the maximum in cloud amount, approximately 37% for the 4-year mean, is located at latitude 5-10°N. This area has also been consistently documented as the mean position of the ITCZ, as seen in both rainfall (Riehl, 1954) and mean cloudiness patterns (Hubert, 1969; Sadler, 1972).

The gradient of cloudiness amount is strong across all three longitudinal sectors between 10°N and 20°N. Thus, near 20 N, the mean cloudiness is less than 15%. This is, of course, a reflection of the pronounced region of subsidence known to exist in association with the sub-tropical high pressure region and the very dry trade wind regime.

Areas on the diagrams with cloud amount greater than 30% have been shaded and may be interpreted as locating the axis of the ITCZ. The ITCZ is, in this case, defined as the region of maximum cloudiness amount,

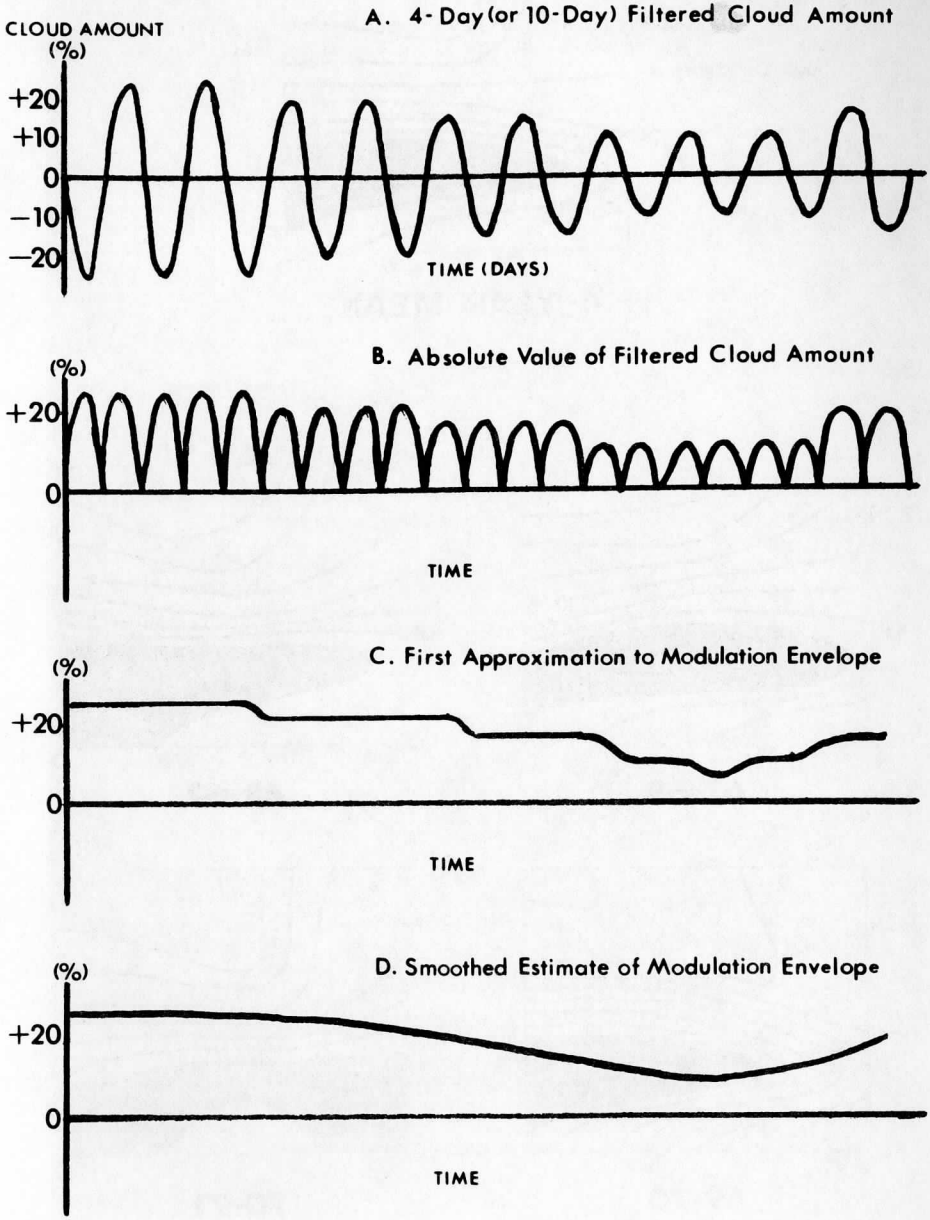

Fig 3. See List of Figures.

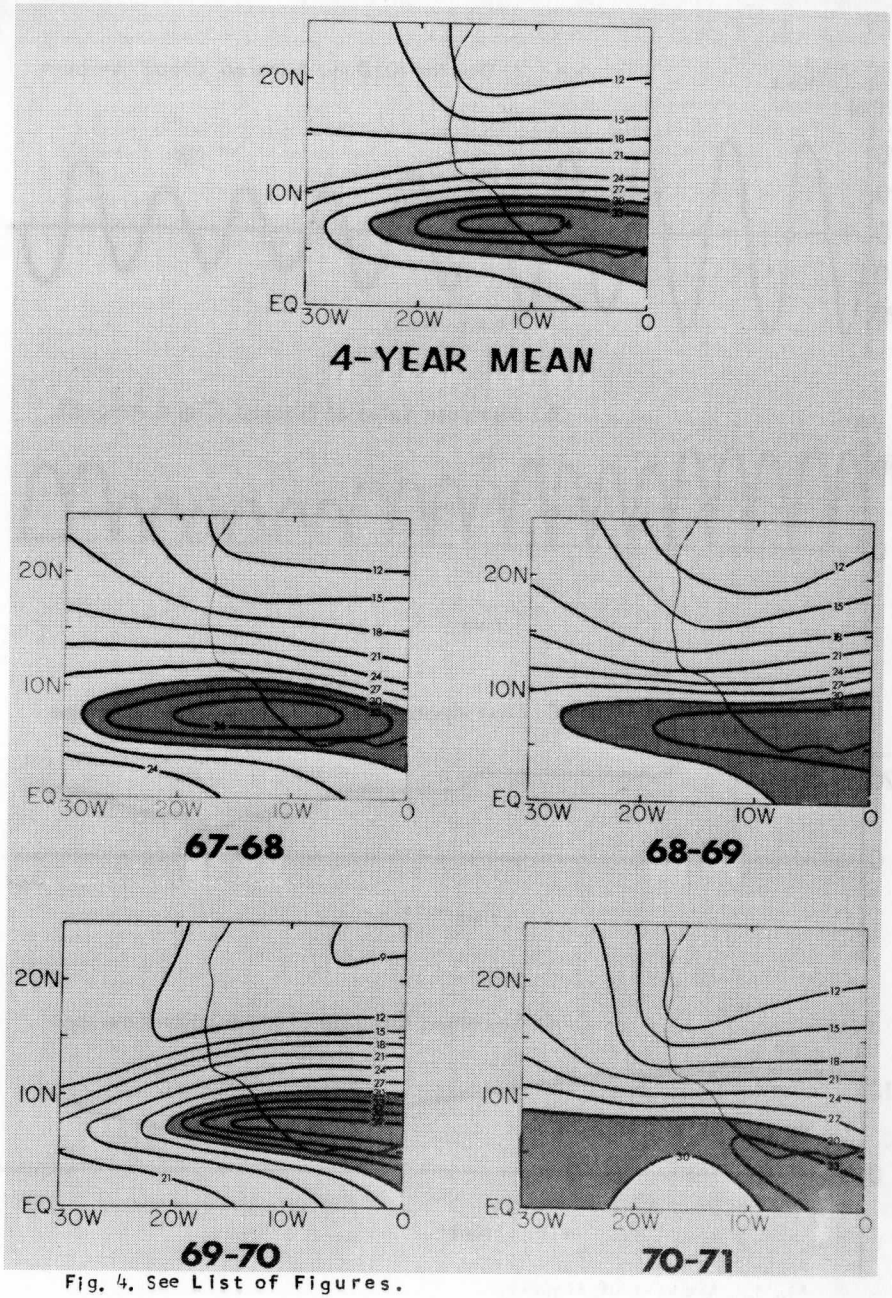

Fig. 4. See List of Figures.

one of several definitions employed in the literature (Sadler, 1972).

It is interesting to note that there seems to have been a gradual southward protrusion of the low cloudiness amounts associated with the desert regime over the four-year period. The mean ITCZ in 1970 was located unusually far south in the eastern part of the area. Lower values of mean cloudiness are observed throughout the eastern sections of the study area. Conversely, over most of the ocean area between the Equator and 10°N, including the GATE region, there are increased cloud amounts relative to 1969.

Annual means, of course, provide little insight into the seasonal nature of the cloudiness regime. To this end, seasonal means of cloudiness amount were prepared for seven 6-month seasonal segments contained within the data set. The choice of seasonal sub-divisions was not arbitrary. It was based on the time when easterly waves are known to affect the region (Simpson, 1969) and on the fact that, for many of the continental regions in the study area, June marks the approximate beginning of the rainy season (Griffiths, 1972). Thus, the year was divided into two segments, from June to November and from December to May. Figure 5 depicts this information; again, shaded areas represent a greater than 30% cloud amount. In light of these factors, it is not surprising that there are great seasonal changes in cloudiness amount. Mean cloudiness amount is seen to reach over 50% in certain areas for the entire six-month summer/fall season while in December to May, the dry season, values between 10-20% are observed. In two out of the three dry seasons illustrated, all parts of the study area were characterized by less than 30% mean cloud amount. Both the dry and rainy seasons in 1970 were characterized by unusually low cloud amounts over wide portions of the study area.

It is interesting to consider these mean cloudiness amounts in light of observed rainfall amounts. Landsberg (1973), in a study of annual rainfall totals at Dakar (15°N, 17°W), notes that 1967 and 1969 were relatively wet years while 1968 and 1970 were unusually dry. In 1967 and 1969, there is a prominent northward protrusion of the isolines of cloudiness amount near Dakar. The years 1968 and 1970 show an opposite southward protrusion of isolines during the rainy season, presumably due to southward shifting of the dry Sahara's influence. Obviously these interannual variations of cloudiness are a reflection of corresponding interannual variations in the large-scale circulation of the tropics, the mechanisms and causes of which are not clearly understood.

B. Spectrum Analysis of Data

By the techniques described in the previous section, the 15 data sets of cloudiness amount were subjected to a spectrum analysis to determine if periodicities are indeed present in the data. Because the data exhibit a substantial annual period of variation, the 15 time series were subjected to the high-pass filter described previously. Using a lag of 135 days, slightly less than 10% of the filtered number of data points, 136 spectral estimates were obtained. These were at intervals of 0.0037 cpd, with approximately 20 degrees of freedom, as given by Equation 2.1. To provide smoothing and thus increase the statistical reliability of the

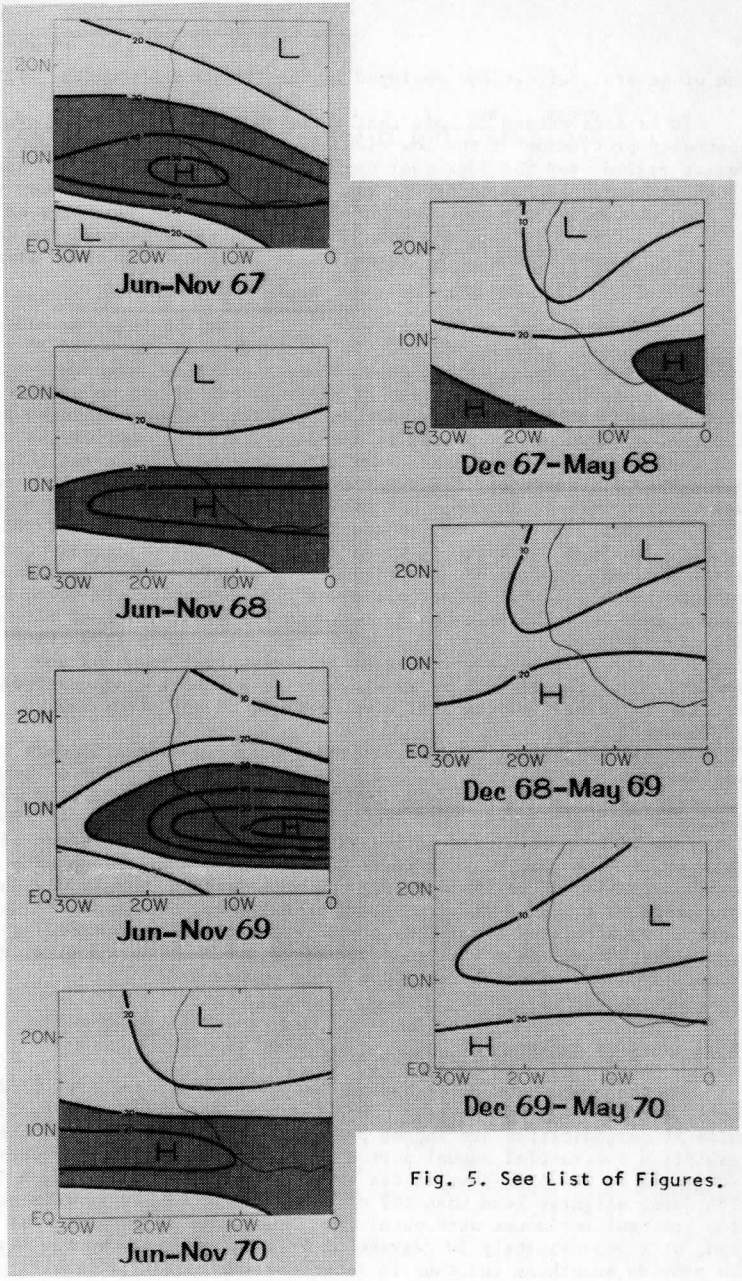

Fig. 5. See List of Figures.

results, adjacent spectral estimates were averaged in groups of three. This produced 46 spectral estimates possessing approximately 60 equivalent degrees of freedom. Thus, there is a 90% probability that the true spectral density for an individual frequency interval is within ± 30% of the estimate given. The power spectra were all normalized to eliminate the undesired domination of the spectra by large spatial differences in total variance. The spectra thus computed are shown in Figures 6a and 6b. Units of the normalized spectral estimate on the ordinate axis are (fractional cloudiness amount)^2/frequency interval. The normalization scheme was such that the sum of all 46 smoothed spectral estimates in each diagram equaled 0.33.

The red noise spectra for each time series, indicated by a dashed line, were computed by Equation 3.1, a technique using the lag 1 auto-correlation coefficient described by Mitchell (1966).

$$S_k = \bar{s}\left(\frac{1-r1^2}{1+r_1^2-2r_1\cos\frac{\pi k}{m}}\right) \qquad (3.1)$$

where r_1 = lag 1 auto-correlation coefficient

$\bar{s}$ = average value of all m+1 raw spectral estimates

m = # of lags

k = frequency band

Using confidence intervals from Hald (1952), the dotted lines above and below the dashed lines represent respectively the 95% and 5% confidence limits for the red noise spectra. The spectra computed are dashed from f = 0.0 to f = 0.02 cpd to indicate that, in this region, power has been severely attenuated by the high-pass filter. At all locations, the time series generally approximate the red noise spectra and thus display a high degree of persistence. However, peaks are in evidence near certain frequencies, indicating some deviations from pure persistence in the time series. The most northerly and northwesterly sectors show evidence of a spectral peak near 25-40 days at 0.03 to 0.04 cpd. To a lesser extent this feature is also present in the lower latitude spectra. It is interesting to note that Madden and Julian (1972) found evidence that circulation cells with a 40-50 day period are a relatively stationary feature in the tropics.

A majority of the sectors also shows peaks in the spectra centered near f = 0.1 cpd, that is, periods centered around 10 days. In addition, a majority of the sectors in the lower to intermediate latitudes (Figure 6b) show substantial amounts of variance at periods in the range of 3-5 days. A small amount of aliasing in the data is suggested by the tendency for minor peaks near the Nyquist frequency in several of the easternmost lower-latitude spectra. These minor peaks are also, undoubtedly, a reflection of the two-day periodicity of the satellite orbit changes mentioned in Section II A.

A clearer picture of the geographical distribution of the contributions to variance by different frequency bands is given by Figure 7. It

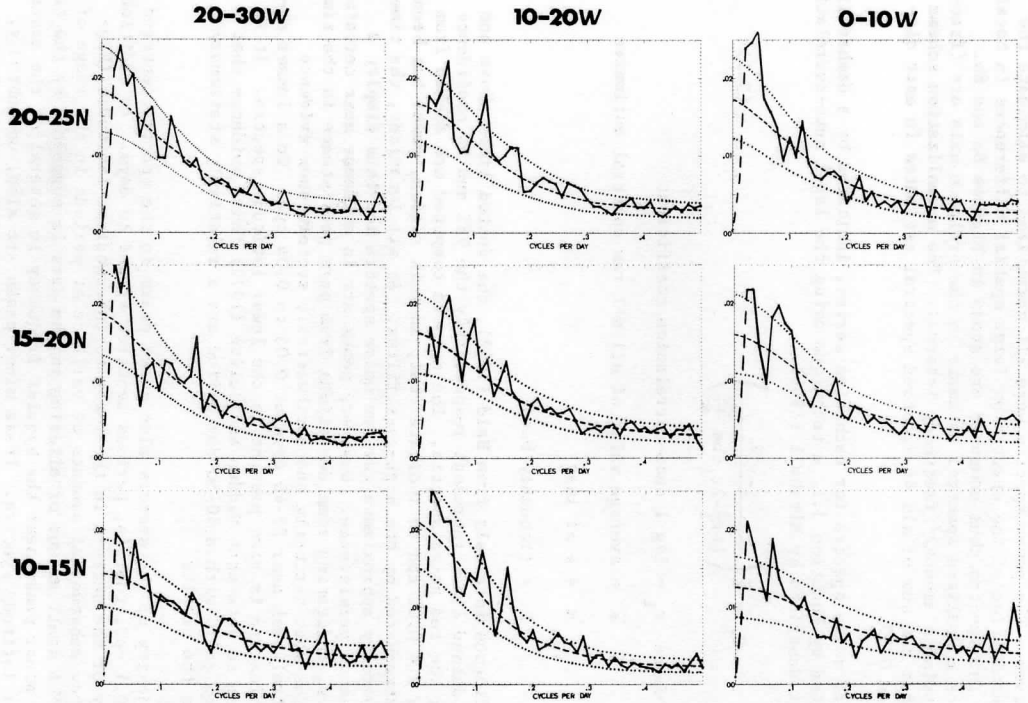

Fig. 6a. Normalized power spectra of areal cloud amount for indicated zones. Power at frequencies < 0.02 attenuated by filtering as indicated by heavy dashed lines. The continuous dashed lines indicated fitted red noise spectra and the dotted lines are the 95% and 5% confidence limits for the red noise spectra. Normalization scheme is such that sum of spectral estimates equals 0.23. The ordinate is the spectral estimate in units of (fractional cloud amount)^2/frequency interval.

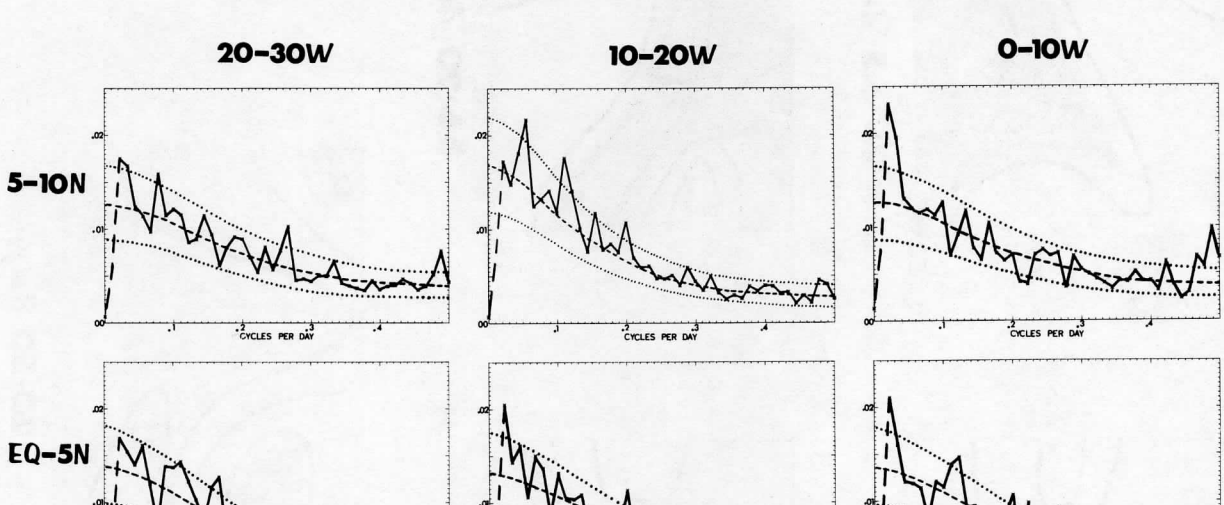

Fig. 6b. Same as Fig. 6a for indicated zones.

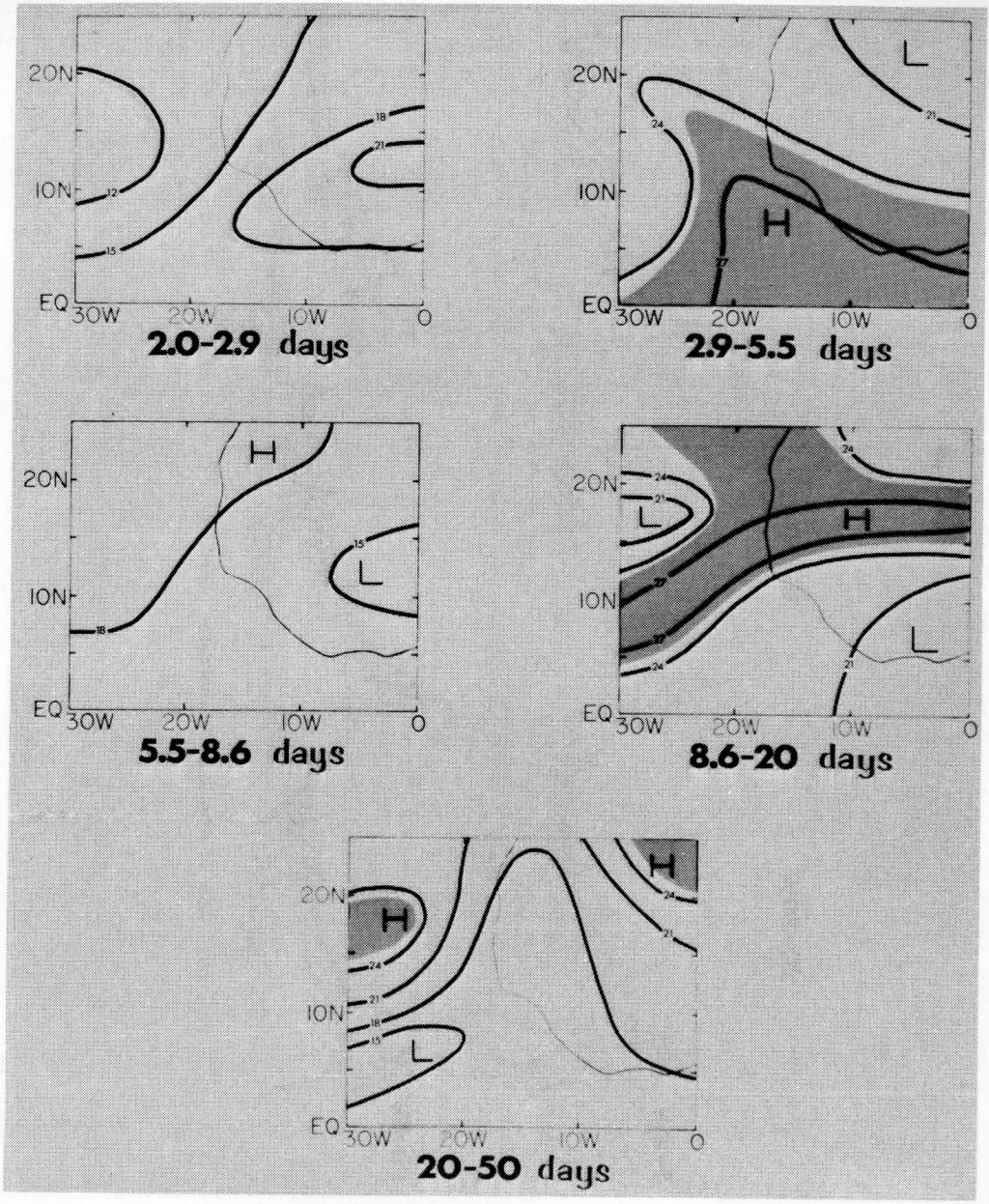

Fig. 7. See List of Figures.

should be noted that the top two diagrams represent contributions from relatively wide bands while the bottom three diagrams depict contributions from narrower bands. All zones show substantial amounts of variance in periods 2.9-5.5 days, with greatest contributions at the lower latitutes. The region of greatest contribution to the 8.6-20 day variance (in excess of 27%) is found in a latitudinal belt extending from 5-10°N in the western part of the study area to 15-20°N in the eastern regions. The GATE area falls very near this region of maximum contribution. The third frequency band for which significant contributions to the total variance are found is in the range of periods from 20-50 days. Here, the far northwest and northeast sectors show greater than 25% contributions to total variance.

Relatively small contributions to total variance are found in the frequency bands comprising periods of 2.0-2.9 days and 5.5-8.6 days. In the highest frequency band, this suggests that the problem of aliasing in the data, unavoidably present to a certain extent, was not too severe. Greatest contributions in this band occur over land where the diurnal cycle is presumably of some importance. The band from 5.5-8.6 days shows a rather amorphous pattern.

These results agree substantially with those found by Sikdar et. al. (1972) in a Pacific study. The authors of this work found a tendency for greater contributions to total variance in the high frequencies near the equator and greater contributions in the lower frequencies at higher latitudes. This is in general agreement with the findings just described.

IV. LOW-PASS FILTERED CLOUD AMOUNT

The power spectra just described represent a combination of effects from the entire length of the data sets. Since they provide no information as to month-to-month, seasonal, or inter-annual variations in oscillations of a given frequency, the data sets were subjected to a low-pass filter function, as described in Section II. The low-pass filtered cloud amount represents a well-smoothed estimate of the long-term cloudiness variation, periods less than 20 days being suppressed. However, it should be noted that a group of successive short-period cloudy intervals lasting longer than 10 days would also contribute to the long period intensity.

Following the example of Young and Sikdar (1973), the low-pass results were tabulated in the form of latitude-time diagrams. These show how, for the given longitude sectors (in this study, three sectors, each of 10° breadth), the low-pass filtered cloud amount varies at different latitudes as a function of time. They are presented in Figures 8a, 8b, and 8c. Shading indicates cloud amount greater than 20%. The isoline interval is 20%. To facilitate inter-annual comparison, the diagrams were separated into four year-long segments, each "year" comprised of data extending from March until the following February.

The advance northward of ITCZ-related cloudiness in the spring months and its retreat southward in the autumn months clearly evidenced in these diagrams. The shaded areas with greater than 20% cloud amount are seen to expand significantly in coverage during the summer months. The more extreme cloud amounts, greater than 40% and occasionally greater than 60%,

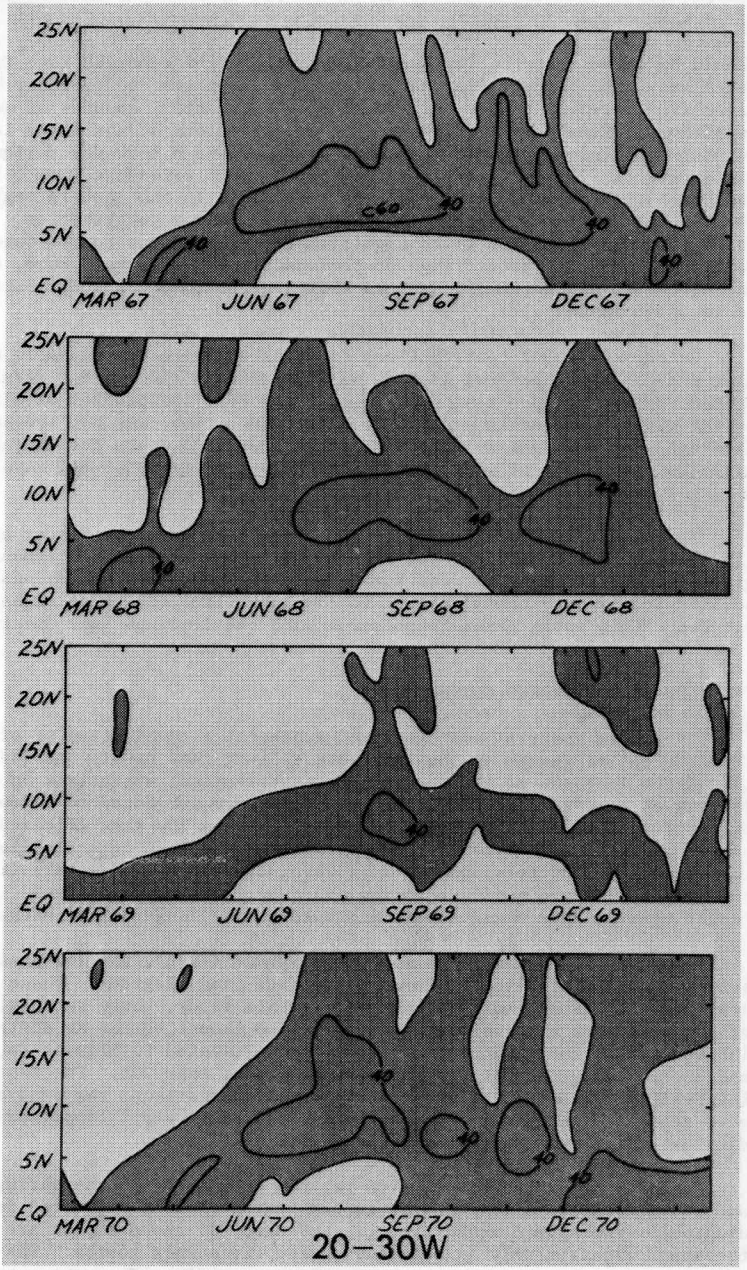

Fig. 8a. See List of Figures

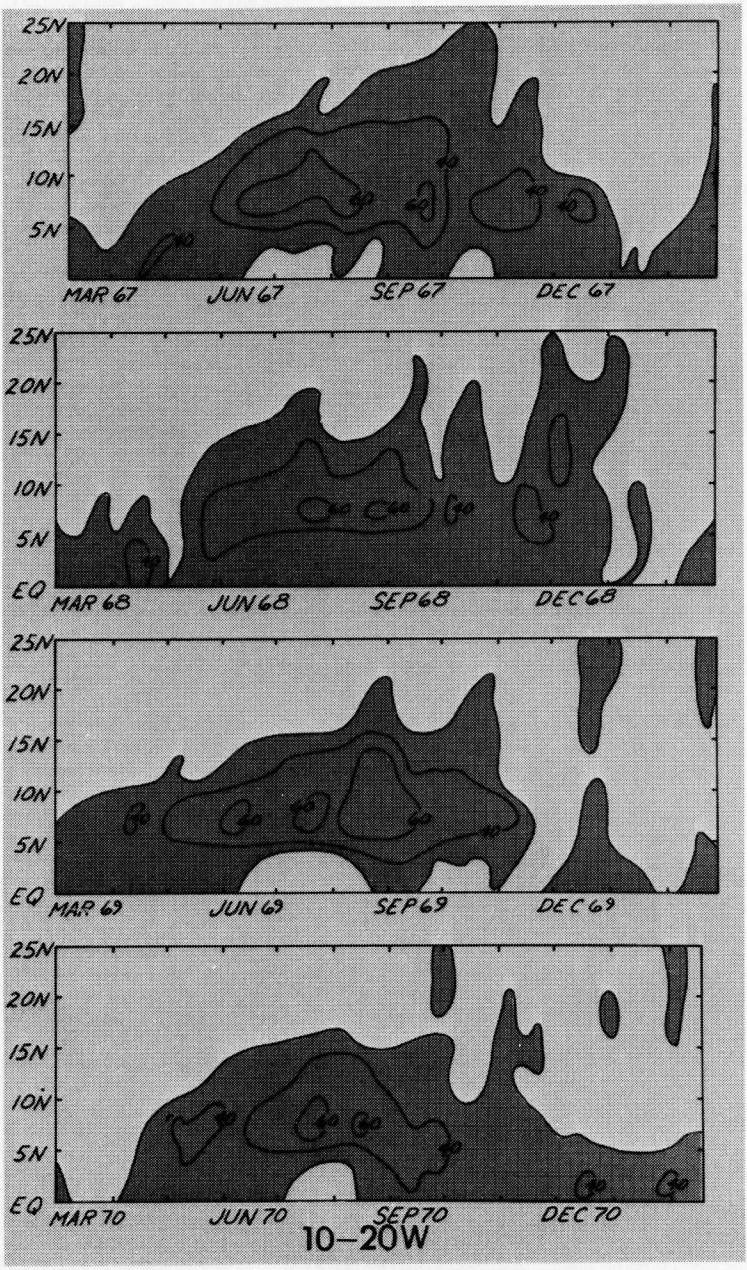

Fig. 8b. Same as Fig. 8a for longitude sector 10-20°W.

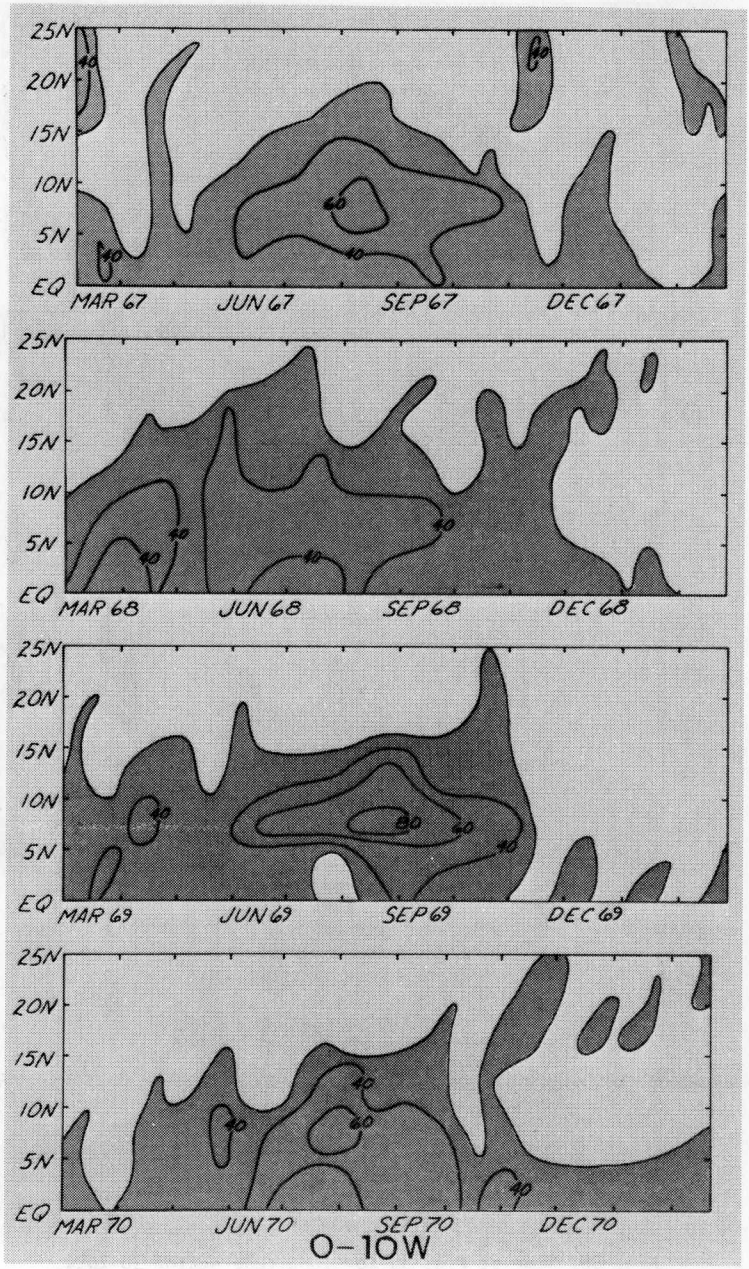

Fig. 8c. Same as Fig. 8a for longitude sector 0-10°W.

occur primarily during the months from June to November. They occur regularly between 5-10°N, the ITCZ latitudes, with rarer occurrences as far north as 15°N. It is also clear from the diagrams that the ITCZ undergoes alternate phases of more and less intense activity, as evidenced by the series of closed isolines of higher cloudiness amount. This is apparent in all three longitudinal sectors but is most pronounced in Figure 8b at longitude 10-20°W. Here, the pulses of more extreme cloud amount seem frequently to come at intervals of 1-2 months. October seems to be a transition month, frequently marked by an abrupt decrease in cloud amount, only to have higher values return again in November. Interestingly, October is the month in which large-scale circulation changes usually occur in the upper atmosphere over the region, the upper level easterlies of the summer months being replaced by a more westerly regime (Simpson, 1969).

As the belts from 5-10°N and 10-15°N become more cloudy in late spring and early summer, the belt near the equator becomes less cloudy for an interval of several months until the ITCZ retreats southward in autumn.

In the longitude sector 20-30°W, while the increase in cloudiness amount starts spreading northward in April, it is usually late May to late June before the effect of increased cloudiness is felt at latitudes 10-20°N, At the higher latitudes the increase is quite sporadic and irregular, lasting for only 1-2 months. Instances of increased cloudiness later in the year are probably attributable to occasional incursions by waves in the westerlies from higher latitudes.

Less cloudy than the other years shown at 20-30°, 1969 has values greater than 40% appearing first in mid-August. These are generally short-lived. Interestingly, Martin and Suomi (1972), in a satellite study of cloud clusters, found significantly fewer clusters and correspondingly less areal coverage in the eastern Atlantic during July 1969 than during July 1970.

Comparing the longitude sector 20-30°W, over ocean, with those from 10-20°W and 0-10°W, which are largely over land areas, the increased latitudinal gradient of cloudiness in the latter sectors becomes apparent. Over the ocean sector, the gradient between 10°N and 20°N seldom exceed 20%; over the land sectors the gradient in the summer season frequently exceeded 40%. In an extreme case, in the summer of 1969, the gradient between 10-20°W exceeded 60%. In all three longitude sectors, the gradient of cloudiness amount between the equator and 10°N was also very strong, commonly exceeding 40%. Comparing all three diagrams, it is seen that the season of increased cloudiness arrives earlier at the more easterly longitudes. It arrives at 10°N in March or April in the sector 0-10°N, in April or May in the sector 10-20°N, and usually not before June in the sector 20-30°W. On the other hand, relatively high values of cloud amount linger at 10°N over the ocean sector commonly into December or January. From 0-20°W, decreased cloud amounts are noted 1-2 months earlier.

A more conventional representation of the low-pass filtered cloud amount is presented in Figures 9a, 9b, 9c, and 9d. Each figure, consisting of 24 maps, represents the seasonal change of the low-pass filtered cloud amount for a one-year interval. Time increases left to right across each row in succession from the top in increments of 15 days. Thus, the first row represents March and April, the second row May and June, etc.

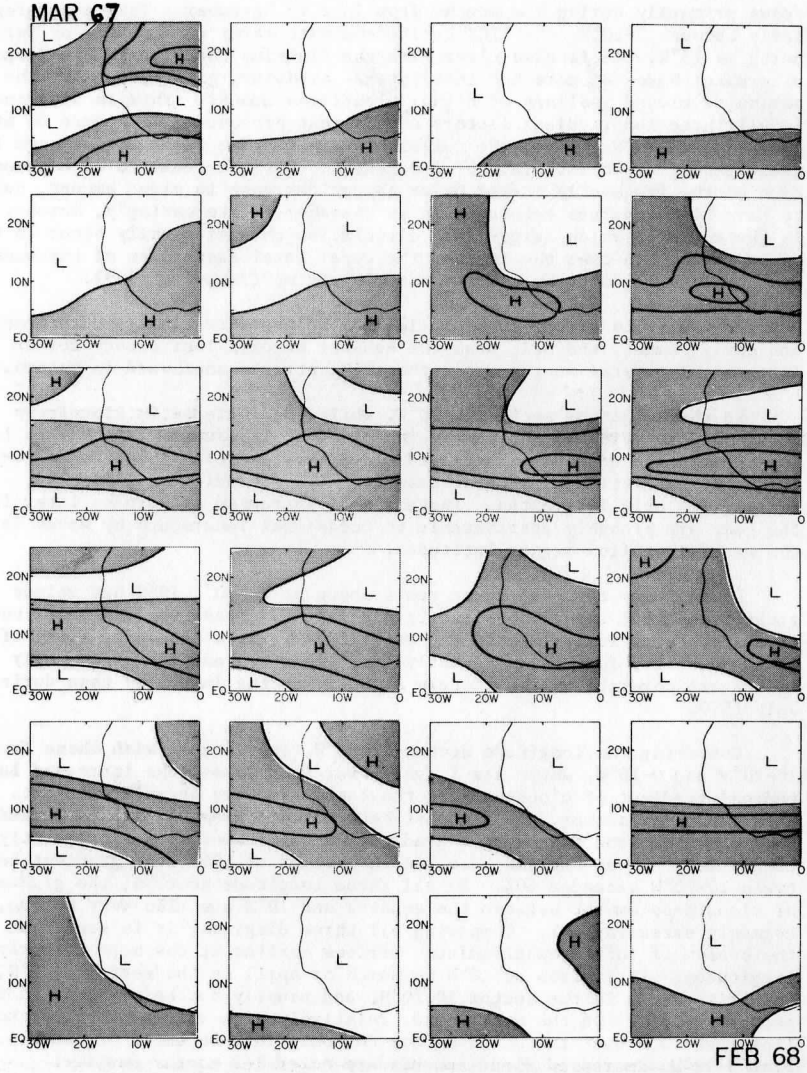

Fig. 9a. Twice-monthly spatial maps of low-pass filtered cloud amount for the p riod from March 1967 until February 1968. Time increases from left to right across each row in succession starting from the top in increments of 15 days. Shading denotes regions with greater than 20% cloud amount. Relative maxima and minima are indicated by H's and L's on each map.

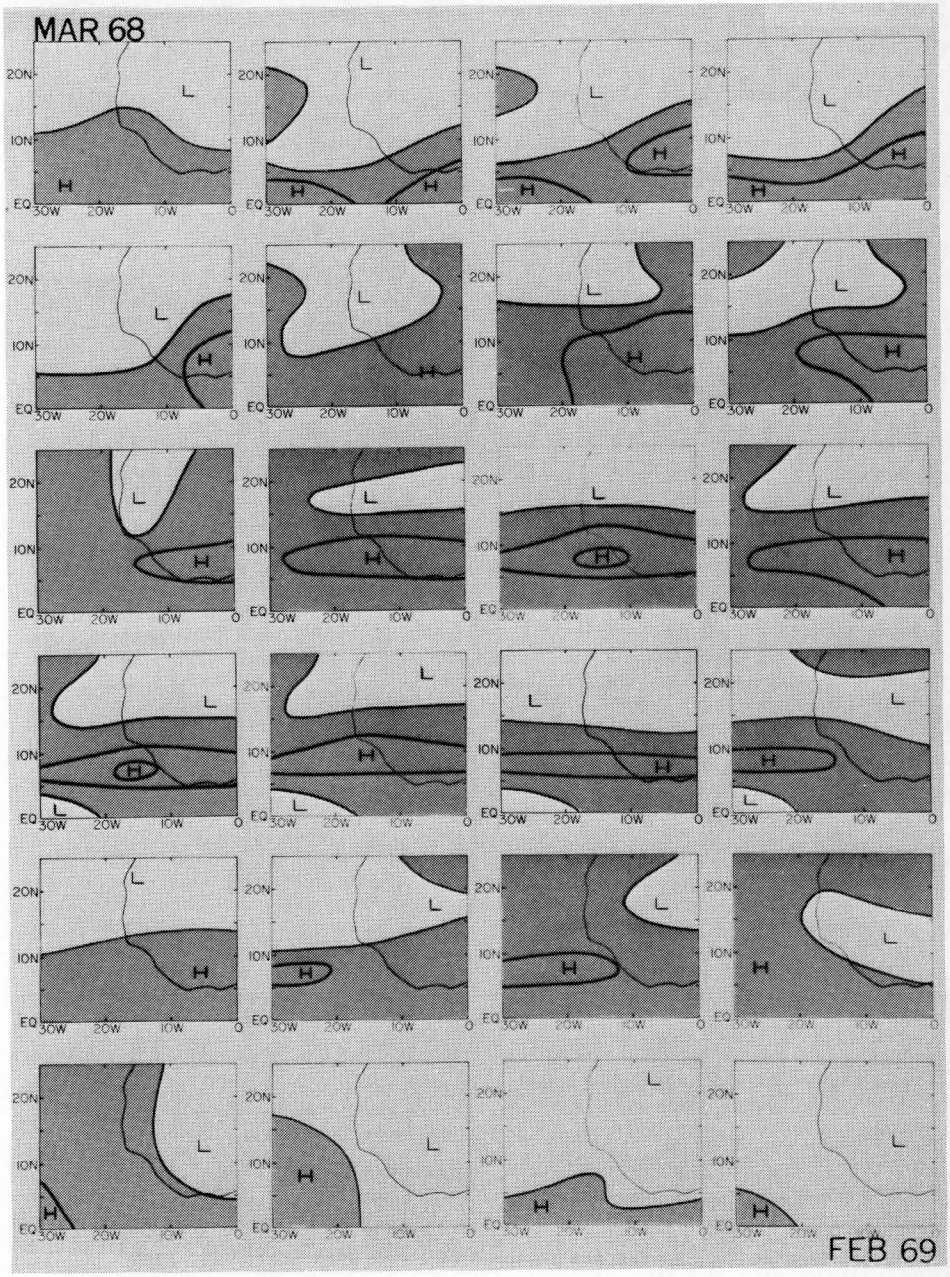

Fig. 9b. Same as Fig. 9a for the period from March 1968 until Feb. 1969.

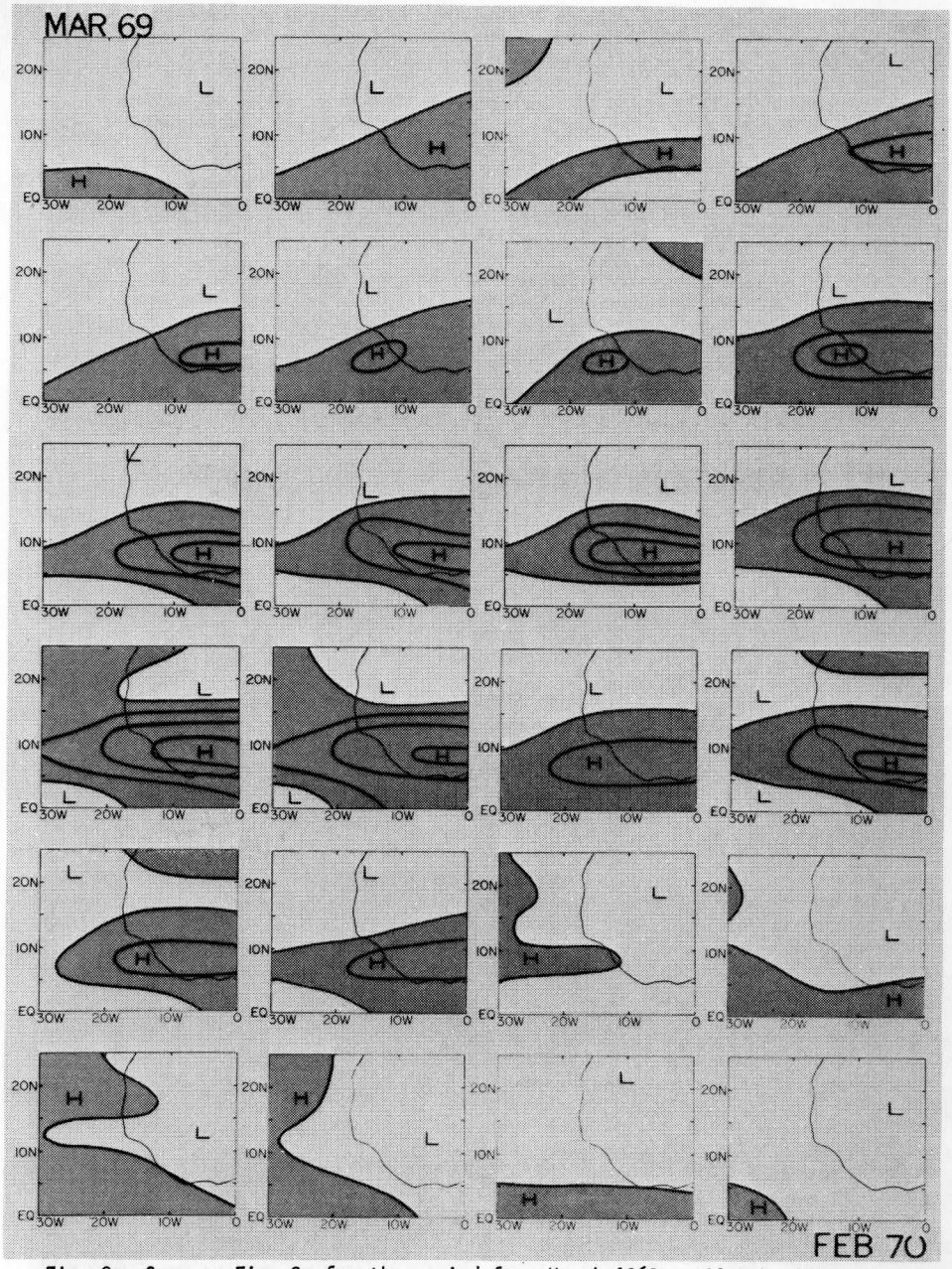

Fig. 9c. Same as Fig. 9a for the period from March 1969 until Feb. 1970.

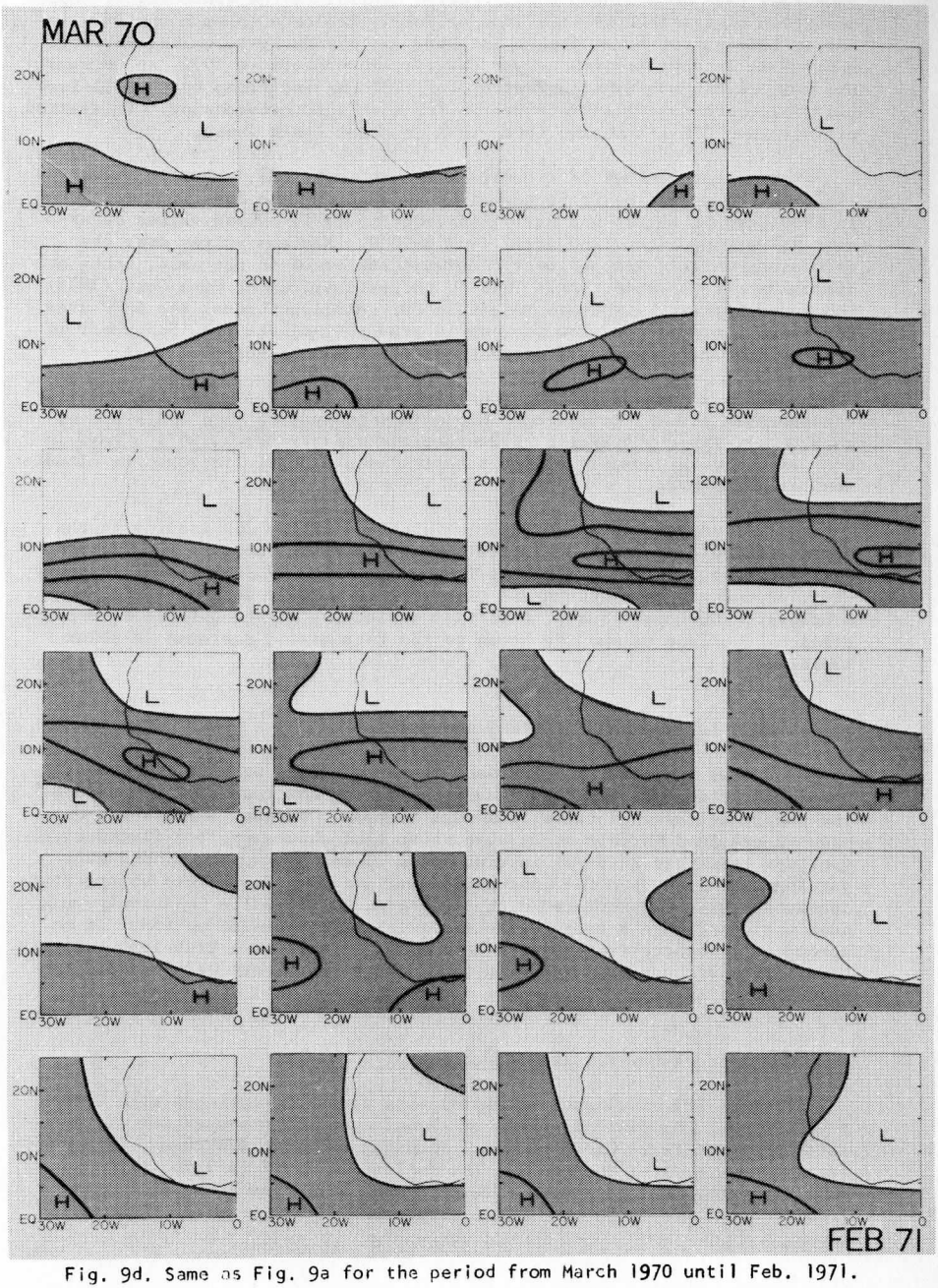

Fig. 9d. Same as Fig. 9a for the period from March 1970 until Feb. 1971.

The 40% isoline which appears first, sometime between late April and early June, may take on a banded configuration similar to the conventional representation of the ITCZ in late June or July. It lasted as such until December in 1967, until late October in 1968, until late November in 1969, and until late October in 1970. Over the eastern sectors in 1970, an unusually dry year in the sub-Saharan region, the ITCZ, as indicated by the 40% isoline, seems to have been retarded in its northward progression. It arrived at latitude 10°N 1-2 months later than in other years shown.

The highest values of cloudiness amount, over 60%, occur in August in 1967, in August and early September in 1968, from late June into October in 1969, and in August and early September in 1970. These values occur over or very near the land areas from 5-10°N. Maximum values over the GATE area, while somewhat lower than adjacent areas to the east, occur at approximately the same time. This is in basic agreement with Oort (1973) who found highest brightness values in July and August over the GATE area. The dates listed above, however, would tend to indicate that September is usually just as cloudy as July in this region (see Figure 8a also).

The Sahara region in the upper right-hand corner of the diagrams is consistently almost cloud-free. Cloud amounts greater than 20% are very rare, short-lived instances. For example, in early March 1967, a wave in the westerlies presumably caused a short-lived dramatic increase in cloudiness over the area.

It is interesting to note the orientation of the 20% isoline in the spring months compared to the late autumn and winter months. During the spring months, the orientation is frequently slightly southwest-to-northeast, whereas in late autumn and winter is it usually more northwest-to-southeast. Quite obviously, this is a reflection of the different response times of the land versus the ocean to the increase or decrease in solar radiation.

V. MODULATED BAND-PASS FILTERED CLOUD AMOUNT

The maps and diagrams discussed in the previous section indicated the long-period variations in cloudiness during the course of a year and the change in these patterns from year to year. Various authors and the spectra examined in this study have shown that shorter-period fluctuations (periods less than 20 days) in cloudiness amount are super-imposed with varying intensity upon the long-period variations. Relatively strong fluctuations could be associated with cluster activity, while relatively weak ones would indicate a comparatively persistent cloudiness period. In an attempt to characterize the slow variations in this more transient activity, time series of band-pass filtered modulated cloud amount were prepared as described in Section II.

A. Modulated 4-Day Filtered Cloud Amount

Figures 10a, 10b, and 10c employ once again the latitude-time format to illustrate the basic features of the time series prepared for the modulated 4-day filtered cloud amount. Shading indicates deviations from the running mean greater than 7.5%. The isoline interval is 7.5%, that is, isolines within shaded areas represent a 15% deviation from the running

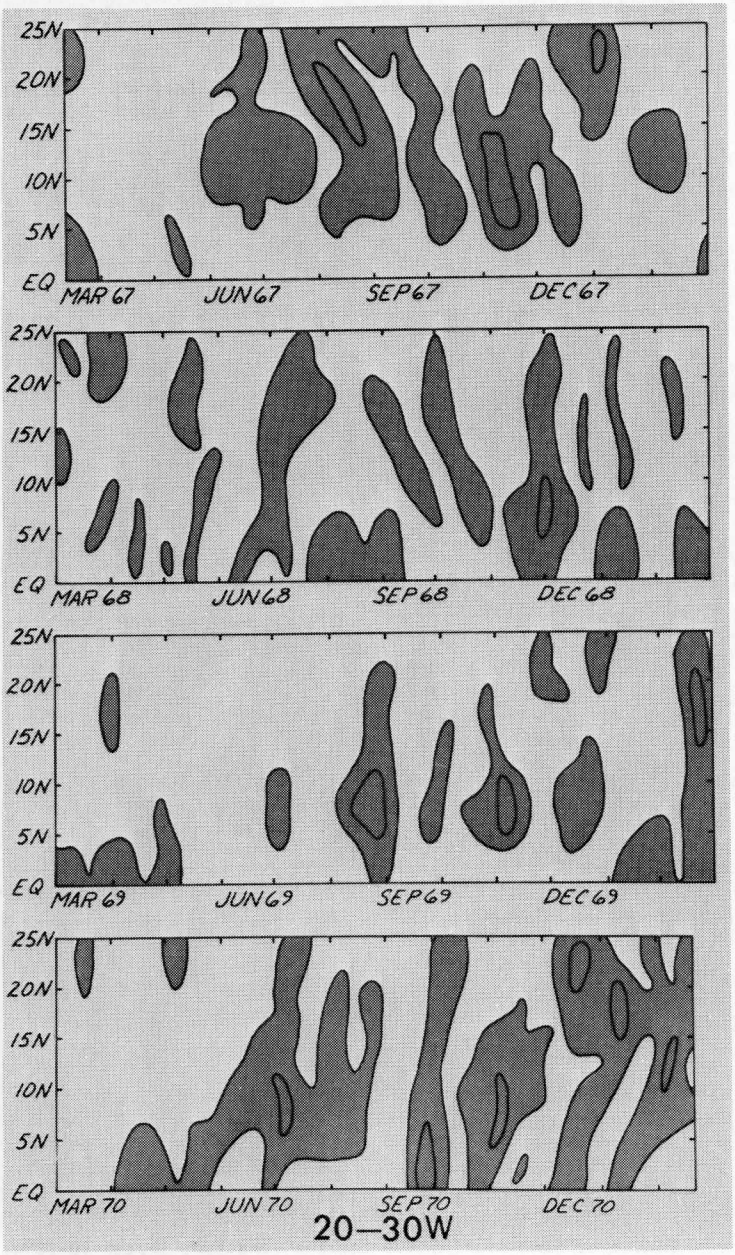

Fig. 10a. See List of Figures.

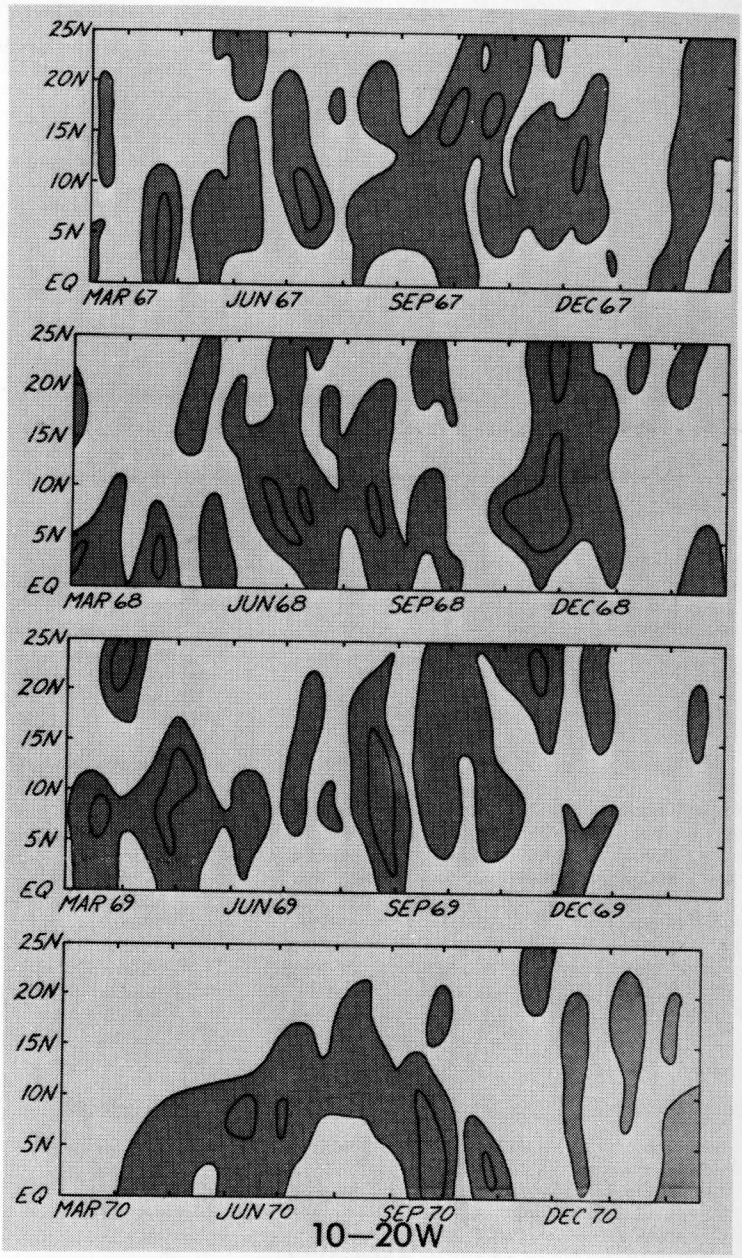

Fig. 10b. Same as Fig. 10a for the longitude sector 10-20°W.

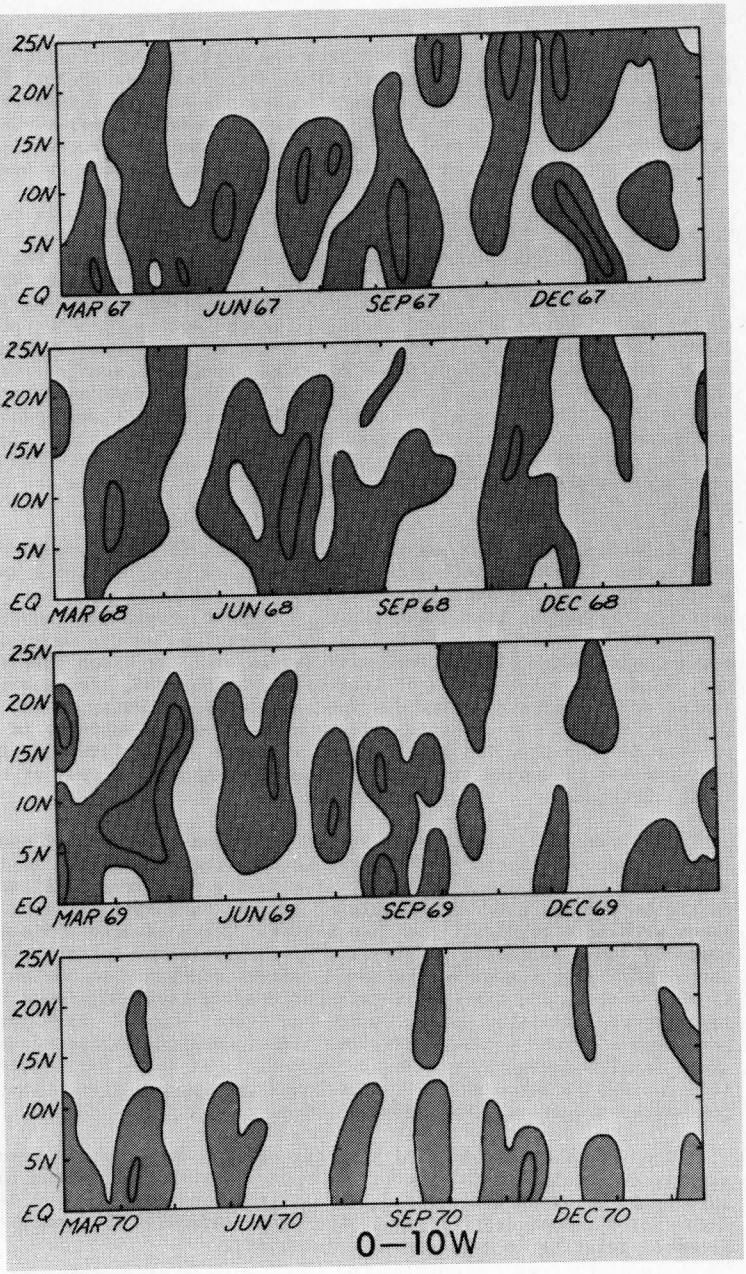

Fig. 10c. Same as Fig. 10a for the longitude sector 0-10°W.

mean. The maximum individual positive and negative departures, observed in the 4-day filtered cloud amount data, varied between 20-25%, depending on the zone. Thus, 7.5% corresponds to regions showing levels of intensity greater than approximately 33% of the absolute maxima observed in the filtered data sets. Solid isolines within shaded areas represent levels of intensity commonly greater by a factor of 2 to 4, relative to unshaded areas.

Again the time series are arranged in year-long intervals to facilitate comparison. Probably the feature which is most striking in the diagrams is the almost north-south-oriented banded structure of the intervals of high intensity 4-day activity. In the latitude belts from 5-20°N, there is a concentration of high intensity activity during the spring and summer months in all three longitude sectors. In the sector 20-30°W, depicted in Figure 10a, the increased intensity of 4-day activity usually begins in June. Somewhat later than in the other two longitude sectors, this is about the time in which the upper level easterlies assume dominance in the region. And, it is also about the time when the ITCZ begins its most prominent northward migration over the ocean sector. This makes it difficult to attribute the increased intensity levels to one single cause. The two processes probably operate in conjunction with one another to produce the observed increase.

A feature of particular interest, however, is the predominant periodicity in the levels of intensity of activity, varying between 1 and 1-1/2 months, intervals of less intense activity alternating with more intense activity throughout the summer season. Highest levels of intensity are especially prevalent from 5-10°N in the summer and autumn months. The autumn months show highest intensity levels over the ocean sector. In winter, occasional high levels of intensity are observed, presumably a manifestation of periodic intrusions into the region by waves in the westerlies. For this reason, the cessation of the high intensity activity is less distinctly defined than its onset in early summer. Some irregular intervals of increased intensity are seen to occur throughout the year at the equatorial latitudes.

The increased intensity of activity is seen to occur 1-2 months earlier in the longitude sector 10-20°W than in the sector 20-30°W. In late March and April, the increased intensity of activity is already well established in the sector 10-20°W. The levels of extreme intensity, greater than 15%, occur with more regularity in this sector. There is also a discernable tendency for a northward progression of the increased intensity activity during the early summer months and a retreat southward in autumn. Again in this sector, the vertically-oriented, banded structure tends to a periodicity of 1 to 1-1/2 months during the summer months. 1970 seems to have been a rather unusual year, the higher latitudes being notably deficient in high intensity cloudiness variations of 4-day periodicity. It is interesting, as noted earlier, that Dakar (at approximately 15°N) experienced its second driest year on record in 1970.

The relative cessation of high intensity 4-day activity seems more clearly delineated in this longitude sector, usually occurring in December, 1970 again being an exception. It is interesting to note a recurrent tendency for a rather significant weakening in intensity in October and early November relative to adjacent time intervals.

In the longitude sector 0-10°W, the increased intensity of four-day

activity seems well advanced as early as mid-March. By the end of September the more consistently recurring increases in intensity in the latitude belts 5-20°W seem to stop. More erratic outbursts continue throughout the autumn months. Again, as in the other two longitude sectors, there seem to be increases in intensity at higher latitudes in the autumn months. This is presumably due to the influence of the re-strengthened westerlies. Also in this longitude sector, 1970 appears as an unusually inactive year with significant intensity increases higher than 15°N almost non-existent. This tends to correlate well with the observation from the mean cloudiness diagrams that, in 1970, the mean ITCZ did not migrate as far north as usual over the African continent.

To illustrate the way in which levels of intensity of the four-day oscillations occur as a function of season and geographical location, spatial maps of the mean monthly modulated four-day filtered cloud amount were prepared. These are presented in Figures 11a, 11b, 11c and 11d. Again to facilitate easier comparison, these are arranged in a month versus year format. The isoline interval is 2.5%, reflecting the greater statistical reliability of the monthly means. Shading denotes regions with departures in excess of 7.5% as in the latitude-time diagrams. In March quite low values are in evidence over almost the entire area; only the lower latitudes in the sector 0-10°W shows relatively high intensity levels. The April maps show a banded structure, oriented southwest-to-northeast, similar to the orientation of the 20% isoline on the low-pass filtered cloud amount diagrams in Figure 9. May, while also showing a banded-structure region of high intensity activity, is characterized by considerable variation from year to year in the location of the relative maximum.

Figure 11b shows the monthly averages for the summer season. Areal coverage and intensity of activity in June evidences an increase relative to May with a more consistent tendency for a concentration of activity in the latitudes from 5-20°N. Most intense activity is usually found over the continent during June except in 1970, a year already noted as being unusual. July shows a tendency for a westward migration over the ocean of the region of most intense activity. This trend is continued in August, the month which shows the most widespread areal coverage of high intensity activity.

Figure 11c depicts the autumn months. September is also characterized by widespread areal coverage of high intensity activity. But it has a tendency for relative maxima in intensity to shift south-eastward to a point near the coast of the continent. October, in relation to September and November, stands out as being a noticeably more inactive month in terms of the intensity of four-day activity. It would be tempting to interpret the lower levels of intensity observed in October as signalling an end to the season of easterly waves. This may indeed be the case, but it does not account for the re-intensification observed in November. It would seem that large-scale circulation changes in October, which bring an end to the season of easterly waves, also have a damping effect on the intensity of the four-day oscillations associated with the ITCZ during this period. A re-intensification of four-day activity, apparently associated solely with the ITCZ, appears in November. In November, the relative maxima in intensity are located over the ocean near 5°N, where the ITCZ might be expected to be strongest at this time of year. Obviously further research is needed to verify this interpretation.

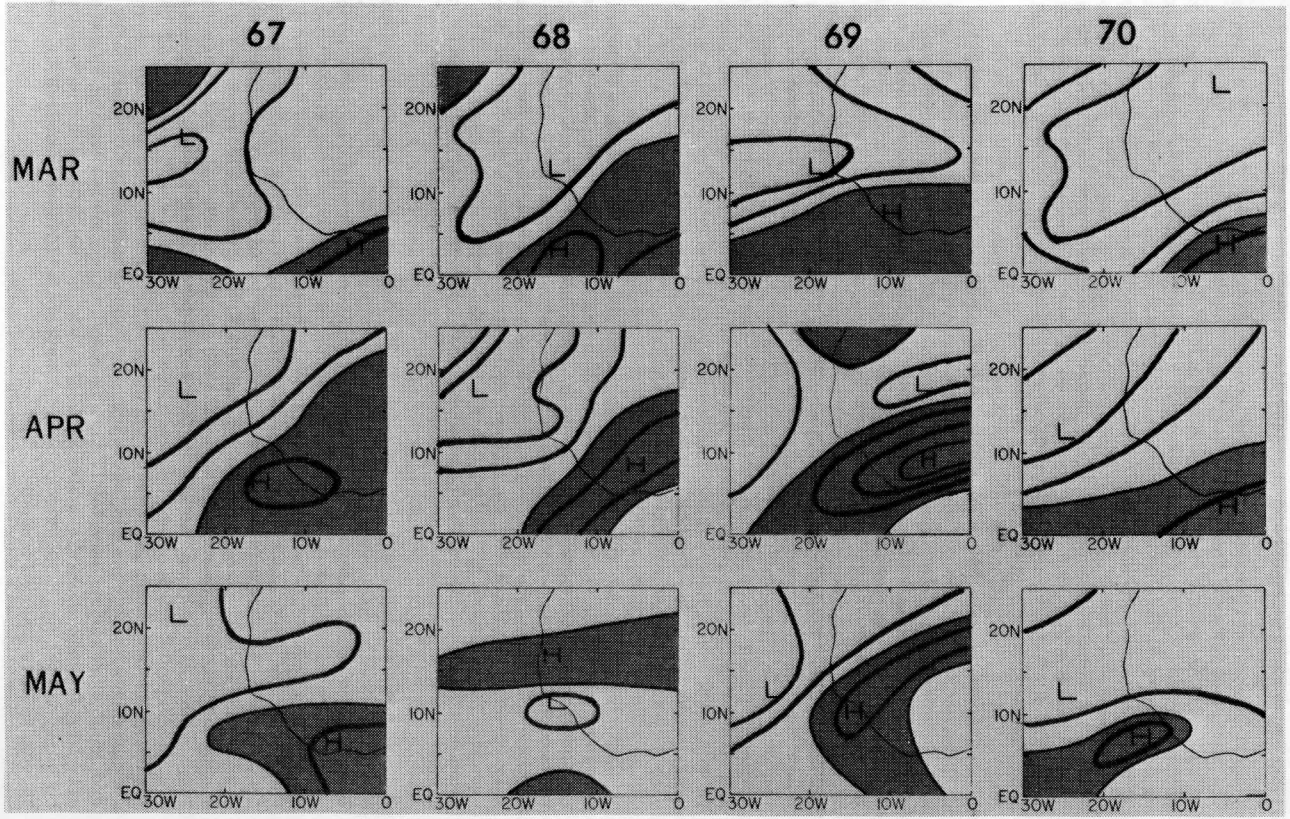

Fig. 11a. Monthly means for the modulated 4-day filtered cloud amount for March, April, and May in each of the 4 years studied. Solid isoline interval is 2.5%. Shading denotes regions with values in excess of 7.5%. Relative maxima and minima are indicated by H's and L's on each map.

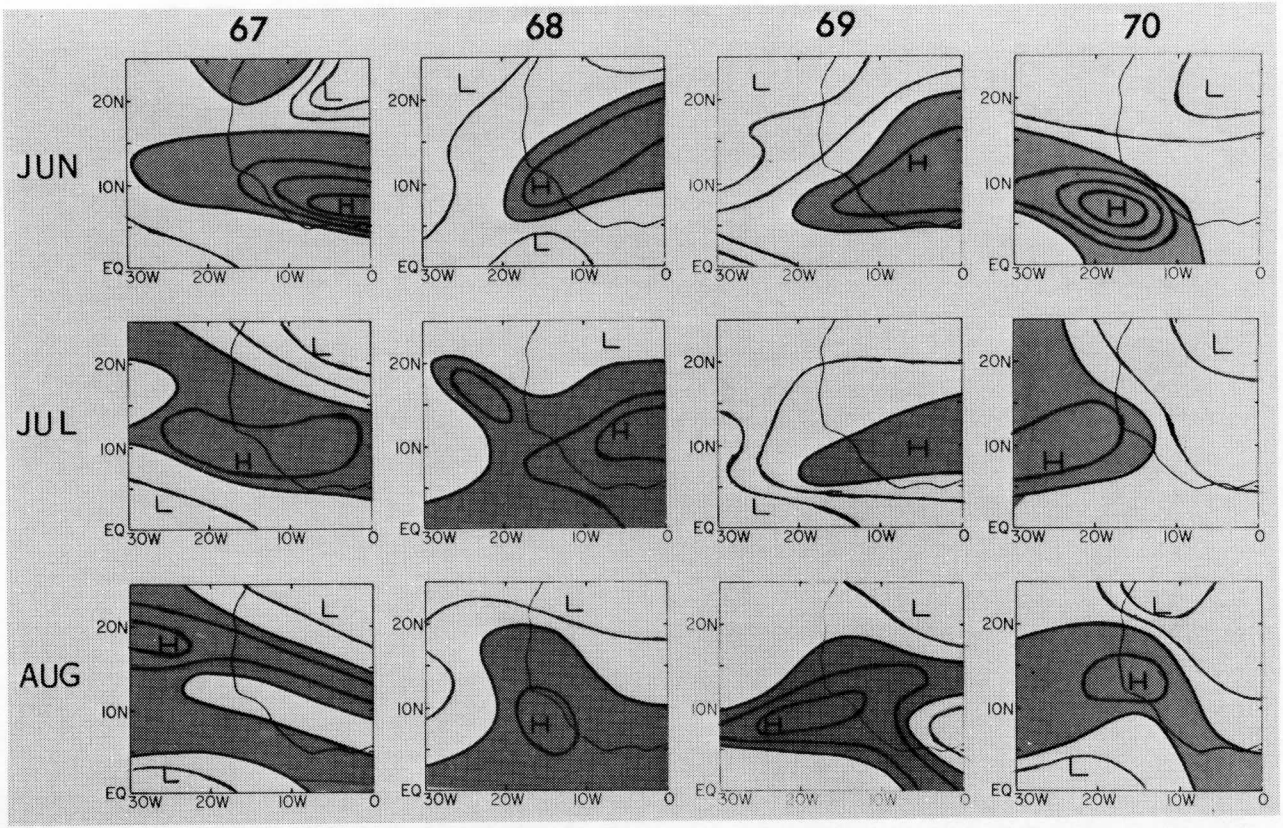

Fig. 11b. Same as Fig. 11a for June, July, and August.

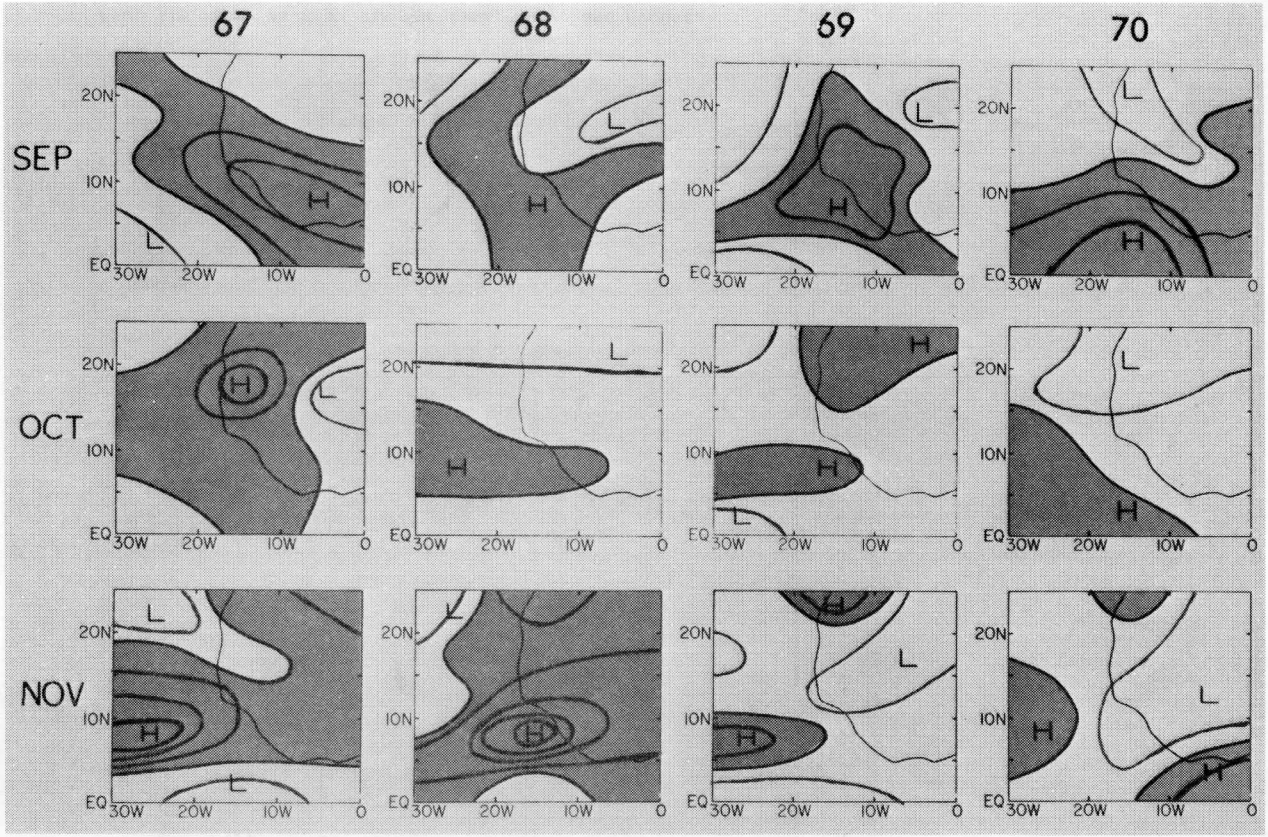

Fig. 11c. Same as Fig. 11a. for September, October, and November.

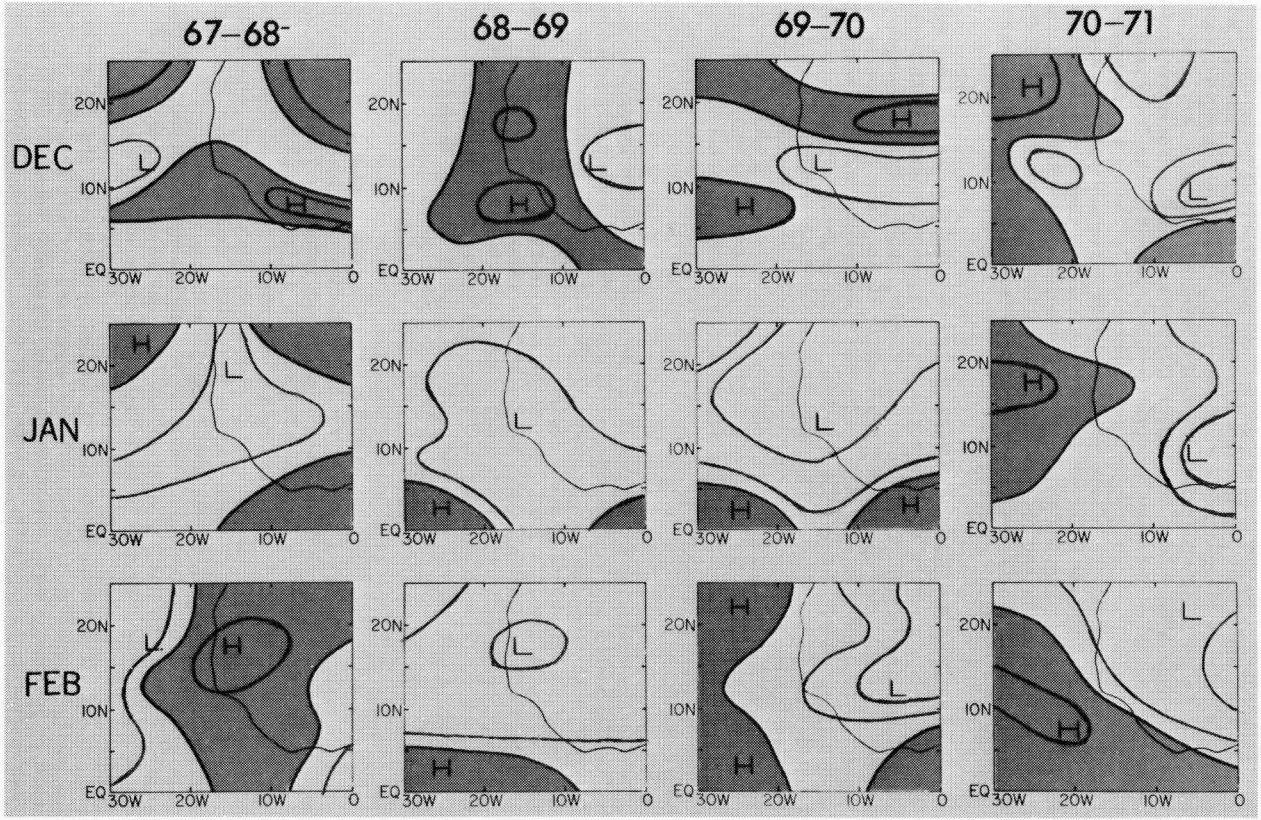

Fig. 11d. Same as Fig. 11a for December, January, and February.

In the last figure, 11d, the winter-month intensity of four-day activity is shown. December shows some sporadic variations from year to year. But there is an indication of the establishment of a double center of activity, one near 5°N and the other near 25°N, with a stable inactive regime between, especially over the continent. Quite probably the increased activity in the northern-most latitudes represents influence by the westerlies from higher latitudes. January seems to be an extremely inactive month because of a significant shift of activity to the far north or far south. February, while continuing this general pattern, shows potential for increased levels of intensity, as evidenced in 1968 and 1971. It is difficult to ascertain whether this occurrence is produced by westerly intrusions or by tropical effects.

Summarizing the preceding discussion, the intensity of four-day oscillations in cloudiness reaches a maximum in August and a minimum in January. The intervening months, from January to August, show gradually increased intensity of activity with a northward shift in location. The months from August to January show gradually decreased intensity with a southward shift in the location of the relative maximum. October shows unusually low intensity levels, relative to the preceding and following months. It is not surprising that this pattern approximates that of the low-pass filtered cloud amount in its latitudinal progressions and its associated patterns of intensity changes, if the cloud activity possesses a strong "cluster-like" behavior. It is also consistent with the association of the oscillations of approximately four days with the ITCZ (Oort, 1973; Simpson, 1969; et. al.).

This is clarified by Figure 12 which shows the seasonal variations in the intensity of the four-day oscillations as a function of location. Diagrams were prepared for the seven complete six month seasonal intervals in the data set. Shading again indicates deviations greater than 7.5%. The isoline interval is 2.5%. It can be seen that, during the summer months, the four-day oscillations reach their maximum intensity near 10°N with expanded coverage of relatively high intensity levels to 15-20°N. In the winter season intensity levels are lower and relative maxima are shifted to the far southeast or southwest sectors adjacent to the Equator.

B. Modulated 10-Day Filtered Cloud Amount

An analysis similar to that for the four-day cloudiness oscillations was carried out for the 10-day modulated cloud amount data sets. Figures 13a, 13b, and 13c illustrate the results in a latitude-time format. In this instance, shading indicates deviations greater than 10% from the mean, since maximum deviations observed in the 10-day filtered data were approximately 35%. The solid isoline interval is 10%. Thus, the isolines within the shaded regions represent deviations from the mean greater than 20%. This commonly indicates an increase in the amplitude of the oscillation by a factor of 2-3, relative to time intervals and shown as unshaded. In extreme cases, the increase is by a factor as great as 10.

The basic north-south-oriented, banded structure of the intervals of intensity maxima are similar to those diagramed for the four-day oscillations. However, close inspection reveals important seasonal differences. Whereas maxima in intensity for the four-day oscillations occurred with most regularity during the summer season, the maxima in 10-day oscillation intensity appear in the autumn months, with a distinct tendency for a

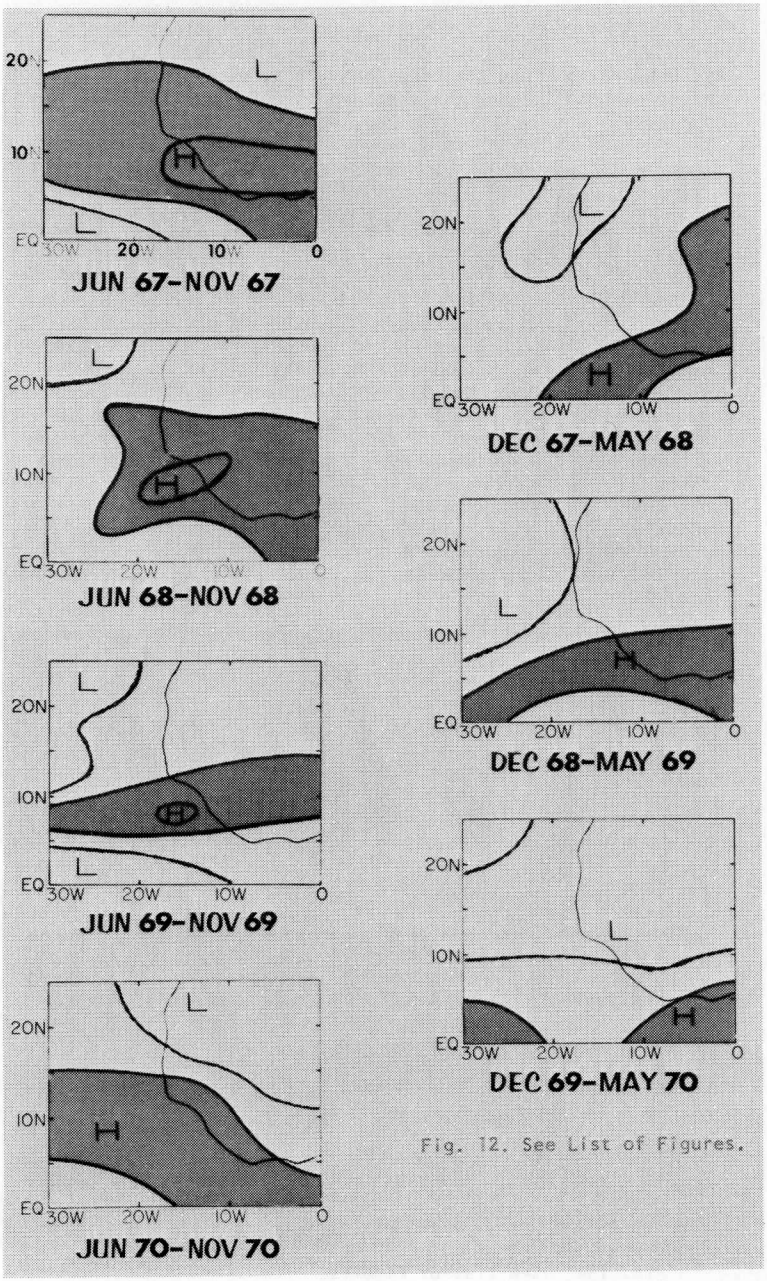

Fig. 12. See List of Figures.

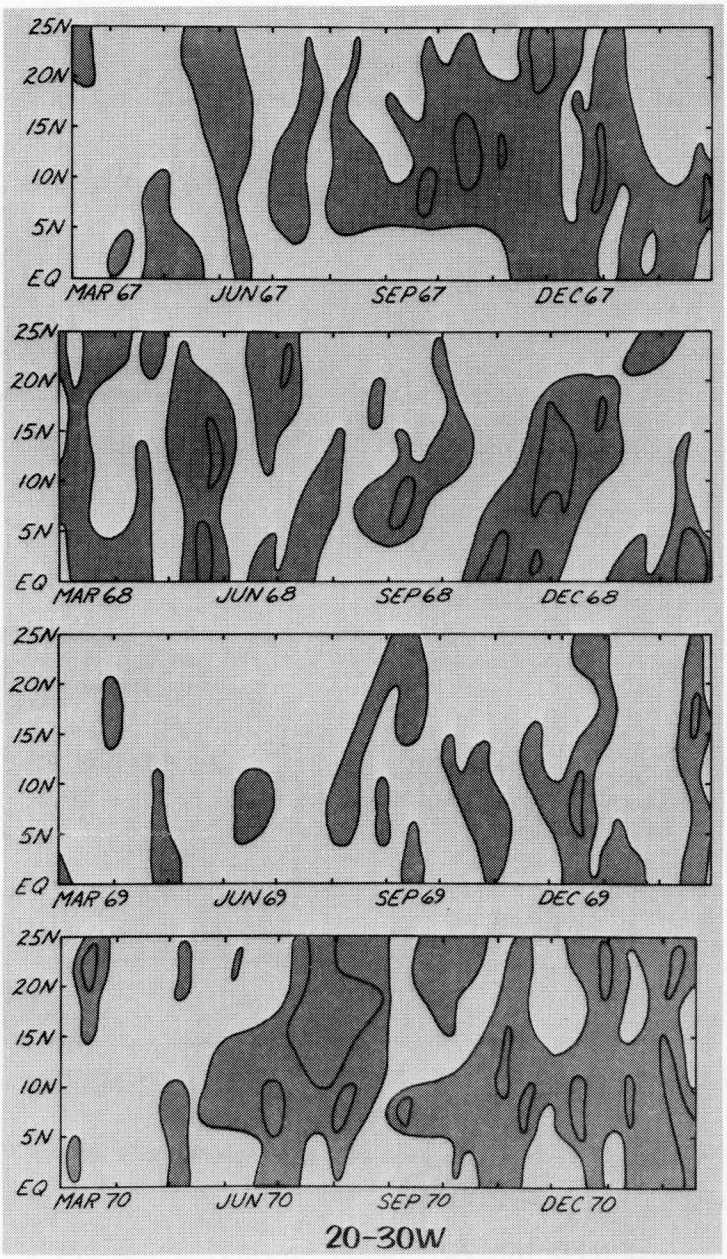

Fig. 13a. See List of Figures.

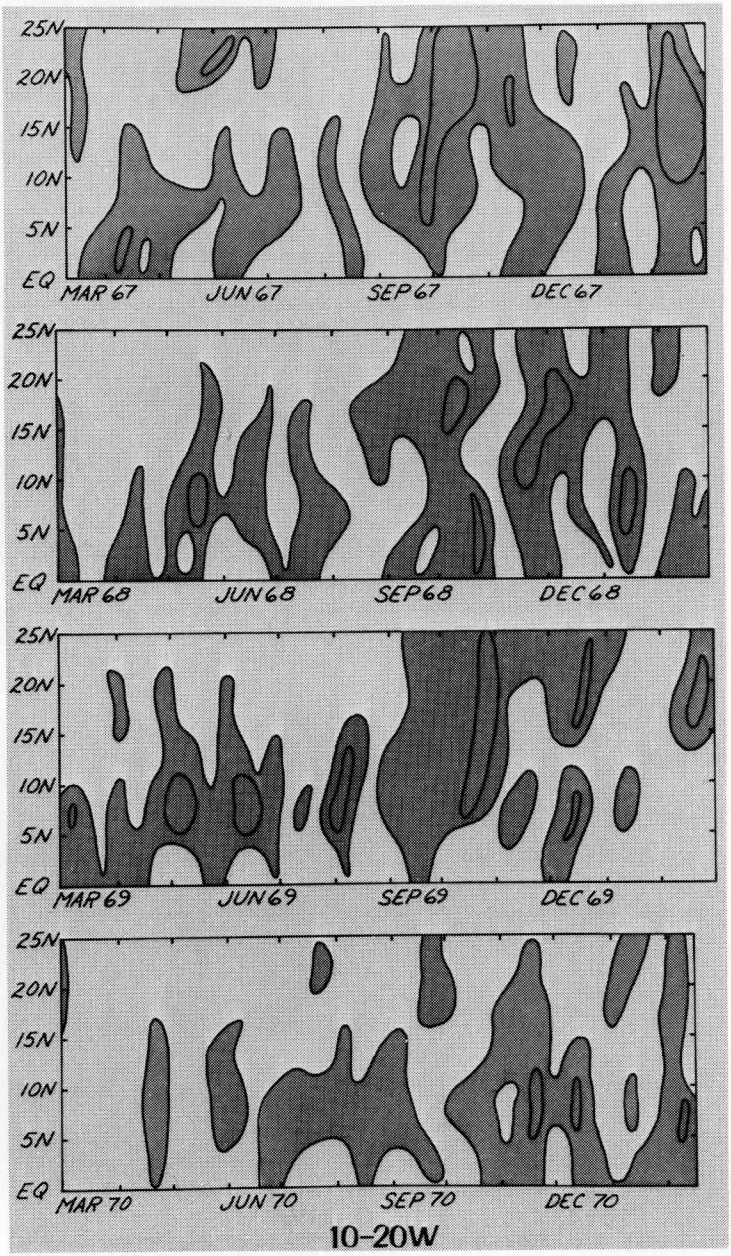

Fig. 13b. Same as Fig. 13a for the longitude sector 10-20°W.

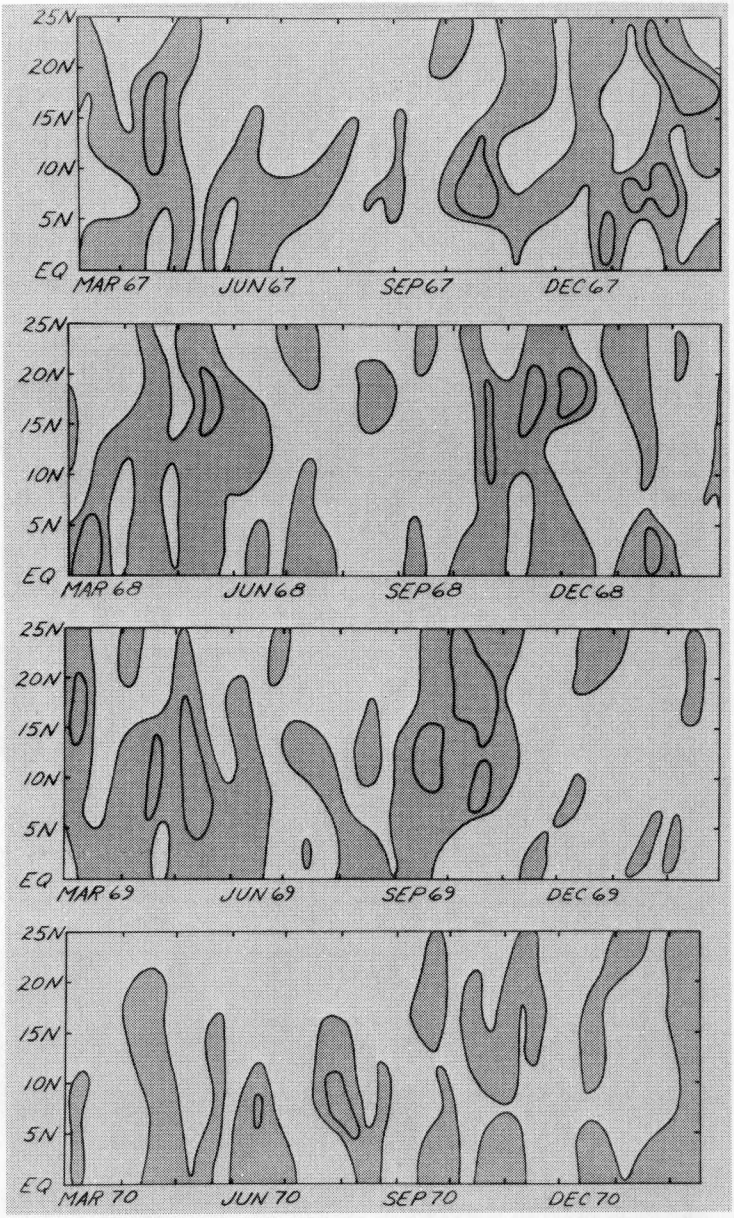

Fig. 13c. Same as Fig. 13a for the longitude sector 0-10°W.

summer-season minima in intensity.

Especially in the two eastern-most longitude sectors, there are indications of a secondary maxima in the spring months. This tends to imply that the 10-day oscillations in cloudiness reach their highest intensity levels during the transition months. The winter and summer months are relatively inactive.

Again, periods of increased intensity seem to alternate with periods of less intense activity at intervals of approximately 1 to 1-1/2 months. Interesting and rather strong variations are observed inter-annually. The year 1969 had relatively little intensification of 10-day activity. On the other hand, 1970 showed frequent intervals of intensification, the contrast being most noticeable in the sector 20-30°W. Centers of increased intensity in the spring and summer months, when they do occur, are usually found from 0-10°N. In the autumn and winter months, centers of increased intensity are most often observed from 10-25°N. An exception is the autumn and winter of 1970 when very little intensification of 10-day activity at latitudes higher than 10°N occurred in the two eastern-most longitude sectors.

To indicate the monthly variation of 10-day oscillation intensity levels over the study area, monthly averages of the modulated 10-day filtered cloud amount were prepared. These are presented in Figures 14a, 14b, 14c, and 14d. Regions showing greater than 10% deviations are again shaded, but the isoline interval is 5%. Figure 14a shows the intensity of 10-day activity im March to be relatively low, with highest values found in the lower latitudes. April shows a tendency for a northward shift and areal expansion of the region of high intensity. In May, curiously, while intensity remains unchanged, the latitude of the relative maximum has again shifted southward.

June, July, and August, illustrated in Figure 14b, show relatively low intensity values, but with the relative maxima in the approximate position of the ITCZ. The September averages in Figure 14c mark a clear change from the preceding summer months. Levels of intensity increase and gradually shift northward from September through November.

In the final figure, the winter months show rather erratic variations in areal coverage and levels of intensity. But it indicates that January is a month of relative inactivity at all latitudes except near the Equator.

Again to summarize, the 10-day data indicates a maximum in intensity in autumn, a minimum in summer, and, similar to the four-day data, a tendency for variations in intensity levels to occur at approximately 1 to 1-1/2 month intervals. Variations that occur between years are rather large compared to those that occur for the modulated four-day cloud amounts. Results from an analysis of six-month means of the modulated 10-day cloud amounts proved inconclusive.

Somewhat more insight into the periodicities of the modulated cloud amount is gained by examining the power spectra for these data sets. Figure 15 shows the power spectra for both the four-day and 10-day modulated cloud amount. The dashed lines on the four-day diagrams represent the average of all four-day spectra and similarly for the 10-day diagrams. The four-day and 10-day average spectra are quite similar, with the 10-day average spectrum showing slightly more power at the very lowest frequencies.

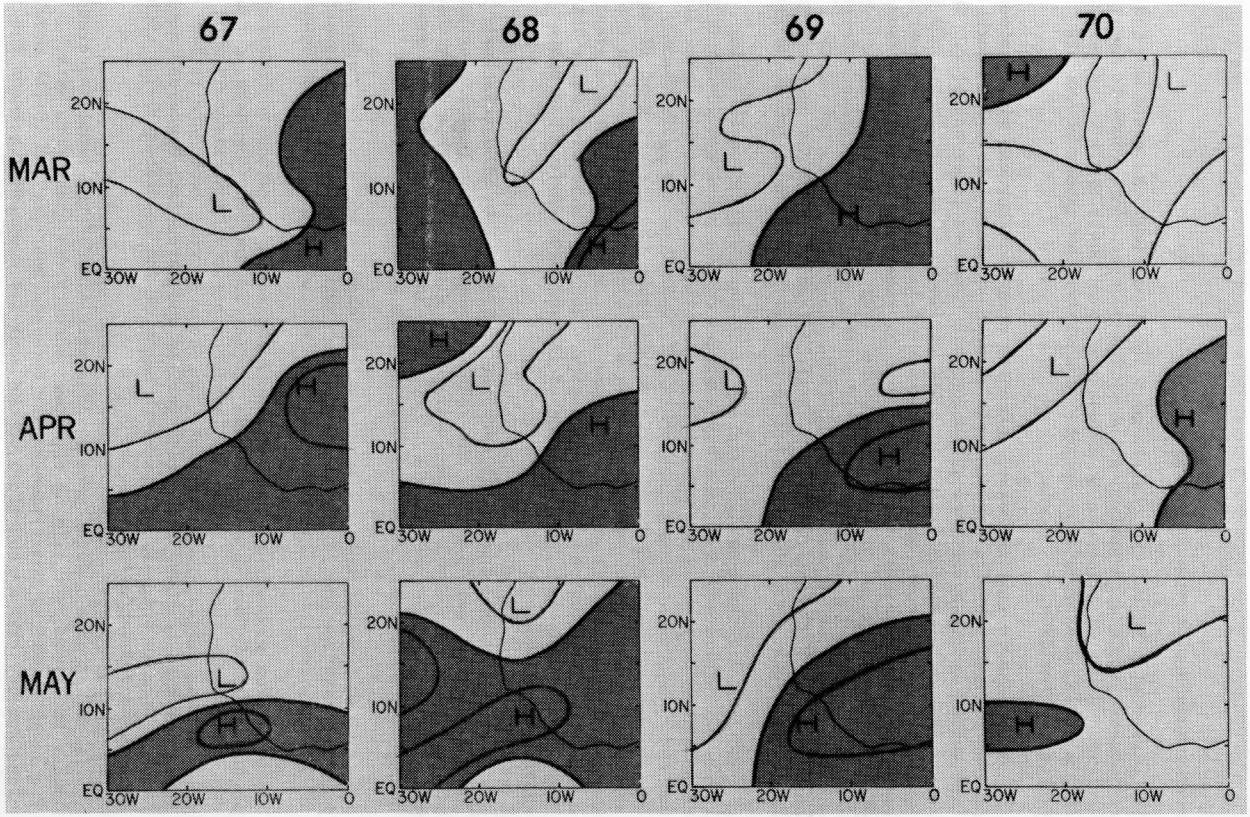

Fig. 14a. Monthly means for the modulated 10-day filtered cloud amount for March, April, and May in each of the 4 years studied. Solid isoline interval is 5%. Shading denotes regions with values in excess of 10%. Relative maxima and minima are indicated by H's and L's on each map.

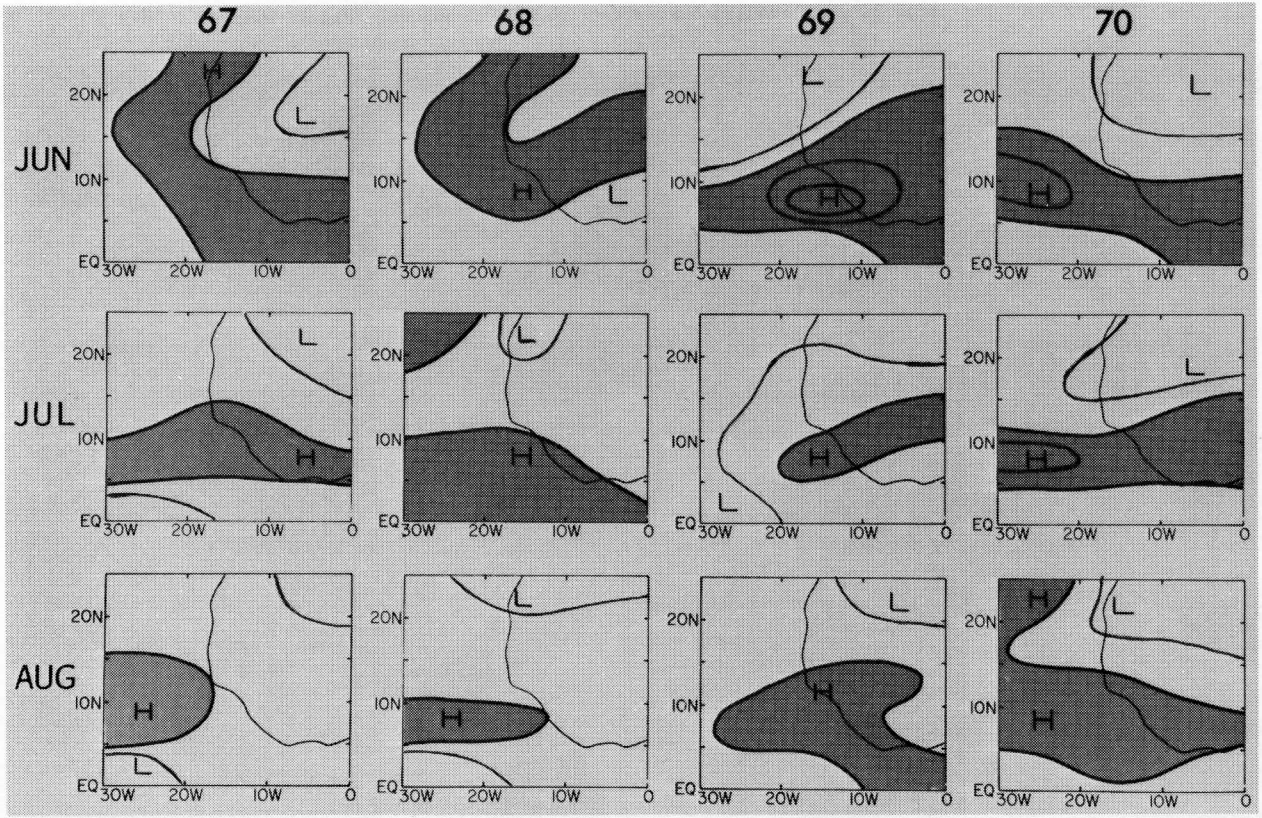

Fig. 14b. Same as Fig. 14a for the months June, July, and August.

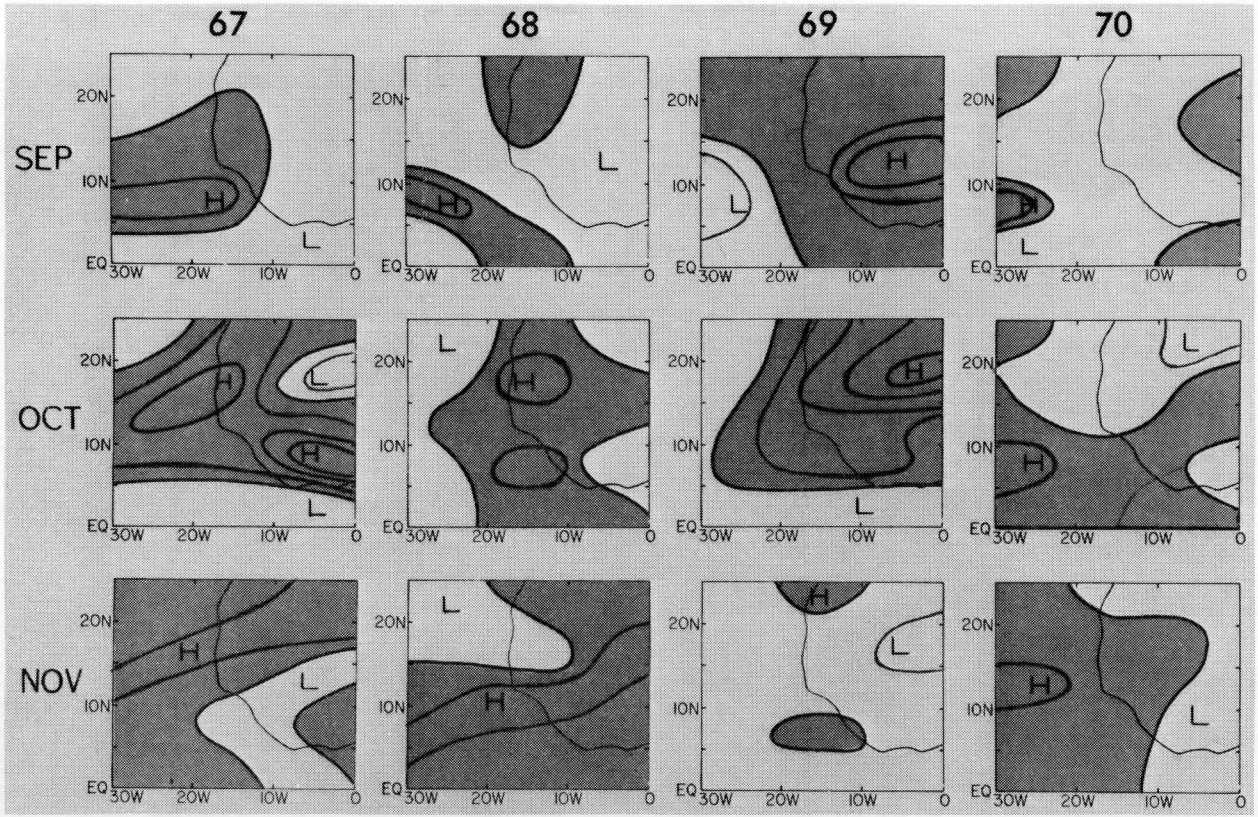

Fig. 14c. Same as Fig. 14a for the months September, October, and November.

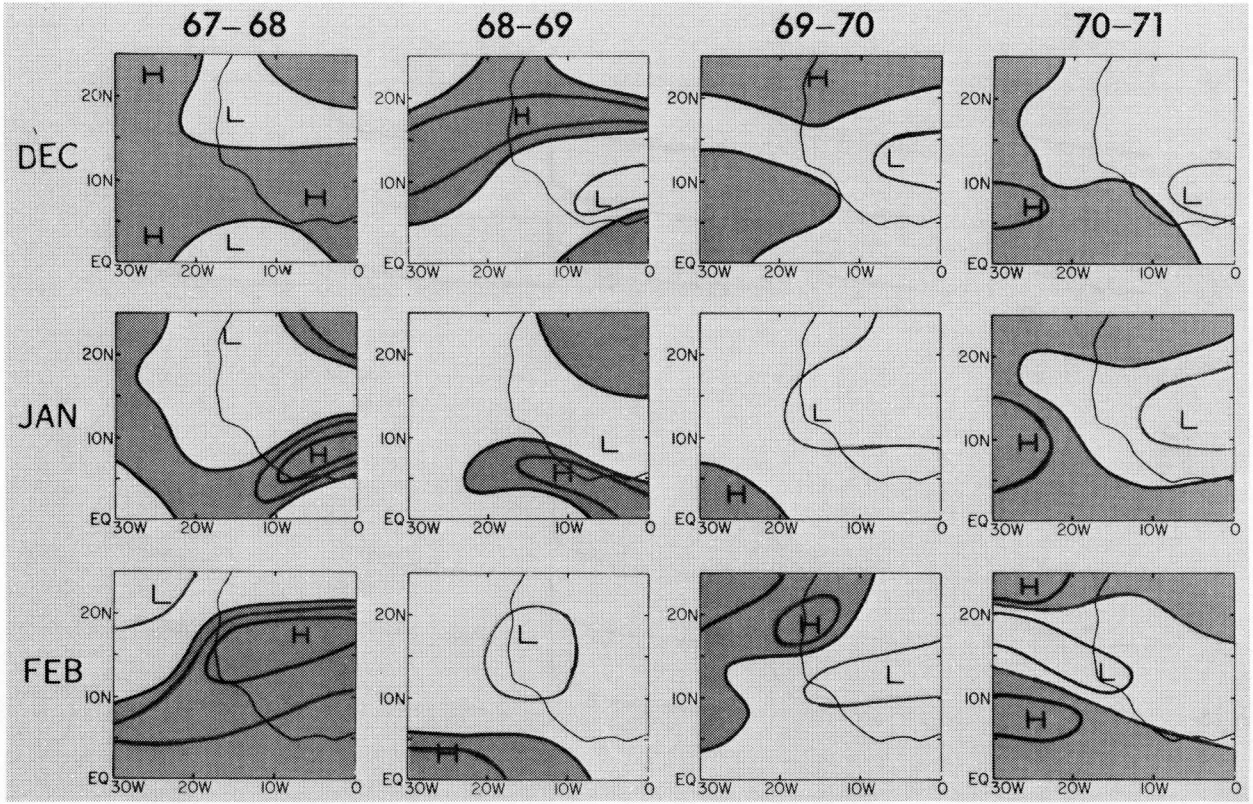

Fig. 14d. Same as Fig. 14a for the months December, January, and February.

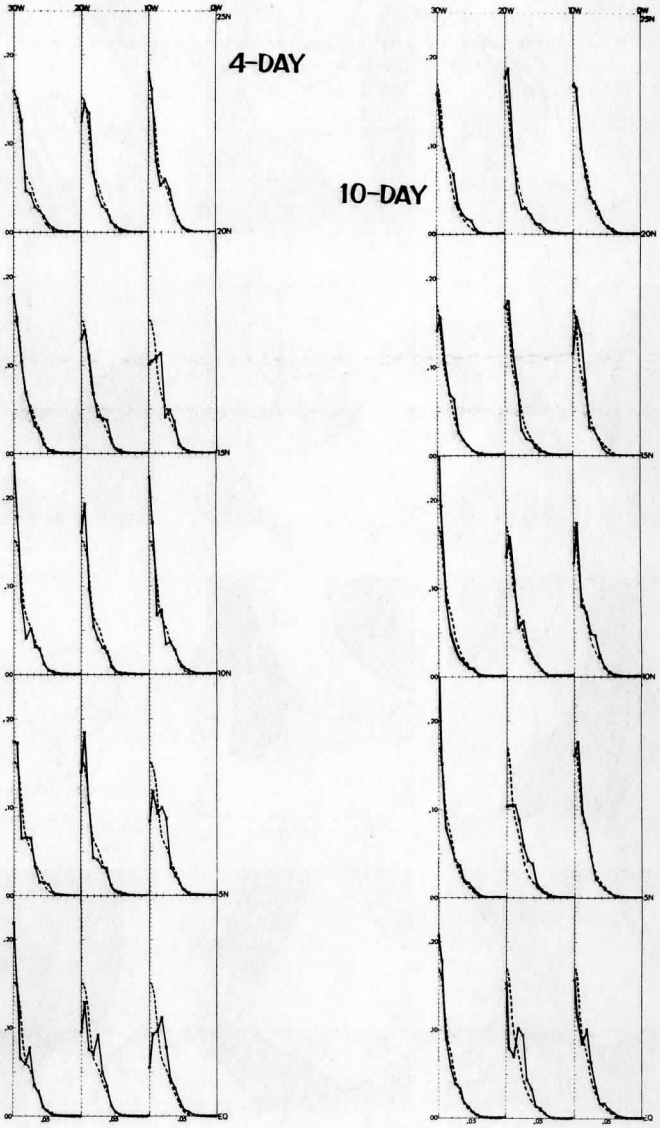

Fig. 15. See List of Figures.

Again all spectra were normalized to allow easier comparison. As can be seen, the spectra contain almost no power at periods less than 16 days, that is, at frequencies greater than 0.06 cpd. This is of course partially a consequence of the technique used in generating the modulated data sets. Nevertheless, the spectra are dominated in general by very strong red noise characteristics. Persistence is thus the dominant feature, but there are some indications of a slight peak. This shows up most strongly in the lower-latitude zones, near f = 0.02-0.03, a period of 1 to 2 months. This is a periodicity noted as especially prevalent in the latitude-time diagrams of the modulated cloud amount variations.

VI. SUMMARY

From the preceding analysis and discussion, several features stand out in retrospect as being of special significance.

(1) The mean annual position of the ITCZ as seen in cloud amount lies in the vicinity of latitude 5-10°N.

(2) The ITCZ shifts southward in the autumn and winter months, but at this time of year values of cloud amount are significantly low. Thus, the mean annual position does not vary much from its summer-season position.

(3) The ITCZ, rather than being continuous in its intensity, is characterized by alternate phases of greater and lesser cloud amount. These often recur at intervals of approximately 1 to 2 months.

(4) Significant variations occur from year to year in the mean intensity of the ITCZ and its mean position. In particular, 1969 was characterized by relatively low cloud amounts in the longitude sector 20-30°W. In the sector from 0-20°W, relatively high cloud amounts were noted. Also, in 1970, the ITCZ was retarded significantly in its northward progression over the African continent.

(5) August is observed to be the cloudiest month, July and September being nearly as cloudy as August. January is the least cloudy month.

(6) Super-imposed upon the long-period cloudiness variation are cloudiness oscillations with periods of less than 20 days. These also undergo variations in intensity on a month-to-month and seasonal basis.

(7) The 4-day oscillations in cloud amount reach their maximum intensity in August at 5-10°N, their minimum intensity in January. They thus show a high degree of correlation with the seasonal variations observed in the mean ITCZ.

(8) The 10-day oscillations in cloud amount reach their maximum intensity in October and November, at latitudes 10-20°N. Their minimum intensity occurs during the summer months.

(9) The GATE location (23°W,8°N) is characterized by mean annual cloudiness of approximately 30%, ranging from approximately 40% during the six-month period from June to November to values around 20% during the six-month period from December to May. August is the cloudiest month. July and September are only slightly less cloudy. January is the least cloudy month. Interannual variations in the patterns of cloud amount variation are relatively minor. However, 1969 was characterized by less cloudiness than usual over the area. Values greater than 40% were experienced for only a one-month period, from August into early September. Four-day oscillations in cloud amount reach their greatest intensity levels over this area from June into December. November curiously shows the highest intensity levels for the four-day oscillations. The ten-day oscillations in cloud amount show somewhat less seasonal and year-to-year regularity.

It must be remembered that these findings apply only to the four-year interval which was studied. The sample is far too small to allow interannual comparison with great statistical reliability. Further research, perhaps involving extension of this data set, would certainly be worthwhile. This could determine whether the patterns observed in the present sample are truly representative. Correlation of the cloud amount data sets with wind, temperature, and rainfall studies would also prove enlightening. Cross-spectrum analysis might better reveal the patterns of propagation and wavelength estimates.

While this study has been able to deal with only gross features, nevertheless the results seem valuable in their indication of the types of cloudiness variations which might be expected to occur over the region throughout the course of the year. The more general patterns of cloudiness distribution and fluctuation found are consistent with the types of meteorological influences known to affect this region and the tropics. However, the causes of certain irregularities and some of the quasi-periodic anomalous patterns observed remain unexplained. It is thus to be hoped that this study will serve as an aid and a stimulus to further research in this area.

ACKNOWLEDGEMENTS

Dr. Verner E. Suomi was kind enough to find time in his busy schedule to review the manuscript. Thanks are also due to Dr. D. N. Sikdar for his generous provision of portions of the data set. Peter Guetter provided much help in formulating several of the computer programs used.

This research was sponsored by NOAA under Grants 1-36036 and NG-26-72.

REFERENCES

Blackman, R. B., and J. W. Tukey, 1958: The Measurement of Power Spectra from the Point of View of Communications Engineering. New York, Dover, 190 pp.

Chang, C. P., 1970: Westward Propagating Cloud Patterns in the Tropical Pacific as Seen from Time-Composite Satellite Photographs. J. Atmos. Sci., 27, 133-138.

Cooley, J. W., and J. W. Tukey, 1965: An Algorithm for the Machine Calculation of Complex Fourier Series. Mathematics of Computation, 19, 297-301.

Craddock, J. M., 1957: A Contribution to the Study of Meteorological Time Series. Meteorological Research Committee, Report No. 1051, London.

Fee, Everett J., 1969: Digital Computer Programs for Spectral Analysis of Time Series. Center for Great Lakes Studies, The University of Wisconsin-Milwaukee, Special Report No. 6.

Frank, Neil L., 1970: Atlantic Tropical Systems of 1969. Monthly Weather Review, 98, 307-314.

Griffiths, J. F., 1972: Climates of Africa, World Survey of Climatology 10, Elsevier Publishing Company, 604 pp., New York.

Gruber, A., 1972: Fluctuations in the Position of the ITCZ in the Atlantic and Pacific Oceans. J. Atmos. Sci., 29, 193-197.

Hald, A., 1952: Statistical Tables and Formulas. Wiley, 97 pp., New York.

Holloway, J. L., Jr., 1958: Smoothing and Filtering of Time Series and Space Fields. Advances in Geophysics, 4, 351-390.

Hubert, L. F., A. G. Krueger and J. S. Winston, 1969: The Double Intertropical Convergence Zone - Fact or Fiction? J. Atmos. Sci., 26, 771-773.

Julian, P. R., 1971: Some Aspects of Variance Spectra of Synoptic Scale Tropospheric Wind Components in Mid-latitudes and in the Tropics. Monthly Weather Review, 99, 954-965.

Kornfield, J., A. F. Hasler, K. J. Hanson and V. E. Suomi, 1967: Photographic Cloud Climatology from ESSA III and V Computer Produced Mosaics. Bull. Amer. Meteor. Soc., 48, 878-883.

Landsberg, H. E., 1973: An Analysis of the Annual Rainfall at Dakar (Senegal), 1187-1972. University of Maryland, Institute for Fluid Dynamics and Applied Mathematics.

Madden, Roland A., and Paul R. Julian, 1972: Description of Global-Scale Circulation Cells in the Tropics with a 40-50 Day Period. J. Atmos. Sci., 29, 1109-1123.

Martin, David W. and V. E. Suomi, 1972: A Satellite Study of Cloud Clusters over the Tropical North Atlantic Ocean. Bull. Amer. Meteor. Soc. 53, 135-156.

Maruyama, T., 1968: Time Series of Power Spectra of Disturbances in the Equatorial Lower Stratosphere in Relation to Quasi-Biennial Oscillation. J. Meteor. Soc. Japan, 45, 404-417

Mitchell, J. M., Jr., 1966: Climatic Change. W.M.O. Technical Note No. 79.

Nitta, T., 1970: Statistical Study of Tropospheric Wave Disturbances in the Tropical Pacific Region. J. Meteor. Soc. Japan, 48, 47-59.

Oort, Abraham H., and Thomas I. Gray, Jr., 1973: Natural Variations in Convective Activity over the GATE Area. Bull. Amer. Meteor. Soc. In Press.

Palmer, C. E., 1951: Tropical Meteorology. Compendium of Meteorology, Boston, Amer. Soc.,,859-880.

Panofsky, H. A., and G. W. Brier, 1965: Some Applications of Statistics in Meteorology. Pennsylvania State University Press, 224 pp.

Riehl, H., 1945: Waves in the Easterlies and the Polar Front in the Tropics. Misc. Rept. 17, Dept. of Meteorology, University of Chicago.

_____, 1954: Tropical Meteorology. New York, McGraw-Hill, 392 pp.

Rosenthal, S. L., 1960: Some Estimates of the Power Spectra of Large-Scale Disturbances in Low Latitudes. J. Meteor., 17, 259-263.

Sadler, J. C., 1972: Monsoons in the Eastern Oceans. Dynamics of the Tropical Atmosphere, Notes from a Colloquium: Summer 1972, National Center for Atmospheric Research, 231-242.

Schwalb, Arthur and James Gross, 1969: Vidicon Data Limitations. ESSA Technical Memorandum NESCTM 17, U.S. Dept. of Commerce.

Sikdar, D. N., J. A. Young, and V. E. Suomi, 1972: Time-Spectral Characteristics of Large-Scale Cloud Systems in the Tropical Pacific. J. Atmos. Sci., 29, 229-239.

_____, and J. A. Young, 1973: Personal Communication.

Simpson, R. H., N. Frank, D. Shideler, and H. M. Johnson, 1968: Atlantic Tropical Disturbances, 1967. Monthly Weather Review, 96, 251-259.

_____, et. al., 1969: Atlantic Tropical Disturbances of 1968. Monthly Weather Review, 97, 240-255.

Suomi, V. E., 1973: Personal Communication.

Wallace, J. M. 1970: Time Longitude Sections of Tropical Cloudiness (December 1966-November 1967). ESSA Tech. Rept. NESC 56, U.S. Department of Commerce, Washington, D. C., 37 pp.

_____, 1971: Spectral Studies of Tropospheric Wave Disturbances in the Tropical Western Pacific. Reviews of Geophysics and Space Physics, 9, 557-612.

_____, 1972: Empirical Orthogonal Representation of Time Series in the Frequency Domain. Part II: Application to the Study of Tropical Wave Disturbances. J. Appl. Meteor., 11, 893-900.

_____, and C. P. Chang, 1969: Spectrum Analysis of Large-Scale Wave Disturbances in the Tropical Lower Troposphere. J. Atmos. Sci., 26, 1010-1025.

Winston, Jay S., 1971: The Annual Course of Zonal Mean Albedo as Derived from ESSA III and V Digitalized Picture Data. Monthly Weather Review, 99, 818-827.

Yanai, M., and T. Maruyama, 1966: Stratospheric Wave Disturbances Propagating over the Equatorial Pacific. J. Meteor. Soc. Japan, 44, 291-294.

_____, _____, T. Nitta and Y. Hayashi, 1968: Power Spectra of Large-Scale Disturbances over the Tropical Pacific. J. Meteor. Soc. Japan, 46, 308-323.

Young, J. A., and D. N. Sikdar, 1973: A Filtered View of Fluctuating Cloud Patterns in the Tropical Pacific. J. Atmos. Sci., 30, 392-407.

LIST OF FIGURES

Figure

Figure

denotes regions with greater than 20% cloud amount. Relative maxima and minima are indicated by H's and L's on each map.

9b. Same as Fig. 9a for the period from March 1968 until February 1969.

9c. Same as Fig. 9a for the period from March 1969 until February 1970.

9d. Same as Fig. 9a for the period from March 1970 until February 1971.

10a. Four years of latitude-time diagrams for modulated 4-day filtered cloud amount for the longitude sector 20-30°W. The planned GATE B array is located at 8°N. Solid isoline intervals are 7.5%. Shaded areas denote values in excess of 7.5%. Day 1 is March 14, 1967. Hatch marks on the abscissa denote monthly sub-divisions.

10b. Same as Fig. 10a for the longitude sector 10-20°W.

10c. Same as Fig. 10a for the longitude sector 0-10°W.

11a. Monthly means for the modulated 4-day filtered cloud amount for March, April, and May in each of the 4 years studied. Solid isoline interval is 2.5%. Shading denotes regions with values in excess of 7.5%. Relative maxima and minima are indicated by H's and L's on each map.

11b. Same as Fig. 11a for June, July, and August.

11c. Same as Fig. 11a for September, October, and November.

11d. Same as Fig. 11a for December, January, and February.

12. Seasonal means for the modulated 4-day filtered cloud amount for the indicated 6-month time periods. Solid isoline interval is 2.5%. Shading denotes regions with values in excess of 7.5%. Relative maxima and minima are indicated by H's and L's on each map.

13a. Four years of latitude-time diagrams for modulated 10-day filtered cloud amount. The planned GATE B array is located at 8°N. Solid isoline intervals are 10%. Shaded areas denote values in excess of 10%. Day 1 is March 14, 1967. Hatch marks on the abscissa denote monthly sub-divisions.

13b. Same as Fig. 13a for the longitude sector 10-20°W.

13c. Same as Fig. 13a for the longitude sector 0-10°W.

14a. Monthly means for the modulated 10-day filtered cloud amount for March, April, and May in each of the 4 years studied. Solid isoline interval is 5%. Shading denotes regions with values in excess of 10%. Relative maxima and minima are indicated by H's and L's on each map.

Figure

14b. Same as Fig. 14a for the months June, July, and August.

14c. Same as Fig. 14a for the months September, October, and November.

14d. Same as Fig. 14a for the months December, January, and February.

15. Normalized power spectra of modulated 4-day and 10-day filtered cloud amount. Dashed lines in each set of spectra indicate the average spectrum for that set. Abscissa is frequency in cycles per day. Ordinate is the spectral estimate in units of (fractional cloud amount)^2/frequency interval.

SOME ASPECTS OF TROPICAL CIRCULATION AS REVEALED FROM BRIGHTNESS ENHANCED ATS-3 PICTURES

D. N. Sikdar and Donald P. Wylie

ABSTRACT

A series of specially processed satellite pictures are used to investigate the time variations of tropical convection in relation to planetary scale disturbances. Visual cloud pictures from ATS-3 are brightness enhanced so that very thick clouds, which are probably intense convective clouds, could be identified as bright white spots. By cutting and re-assembling these pictures from the BOMEX period into longitude-time montages, the life time and movement of both deep convective clouds and cloud clusters could be studied.

This analysis revealed that the convective cores generally follow the organization of the cloud clusters and in most cases persist over a period of 2 1/2 hours (data did not permit longer measurements). The area occupied by these cores is only a few percent of the total cloud cover. The total core area appears to pulsate with a periodicity of 2-5 days. This is shorter than the periods of cloud cover fluctuations, 6-8 days. The cores generally follow the large-scale cloud motions, suggesting that they also result from large-scale circulations.

The cloud cover oscillations of the tropics (0-15°N), when compared to the subtropics (15-30°N), consistently showed indications of an opposite phase relation for a part of the study period. If the changes in cloud cover are considered to be changes in vertical motion, then oscillations in the Hadley cell circulation on the planetary-scale are implied. Such a theory could not be proved by this data. It should, however, be considered in future studies.

1. INTRODUCTION

Satellite time lapse cloud pictures have been of special interest to scientists dealing with the statistics of cloud cover. These pictures make it possible to determine the macro-fluctuations in cloud amount and distribution (Kornfield et. al., 1969: Sikdar et. al., 1971). In the tropics, these fluctuations result from many individual cumulus clouds. These clouds are said to be controlled by large-scale circulations. While the large-scale circulation controls the smaller scale features, the latter provides feedback to the former, an interacting mechanism to be intensively studied in the GATE (GARP Atlantic Tropical Experiment) program. Interestingly, most of this feedback is accomplished by only a few deep convective systems, lasting a few hours, in the whole extensive tropical cloud field.

The identification of these convective cores and the examination of their individual contributions of heat and moisture fluxes to the upper layers of the atmosphere will be important GATE objectives. Sikdar and Suomi (1971), and Sikdar (1973) have adequately demonstrated that such observations are possible from satellite data. With the improved resolution of the latest satellites, these estimates can be considerably refined.

The purpose of this paper is to demonstrate the large-scale time variant activity of the deep convective cores using specially processed satellite pictures.

2. THE METHOD OF IDENTIFYING THE CONVECTIVE CORES

The areas of most active convection can be identified by a simple brightness enhancement technique which emphasizes only selected portions of the satellite signal. The hypothesis underlying this technique is that brighter clouds are deeper clouds and also have the highest liquid water content. Sikdar (1973) and Martin and Suomi (1972) have qualitatively demonstrated this hypothesis by comparing satellite pictures to radar echoes. Further support came from Park (1973). He found a strong correlation between visual cloud brightness and infrared temperature (brightest clouds were colder). This implies that the brightest clouds extend to higher levels in the atmosphere and thus are deep convective clouds.

The technique of signal enhancement was developed at the Space Science and Engineering Center, University of Wisconsin under a grant from the National Science Foundation (1970, 1971). This technique is also discussed in a recent paper by Martin and Suomi (1972). In this operation, the uppermost 13% of the ATS-3 satellite signal is enhanced. This closely corresponds to the observed albedo range of 80-90% for the cumulonimbus clouds. In the resulting pictures, the convective cores stand out clearly as white spots. The other clouds and background appear gray.

It should be noted that, in producing these specially processed pictures, a number of difficulties were encountered. The most significant problem was the unrecorded changes in satellite signal gain made at the receiving stations. At times, higher gain settings caused saturation of the brightest clouds. This problem could not be corrected in the processing of the pictures.

3. LONGITUDE-TIME MONTAGES

The specially processed pictures were cut into strips 5° of latitude wide (Figure 1) and placed in succeeding order to form montages in the longitude-time mode (Figure 2). This is similar to the presentation of ESSA pictures made by Sikdar and Suomi (1971). One picture taken around noon, local time, (1500Z to 1700Z) each day was selected for the montages. The period covered was from May 3 to July 28, 1969. Each strip on the montages extended from 90°W,

eastward across the Atlantic ocean to 20°W. The satellite pictures were cut into 8 strips from 10°S to 30°N latitude covering most of the proposed GATE area. The dates of the pictures were indicated to the left of the strips on the montages. The white gaps indicated omission of strips because of missing pictures or poor data quality.

The uneven edge of the time sections, seen on Figure 2, was a result of the cutting of the satellite pictures. Grids had to be overlaid on the pictures and aligned with the land marks. Unfortunately, a shift in the locations of the satellite through the period caused a change in the orientation of the pictures and, thus, problems in marking grid locations. The subpoint of the satellite shifted by about 10° during the period. This caused the edges to curve slightly on the montages and an increase in strip length. Both of these effects had little bearing on the analysis presented in the discussion.

The brightness enhanced convective cores were all not easily distinguished on the reproductions presented in this report (Figure 2). This was a result of a slight loss in contrast incurred in the reproduction of the montages. The enhanced clouds, however, could be more easily identified on enlarged photos (Figure 3).

4. DISCUSSION

The most intense convective clouds appeared mostly over land areas in the western Atlantic. This was clearly evident from the vertical alignment of bright spots on the left side of the time sections. These land areas included the Lesser Antilles islands (15°-20°N time section), around 70°S longitude, and the east coast of the Honduras along with the Isthmus of Panama, around 80°W (10°-15°N time section). Other intense convection, commonly found over the South American continent (all time sections from 10°S to 10°N), dominated all the left sides of the lower latitude time sections.

Of particular interest is the expanding influence of the tropics in the spring season. During the winter, the subtropics are dominated by the westerly wind mid-latitude circulation system; cold fronts commonly move into this area. Then, as the tropics move northward in the late spring, the subtropics are influenced by tropical weather systems. An example of this change-over can be seen in the two subtropical time sections (30°-25°N and 25°-20°N latitude). From 6-3, an extensive cloud band can be seen on the left side of the time sections. This cloudiness is associated with a cold front extending over northern Florida (Figure 4). On 6-14, this front moved eastward. Its movement is depicted as a line of clouds extending from the upper left towards the lower right of the time sections. On 6-19, the influence of the cold front diminished and it became a trough of low pressure on the surface analysis. The cloud cluster associated with the front switched to westward movement thereafter. Then a second cluster formed off the east coast of Florida and moved eastward (25-30°N time section). The two clusters apparently merged around 6-24 and moved westward with an approximate speed of

3-4° long/day. After this period, only westward moving cloud clusters can be seen on the time sections. Similar cloud cluster motions, depicting the expansion of the tropics, can be seen on time sections of ESSA pictures made by Wallace (1970).

In the lower latitudes (0-15°N), most of the convective cores were found in the ITCZ (5-10°N). The longitudinal distribution of these bright spots was more randomly distributed in the low latitudes 5-10°N than just north of the ITCZ. This shows that intense convection is common in the ITCZ across the oceans. In the 10-15°N time section, however, a systematic westward propagation of cloud clusters is seen. The bright spots appear well organized, especially over the ocean.

South of 5°N there is very little cloud and core activity over the ocean. This is clearly denoted by the presence of darkness in the eastern region of the time sections, 10°S to 5°N. At these latitudes, convection is mostly concentrated over South America, the left side of these time sections.

The duration of a convective core is found to be greater than two hours in most cases and, on many occasions, their organization in a cluster barely changed in the course of the day. This is illustrated in Figure 5. For lack of a suitable brightness normalization scheme, the brightness enhancement was not attempted on pictures taken at low sun angles. Therefore, the full life time of the cores could not be investigated. On the average the cores consisted of a small fraction of the total cloud cover 1% to 6% (Figure 6). The ITCZ region (5-10°N) contained the most core area. Mean cloudiness ranged from 26% in the high latitudes (10-30°N) to 60% in the low latitudes (5°S-10°N). The standard deviation (not presented) suggested a relatively higher variability in cloudiness in the ITCZ area, implying the occurrence of a wider spectrum of convective activity.

Over the zonal belt as a whole, the total core area fluctuated at a much higher rate than the total cloud cover in respective latitude belts (Figure 7). These core area fluctuations seemed to follow cycles from 2 to 5 days duration, as compared to the total cloud cover fluctuations of 6 to 8 days. This agreed with the periodicity observed in the fluctuations of cloudiness amount in the tropical Pacific by Sikdar and Suomi (1971). Just north of the ITCZ (10-15°N) the cloud cover appeared to undulate in shorter periods with some agreement with core area variations. This agreement was possibly due to cirrus blow-off from tropical thunderstorms spreading northward. Also clearly seen in Figure 7 is that trends in the core area fluctuation (increasing or decreasing area) generally followed those of the total cloud cover undulation, for example, days 2, 7, 8, 13, 17, 20, 24, 26, etc. in 5-10°N. This may imply that the upward mass transport in the tropical Hadley cell, accomplished by ITCZ convection, is controlled by large-scale planetary circulations.

The daily average cloud cover in the tropics, 0-15°N, was compared to the subtropics, 15-30°N in Figure 8. Apparent in this diagram is a consistent phase opposition in their time variations for a part of the study-period, for example, days 12, 15, 19, 21, 23, and 25. This phase opposition could be an indication of short period oscillations in the tropical Hadley cell circulation. A cloud cover increase in the low latitudes implies increased rising motion. At the same time, a corresponding strengthening of the subsidence probably causes the observed cloud cover decrease in the higher latitudes. How such a planetary-scale mass exchange was possible on a short time scale is not clear to us at this time. This conjecture needs verification from other extensive observations. GATE and FGGE will hopefully provide such an opportunity.

5. SUMMARY AND CONCLUSIONS

The time section montages of satellite pictures are very useful for tracking cloud clusters in the time domain. Such movements are not often obvious when searching through individual satellite pictures. The expanding influence of the tropics in the spring of the year can be recognized by the change in cloud motion patterns.

By brightness enhancing the satellite pictures, the relationship between the intense convective areas and the cloud clusters can be seen. It appears from this analysis, that the convective cores are found well organized in oceanic cloud clusters. Over the land masses, however, the cores appear stationary because the orographic influence is more dominant. The cores generally persist much longer than the normal duration of a single thunderstorm (2 hours or longer). The time sections suggest that the cores possibly are controlled by large scale tropical circulations. They seem to develop in cycles from 2 to 5 days duration.

In general, the cloud cover across the tropical Atlantic (spanning 70° of longitude) follow oscillation cycles of 6-8 days. When these cloud cover oscillations were compared to the subtropical variations, a consistent phase opposition is revealed, at least for a part of the study period. This may indicate short period planetary scale fluctuation in the tropical Hadley cell.

ACKNOWLEDGEMENT

The research report in this paper is partly supported by NSF under grants GA 25059 (1970), GA 24641 (1971) and in part by NOAA under grant NG-26-72.

REFERENCES

Kornfield, J., A. F. Hasler, K. J. Hanson and V. E. Suomi, 1967; Photographic Cloud Climatology from ESSA III & V Computer Produced Mosaics - Bull. Amer. Meteor. Soc., 48, 878-883.

Martin, D. W., and V. E. Suomi, 1972; A Satellite Study of Cloud Clusters over the Tropical North Atlantic Ocean, Bull. of Am. Meteor. Soc., 53 p. 135.

Meteorologische Abhandlungen, Institute for Meteor. and Geophysics, Freien University, Berlin, Germany, Vol. CII No. 2 (1969)

Park, S., 1973: Correlation Between Cloud Thickness and Brightness Using NIMBUS-IV THIR Data (11.5 channel) and ATS-3 Digital data. This volume.

"Preparation of a Series of ATS-3 Images-Enhancement, Precision-Display Pictures of the BOMEX Period" Principal Investigator: V. E. Suomi; Co-Investigator: D. N. Sikdar. NSF Grant #GA-24641 (1970).

"Preparation of a Series of Specially Processed Pictures from the ATS Satellites for Three Periods of Special Interest". Principal Investigator: V.E. Suomi; Co-Investigator: D.N. Sikdar. NSF Grant #GA-29059 (1971).

Sikdar, D. N. and V. E. Suomi, 1971: Time Variations of Tropical Energetics as Estimated from a Geostationary Satellite Altitude. J. Atmos. Sci. 28, 170-180.

Sikdar, D. N., J. A. Young and V. E. Suomi, 1972; Time-Spectral Characteristics of Large-Scale Cloud Systems in the Tropical Pacific. J. Atmos. Sci. 29, 229-239.

Sikdar, D. N., 1973: ATS-3 Observed Cloud Brightness Field Related to a Meso-to-Subsynoptic Scale Rainfall Pattern. Tellus, 24, 400-413.

Wallace, J. M., "Time-Longitude Sections of Tropical Cloudiness (December 1966 - November 1967)", ESSA Tech. Report NESC 56, Washington D. C., (July, 1970).

LEGEND

Figure 1: Overlay grid used for cutting the ATS-3 satellite pictures into latitude strips to form the time sections montages.

Figure 2: Longitude time section montages of ATS-3 brightness enhanced pictures. The dates of the pictures from which each strip was taken are given on the left (May-July 28, 1969).

(Figure 2 continued)

Figure 3: Blow-up of Figure 2, 25°-30°N latitude section on the left; 20°-25°N latitude section on the right(June 3-July 13, 1969).

Figure 3 continued: Blow-up of Figure 2, 15°-20°N section on the left; 10°-15°N section on the right.

Figure 3 continued: Blow-up of Figure 2, 5°-10°N latitude section on left; EQ-5°N latitude section on the right.

Figure 4: Surface analysis, June 8, 1969. Analysis made by Freien University, Berlin, Germany.

Figure 5: Time section of pictures over one day, June 23, 1969.

Figure 6: Average cloud cover & bright core fraction of the cloud cover (average across the zonal belt, 90°W-20°W long).

Figure 7: Daily cloud cover area and bright core area. Day no. 1 corresponds to June 3, 1969; day 43 is July 13, 1969. This time series was taken from the time sections shown in Figure 3.

Figure 8: Daily cloud cover area and core area for the tropics, 0°-15°N latitude, and the subtropics, 15°N-30°N latitude (90°W-20°W longitude).

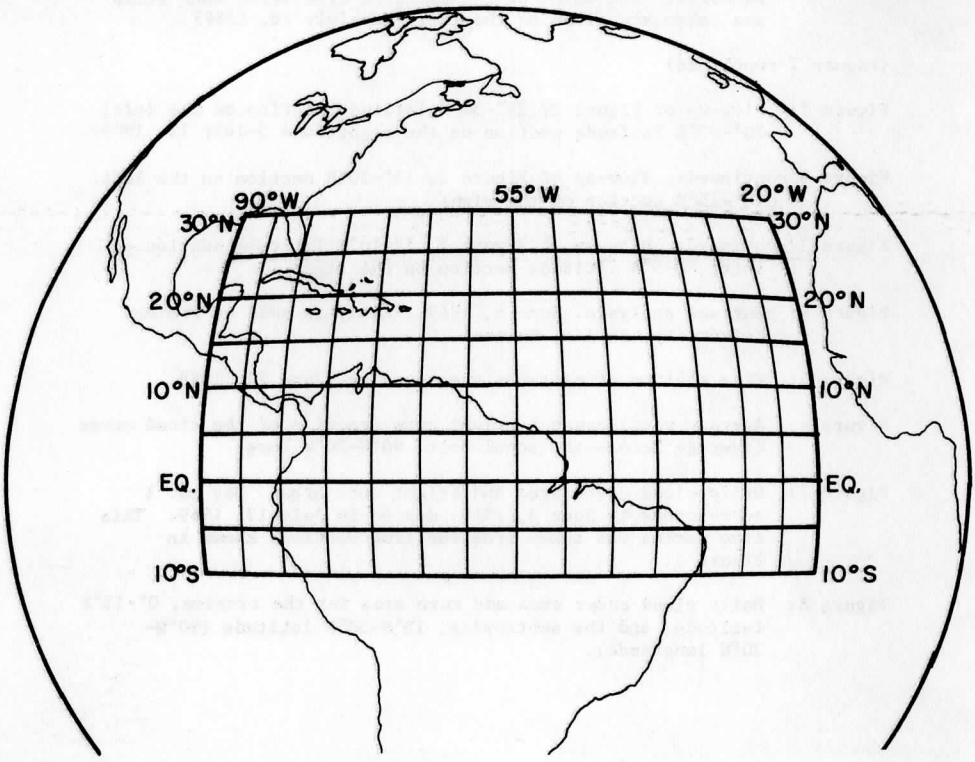

Figure 1

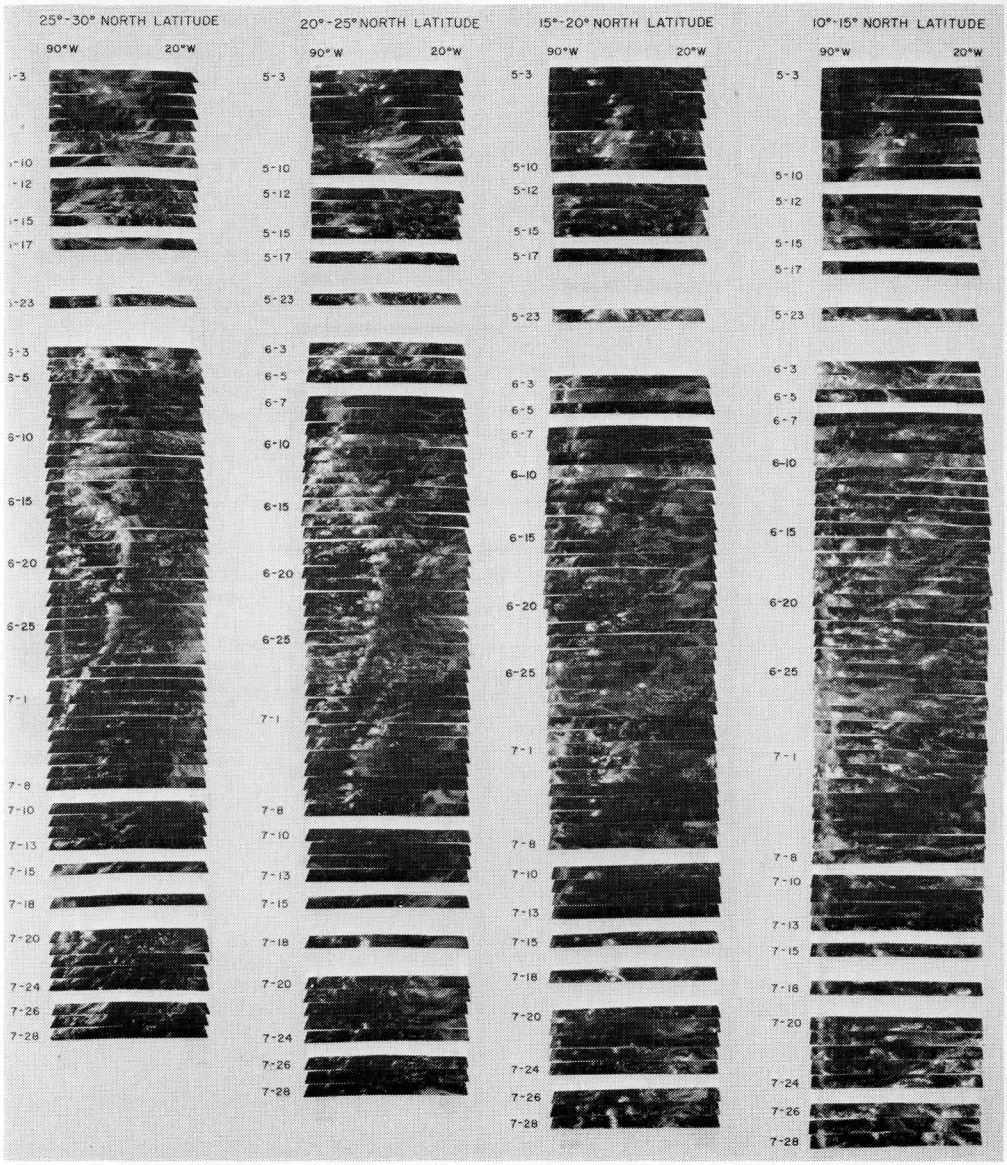
25°-30° NORTH LATITUDE
90°W
20°W
20°-25° NORTH LATITUDE
90°W
20°W
15°-20° NORTH LATITUDE
90°W
20°W
10°-15° NORTH LATITUDE
90°W
20°W

Figure 2a

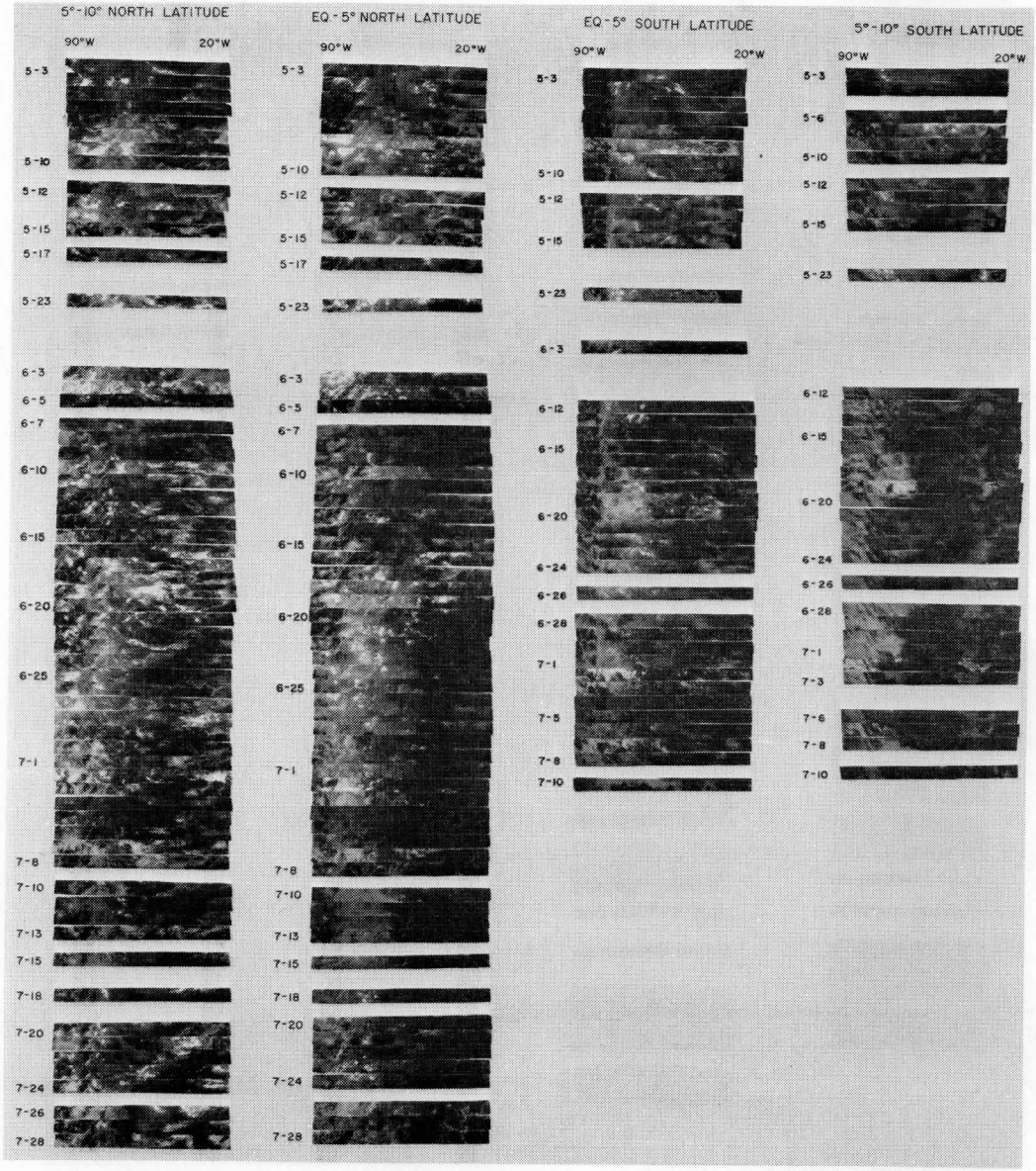
5°-10° NORTH LATITUDE
EQ.-5° NORTH LATITUDE
EQ.-5° SOUTH LATITUDE
5°-10° SOUTH LATITUDE
90°W
20°W
5-3
5-10
5-12
5-15
5-17
5-23
6-3
6-5
6-7
6-10
6-15
6-20
6-25
7-1
7-8
7-10
7-13
7-15
7-18
7-20
7-24
7-26
7-28
5-6
6-12
6-15
6-20
6-24
6-26
6-28
7-3
7-5
7-6
7-8
7-10

Figure 2b

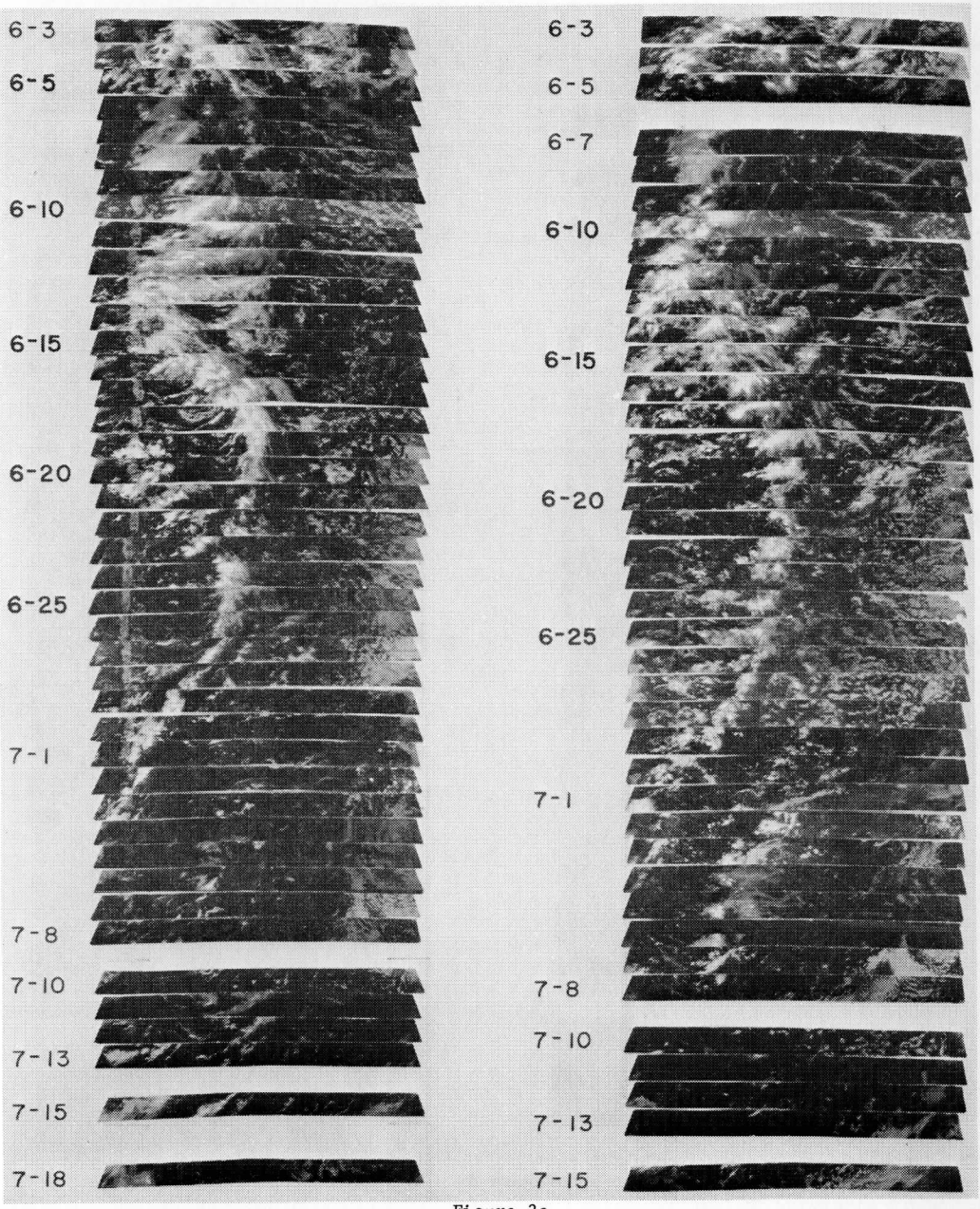
6-3
6-5
6-10
6-15
6-20
6-25
7-1
7-8
7-10
7-13
7-15
7-18
6-3
6-5
6-7
6-10
6-15
6-20
6-25
7-1
7-8
7-10
7-13
7-15

Figure 3a

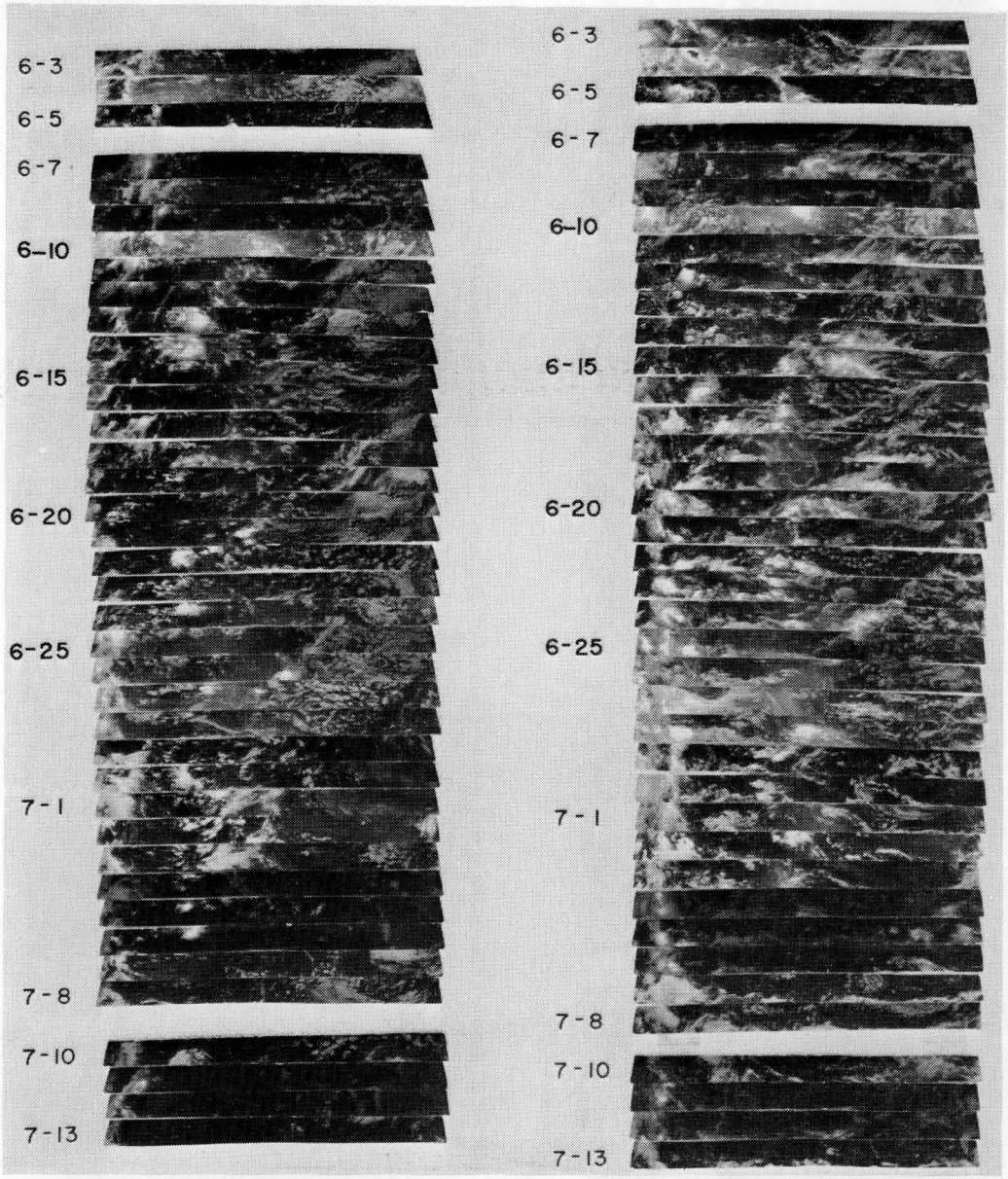
6-3
6-5
6-7
6-10
6-15
6-20
6-25
7-1
7-8
7-10
7-13
6-3
6-5
6-7
6-10
6-15
6-20
6-25
7-1
7-8
7-10
7-13

Figure 3b

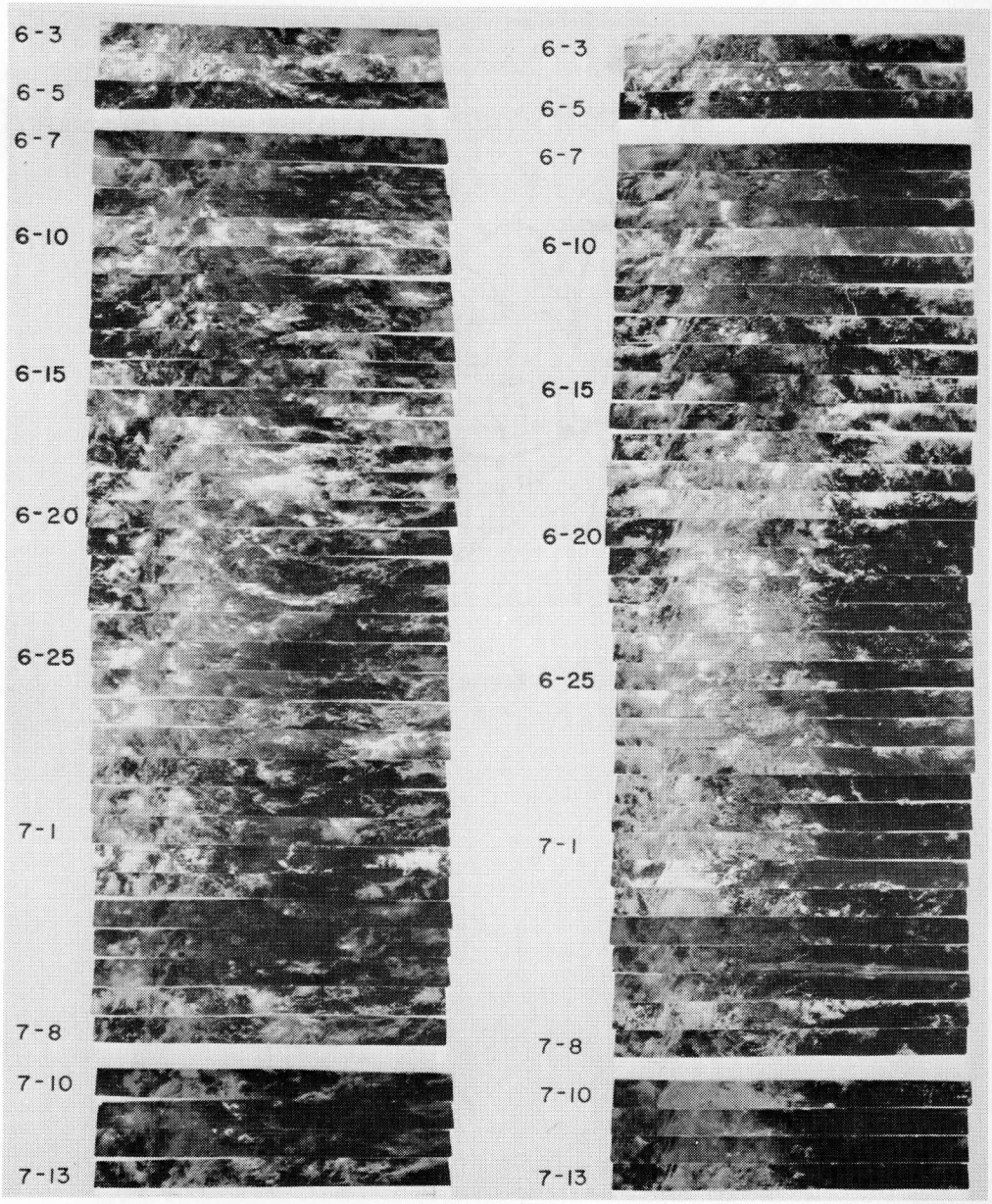
6-3
6-5
6-7
6-10
6-15
6-20
6-25
7-1
7-8
7-10
7-13
6-3
6-5
6-7
6-10
6-15
6-20
6-25
7-1
7-8
7-10
7-13

Figure 3c

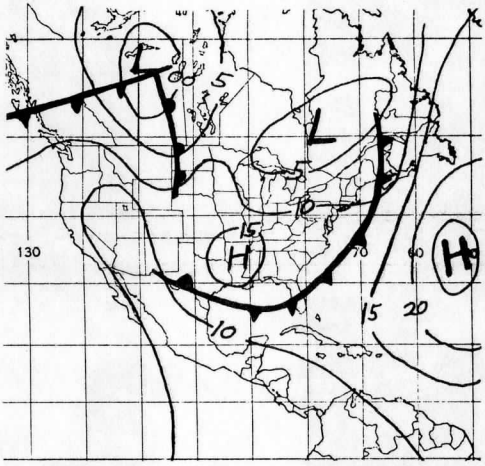

Figure 4

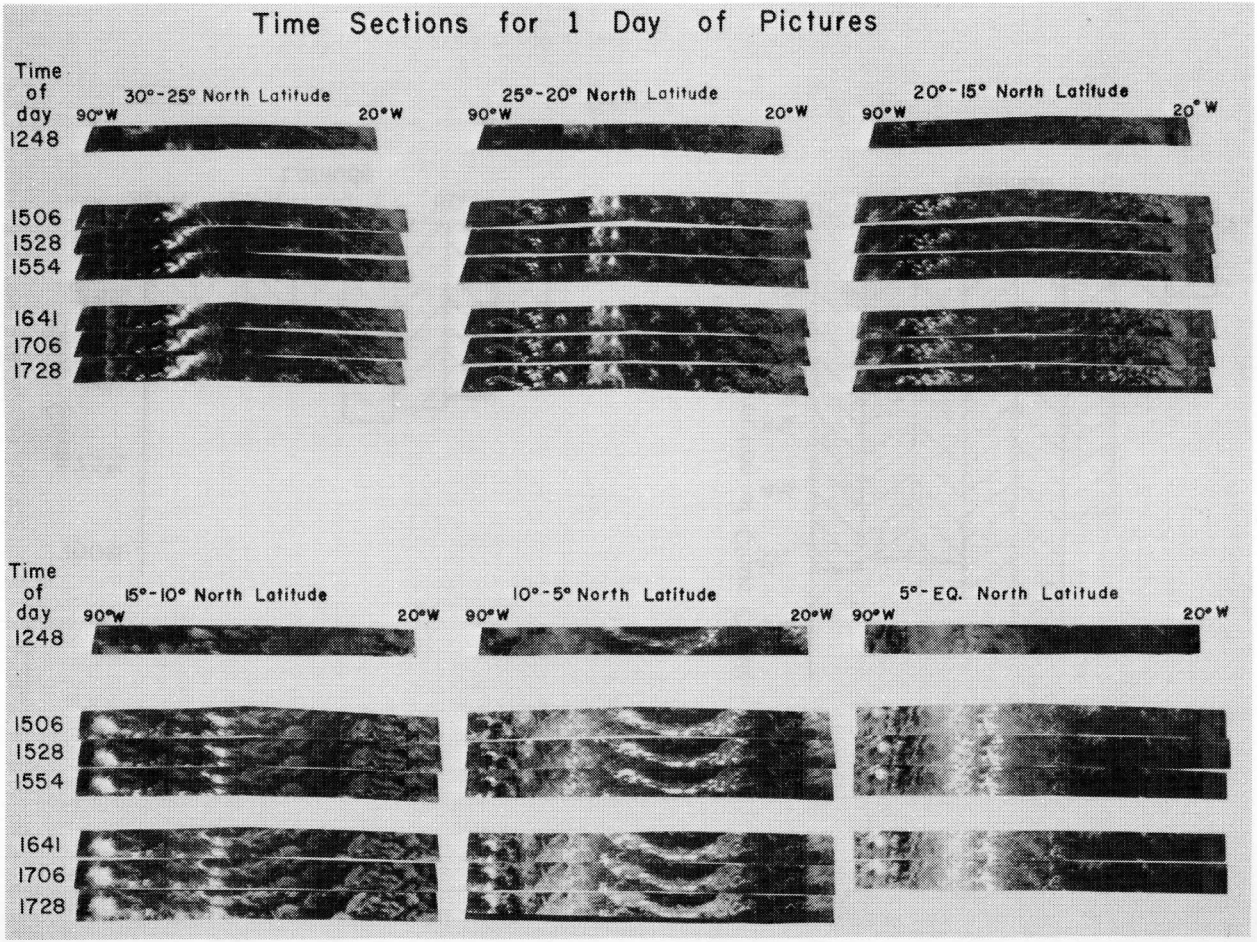
Time Sections for 1 Day of Pictures
Time of day
30°-25° North Latitude
25°-20° North Latitude
20°-15° North Latitude
90°W
20°W
1248
1506
1528
1554
1641
1706
1728
15°-10° North Latitude
10°-5° North Latitude
5°-EQ. North Latitude

Figure 5

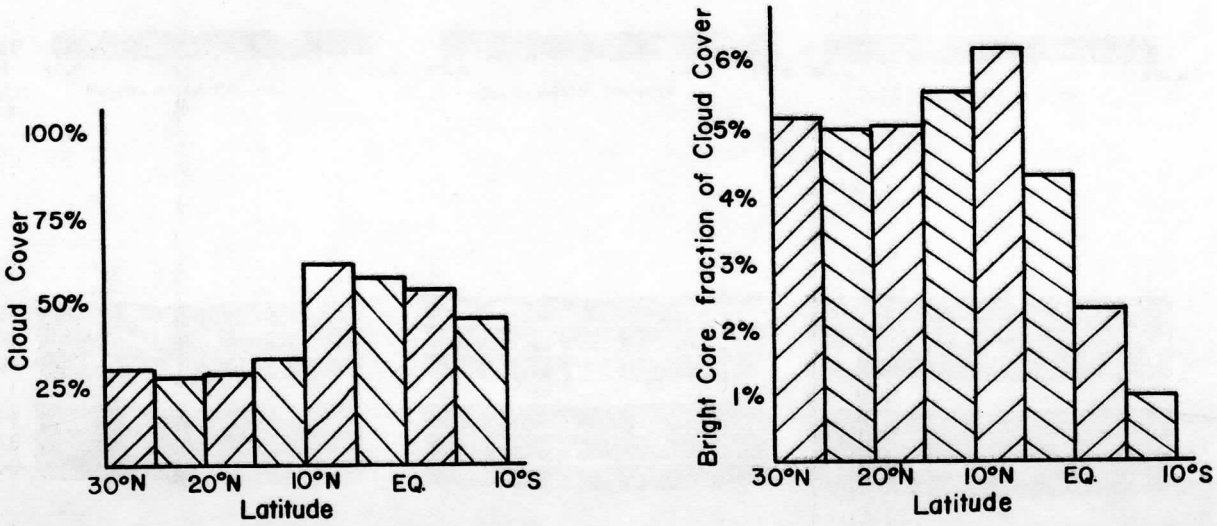
100%
75%
50%
25%
Cloud Cover
30°N
20°N
10°N
EQ.
10°S
Latitude
6%
5%
4%
3%
2%
1%
Bright Core fraction of Cloud Cover
30°N
20°N
10°N
EQ.
10°S
Latitude

Figure 6

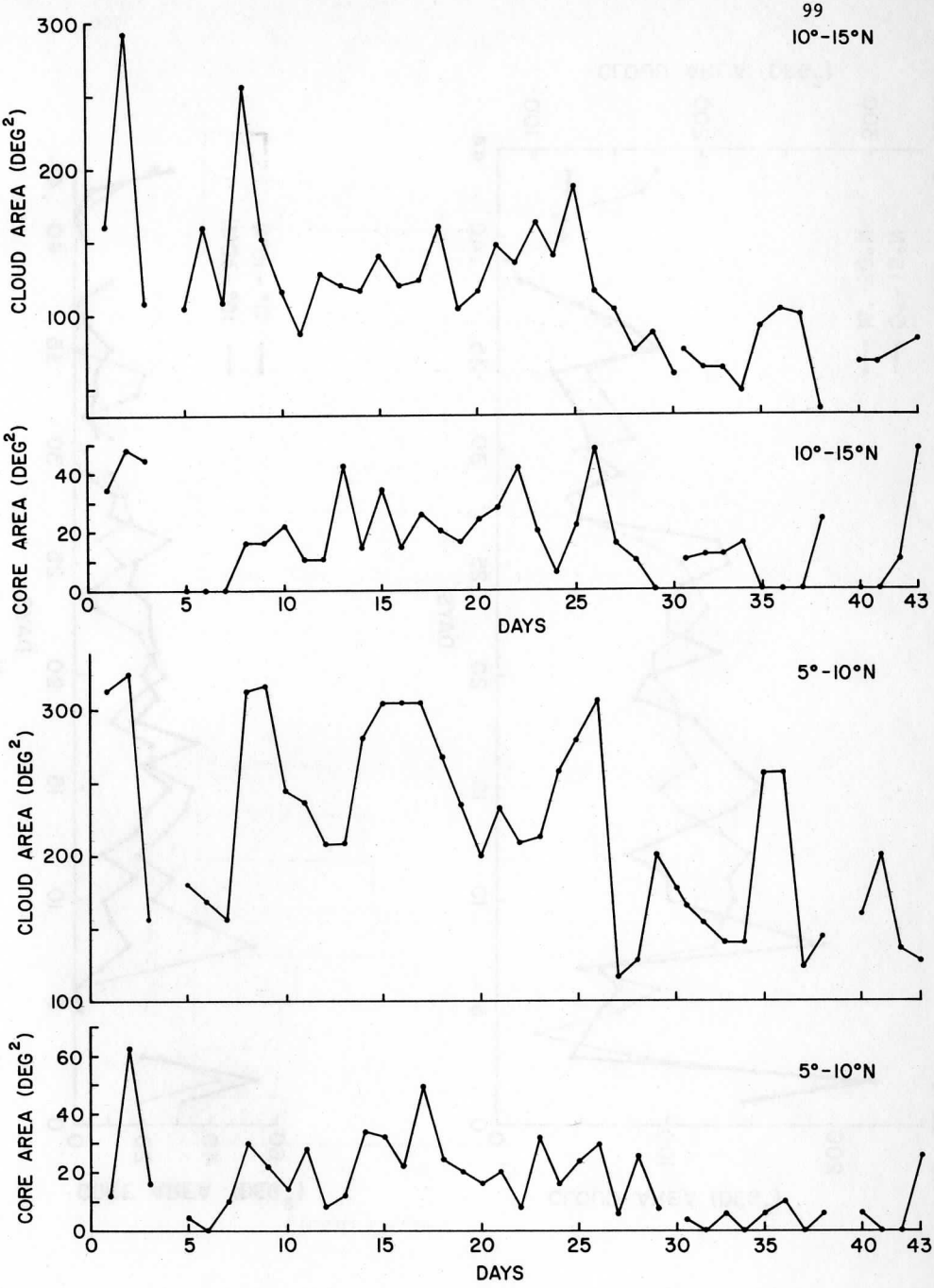
10°-15°N
CLOUD AREA (DEG²)
300
200
100
CORE AREA (DEG²)
40
20
0
10°-15°N
0
5
10
15
20
25
30
35
40
43
DAYS
5°-10°N
CLOUD AREA (DEG²)
300
200
100
CORE AREA (DEG²)
60
40
20
0
5°-10°N
0
5
10
15
20
25
30
35
40
43
DAYS

Figure 7

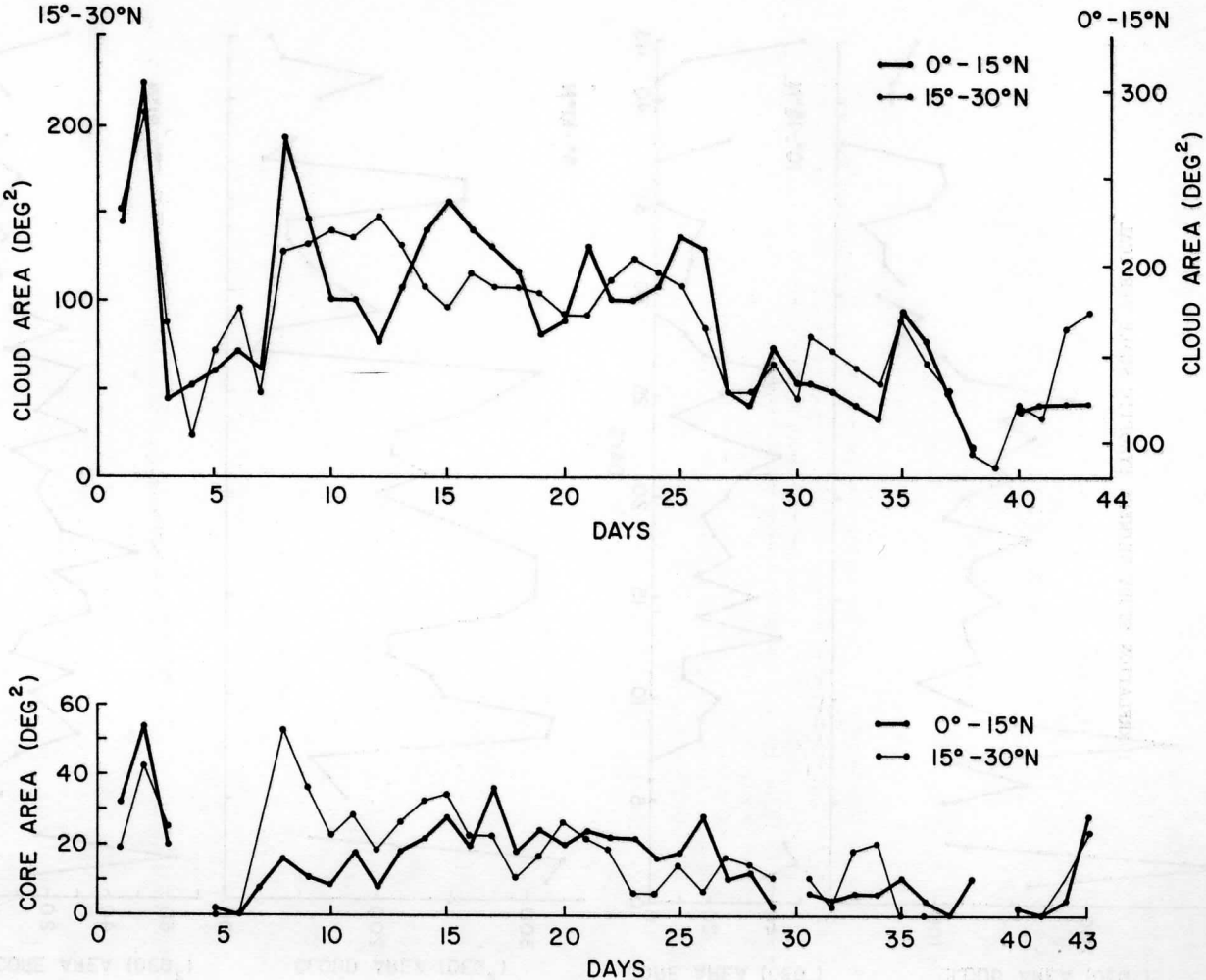
15°-30°N
0°-15°N
0°-15°N
15°-30°N
CLOUD AREA (DEG²)
CLOUD AREA (DEG²)
DAYS
CORE AREA (DEG²)
0°-15°N
15°-30°N
DAYS

Figure 8

A CORRELATION STUDY BETWEEN SYNOPTIC SCALE VERTICAL VELOCITY AND THE DAILY CHANGE IN CUMULUS CLOUDINESS IN THE CARIBBEAN

Sanjay Limaye and D. N. Sikdar

ABSTRACT

An attempt was made to study any correlation between cumulus-cloudiness-change over a day and the synoptic scale vertical motion at the 700 mb level. The daily cumulus cloud-cover was obtained from ESSA 9 satellite photographs for the first ten days in July 1969. The vertical motion at 700 mb for the same period was computed from upper air observations which were first interpolated onto a 4° latitude x 4° longitude grid.

The regression analysis showed a rather low correlation between the daily cumulus-cloudiness change and the 700 mb vertical velocity (coefficient of linear correlation = 0.26). The scatter about the regression line was significant ($\sigma_{cloudiness}$ = 14.9%). Many instances of increasing cloudiness due to cumulus clouds in regions of large-scale descent were seen.

1. INTRODUCTION

The large-scale vertical motion has been a perennially elusive quantity as far as measurements are directly concerned. In the tropical atmosphere the magnitude of the mean vertical motion, in the absence of precipitation is usually small (~ a few cm/sec). In the cumulus clouds the upward motion is much larger than the mean large-scale value. The resultant upward transport of mass is balanced mostly by a relatively slow (compared to the in-cloud upward motion) descent in the cloud-environment. While it is difficult to measure the upward motion in individual clouds its effects are nevertheless seen through cloud-growth and decay. Satellite photographs taken at reasonable intervals over the same geographical area are excellent for delineating such changes.

Noting that the large-scale vertical velocity can be expressed as an ensemble mean of the in-cloud upward motion and a downward component in the cloud environment (see for example, Arakawa, 1971), it was hypothesized that the change in the cloud-cover amount which is of convective origin should reflect the influence of the large-scale component or vice versa. The present study is an effort to estimate

the extent of the said influence, i.e. to test the validity of the hypothesis. The study is admittedly crude and is meant to be exploratory.

The amount of cumulus-cloud-cover in percent was obtained from photographs taken from the ESSA 9 satellite, a polar orbiter. The photographs are available only once a day for a given area. The change in the cumulus-cloudiness was found as the difference between the amount (percent) on a given day and that on the next day.

2. COMPUTATION OF VERTICAL VELOCITY

It was decided to focus attention on the Caribbean region. Upper air observations of wind and temperature were obtained for July 1969 from the World Meteorological Organization Regional Office in Miami, Florida in the form of synoptic analyses. The period chosen for the study (first ten days in July 1969) coincides with part of the Phase IV of the Barbados Oceanographic and Meteorological Experiment (BOMEX) and during this period the regular observations were supplemented by pilot balloon soundings from many ships.

Wind and temperature observations from stations were first interpolated onto a 4° latitude x 4° longitude grid shown in Figure 1 at 850 mb, 700 mb, and 500 mb levels using a modified version (Whittaker, 1974) of Cressman's (1959) interpolation scheme. The vertical velocity, ω (= dp/dt) at 700 mb is computed by the adiabatic method as follows. The total change in the potential temperature for a parcel of air can be expressed as:

$$\frac{d\theta}{dt} = \frac{\partial\theta}{\partial t} + \tilde{V}\cdot\nabla\theta + \omega\frac{\partial\theta}{\partial p} \qquad (1)$$

θ : potential temperature

$\tilde{V}$: horizontal velocity

$\omega = \frac{dp}{dt}$

The above equation is valid following a fluid parcel in motion. In order to apply it to the available data, it has to be averaged over space (4° x 4°) and time (24 hours), yielding one value for 4° x 4° box. On space averaging:

$$\left\langle\frac{d\theta}{dt}\right\rangle = \left\langle\frac{\partial\theta}{\partial t}\right\rangle + \left\langle\tilde{V}\cdot\nabla\theta\right\rangle + \left\langle\omega\frac{\partial\theta}{\partial p}\right\rangle$$

$$= \left\langle\frac{\partial\theta}{\partial t}\right\rangle + \left\langle\tilde{V}\right\rangle\cdot\left\langle\nabla\theta\right\rangle + \left\langle\omega\right\rangle\left\langle\frac{\partial\theta}{\partial p}\right\rangle + \left\langle\tilde{V}'\cdot(\nabla\theta)'\right\rangle + \left\langle\omega'\left(\frac{\partial\theta}{\partial p}\right)'\right\rangle \qquad (2)$$

wherein $\langle\ \rangle$ denotes space average and prime denotes deviations from the space average. On time averaging next:

$$\overline{\left\langle \frac{d\theta}{dt} \right\rangle} = \overline{\left\langle \frac{\partial\theta}{\partial t} \right\rangle} + \overline{\left\langle \tilde{\vec{V}} \right\rangle \cdot \left\langle \nabla\theta \right\rangle} + \overline{\left\langle \omega \frac{\partial\theta}{\partial p} \right\rangle} + \overline{\left\langle \tilde{\vec{V}}' \cdot (\nabla\theta)' \right\rangle} + \overline{\left\langle \omega' \left(\frac{\partial\theta}{\partial p}\right)' \right\rangle}$$

$$= \overline{\left\langle \frac{\partial\theta}{\partial t} \right\rangle} + \overline{\left\langle \tilde{\vec{V}} \right\rangle} \cdot \overline{\left\langle \nabla\theta \right\rangle} + \overline{\left\langle \omega \right\rangle \left\langle \frac{\partial\theta}{\partial p} \right\rangle} + \overline{\left\langle \tilde{\vec{V}} \right\rangle^* \left\langle \nabla\theta \right\rangle^*} + \overline{\left\langle \omega \right\rangle^* \left\langle \frac{\partial\theta}{\partial p} \right\rangle^*}$$

$$+ \overline{\left\langle \tilde{\vec{V}}' \cdot (\nabla\theta)' \right\rangle} + \overline{\left\langle \omega' \left(\frac{\partial\theta}{\partial p}\right)' \right\rangle} \qquad (3)$$

In the above equation a horizontal bar $\langle\ \rangle$ denotes a 24 hour average of any quantity and (*) denotes the deviation from the 24 hour average of that quantity.

It is difficult to account for all terms in equation (3) with the available data. Although the eddy terms may be large at times, we have assumed a large-scale adiabatic flow over the period of 24 hours and attempted to evaluate the mean terms. The local time rate of change of potential temperature was obtained as mean from one day to the next at 00Z and 1200Z. The lapse rate at 700 mb was similarly obtained as the mean from the 850 mb and 500 mb difference.

Equation (3) reduces to:

$$\omega = -\frac{1}{\frac{\partial\theta}{\partial p}} \left[\frac{\partial\theta}{\partial t} + \vec{V} \cdot \nabla\theta \right]$$

Once again, the interest here is not in the absolute magnitude of ω but in its relationship to tropical cloudiness-change.

3. RESULTS

The locations of the upper air sounding stations and ships used in this computation scheme are shown in Figure 1. Figure 2 presents a series of computed ω-fields and parts of ESSA-9 cloud photographs for that area. However, a time difference between the two precludes any direct comparison. The satellite pictures have been taken at approximately 1500 LST (~2000 GMT), while the upper air data pertains to 00 and 12 GMT observations. For a realistic comparison, two successive cloud pictures have been used to compare to the ω-field of the previous day. Obviously, such a comparison is more appropriate for disturbances having a lifetime of more than a day.

Figure 3 shows the correlation between the ω-field which was first weighted linearly for the time lag between the satellite observation and the mid-point of the interval between the upper air observations; and change in the cloudiness amount. The error bars are at $\pm$ 1σ level. The correlation coefficient is 0.26. The scatter

diagram, in general, shows an upward motion related to the increased cloud cover amount. Although a linear correlation has been attempted here, a wide scatter (σ = 14.9) implies a complicated relationship between the two. The cloud cover change depends not only on the ω-field but also on the other atmoshperic variables such as stability and advection. Most of the scatter in cloudiness change in Figure 3 appears for vertical velocity values around +5 to -5 x 10^{-4} mb/sec. This probably suggests that the grid size chosen for computing ω-field may be too large to detect small changes in mesoscale cloudiness. The scatter, which indicates increasing cloudiness in descending motion, need not be interpreted as erroneous. It probably implies a large scale descent around isolated growing cumulus clouds. The cloud growth depends on, among other things, the cloud-area density i.e. ratio of the area of the cloud to that of the whole system which includes the descent area around the cloud. For example, from numerical simulation studies, Asai and Kasahara (1967) found that maximum growth i.e. a deep convection case, occurs when the convective cloudiness is initially only several percent.

It should also be noted that, although the synoptic-scale vertical motion has been computed from observations 24 hours apart, the typical lifetime of the small cumulus clouds is much smaller. The results in the present case are thus contaminated by the departure from a quasi-steady state regarding the synoptic conditions implicitly assumed and including the diurnal variation of ω.

Figure 4 is a typical time series of cloudiness-change and computed vertical motion for a particular grid element. While small changes in vertical motion show some anomaly in the cloudiness-change, a pronounced upward motion results in a definite increase in the cloudiness amount.

5. CONCLUDING REMARKS

We have attempted a crude analysis of the correlation between the synoptic-scale adiabatic vertical velocity at 700 mb and convective (small Cu) cloudiness-change. In this admittedly small data sample, we found a poor correlation (r = 0.26) with a broad scatter in the approximate band $\pm$ 5 x 10^{-4} mb/sec. It is interesting to note, however, from this scatter diagram, that the small convective clouds could grow occasionally despite the synoptic-scale descending motion around them. In most of these cases, the clouds are found isolated and their intensity of convection, as estimated from the cloud brightness intensity, appears weak (brighter clouds are assumed thicker clouds). The situation is certainly different in synoptic-scale intense disturbances regime. Here organized bright cumulonimbus clouds are seen to grow in the environment of large-scale convergence field. The slope of the regression line does suggest a significant influence of a large scale motion on the convective cloud population and intensity. However, for a confident statistical relationship, higher resolution satellite data and also more frequent closely spaced conventional observations are needed. Both these needs will hopefully be met during the GARP (Global

Atmospheric Research Program) Atlantic Tropical Experiment to be conducted during the summer of 1974.

ACKNOWLEDGEMENTS

The authors wish to thank Professor David D. Houghton for frequent discussions regarding the work and Miss Katherine Hui for help in the analysis of data. This research was supported by NOAA under grant 1-36036.

REFERENCES

Asai, T. and Akira Kasahara, 1967: A Theoretical Study of the Compensating Downward Motions associated with Cumulus Clouds, J. Appl. Meteor., Volume 24, 487-496.

Asakawa, A., 1971: Parameterization of Cumulus Convection (Lecture notes distributed at Workshop of the UCLA General Circulation Model, 14-22 June 1971). Also, Design of the UCLA General Circulation Model, Numerical Simulation of Weather and Climate, Technical Report No. 7, Dept. of Meteorology, University of California, Los Angeles.

Cressman, G. P., 1959: An Operational Objective Analysis System, Mon. Wea. Rev., 87, 367-374.

Whittaker, T., 1973: Master's Thesis (in preparation), Dept. of Met., University of Wisconsin, Madison.

FIGURE LEGENDS

Figure 1: Location of stations (including travelling ships) from which upper air observations are available, and were used for interpolation.

Figure 2a: Analysis of the synoptic scale vertical motion (x 10^{-4} mb/sec.) and the cloud cover over that area on July 1 (on the left of the analysis) and July 2, 1969 (on the right).

Figure 2b: Same as Figure 2a. The ESSA-9 photograph is for July 2-3, 1969.

Figure 2c: Same as figure 2a. The photographs are for July 3-4, 1969.

Figure 2d: Same as Figure 2a. The photographs are for July 5-6.

Figure 2e: Same as figure 2a. The photographs are for July 9-10, 1969.

Figure 3: A scatter diagram of the 700 mb large scale vertical velocity and the change in cumulus cloud cover in one day (the daily cloudiness is expressed in percent). The linear correlation coefficient is 0.27 and the error bars are at one standard deviation, 14.9.

Figure 4: Time series plots of cloudiness change and vertical velocity.

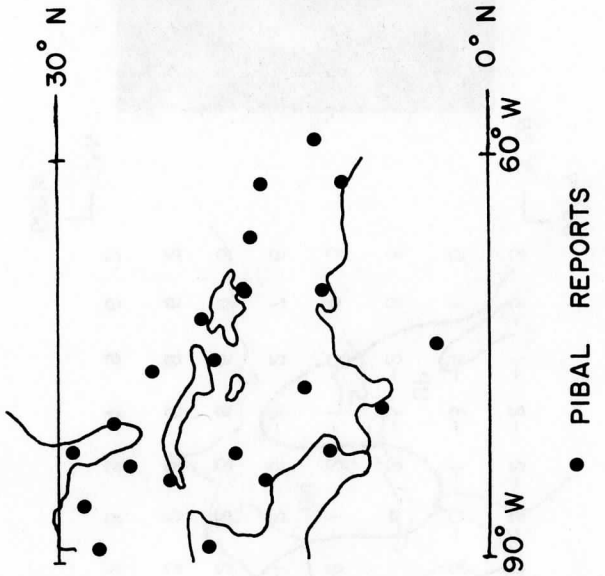

Figure 1

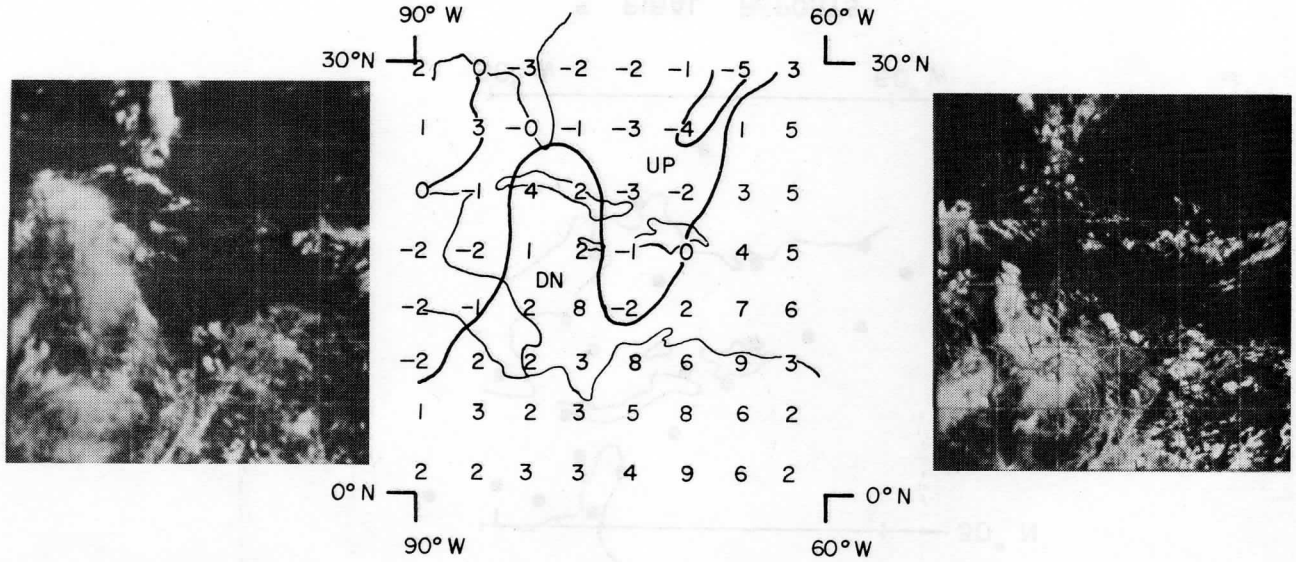
90° W
60° W
30°N
30° N
2 0 -3 -2 -2 -1 -5 3
1 3 -0 -1 -3 -4 1 5
UP
0 -1 4 2 -3 -2 3 5
-2 -2 1 2 -1 0 4 5
DN
-2 -1 2 8 -2 2 7 6
-2 2 2 3 8 6 9 3
1 3 2 3 5 8 6 2
2 2 3 3 4 9 6 2
0° N
0° N
90° W
60° W

Figure 2a

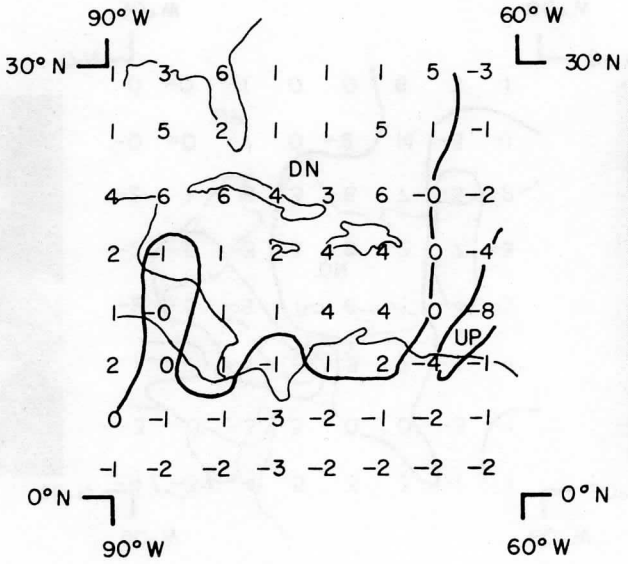
90° W
60° W
30° N
30° N
1 3 6 1 1 1 5 -3
1 5 2 1 1 5 1 -1
DN
4 6 6 4 3 6 -0 -2
2 -1 1 2 4 4 0 -4
1 -0 1 1 4 4 0 -8
UP
2 0 -1 -1 1 2 -4 -1
0 -1 -1 -3 -2 -1 -2 -1
-1 -2 -2 -3 -2 -2 -2 -2
0° N
0° N
90° W
60° W

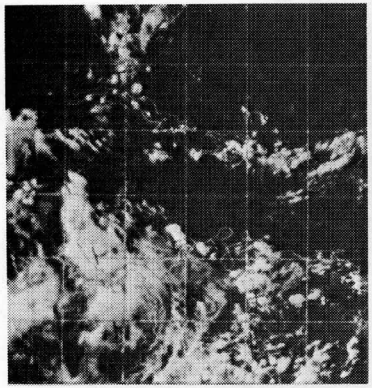

Figure 2b

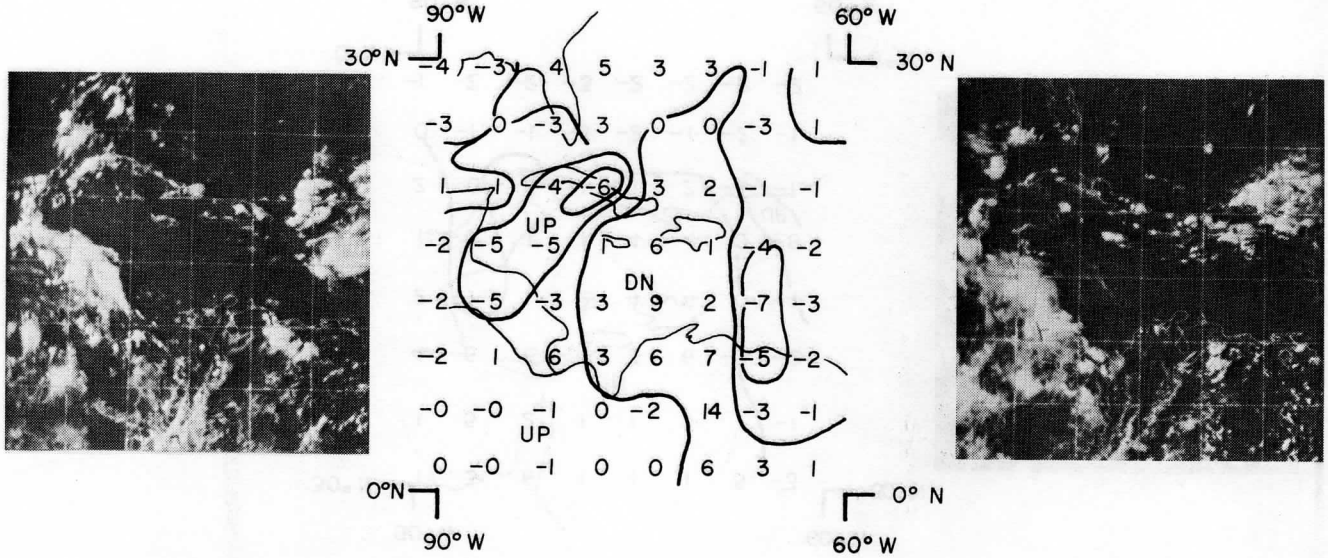

Figure 2c

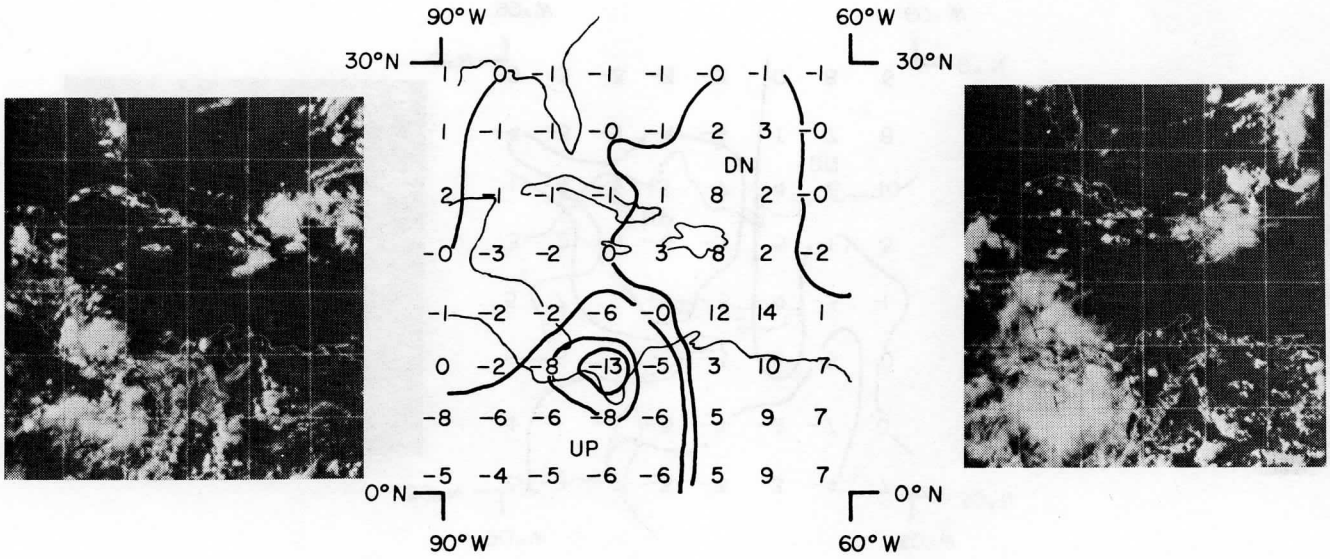

Figure 2d

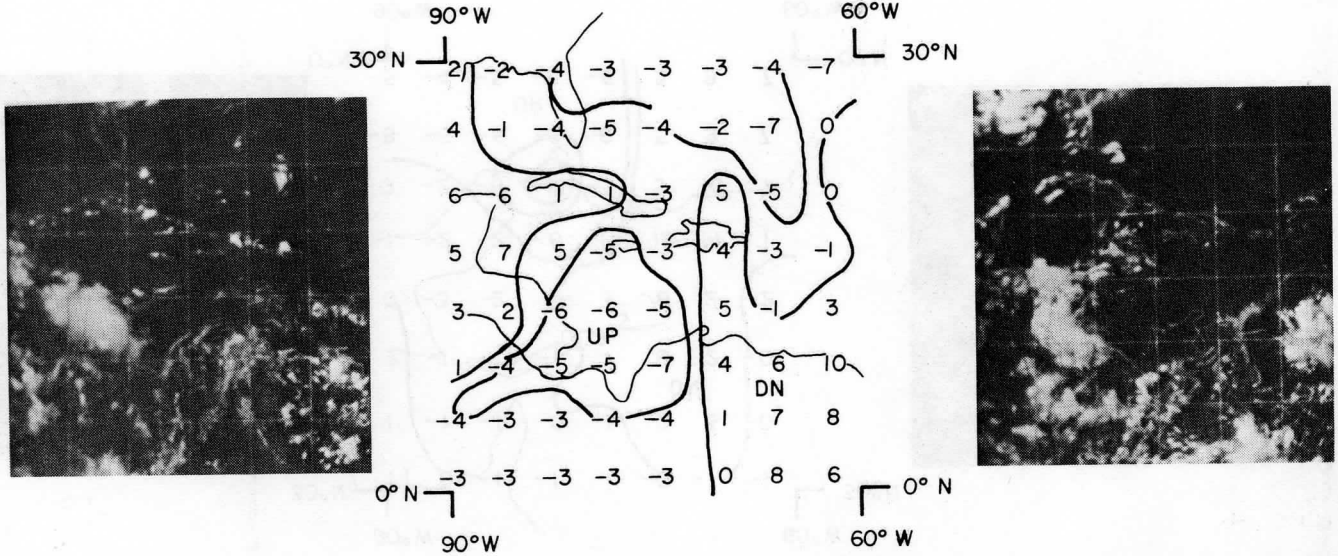
90° W
60° W
30° N
30° N
2 -2 -4 -3 -3 -3 -4 -7
4 -1 -4 -5 -4 -2 -7 0
6 6 1 1 -3 5 -5 0
5 7 5 -5 -3 4 -3 -1
3 2 -6 -6 -5 5 -1 3
UP
1 -4 -5 -5 -7 4 6 10
DN
-4 -3 -3 -4 -4 1 7 8
-3 -3 -3 -3 -3 0 8 6
0° N
0° N
90° W
60° W

Figure 2e

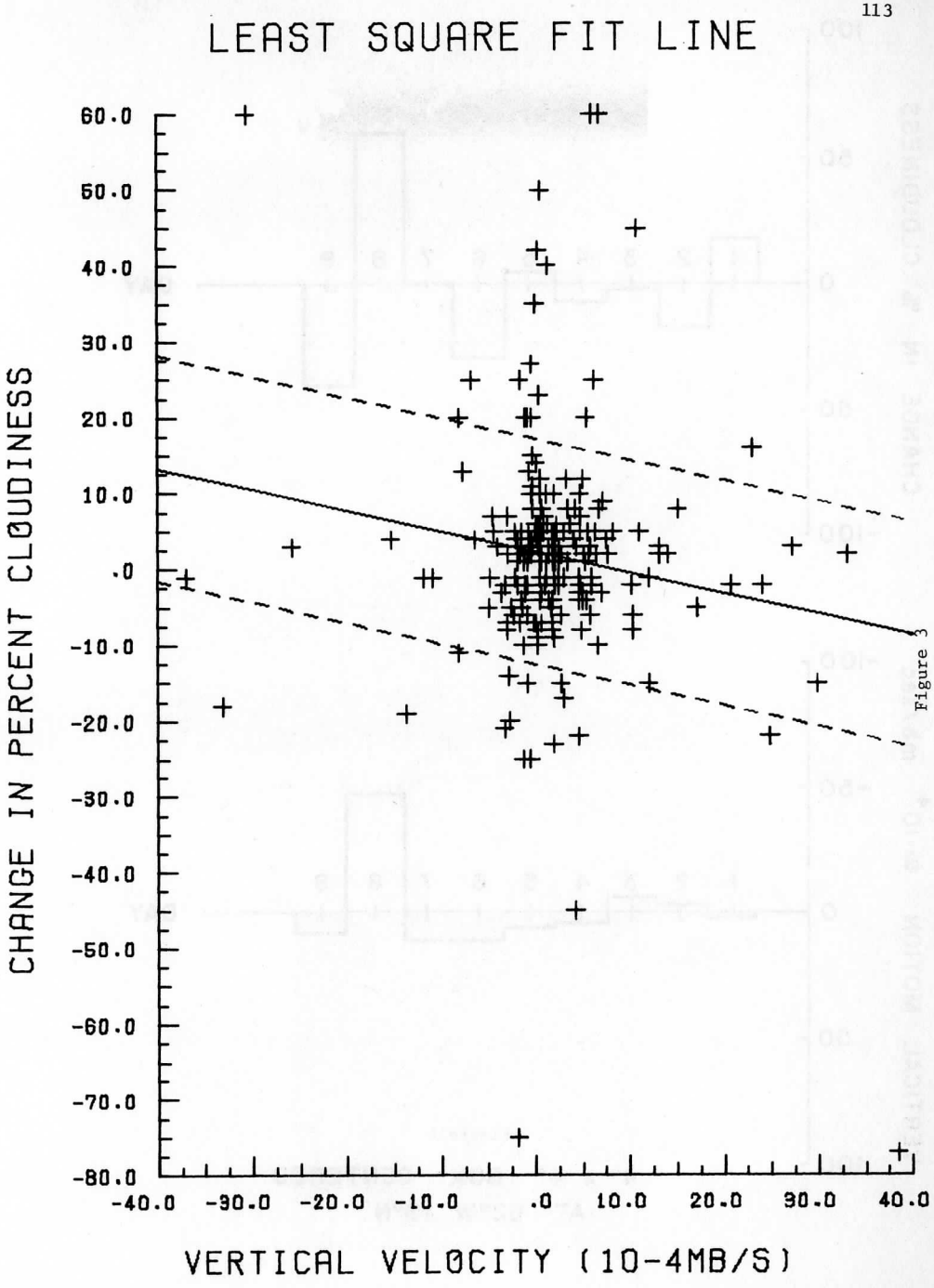
LEAST SQUARE FIT LINE
CHANGE IN PERCENT CLOUDINESS
60.0
50.0
40.0
30.0
20.0
10.0
.0
-10.0
-20.0
-30.0
-40.0
-50.0
-60.0
-70.0
-80.0
-40.0
-30.0
-20.0
-10.0
.0
10.0
20.0
30.0
40.0
VERTICAL VELOCITY (10-4MB/S)

Figure 3

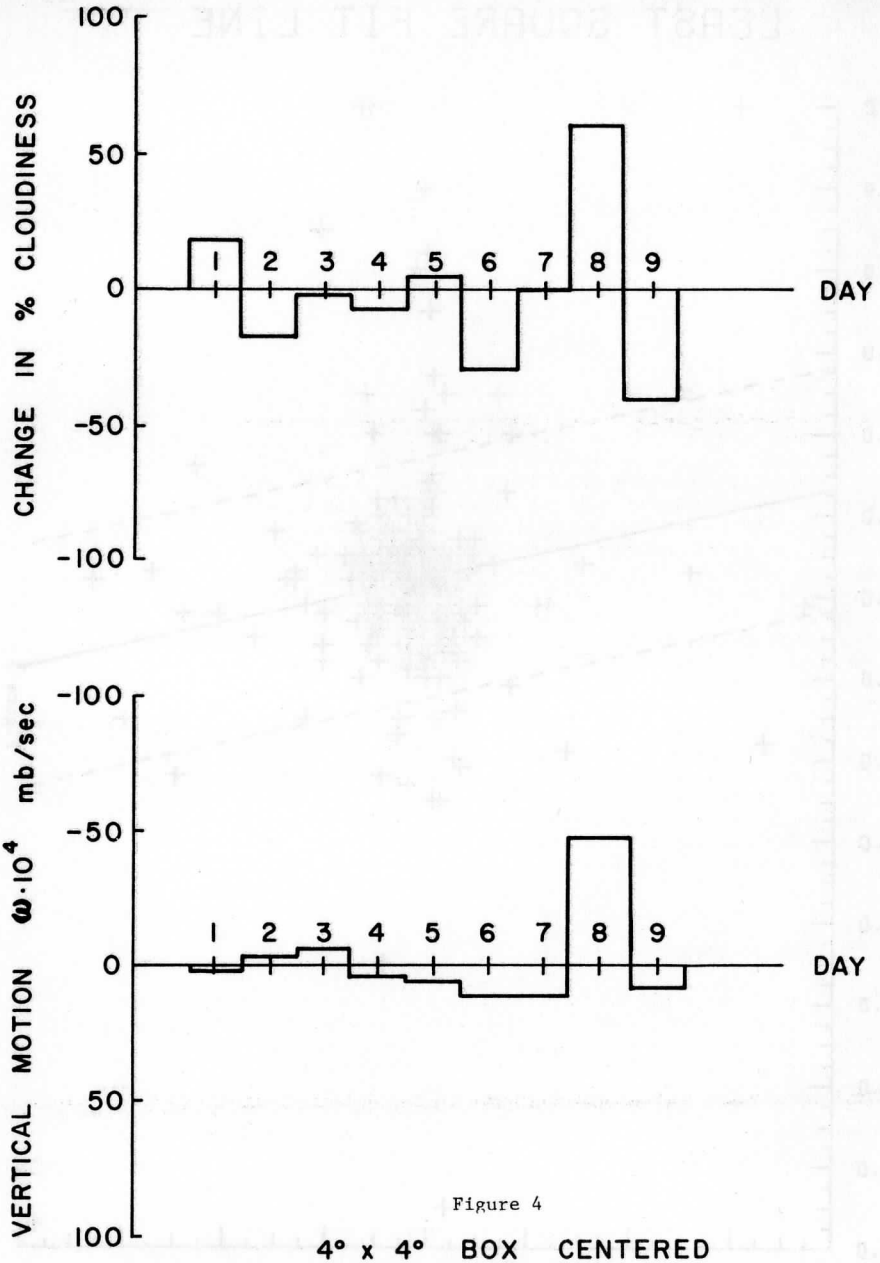

Figure 4

4° x 4° BOX CENTERED
AT 62°W 10°N

THE MOVEMENT OF SYNOPTIC WEATHER SYSTEMS AS SEEN BY THE NIMBUS 4 THIR WATER CHANNEL

Donald P. Wylie

ABSTRACT

Upper tropospheric water vapor locational characteristics and movement were analyzed from the Nimbus 4 THIR water channel data. The analysis showed that mid-latitude trough circulations could be tracked in their eastward movement by this data. Dry jet tongues in these circulation systems could be distinguished over several days on the infrared pictures from the water channel. Monitoring the movement of these systems by the water channel was thus possible. The locations of other large scale rising and subsiding air motions could also be identified on the water channel by upper level moisture presence or absence. Subtropical highs and the easterly jet (over India) circulation systems could be identified by the upper level moisture absence associated with these systems. The moisture was found to be linked to large area cloud cover, as both appeared simultaneously. Convection in the clouds was a possible mechanism for lifting the moisture to the upper levels. In the tropics only the long period wave disturbances, 10-30 day periods, appreciably affected the upper level moisture. The shorter period waves had little effect on the water vapor.

1. INTRODUCTION

One of the problems in weather analysis and forecasting is the lack of data in many regions of the world, especially over the oceans. This makes analyzing the position and movement of synoptic scale circulation systems difficult. In this study, we will show the movement of mid-latitude troughs and tropical waves by using Nimbus 4 satellite Temperature-Humidity Infrared-Radiometer (THIR) water channel data. Figure 1 is an example of the type of data available from this instrument.

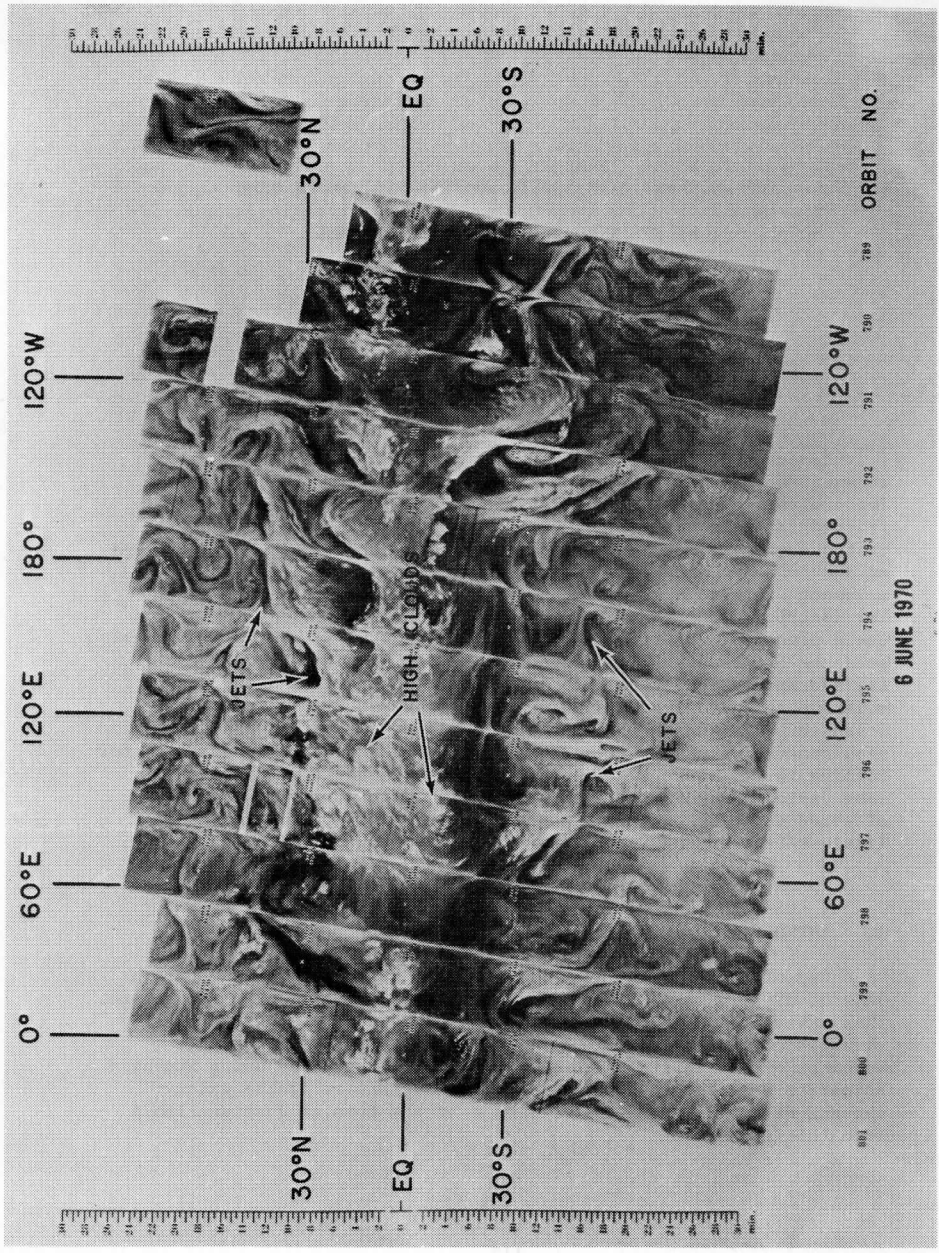

Figure 1: Nimbus 4 THIR water channel montage.

The THIR instrument indirectly measures the height of the uppermost layer of atmospheric moisture. It actually measures the amount of infrared radiation emitted by the atmospheric water vapor in that layer. This radiation originates from the upper level moisture only, because any radiation emitted in the lower layers will be absorbed and re-emitted in the upper layer. The amount of radiation received by the satellite depends on the temperature of the layer which, in turn, is height dependent. Moisture in higher levels is colder and therefore emits less radiation than the warmer moisture in lower levels. Large amounts of upper level moisture (reduced upwelling radiation) are indicated in Figure 1 by white areas. The dark areas (stronger upwelling radiation) denote an absence of upper level moisture. The radiation in these dark areas originates from moisture lower in the atmosphere. This warmer radiation can then pass through the upper levels to the satellite. In this study, these light and dark patterns will be used to identify synoptic weather systems.[1] The manner in which the water channel responds to the upper tropospheric moisture patterns will be discussed in greater detail in Section 2.

The source of atmospheric water vapor is evaporation at the surface. Therefore, to reach higher levels, it must be lifted by rising air motions. Similarly sinking air motion will remove moisture from upper levels. Drier air from aloft will be advected downward. Raschke and Bandeen (1967), Martin and Salomonson (1970), and Holub and Shenk (1972) have all shown that subsident air motion near jet streams in mid-tropospheric troughs can be recognized on the water channel data by the absence of moisture in higher levels. The upper level moisture patterns produced by these rising and subsident air motions will be used in Section 3 to monitor the movement of mid-latitude trough and jet systems by a series of water channel pictures.

In the tropics, atmospheric waves have been known to have rising and subsident motion patterns. This was first noted by Riehl (1945). Increased cloud activity produced by the rising motion in these waves has been identified by Chang (1970), Wallace (1970), Sikdar and Suomi (1971), Reed and Recker (1971), Sikdar, Young and Suomi (1972),

---

[1]The exact quantity of moisture cannot be determined from this data unless one has other information.

and Young and Sikdar (1973) from satellite pictures. Some of the same waves can also be identified in the water channel images. The water channel images differ from cloud images of waves in that they respond only to moisture that has reached the upper levels of the troposphere. Clouds can form at all levels in the troposphere and the upward and downward motions are more difficult to identify in cloud pictures. In Sections 3 and 4 the strength of these tropical weather systems in the upper troposphere will be shown by the water channel. Finally, Section 5 treats the relationship between upper level moisture patterns and cloud cover on the large scale.

2. CHARACTERISTICS OF THE WATER CHANNEL

Water vapor will absorb and emit infrared radiation in two broad bands of the spectrum. The Nimbus 4 THIR water channel measures the radiation emitted in the band from 6.3 to 7.2 microns as shown in Figure 2. The level from which this radiation originates will depend on the distribution of moisture in the atmosphere. If the moisture is confined mainly to the lower levels and is very dry in the upper levels, the radiation received by the satellite will come from the lower levels. But, if more moisture is present in upper levels, then more of the radiation will have come from the upper levels because of the moisture which absorbs and re-emits it. The contribution of each level to the total radiation received by the satellite is schematically shown in Figure 3.[2] The upper curve (dashed line) represents a higher amount of water vapor in the upper levels than does the lower dotted curve. The satellite will receive less radiation from the upper curve because it is coming from the colder part of the atmosphere. Also, if high clouds are present, less radiation will reach the satellite. Clouds are usually opaque to radiation at this wavelength. The satellite receives the blackbody radiation from the cloud top attenuated by the moisture above the cloud. High clouds appear in the water channel images (Figure 1) as very bright spots because of the cold temperatures at their tops. The location and movement of the high clouds seen in the images will be discussed in greater detail in Section 3.

The data from each orbit of the satellite were recorded on filmstrips. In the form of a crude mercator map projection of the global moisture distribution, filmstrips for each day were available from Goddard Space Flight Center. Figure 1 is an example. Areas of subsiding air in the vicinity of jets appear as dark streaks (less upper level moisture) spiralling into white areas. Allison et al. (1973) and Steranka (1973) have shown that upper level winds are parallel to these dark streaks. Thus, these streaks represent tongues of dry air spiralling into mid-tropospheric weather systems.

---

[2]Figure 3 is a schematic sketch and was not calculated from the radiative transfer function. It only represents the relative change in the contribution function and does not represent actual values.

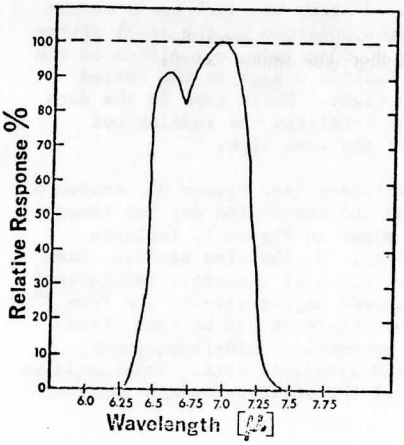

Figure 2: Spectral response of the water channel (solid line) and water vapor emission spectrum (dashed line).

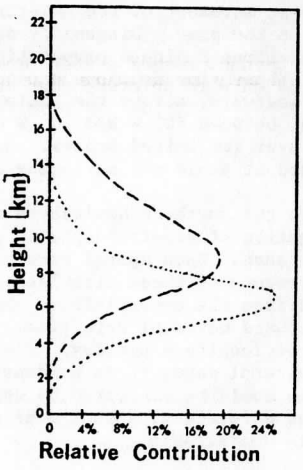

Figure 3: Relative vertical contribution function. Dashed line represents more moisture in higher levels than dotted line. This is a schematic and does not represent actual data.

The data montages, such as Figure 1, were obtained from the Nimbus 4 data catalogue. A plastic transparent overlay grid was used for navigation. The grid can be shifted to align with the grid on the filmstrips. Latitudes and longitudes every 10° are marked on each filmstrip by small dotted lines. The equator, 30° and 60° latitude crossings of the satellite are also marked by X's on the filmstrips. The montages form an approximate mercator map in the tropics. However, distortions increase toward the poles because the meridians converge toward these points on each filmstrip. The grid is useful mainly in the tropics and subtropics where the distortions are smallest. Hard copy photographic prints of the montages were obtained from Goddard Space Flight Center for this study. Only nighttime passes were used. Little daytime data was available, due to daylight interference with the instrument. These pictures were used to form the time sections discussed next.

3. ANALYSIS OF THE TIME SECTIONS

To show movement of the upper level moisture patterns, time sections were made from the data montages. The montages, such as Figure 1, were cut into 10° of latitude strips. The strips for one zonal belt were placed together in consecutive order so that time increased down the page. These time sections, Figure 4-8, show the

east-west movement of the moisture patterns as a left-right shift on the page. Diagonally orientated light and dark bands on the time sections indicate propagation of the moisture in the zonal direction. These time sections extend from 0° longitude over Africa on the left, westward, across the Indian and Pacific Oceans to the United States, between 90° W and 60° W on the right. White gaps in the data occur over the United States. Here the satellite was reading out data and it could not be taking data at the same time.

In the northern hemisphere mid-latitudes (see Figure 4), eastward propagation of mid-tropospheric troughs and associated dry jet tongues can be seen. Dark spiral streaks, as shown in Figure 1, indicate the presence of these circulation systems. On the time section, they extend from the upper left to the lower right of the page, indicating an eastward movement with time. The speeds of the streaks are from 7° to 9° of longitude per day. Since these features can be identified over several days, it is evident that movement of mid-tropospheric troughs could be monitored by using this satellite data. This could be used as a forecasting tool over areas of the world where conventional data is unavailable.

High cloud tops can also be seen on Figure 4 over Africa and India (0° to 120° E). More appear in Figure 5 in the subtropics, 20° to 30° north latitude. These clouds result from the strong continental heating in the area during the summer. To appear on the water channel images, the convective activity must extend to the upper levels of the troposphere. This indicates the high intensity of the convection in this area.

The bright images stream to the west of the clouds, having the appearance of moisture carried toward the west by the wind. The easterly jet which is present in this area during the summer, as noted by Koteswaram (1958), may be carrying this moisture.

To the west of India, a dark region from 0° to 70° east can be seen in Figure 5. Subsidence occurs in this region, removing the moisture from the upper levels. The subsidence results from the easterly jet deceleration. A northward component of the air motion caused by the jet deceleration produces upper level convergence in this area. Sinking of the air is forced by the convergence and is clearly marked on the water channel by a dark image.

Another dark region appears in the eastern Pacific, 120° west-160° west. The absence of moisture in this area again indicates large scale subsidence. The subsidence is due to the subtropical high pressure system in this area. Subsidence associated with these climatological circulation systems, the easterly jet and subtropical high, appear as dark areas on the water channel images. The breakdown and movement of these systems with the seasons could also be seen with longer time sections.

In the ITCZ region from the equator to 10° north (Figure 6)

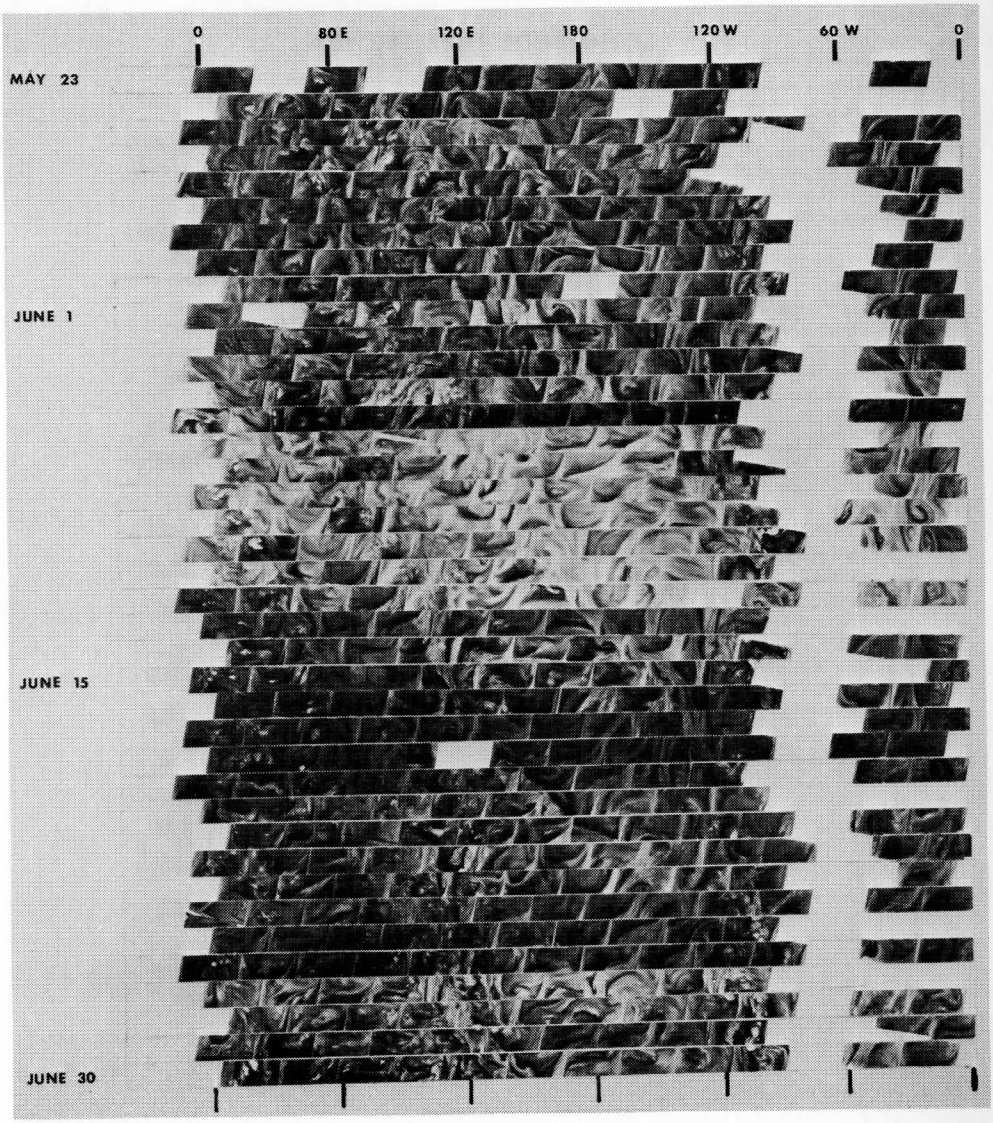
LONGITUDE TIME SECTION
40 TO 50 DEGREES NORTH LATITUDE
0
80 E
120 E
180
120 W
60 W
0
MAY 23
JUNE 1
JUNE 15
JUNE 30

Figure 4

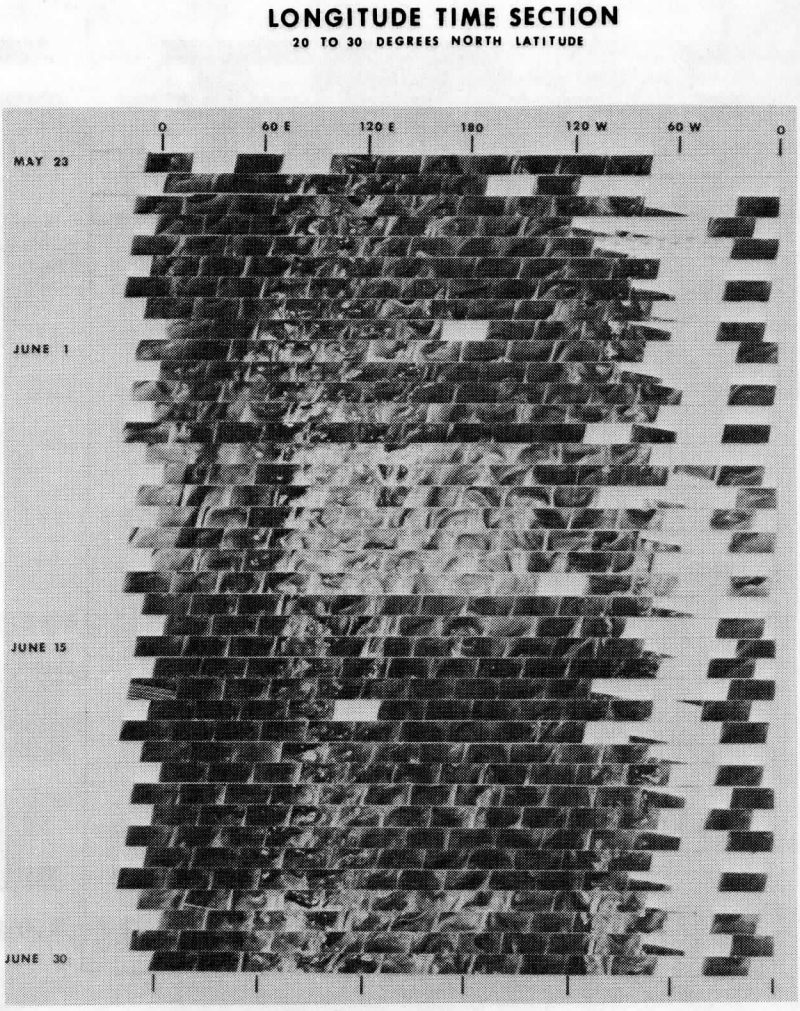
LONGITUDE TIME SECTION
20 TO 30 DEGREES NORTH LATITUDE
0
60 E
120 E
180
120 W
60 W
0
MAY 23
JUNE 1
JUNE 15
JUNE 30

Figure 5

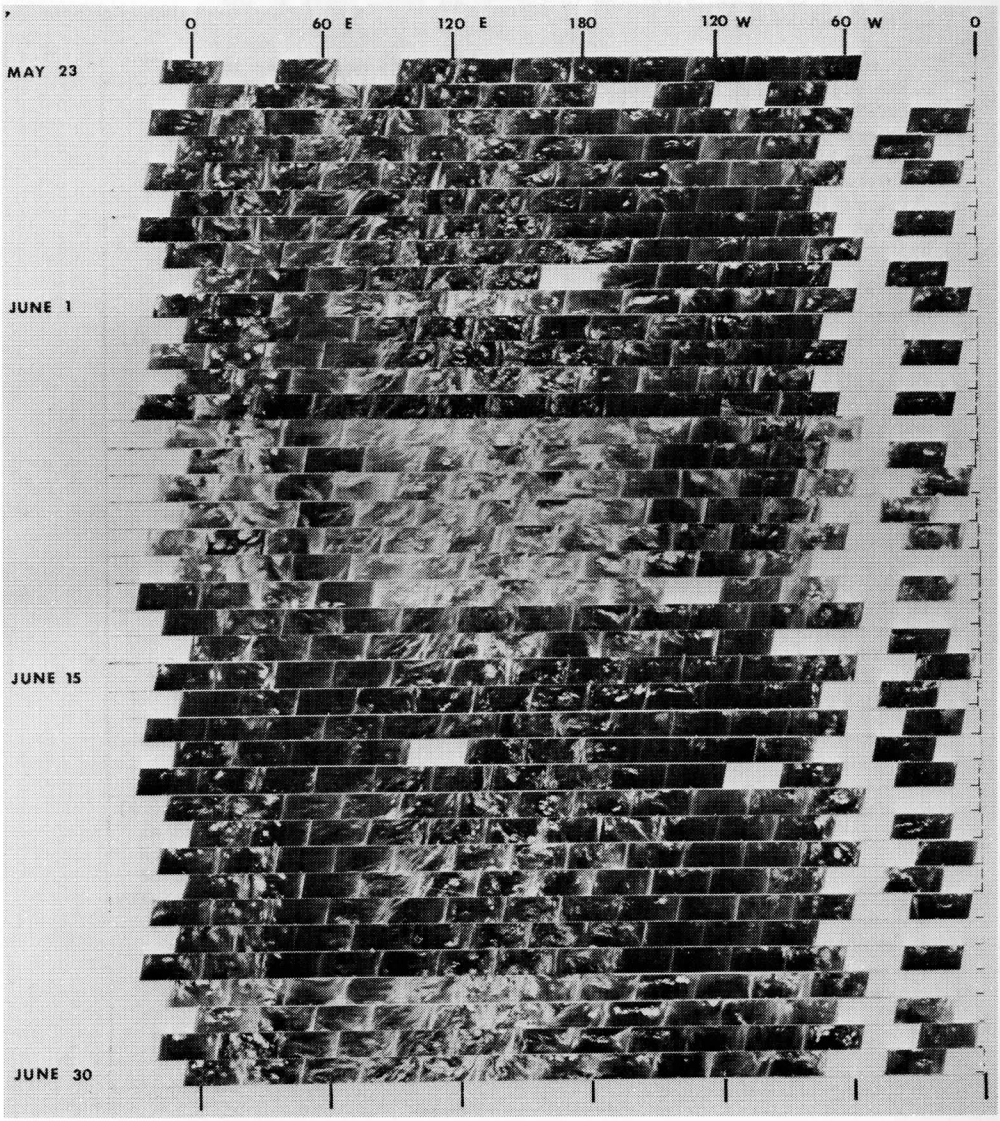
LONGITUDE TIME SECTION
EQUATOR TO 10 DEGREES NORTH LATITUDE
0
60 E
120 E
180
120 W
60 W
0
MAY 23
JUNE 1
JUNE 15
JUNE 30

Figure 6

moisture trailing to the west from clouds is very predominant. Still part of the easterly jet, this moisture is possibly being carried away from the clouds by easterly winds. West of the clouds is a clear region over the western Indian Ocean, 40° east to 70° east. The lack of water vapor indicates upper level subsidence in this area. This subsidence is possibly related to the colder ocean water in the western Indian Ocean.

Over the continent of Africa itself there is more upper level water vapor. High cloud tops also appear because this area is convectively active from the summer continental heating as is the southern part of the Asian continent. Rising motion in this area is also produced by the upper level divergence from the easterly jet deceleration. Divergence results from the northward transport of air over this area. The net result of the jet and convection is a large amount of moisture lifted to upper levels. This is depicted by the high level of brightness on the water channel images.

Easterly waves in the ITCZ region do not appear on the water channel images in Figure 6. Waves traveling from west to east in this region were identified on satellite cloud pictures by Chang (1970), Wallace (1971), Reed (1971), and Sikdar (1972). They were also identified in the wind fluctuations (radiosonde data) by Rosenthal (1960), Yanai et al. (1968), Maruyama (1968), Wallace and Chang (1969), and Nitta (1970). These waves would then be expected to appear on the water channel data. Their absence, thus, comes as a surprise. However, the vertical profile of the wind variance, as shown by Yanai, notes that most of the variance is above 10 km and decreases below this level. This indicates a weakening of the waves below the stratosphere. Since the waves also appear in cloud formations, they must be present in the lower troposphere. Their failure to appear on the water channel images then implies that the waves weaken in the upper troposphere. Insufficient lifting of water vapor to the upper levels occurs for them to be seen on the water channel.

High clouds appear in this area, but their organized propagation cannot be seen. It is possible that the convection is triggered by the waves, thus producing the high clouds. But the clouds do not consistently grow to the upper troposphere in the wave passage to show any propagation on the water channel.

Waves are obvious in the southern hemisphere subtropics (Figure 7) from 10° south to 30° south. These disturbances propagate eastward at 6° to 10° of longitude/day. This is generally a dry region, indicated by the lack of brightness on the water channel images. The absence of high clouds in this region suggests a lack of strong convective activity. However, eastward propagating cloud disturbances were found by Sikdar in this region. Therefore, water vapor may still be lifted by convection of smaller clouds, even though high clouds are absent from the water channel images.

In the southern hemisphere mid-latitudes (Figure 8), dry tongues

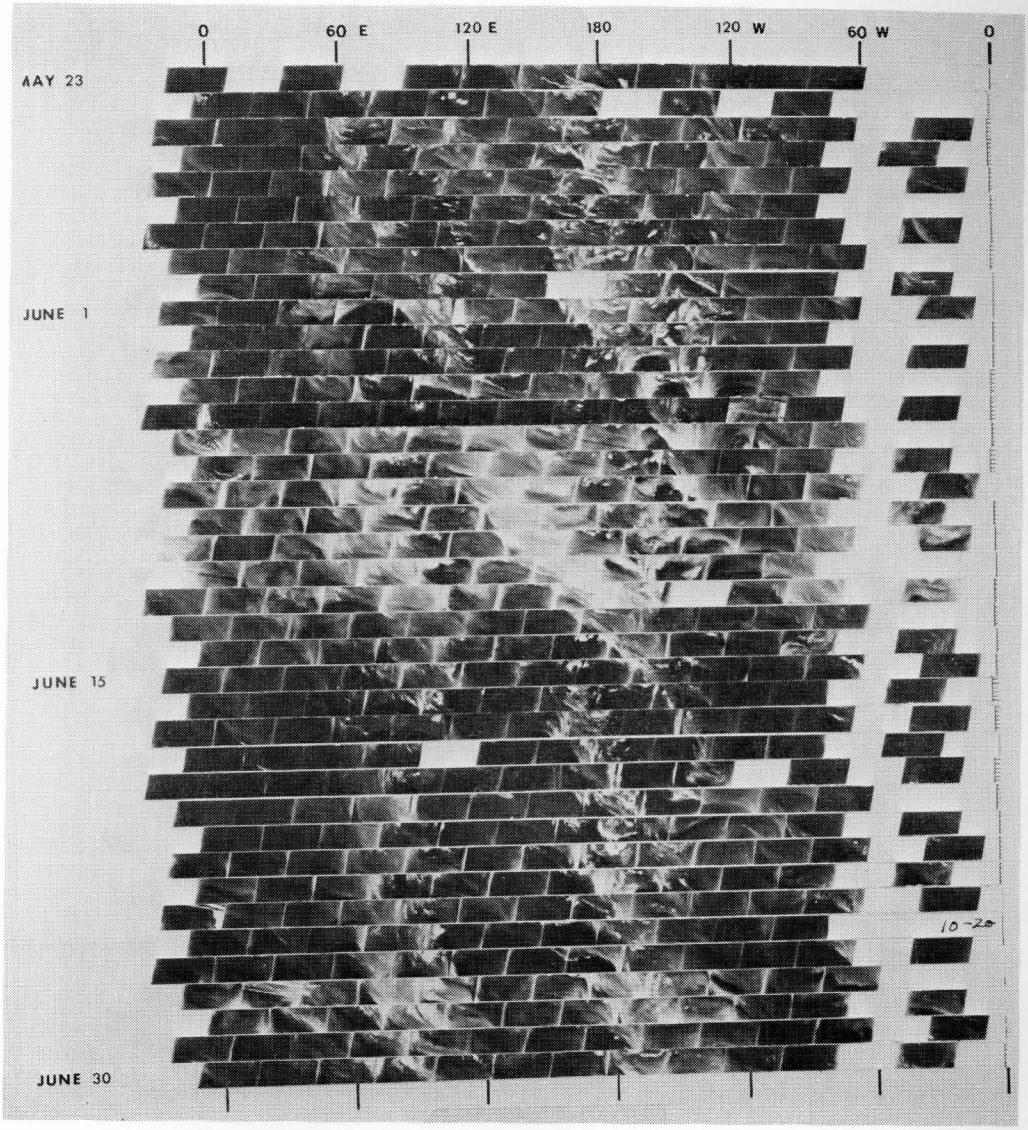
LONGITUDE TIME SECTION
20 TO 10 DEGREES SOUTH LATITUDE
0
60 E
120 E
180
120 W
60 W
0
MAY 23
JUNE 1
JUNE 15
JUNE 30
10-20

Figure 7

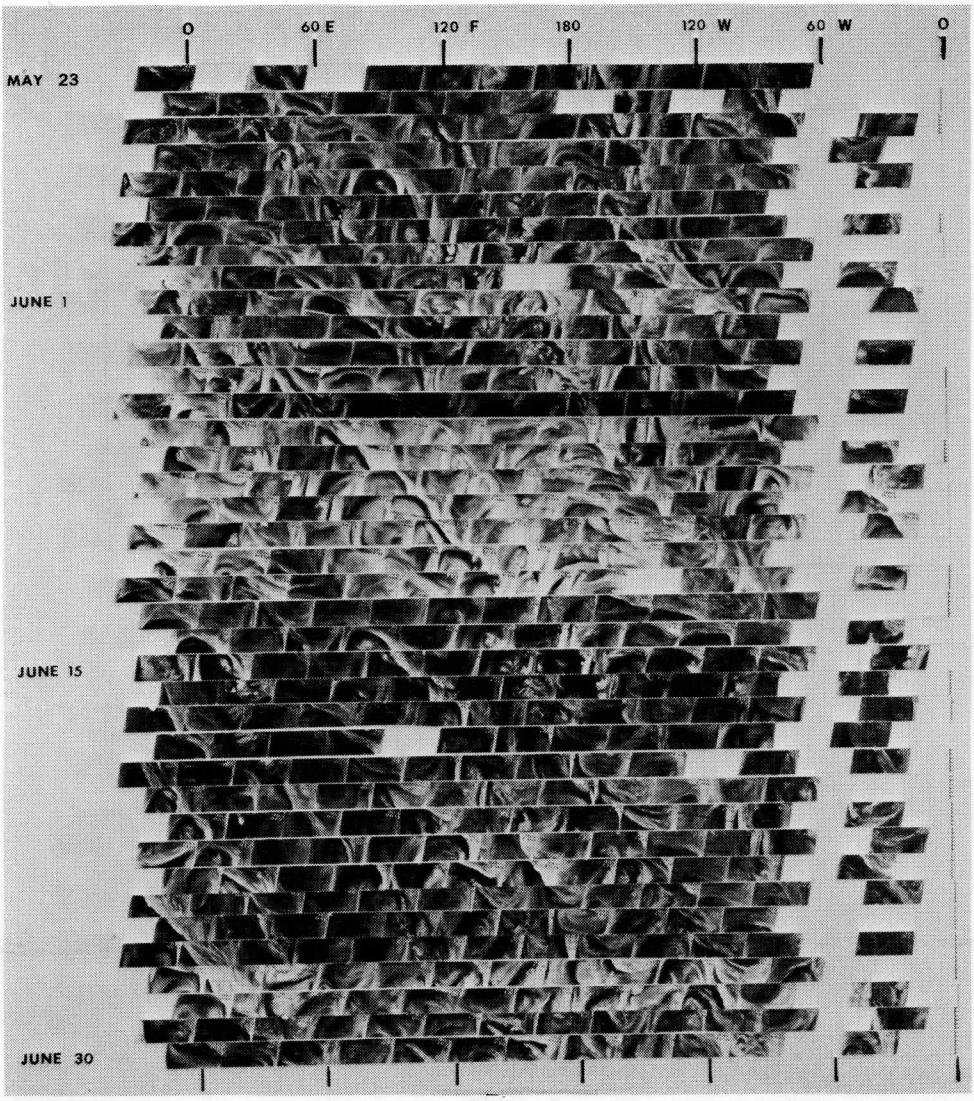
LONGITUDE TIME SECTION
40 TO 30 DEGREES SOUTH LATITUDE
0
60 E
120 F
180
120 W
60 W
0
MAY 23
JUNE 1
JUNE 15
JUNE 30

Figure 8

appear, as in the northern hemisphere mid-latitudes. The concentrations of water vapor are slightly lower and fewer high clouds can be seen on the images. As in the northern hemisphere these dark streaks (dry tongues) indicate the movement of mid-tropospheric troughs and associated jets. The motion of these troughs, apparent in the eastward direction, travels at about the same speeds as the northern troughs.

Meridional time sections were made by cutting the montages into longitudinal strips and placing them together (Figure 9). The ITCZ region and the subtropical high can clearly be seen on these time sections. The ITCZ appears as a large band of brightness from the equator to 20° north or 30° north. The STH appears as a dark band from 10° to 30° south because of its subsidence. Some northward movement of moisture patterns from the ITCZ region can also be seen. A few dry tongues (black spiralling streaks) appear to propagate northward. The meridional propagation, in general, is not as obvious as the zonal propagation seen on the longitude time sections (Figures 4 and 8). The features move out of the meridional time section area before any meridional motion can be seen.

The dark region from 10° south to 30° south is the area in which the waves appear on the longitude time section in Figure 7. These waves are vaguely seen on the meridional time section, indicating that their direction of propagation is mainly zonal, as in the mid-latitude troughs.

4. THE STATISTICAL ANALYSIS

To form a more quantitative picture of the water channel data, we performed statistical analysis of the brightness on the montages. The transparent overlay grid was used to divide the montages into boxes of 10° latitude by 10° longitude. The tropics were analyzed from 30° north to 30° south, 0° longitude east to 120° west longitude. The amount of brightness in each box was estimated by eye observations. A scale of brightness from 0 for total box black to 8 for total box white was used. The quantity of brightness for the box was weighted for the fraction of the box that it covered. A time series was made for each box from April 19 to September 30, 1970 (165 days) for the area from 140° east to 120° west longitude. Only night pictures were used. Examples of the series are shown in Figure 10. The averages and variances of these series are presented in Figures 11 and 12.

The average brightness (Figure 11) shows a large maximum area over the southern tip of the Asian continent, India and Thailand, and another maximum over central Africa. The Indian and African maxima are linked to the convective activity caused by summer continental heating, discussed in the analysis of the time sections. Areas of lesser brightness also occur over northern Africa and south of India. The position of the high average brightness areas agrees with the rising and subsident motions in the areas of lesser brightness. An imaginary axis running through the center of the easterly jet could be drawn at about 12° north latitude (dashed line). Across the axis opposite the

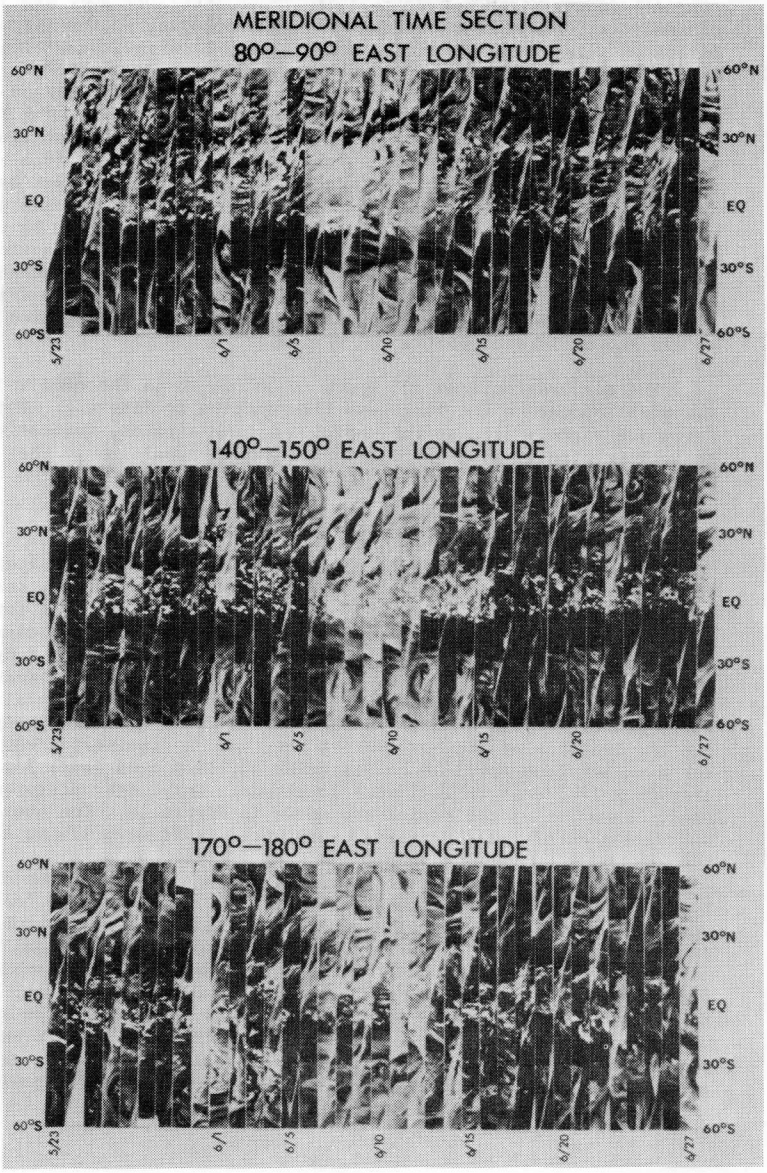
MERIDIONAL TIME SECTION
80°—90° EAST LONGITUDE
140°—150° EAST LONGITUDE
170°—180° EAST LONGITUDE
60°N
30°N
EQ
30°S
60°S
5/23
6/1
6/5
6/10
6/15
6/20
6/27

Figure 9

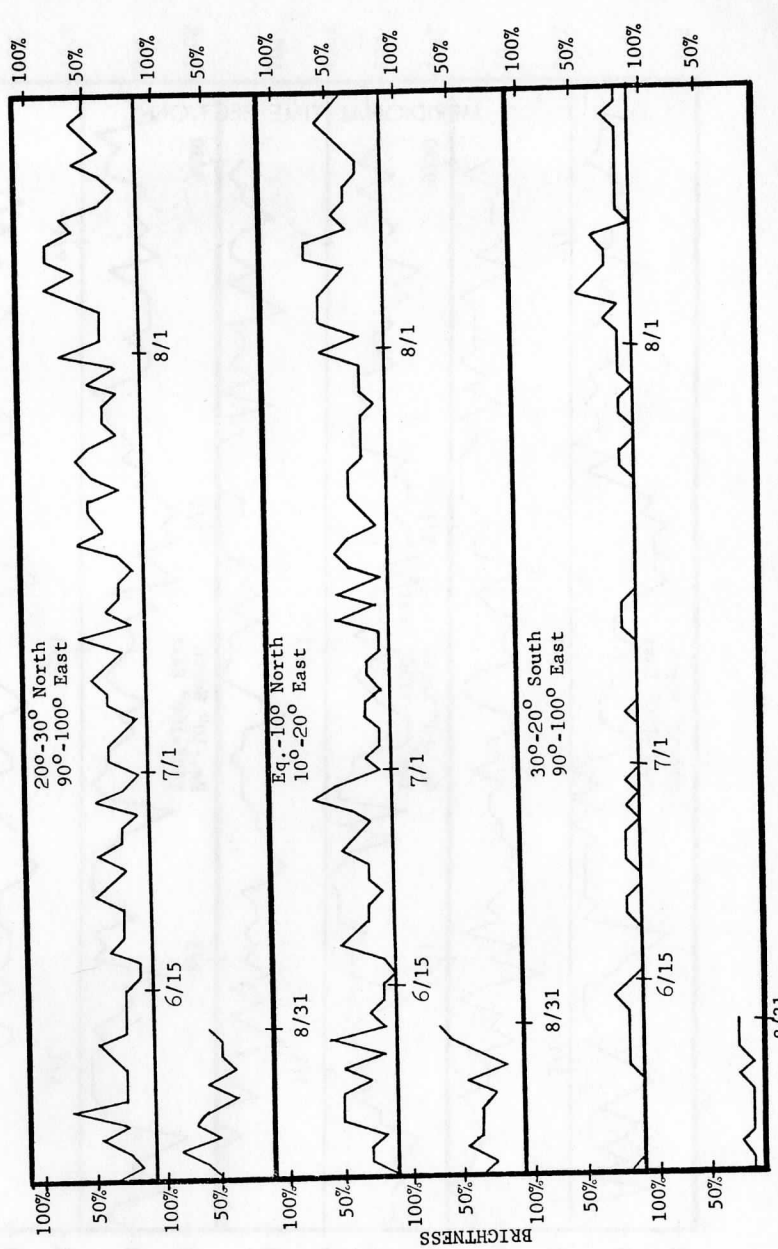

Figure 10: Sample time series of brightness on water channel pictures.

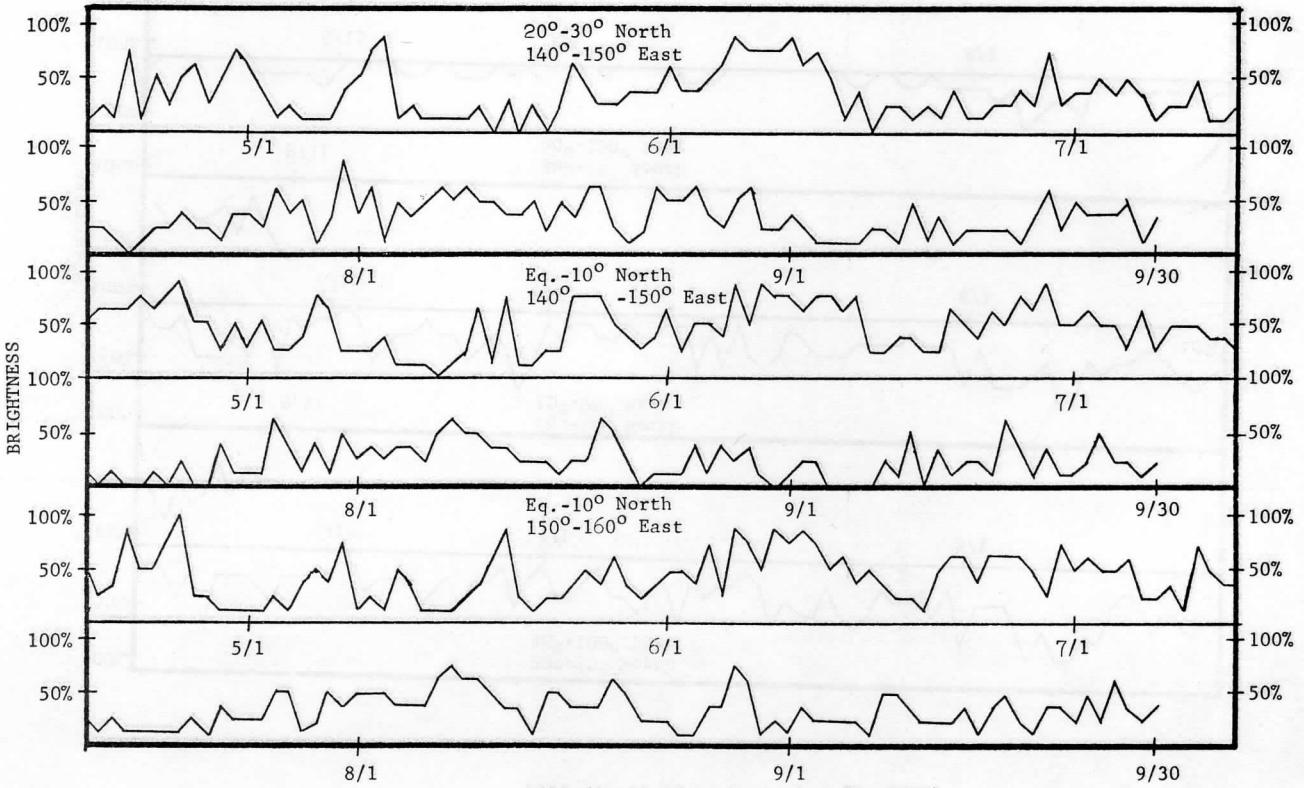

Figure 10 (continued).

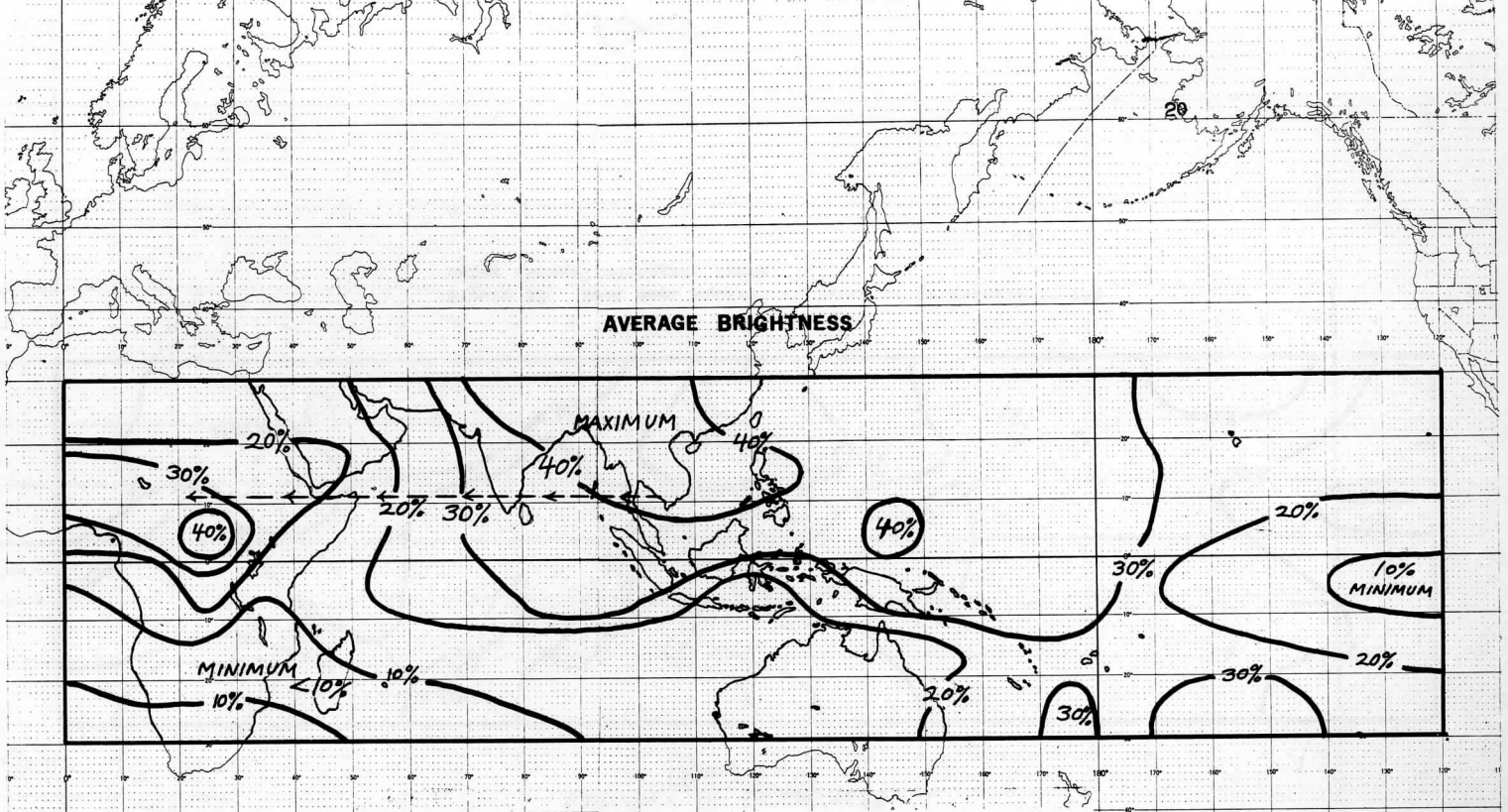

Figure 11: Average brightness on the water channel montages which indicates the relative amounts of upper level moisture for the summer of 1970. Dashed line represents an approximate position of the easterly jet axis.

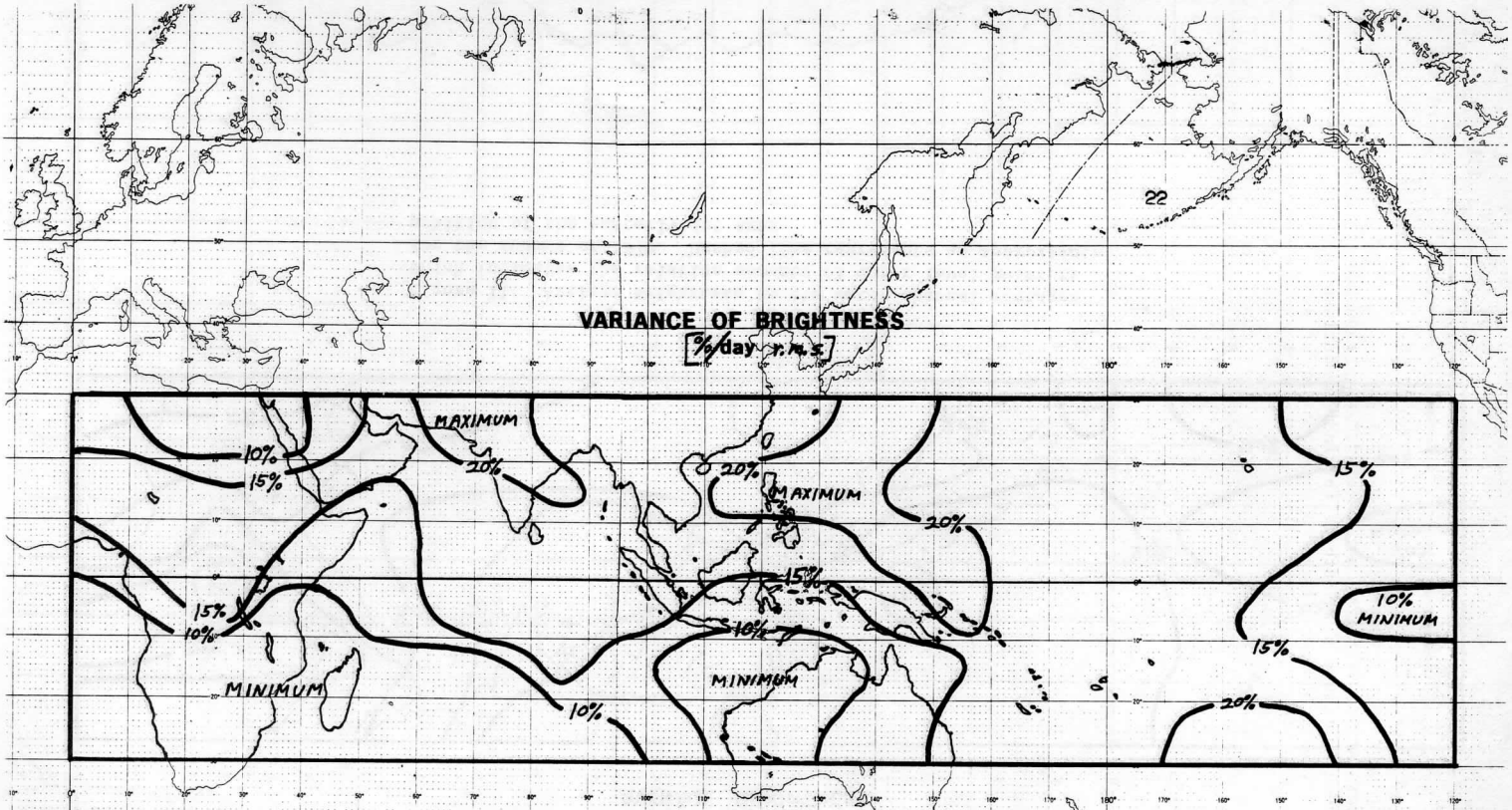

Figure 12: Root mean squared variance of brightness on the water channel montages, summer 1970.

maximum brightness areas, less brightness was found. This is possibly a result of sinking motion caused by the jet system. The convergence area over northern Africa is due to jet deceleration, discussed in Section 3 and seen in Figure 5. South of the Indian continent slight sinking motion may also be induced by the acceleration of air into the easterly jet. A southward component in the flow is caused by the air acceleration. Upper level convergence from this flow may force some subsident motion. As a result, less upper level moisture was found over this area.

Other areas of minimum moisture were found over the southern African tip and the eastern south Pacific from the equator to 10° south, extending westward to approximately 130° west. Dryness in these areas results from subtropical high subsidence which appears as a dark area on the water channel pictures.

The variance of brightness (see Figure 12) occurs mainly over the western India and the western Pacific. On the edges of the average maximum brightness, these brightness fluctuations indicate that the area of the largest upper level water vapor is mostly a steady feature and that the transient fluctuations are on its edges. In the eastern Pacific, little variance in brightness was found because of the area's dryness.

To form a more detailed analysis of the fluctuations, a spectral analysis of the time series for each box was performed. Examples of the spectra are shown in Figure 13. The spectrum breaks down the variance into the fractions occurring in 30 frequency intervals. The equations used are from Applications of Statistics to Meteorology (Panofsky and Brier, 1968). In each box the low frequency or long period fluctuations from 10 to 30 day periods were dominant and accounted for most of the variance. This means that large amounts of moisture endure in each area from 5 days to one-half month and are followed by drier periods of similar duration. Dominance of the longer periods was also found in spectrum analyses of wind fluctuations and cloud fluctuations by the other investigators. The longer period motions in the atmosphere appear to cause the largest change in water vapor.

Less variance was contained in the shorter periods. The 4-5 day period waves, commonly studied by other investigators of tropical waves, did not cause any large moisture variances. The spectra showed some peaks at shorter periods between 3 and 10 days, but none were sufficiently large to indicate any clear cut wave action. It appears that the 4-5 day period waves do not have strong enough lifting over a long enough time to appreciably affect the upper level water vapor.

A large amount of moisture variance appears to be contained in the short periods from 2 to 3 days. This variance cannot be considered a wave fluctuation because it is noise in the data caused by the edges of the filmstrips. The edges are brighter than the center of the

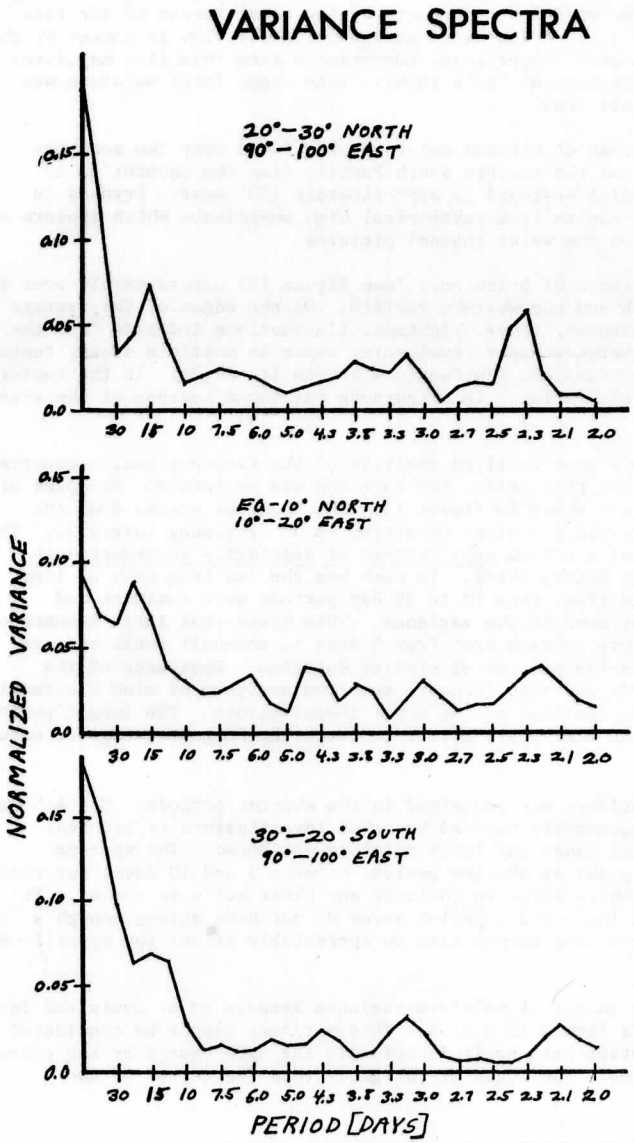

Figure 13: Sample spectra of water channel time series. Spectral peaks at 2 to 3 days are the result of filmstrip edge brightness noise.

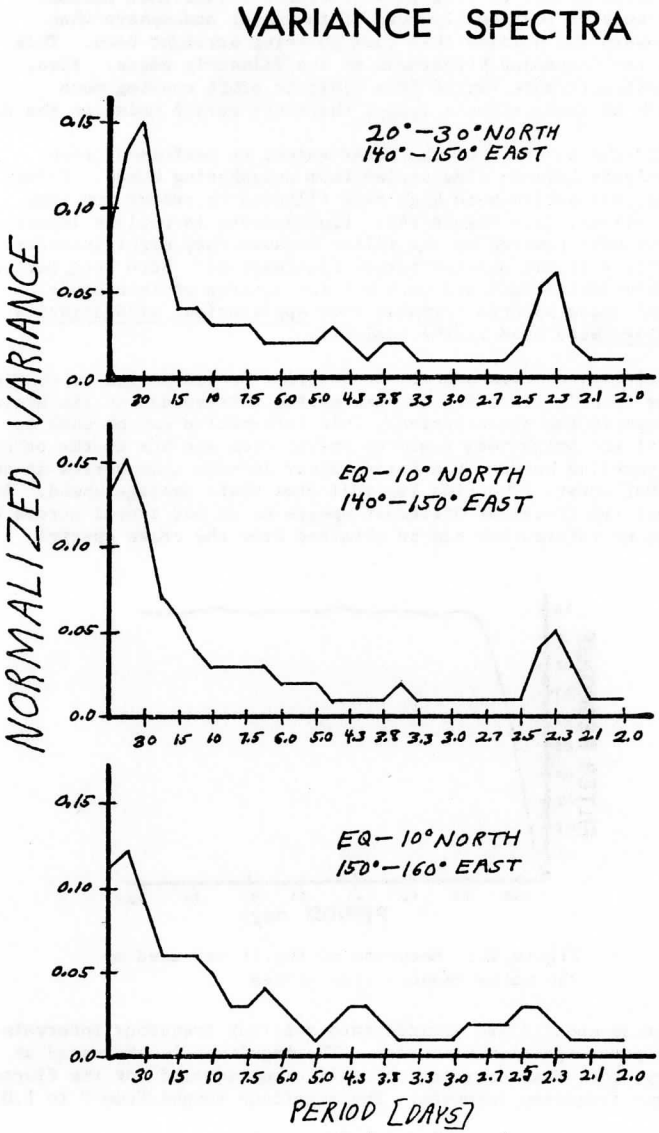

Figure 13 (continued).

filmstrips and can be seen on Figures 4-8 as vertical lines on the time sections. They appear in each box approximately every 2.5 days, causing a large amount of brightness variance around that period. The sensor sees proportionally more of the upper atmosphere when pointing toward the horizon than when pointing straight down. This results in the increased brightness of the filmstrip edges. Also, the filmstrip contrasts varied from orbit to orbit causing more noise. Both of these effects formed the short period noise in the data.

To find the movement of the water vapor, we performed cross spectra analysis between time series from neighboring boxes. Before correlating, all series were high pass filtered to remove any long period variations, (see Figure 14). Fluctuations in periods longer than 60 days were removed by the filter because they might interfere statistically with the shorter period fluctuations. Such long periods represent seasonal trends and were not the concern of this study. The standard cross spectra formulae from Applications of Statistics to Meteorology were used in the analysis.

Essentially, a cross spectra of two time series indicates whether an increase in brightness in one time series corresponds on the average to any change in the other series. This information can be used to determine if the brightness features travel from one box to the other. Features traveling between the boxes appear in both time series at one time interval apart. The time lag indicates their average speed. If all the features travel at different speeds or do not travel across the boxes, then no information can be obtained from the cross spectra analysis.

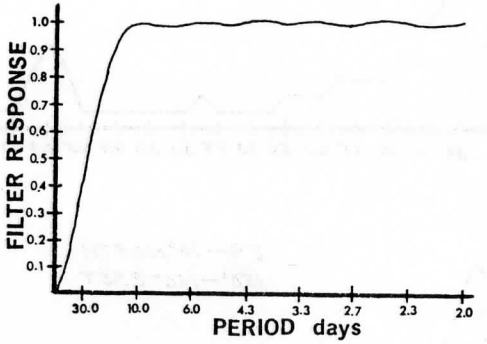

Figure 14: Response of the filter used on the water channel time series.

The cross spectra are divided into spectral frequency intervals as are the power spectrum variances. The magnitude is expressed as a coherency, the cross correlation coefficient squared for the fluctuations in one frequency interval. The magnitude ranges from 0 to 1.0;

0 indicating the lack of correlation over the frequency interval. Therefore, no information on the relationship between brightness fluctuations can be obtained from this analysis. A 1.0 would indicate that all fluctuations of one box correspond to fluctuations in the other box. Moisture is being advected across boxes or waves are propagating across boxes, lifting the moisture to upper levels in this case. The predominance of these mechanisms will be discussed for the areas in which cross correlations are found.

Associated with coherency is the phase lag which tells the time difference between occurrences in the two boxes. The phase lag is expressed in degrees of the wave from 0° to 360°. A lag of 0° means brightness fluctuations occur in both boxes, at the same time, in one frequency interval. By similar reasoning, a 180° (1/2 of the period) lag indicates that, while a brightness maximum (wave crest) occurs in one box, a minimum (trough) occurs in the other.

Phase lags can be used to determine the wavelengths of the disturbances and their speed of propagation. The relationships are simple. The centers of each box are 10° of latitude or longitude apart. The phase lag expresses the portion of the wave contained between the box centers. For example, if the phase lag is 90° (phase degrees), then 1/4 of the wavelength (90°/360°) is between the two box centers and the wave is 40° of latitude or longitude long. The formula is as follows:

$$(a) \quad L = \frac{d}{\phi/360^\circ}$$

L = wavelength
d = distance between boxes (10°)
ϕ = phase lag

The propagation speed can be determined by considering the wave period and the phase lag. If a wave or disturbance has a 12 day period and the phase lag is found to be 90°, then the brightness maximum in the second box follows the first by 1/4 of the period (90°/360°), which is 3 days. It takes the brightness feature on the picture 3 days to travel between the boxes, 10° of latitude or longitude. The speed is 3.3°/day. The formula for propagation speed is:

$$(b) \quad C = \frac{d}{(\phi/360^\circ)T}$$

C = speed of propagation
d = distance between boxes
T = period of the fluctuations
ϕ = phase lag

The phase lag thus gives the statistical average disturbance length and average speed of propagation for one frequency interval.

The coherency is used mainly to decide whether there is any organization between brightness fluctuations in two neighboring boxes.

A level of coherency must be established in order that fluctuations between boxes can be distinguished from coherencies resulting strictly by random chance. If a coherency is above the pre-set confidence level, then it will be interpreted as a coupling between the brightness fluctuations in the two series. But if the coherency is below this level, then no significant coupling between the series exists. Coherency numbers and phase lags are calculated for each frequency interval of the spectrum, just as the spectrum variances are. Thus, each coherency is only an indicator of the coupling between series in one interval of the total spectrum.

The confidence level formula is from Applications of Statistics to Meteorology.

$$(c) \quad B = \sqrt{1-(p)^n}$$

B = coherency level for a confidence of 1-p.
p = probability of error
n = 1/(df-1)
df = the degrees of freedom

Where the degrees of freedom are:

$$(d) \quad df = \frac{2N - m/2}{m}$$

N = number of data prints in the time series
m = number of spectral intervals.

The probability of error (p) is the probability that a confident correlation would be found when there was no real correlation between brightness fluctuations. Such an error could be due to usage of a particular data set. With a short time series there is a greater chance that a high coherency could be found because it may be influenced by only a few disturbances. A longer series, however, is less likely to have a large coherency because more data is used in the average correlation. The degrees of freedom (equation d) reflect the length of the time series as a ratio to the number of spectral intervals. The more degrees of freedom, the lower the level of coherency that can be used for a confidence level from formula (c).

In the water channel data, the probability of error used is 10%. This means that all coherencies above the confidence level will have a 90% confidence that real coupling exists, or a 10% chance that no coupling exists and such a correlation was found by mistake. The area from 0° to 140° east had a shorter time series, 92 days (see Table I), whereas more data was used in the area from 140° east to 120° west, 165 days. Therefore, a coherency level of 0.5 was required for the first, while 0.36 was required for the second. The degrees of freedom are given in Table I.

TABLE I:

Area	Series Length	Length After Filtering	Degrees Freedom	Coherency Level*
0°-140°E	92 days	70 days	9	0.50
140°-120°W	165 days	143 days	18	0.36

* 90% confidence level.
Number of spectral intervals = 15.

The number of significant correlations found in the zonal direction is shown in Figure 15. The correlations for the meridional direction are in Figure 16. Most correlations were found in the long periods, 10 days and longer. Few correlations were found in the shorter periods. The 2-3 day period correlations are a result of the filmstrip edges and are regarded as noise.

The locations of the vector-averaged correlations from 10-30 day periods are shown in Figure 17. Arrows indicate the directions of propagation. Arrows pointing in both directions indicate that phase lags were small ($\leq 10°$). This means that fluctuations occurred in both boxes at nearly the same time, a possible standing wave. It was interpreted as meaning that the brightness features spanned more than one box. By formula (b), large phase speeds of waves would be calculated from the small phase lags. However, these speeds are unrealistic. The interpretation of a large areal extent of the brightness feature is preferred.

Most cross correlations were found in the southern hemisphere from 10° south to 30° south on Figure 17. These eastward moving disturbances are the same as those in the time section of the area, Figure 7. Phase lags for the zonal correlations are shown in Figure 18. Correlations for these southern hemisphere boxes over more than one box length revealed the wavelength and speed (see Figure 19). The phase lags from these correlations over longer distances established an average wavelength of 20,000 km, which is planetary scale. The average speed was 13° longitude/day. This is somewhat faster than the measurement on the time sections because the time sections contained few cases. The statistical correlation gives a more accurate speed because all cases are averaged in the analysis. Meridional phase lags are shown in Figure 20. These small lags indicate that the waves span at least 20° of latitude in width. A southward trend in propagation can also be seen in the phase relations. This result is new to wave studies; meridional motions were not reported by the other wave investigators. However, eastward moving waves agree, in general, with the cloud studies of Sikdar (1972) in this region.

Other couplings between boxes were found in the ITCZ region, equator to 10° north, over the Indian Ocean 10° north to 20° north, and

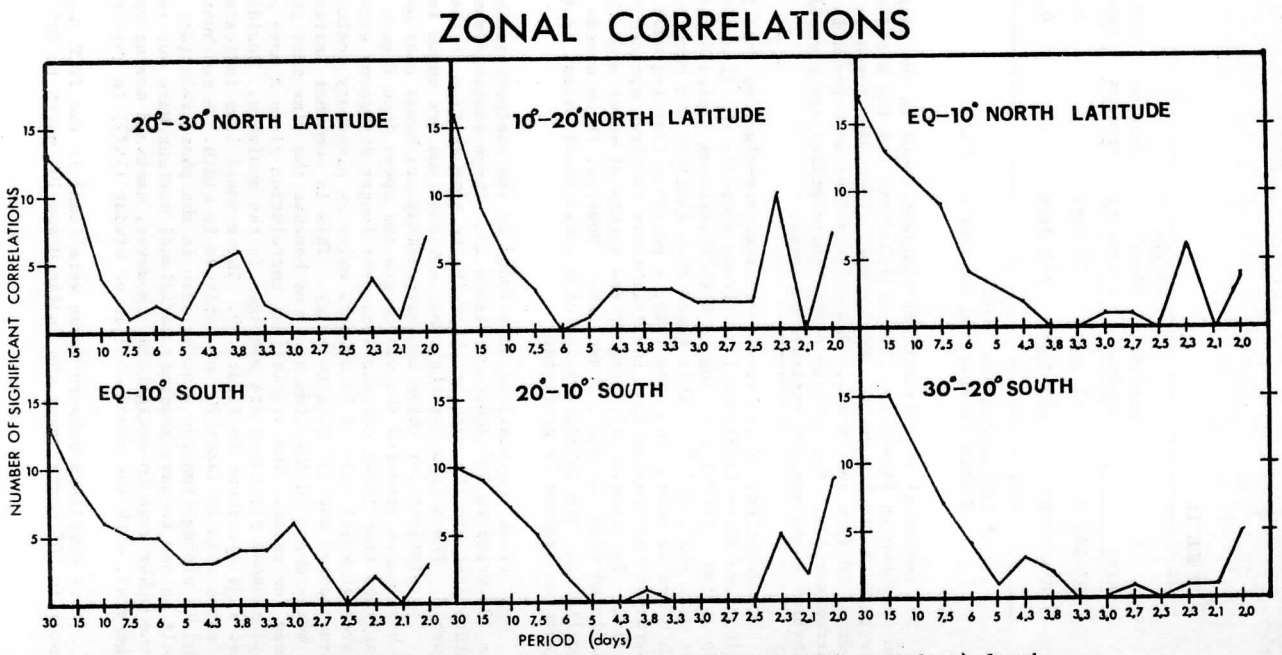

Figure 15: Number of zonal direction correlations (90% confident) found in each latitude belt. 23 are possible. All correlations found between 2 and 3 day periods are a result of filmstrip edge noise and should be disregarded.

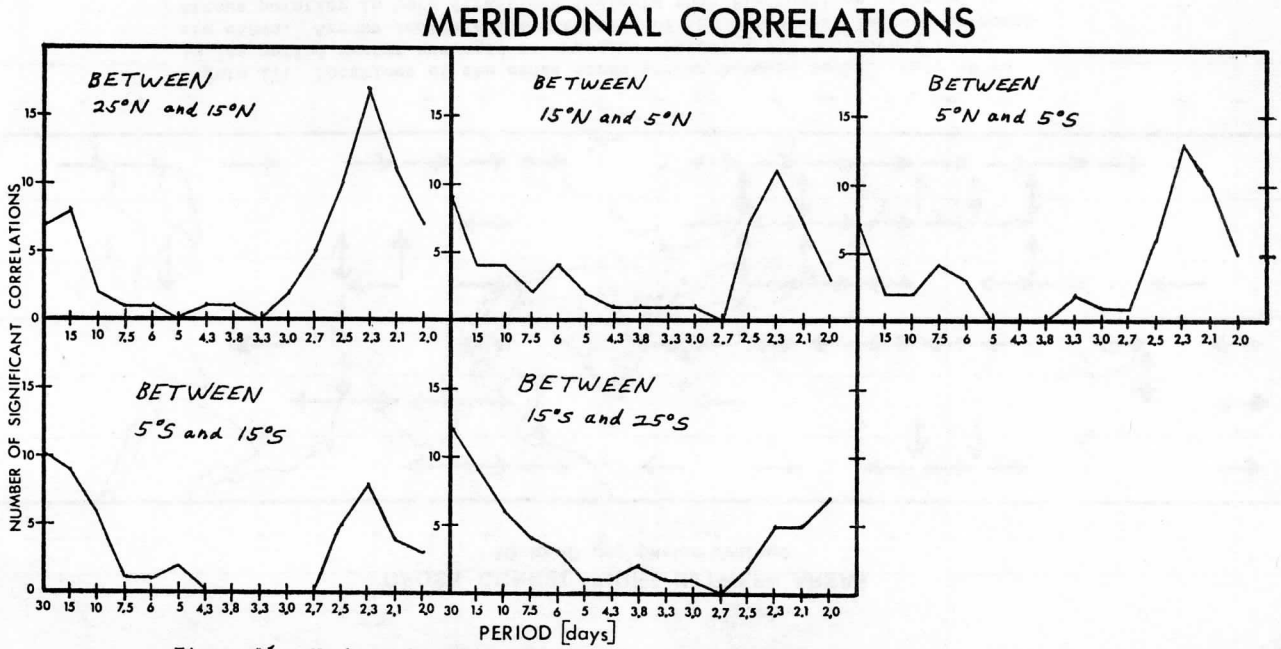

Figure 16: Number of meridional direction correlations (90% confident) found in each latitude belt. 24 are possible. All correlations found between 2 and 3 day periods are a result of filmstrip edge noise.

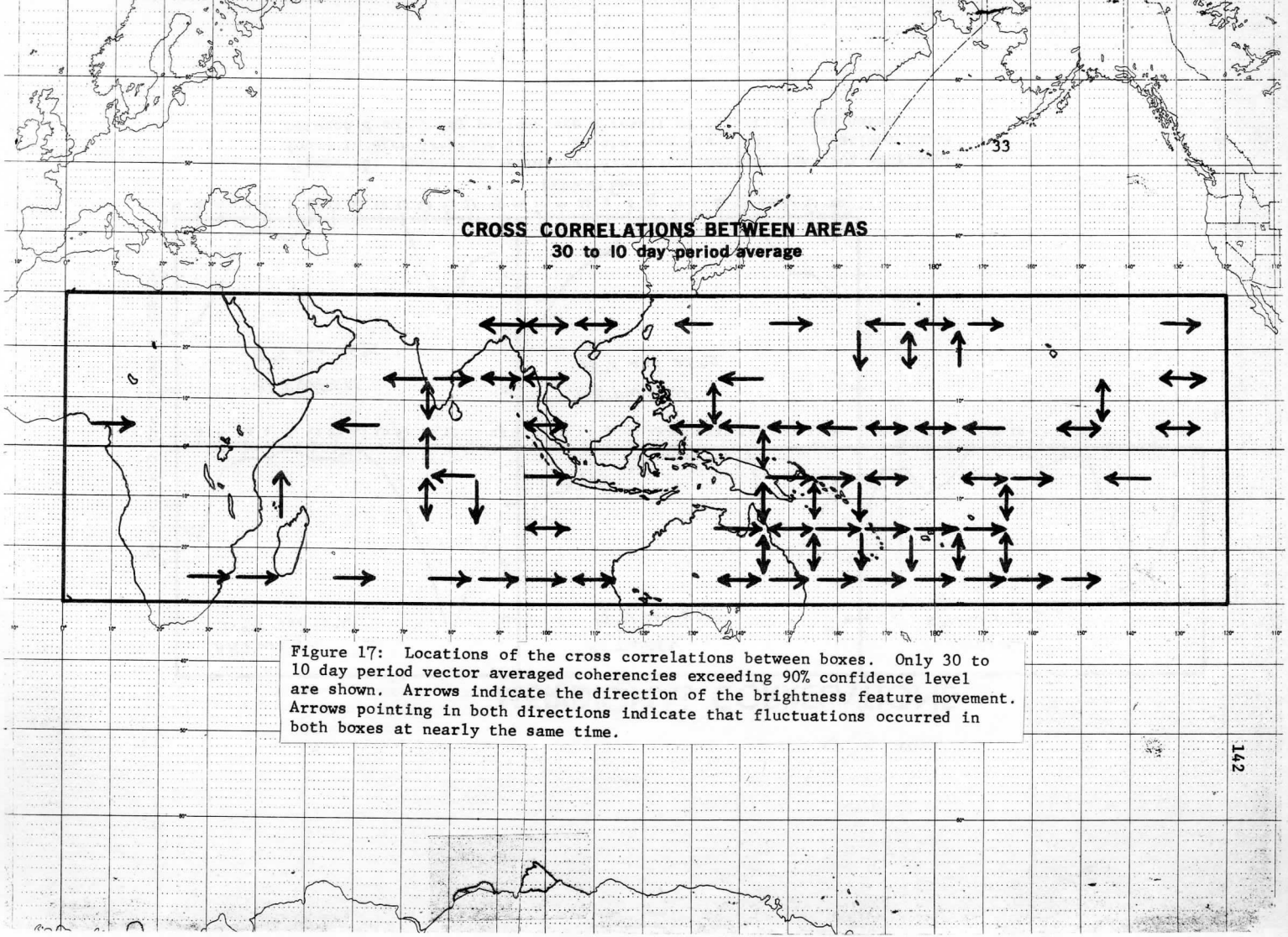

Figure 17: Locations of the cross correlations between boxes. Only 30 to 10 day period vector averaged coherencies exceeding 90% confidence level are shown. Arrows indicate the direction of the brightness feature movement. Arrows pointing in both directions indicate that fluctuations occurred in both boxes at nearly the same time.

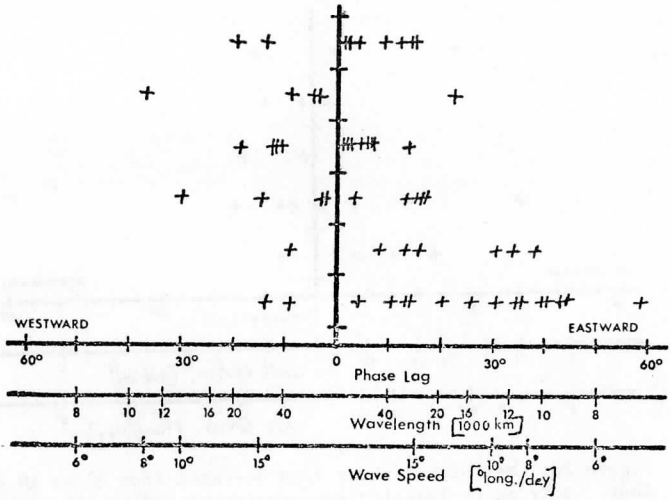

Figure 18: Zonal direction correlation phase lags for 30 to 10 day periods. Only lags for coherencies exceeding 90% confidence level are shown.

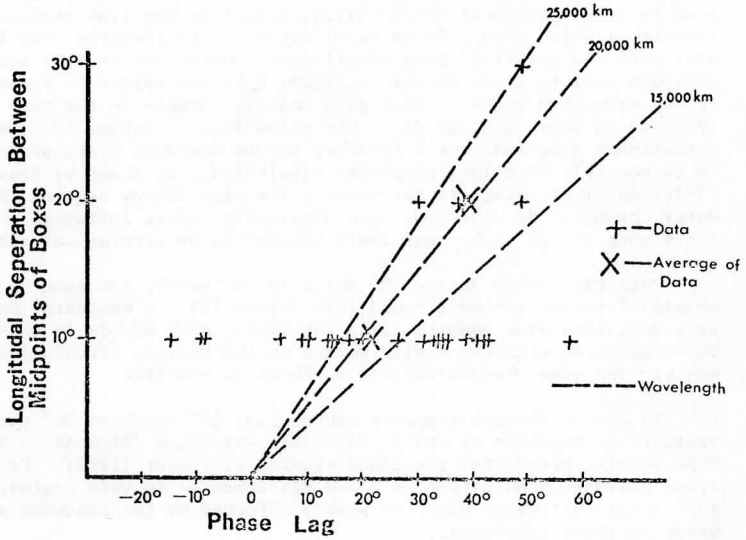

Figure 19: Phase lags for cross correlations over distances of more then one box width. Only lags for coherencies exceeding 90% confidence level are shown.

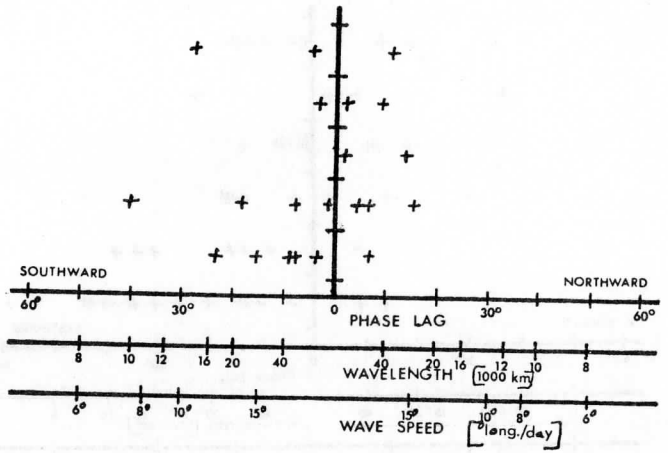

Figure 20: Meridional phase lags averaged from 30 to 10 day periods. Only phase lags for coherencies exceeding 90% confidence level are shown.

over the northern Pacific 20° north to 30° north (see Figure 17). In the ITCZ region, the small zonal phase lags again indicate that brightness features spread across more than one box. This can be seen by the high clouds (large bright spots) in the time section (Figure 6) which have a large areal extent. Correlations over longer distances did not yield many significant coherencies in this area probably because these clouds on Figure 6 do not appear to propagate in any organized manner. They grow and die largely in the same location in less than one day. The phase lags on Figure 18 (zonal directions) also indicate a tendency toward westward propagation. It is possible that long planetary wavelengths, as found by Sikdar (1972) in cloud data, are influencing the high clouds seen on the water channel. But, as mentioned previously, their influence is not strong enough to be positively identified by statistical analysis.

Over the Indian Ocean, 10° north to 20° north, the same closely coupled fluctuations were found (see Figure 17). A westward tendency of propagation also appears as in the ITCZ. High clouds in this area are associated with the rising motion in the monsoon circulation and exhibit the same characteristics as those in the ITCZ.

In the northern hemisphere subtropics, 20° north to 30° north, eastward propagation at small phase lags was found (Figures 17 and 18). This result agrees with the cloud studies of Sikdar (1972). He also found eastward propagation of cloud disturbances in this region, indicating that water vapor is weakly affected by the eastward moving waves in these latitudes.

A number of zonal correlations were found in the intermediate periods of 4.3 to 3.8 days at 20° north to 30° north latitude and at periods of around 3.0 days at 10° south to the equator indicated in Figure 15. They were scattered across the zonal band. Phase lags were small, grouped around 10° eastward direction, suggesting large brightness features with an eastward tendency of propagation. These fluctuations are possibly related to the 4-5 day period waves commonly studied by other investigators. The lack of many correlations in this period range, along with the lack of any large amount of variance in these periods, shows that the 4-5 day waves have only a very minimal affect on the upper level moisture.

5. CORRELATION OF UPPER LEVEL WATER VAPOR WITH CLOUD COVER

A cross correlation of water vapor with clouds in the same area yielded a close coupling between the two. The only exception is in the area in which clouds were not convectively active. ESSA 3 mosaic pictures were used to determine daily cloud amounts in the area from 140° east to 120° west. Time series were made for 10° by 10° boxes in the same manner as for upper level moisture. The length of the data set was 125 days, April 19 to August 21, 1970. The average cloud cover is presented in Figure 21. In general, the higher average upper level moisture areas on the water channel in the western Pacific (see Figure 11) agree with the areas of higher average cloud cover.

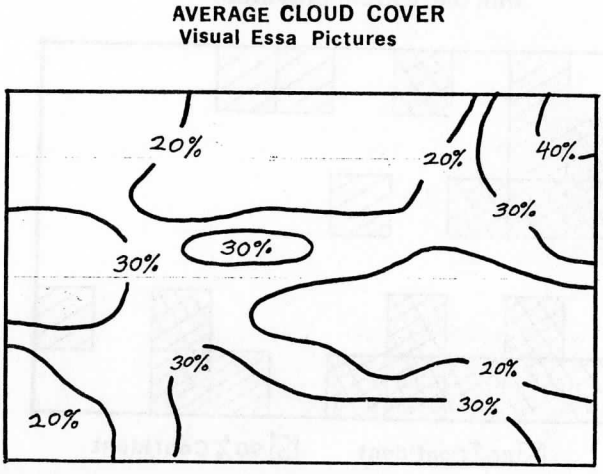

Figure 21: Average brightness on ESSA 3 mosaic visual cloud pictures for summer 1970.

The exception is on the eastern side of the Pacific. Here, the increase in cloud cover in the northeastern boxes do not register larger amounts of water vapor on the water channel. This can be explained by the nature of the clouds. The eastern side of the Pacific is the root of the trades region. There is subsidence in this region because it is on the edge of the subtropical high. These are stratus clouds which are not convectively active due to the stable conditions in the area. They have little rising motion in them and no rising motion above them. Moisture is absent in the upper levels because of the absence of any mechanism to lift it to the upper levels.

Cross spectra analyses between water channel time series and cloud cover time series in the same box were performed. The water channel data correlated well with the cloud cover in most areas (see Figure 22). The correlations were mainly found in areas of higher upper level moisture and higher cloud cover. The drier areas (less upper level moisture) did not have many non-zero correlations. The phase lags for the correlations were small. The moisture maxima occurred within one day of the cloud cover. This close coupling indicates that the upper level moisture is linked closely to the cloud cover. Therefore, convection is a possible mechanism for lifting water vapor to the upper levels.

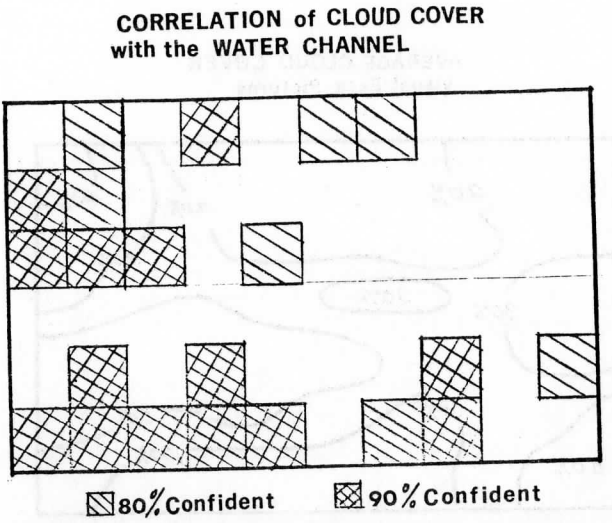

Figure 22: Areas of confident cross correlations between ESSA 3 cloud pictures and Nimbus 4 infrared water channel pictures. Coherencies and phase lags were averaged from 30 to 7.5 day periods. All phase lags were within ±1 days.

6. CONCLUSIONS

a) Upper tropospheric water vapor (brightest area on the Nimbus 4 THIR water channel photographs) is mainly found in the areas of rising air motion. Its presence indicates rising motion and its absence indicates subsidence in the area. The water channel thus can be used to locate atmospheric circulation features from the synoptic to global scales by their vertical motion patterns. Locations of mid-tropospheric trough systems can be seen on the water channel by tongues of dry air. Movement of these troughs was monitored over several days by the moisture patterns on the water channel. Satellite data is, therefore, useful for synoptic forecasting for areas in which conventional data is too sparse to locate these troughs.

b) Global circulation features, subtropical highs and the subtropical easterly jet, can be seen on the water channel by their patterns of rising and subsident motions. Location and movement of these systems and their change with the seasons thus could be monitored by the water channel.

c) Convection is probably the most important mechanism by which water vapor reaches the upper levels. Upper level moisture was found at the same time as cloud cover in the area. Also, in areas of non-convectively active clouds, upper level moisture was absent. The water channel can possibly be used to indicate the strength of the convection in these areas.

d) Movement of the upper level water vapor is mainly by advection by the wind field, or by propagation of synoptic scale dynamic lifting systems, mid-latitude troughs, or tropical waves. Moisture streaming down wind from large cumulonimbus clouds can be seen on the water channel. This moisture could be carried away from the clouds by the wind. However, after about 20° of latitude or longitude down wind from the clouds, it disappears. This indicates that subsidence in the wind field removes the moisture from upper levels before it covers any global scale distance.

e) The effect of tropical waves on lifting water vapor is most prominent in the longer period fluctuations, from 10 to 30 days. These waves have large amounts of convective activity associated with them over large areas, producing upper level moisture changes in their passage. The most prominent wave activity was in the southern hemisphere subtropics, 10° to 30° south latitude. South eastward movement of wave disturbances was found in this area. The commonly studied 4-5 day period westward moving waves in low latitudes near the equator were not clearly seen on the water channel. This indicates that the shorter period waves have a smaller vertical mass flux than the longer period waves. More energy is thus contained in the longer period waves.

BIBLIOGRAPHY

Allison, L.J., J. Steranka, G.T. Cherrix, and E. Hilsenrath, "Meteorological Applications of the Nimbus 4 Temperature-Humidity Infrared-Radiometer, 6.7 Micron Channel Data," Bulletin of the American Meteorological Society, 53:526-535, (June, 1972).

Chang, C.P., "Westward Propagating Cloud Patterns in the Tropical Pacific as seen from Time-Composite Satellite Photographs," Journal of the Atmospheric Sciences, 27:133-138 (1970).

Holub, R. and W. Shenk, "A Multispectral Study of an Extratropical Cyclone with Nimbus 3 MRIR Data," Paper presented at the Fourth Conference on Weather Forecasting and Analysis, Portland, Oregon, (May 1-4, 1972).

Koteswaram, P. "The Easterly Jet Stream in the Tropics," Tellus, 10:43-57, (1958).

Martin, F.L., and V.V. Salomonson, "Statistical Characteristics of Subtropical Jet Stream Features in Terms of MRIR Observations from Nimbus 2," Journal of Applied Meteorology, 9:508-520 (1970).

Maruyama, T., "Time Series of Power Spectra of Disturbances in the Equatorial Lower Stratosphere in Relation to Quasibiennial Oscillations," Journal of the Meteorology Society of Japan, 45:404-407 (1968).

Nitta, T., "Statistical Study of Tropospheric Wave Disturbances in the Tropical Pacific Region," Journal of the Meteorology Society of Japan, 48:47-59 (1970).

Panofsky, H.A., and G.W. Brier, Some Applications of Statistics in Meteorology, Pennsylvania State University Press, 224 pp. (1968).

Reed, R.J., and E.E. Recker, "Structure and Properties of Synoptic-Scale Wave Disturbances in the Equatorial Western Pacific," Journal of the Atmospheric Sciences, 28:1117-1133 (October, 1971).

Riehl, H., "Waves in the Easterlies and the Polar Front in the Tropics," Research Report Number 17, Department of Meteorology, University of Chicago, (1945).

Rosenthal, S.L., "Some Estimates of the Power Spectra of Large-Scale Disturbances in Low-Latitudes," Journal of Meteorology, 17: 259-263 (1960).

Sikdar, D.N., and V.E. Suomi, "Time Variations of Tropical Energetics as Estimated from Geostationary Satellite Altitude," Journal of the Atmospheric Sciences, 28: 170-180 (March, 1971).

Sikdar, D.N., J.A. Young, and V.E. Suomi, "Time-Spectral Characteristics of Large-Scale Cloud Systems in the Tropical Pacific," Journal of the Atmospheric Sciences, 29:229-239 (March, 1972).

Steranka, J., L.J. Allison, and V.V. Salomonson, "Applications of Nimbus 4 THIR 6.7 Micron Observations to Regional and Global Moisture and Wind Field Analyses," Journal of Applied Meteorology, 2:386-395 (March, 1973).

Wallace, J.M., "Time Longitude Sections of Tropical Cloudiness (December 1966-November 1967)," ESSA Report NESC 56, U.S. Department of Commerce, Washington, D.C., 37 pp. (1970).

_____, "Spectral Studies of Tropospheric Wave Disturbances in the Tropical Western Pacific," Reviews of Geophysics and Space Physics, 9:557-612 (August, 1971).

Yanai, M., T. Nitta, and Y. Hayashi, "Power Spectra of Large-Scale Disturbances over the Tropical Pacific," Journal of the Meteorology Society of Japan, 46:308-323 (1968).

Young, J.A., and D.N. Sikdar, "A Filtered View of Fluctuating Cloud Patterns in the Tropical Pacific," Journal of the Atmospheric Sciences, 30:392-407, (April, 1973).

SATELLITE DERIVED UPPER LEVEL DYNAMICAL FEATURES NEAR THE JET STREAM ON TWO SEVERE STORM DAYS

B. Auvine and D. N. Sikdar

ABSTRACT

The upper tropospheric wind field on two severe storm days is examined using satellite derived cloud motion vectors. Fields of divergence and relative vorticity obtained from the vectors exhibit a consistent pattern with reference to the location of the jet axis and thunderstorm precipitation area. A compatible wind maximum was observed to the southwest of the precipitation area and to the south of the area of subsidence. Also seen in this small data sample is a quasi-periodic fluctuation in the cirrus tracer motions near the jet stream. A similar fluctuation in the nearby severe storm intensity implies some kind of interaction between these fluctuations and the storms themselves.

1. INTRODUCTION

The use of ATS-III satellite data to determine the wind velocities at various levels of the atmosphere has recently attracted attention as a means of deducing the subsynoptic wind field or the wind field in data sparse areas. These wind fields have been used in a variety of ways. They supplied additional analyses of the upper-level flow in severe storm situations (Ninomiya, 1971b) and were used to study divergence, vorticity, and deformation fields associated with the outflow layer of the mature thunderstorm complex (Ninomiya, 1971a), and to calculate the mass outflow from a thunderstorm complex (Fujita and Bradbury, 1968).

The purpose of this analysis was to determine the wind field divergence and vorticity using the increased time and space resolution available from such satellite data. These characteristics of the wind field were related to the location of the jet axis and the areas of active convection and precipitation. Divergence in the upper atmosphere gives a general indication of the region of upward motion. Indeed, such diffluence aloft is considered to be an important indicator of severe weather (Endlich and Mancuso, 1968), although there is disagreement as to the cause or effect relationship that exists between the observed diffluence and the storms themselves. Vorticity is also related to the vertical motion, through the vorticity and continuity equations. In particular, one would expect that, at upper levels,

anticyclonic relative vorticity would be found south of a jet stream.

A study of the divergence and vorticity fields with good time resolution allows the relation of various maxima and minima of vorticity and divergence to features such as the jet stream core and the precipitation field. Unlike most conventional observations, satellite-derived winds have good continuity. This allows features to be followed during the lifetime of the storms.

Methods for determining such cloud motions range from the use of film loops to track the motions of individual clouds (Ninomiya, 1971a) to sophisticated cross-correlation computer techniques (Smith and Phillips, 1971; Leese et. al., 1971). In this study, a cross correlation technique was used to derive cloud motion vectors from successive satellite pictures on April 19, and 23, 1968. A selection of proper cloud tracers was a prerequisite to the efficient use of the cross correlation technique. This was done by navigating the digitized satellite photographs, displaying them in rapid time sequence on a television screen, and then selecting out those clouds which appear to the eye to have a consistent motion. To increase the data coverage, we also included Ninomiya's (1971a) film loop study of upper tropospheric cloud motions on April 23, 1968.

Only cirrus cloud motions were used in these studies to limit the data to the near-tropopause region. The days used generally had clearly definable areas of such cirrus cloud. This insured adequate data for analysis on a one degree latitude by one degree longitide grid. As noted by Hubert and Whitney (1972), the use of cirrus cloud motions to determine the wind field is made difficult by the height variation of the tropopause over large synoptic-scale regions. Accordingly, our analysis was limited to a relatively small region near the area of convection in order to decrease the magnitude of this height variation. In addition, the derived winds were compared to conventional rawinsonde data. This was done to confirm that such winds were indeed representative of and consistent with existing synoptic analyses of the tropopause level of 250 to 300 mb. It was found that the wind field obtained from such satellite data is within the range of variability of this rawinsonde data (compare Figures 3 and 5). This suggests that our techniques provided results which were reasonably accurate and well correlated with a particular atmospheric pressure level.

2. DATA AND ANALYSIS

The days used for this study were April 19th and 23rd, 1968. Both days produced severe weather, including tornadoes, over a wide area of the central United States. For details on the severity and nature of these storms, the reader is referred to the paper by Sikdar et. al. (1970). Figures 1 and 2 present a satellite view of the convection area for those dates. The relation of these cloud features to the synoptic scale isotach pattern may be seen by comparing these figures with Figures 3 and 4. In both cases, the jet core, or its extension,

is located prominently to the west of the storm region, although, on April 23rd, no synoptic wind field is available during the maximum convection activity.

Only one set of rawinsonde observations before and one after the storm period are available. During the actual time of maximum storm activity no conventional wind data is available. Also, conventional rawinsonde data depict the synoptic scale field of motion only, without providing a view of the smaller scale motions important to the study of the convection processes. Thus, a geostationary satellite derived wind field provides potentially useful data because it allows a finer time resolution and a better horizontal space resolution of the wind field.

On both days, analysis was performed on a one degree by one degree grid. Time resolution varied from 14 minute intervals on the 19th of April to approximately two hour intervals on the 23rd. An example of the satellite derived winds for April 19th is provided in Figure 5. Variations in spacing of the clouds obviously would allow finer space resolution in small areas around the storm area. However, in order to obtain an overall picture of the wind field and its relation to the severe storm area, a subsynoptic resolution of one degree by one degree was chosen. A computer analysis of the divergence and relative vorticity was obtained using Mancuso and Endlich's (1973) Wind Editing and Analysis Program.

3. RESULTS

Shown in Figures 6 through 8 are the vorticity and divergence analyses for April 19th, followed by similar analyses for April 23rd in Figures 9 and 10. The location of the jet axis (determined from the same satellite derived wind data) and the location of the radar echo areas (shaded) are also indicated.

In the data presented, the jet axis is always to the northwest of the precipitation region and it frequently defines the boundary between the areas of convergence and divergence. Miller (1969) and others noted the presence of an upper level jet stream to the north or northwest of a severe weather area. In figures 6 through 10, we see that the jet axis usually defined the northern or northwestern boundary of the region favorable to the formation of convective cells.

Likewise, the jet axis closely follows the zero vorticity line with anticyclonic vorticity to the southeast and cyclonic to the northwest. This was in accord with the theoretical expectation for a westerly jet stream. The storms themselves were located in the region of anticyclonic vorticity. Also, as would be expected, maximum vorticity values ranged between 10^{-5} to 10^{-4} sec^{-1}. This is at least one order of magnitude higher than that usually quoted for the synoptic scale.

The majority of the cloud tracers selected for deriving the upper level flow field are near the jet stream; only a few could be traced to an origin in the cirrus outflow of severe storms. Divergence computed from this motion field coincides closely with the region of convection. This indicates that the divergence is partly associated with the outflow from the cumulonimbus anvil cirrus. The location of maximum divergence, however, does not agree exactly with the areas of precipitation (Figures 7, 9), suggesting that there may be other dynamical causes for these areas of subsynoptic scale divergences. Maximum divergences on both the 19th and 23rd show first an increase in the storm region, then a gradual decrease (Figure 11 and 12). The greatest strength of divergence was near the time when severe weather was sighted in the area. Orders of magnitude of the computed divergence ranged from 10^{-5} to 10^{-4} sec^{-1}, again one order of magnitude higher than that usually quoted for the synoptic scale fields.

A careful scrutiny of the cirrus shield motion field reveals a local maximum (10 to 20 kts greater than the surrounding jet velocities) in the jet to the southwest of the precipitation area and south of the area of maximum convergence. Because the maximum is fairly consistent in its relative location to these other features and is evident in all the analyses in this series, it is a real feature in the wind analysis and not a random fluctuation. This interpretation of the maximum in the wind field may be related to Fujita's finding that the storms act as an obstable to the wind flow causing higher wind speeds on the flanks of the storms. It might also explain the existence of convergence in this same area (as for example in Figures 6 and 8), although synoptic scale subsidence behind the front must also be considered as a factor in the total divergence pattern.

There is general continuity in the locations of areas of divergence and vorticity. However, the size and shape of these areas shift considerably, even over the 13 minute periods between the observations of April 19th. The nature of these alterations can be seen more clearly in Figure 13. Here, a longitudinal time cross section of divergence shows variations of divergence at different latitudes as a function of time. In particular, there appears to be a periodicity of about 40 minutes in the variation of convergence, although the time period covered is too short to verify such a pattern. Vorticity (Figure 14) exhibits a similar pattern as does the momentum (Figure 15) where u and v have been averaged zonally.

Time variations in the growth rate of severe storms south of the jet on April 19th also had similar periodic pulsation (Sikdar et. al., 1970). This suggests some sort of direct interactions of the severe storm evolutions with the jet stream flow field. Such periodic undulation in the mesoscale upper tropospheric wind field around severe storms may result from gravity waves generated by these interactions. This situation can be clarified when better time series data are available.

4. CONCLUDING REMARKS

The clearest conclusion of this study is that the geostationary satellite data in time lapse mode provides a good opportunity for studying meso-scale dynamics. Cirrus tracer motions were found to adequately represent subsynoptic scale wind field near 300 mb. These had fine time resolution, ordinarily not obtained from conventional network.

The case studies presented revealed a consistent relationship between the locations of the jet maxima, vorticity, and divergence maxima, and the area of active precipitation. The location of maximum divergence does not coincide exactly with the location of the severe storm precipitation area, although a large area of weak divergence extends over it. The absence of such a unique spatial coexistence may be attributed to dynamical causes and not simply to convective outflow in the upper troposphere. An interesting finding was the presence of a consistent local wind speed maximum to the southwest of the precipitation zone and to the south of the subsidence region. Finally, there appears to be some kind of undulation in the field of divergence, vorticity, and momentum with time. The cause of this undulation is not clearly elicited by our small data sample.

ACKNOWLEDGEMENT

The authors are thankful to Professor David Houghton for reading the manuscript and offering helpful suggestions. Thanks are also due to many individuals at SSEC who helped in various ways in this research program. The research reported in this paper was partly supported by NOAA under grant NG-26-72 and partly by NASA under contract NAS5-21798.

BIBLIOGRAPHY

Endlich, R. and R. Mancuso, 1968: Objective analysis of environmental conditions associated with severe thunderstorms and tornadoes. Mon. Wea. Rev., 96, 342-350.

Fujita, R. and D. Bradbury, 1969: Determination of mass outflow from a thunderstorm complex using ATS-III pictures. Proc. Severe Wea. Conf. 1969, 38-43.

Hubert, L. F. and L. F. Whitney, Jr., 1971: Wind estimation from geostationary-satellite pictures. Mon. Wea. Rev., 99, 665-672.

Leese, J. A., C. S. Novak, and B. B. Clark, 1971: An automated technique for obtaining cloud motion from geosynchronous satellite data using cross correlation. J. Appl. Meteor., 19, 118-132.

Mancuso, R. L. and R. M. Endlich, 1973: User's Manual Wind Editing and Analysis Program--Spherical Grid. Stanford Research Institute, 20 pp.

Miller, R., 1969: Forecasting the degree of intensity of severe thunderstorms. Proc. Severe Wea. Conf. 1969, 197-201

Ninomiya, K., 1971a: Dynamic analysis of outflow from tornado-production thunderstorms as revealed by ATS-III pictures. J. Appl. Meteor., 10, 275-294.

Ninomiya, K., 1971b: Mesoscale modification of synoptic situations from thunderstorm development as revealed by ATS-III and aerological data. J. Appl. Meteor., 10, 1103-1121.

Reiter, E., 1963: Jet Stream Meteorology, U. Chicago Press, Chicago, 515 pp.

Sikdar, D. N., V. Suomi and C. Anderson, 1970: Convective transport of mass and energy in severe storms over the United States--an estimate from a geostationary altitude, Tellus, 22, 521-532.

Smith, E. and D. Phillips, 1971: Automated cloud tracking using precisely aligned digital ATS pictures. Proc. Two-Dimensional Digital Signal Processing Conf., Columbia, Mo., 1-26 February 1972.

Viezee, W., S. Serebreny, R. Mancuso, and W. Shenk, 1972: A sample computation of kinematic properties from cloud motion vectors. J. Appl. Meteor., 11, 731-741.

LIST OF FIGURES

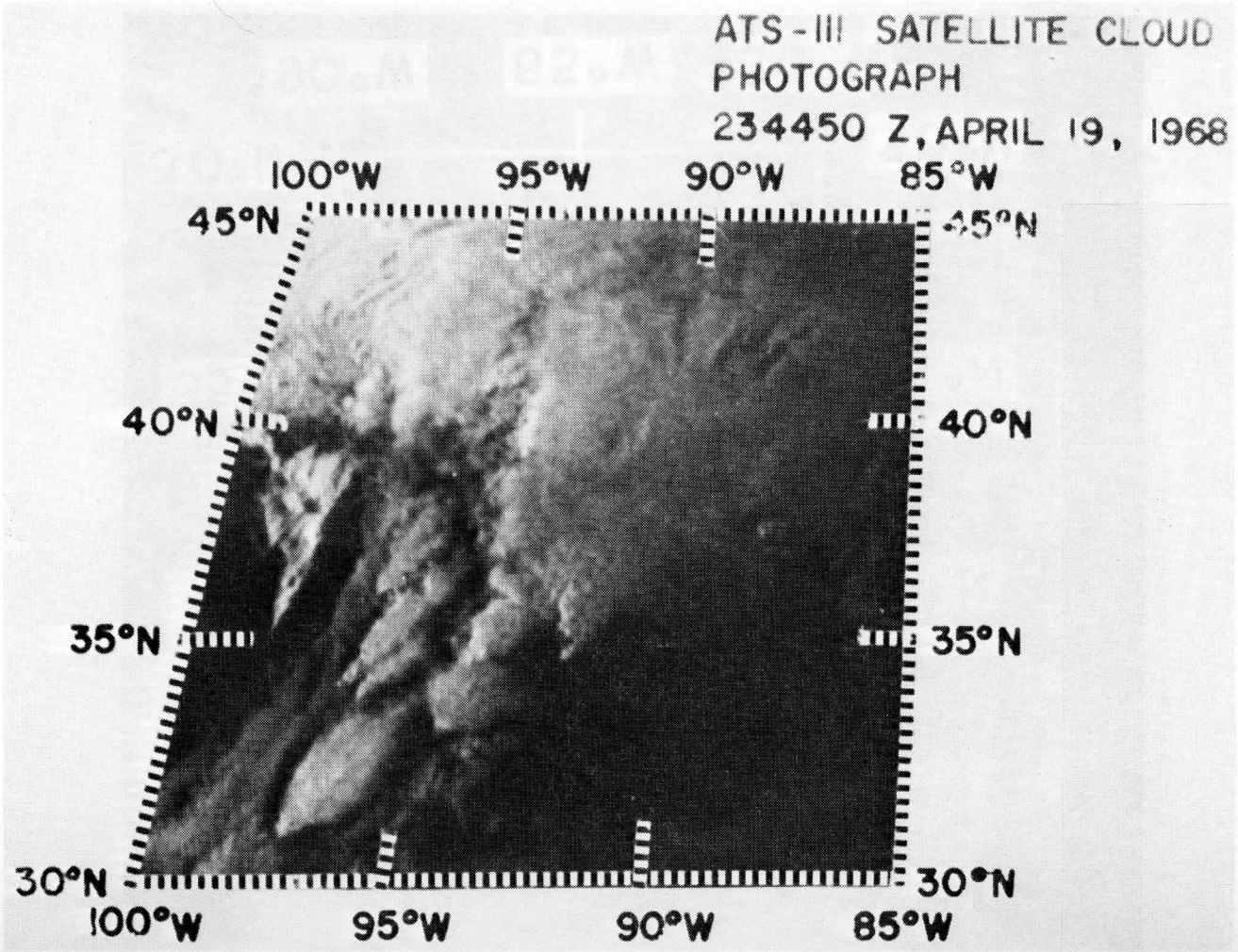
ATS-III SATELLITE CLOUD
PHOTOGRAPH
234450 Z, APRIL 19, 1968
100°W
95°W
90°W
85°W
45°N
40°N
35°N
30°N

Figure 1

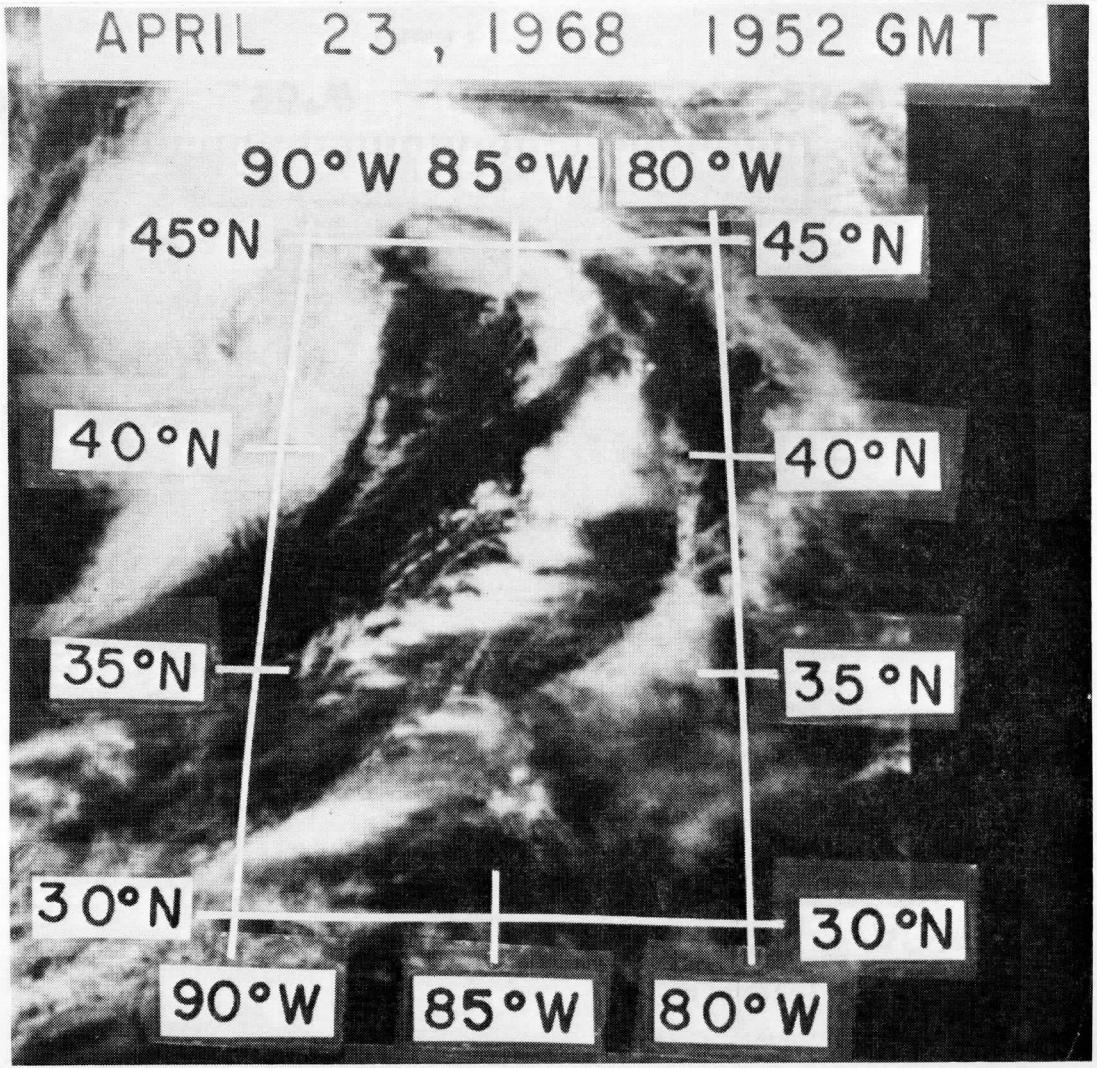
APRIL 23, 1968 1952 GMT
90°W 85°W 80°W
45°N
45°N
40°N
40°N
35°N
35°N
30°N
30°N
90°W
85°W
80°W

Figure 1

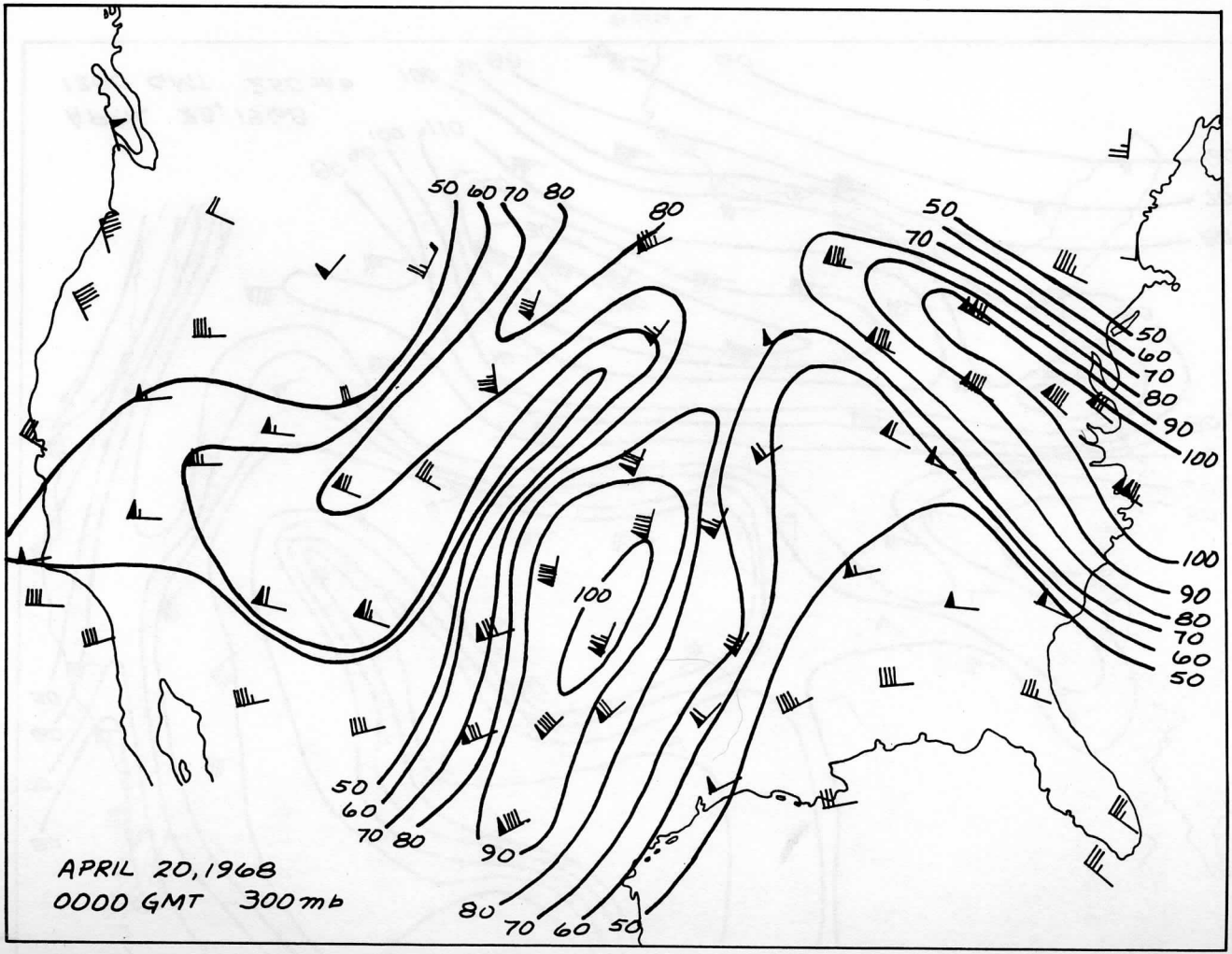

Figure 3

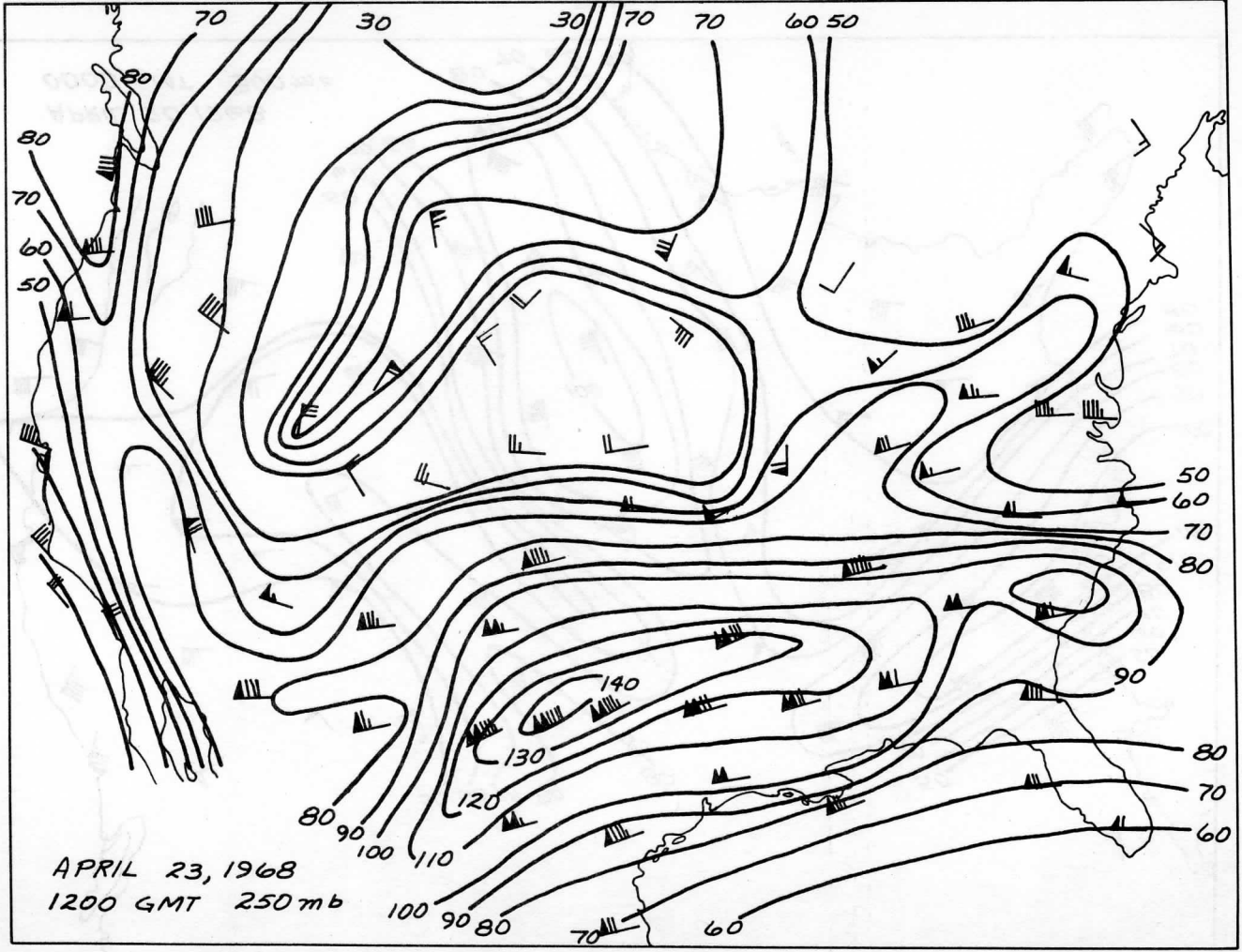
70
30
30
70
70
60
50
80
80
70
60
50
50
60
70
80
90
140
130
120
80
90
100
110
80
70
60
100
90
80
70
60
APRIL 23, 1968
1200 GMT 250 mb

Figure 4

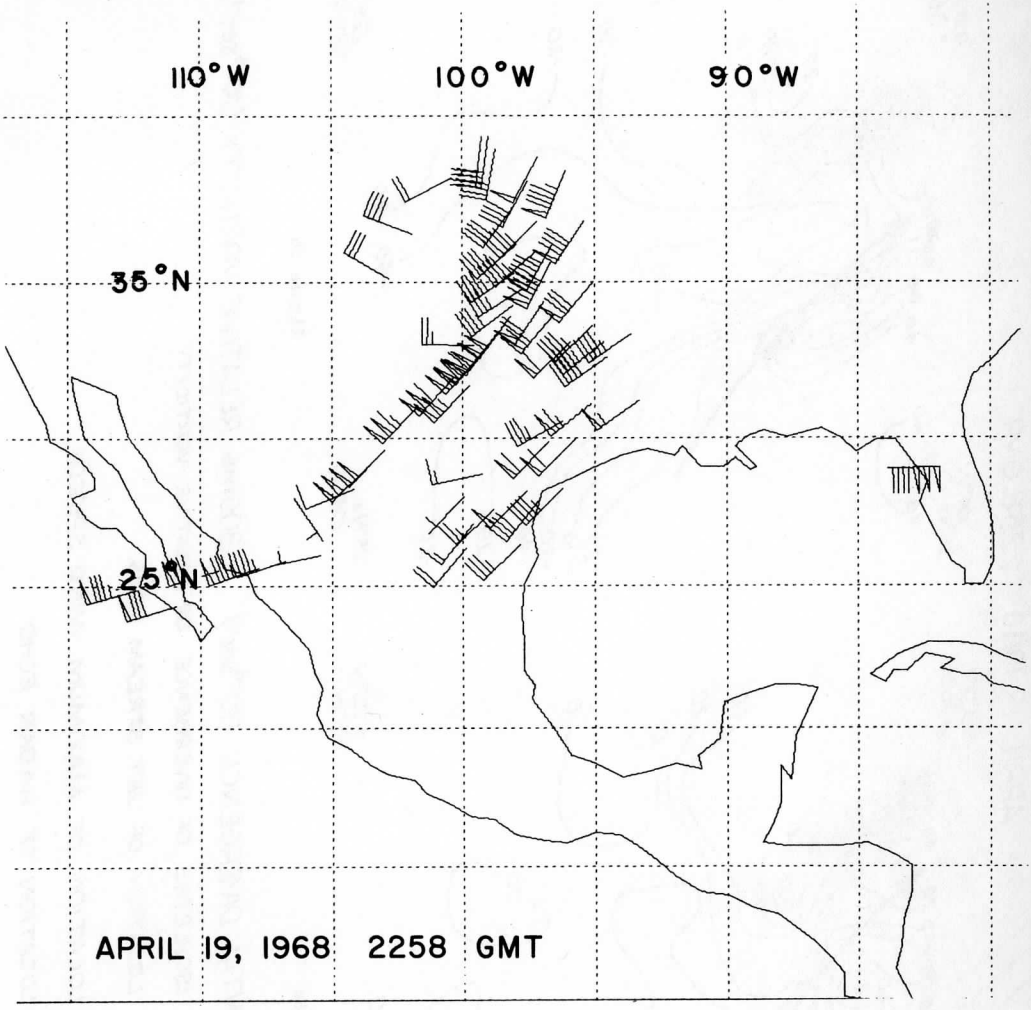

Figure 5

APRIL 19, 1968 2258 GMT

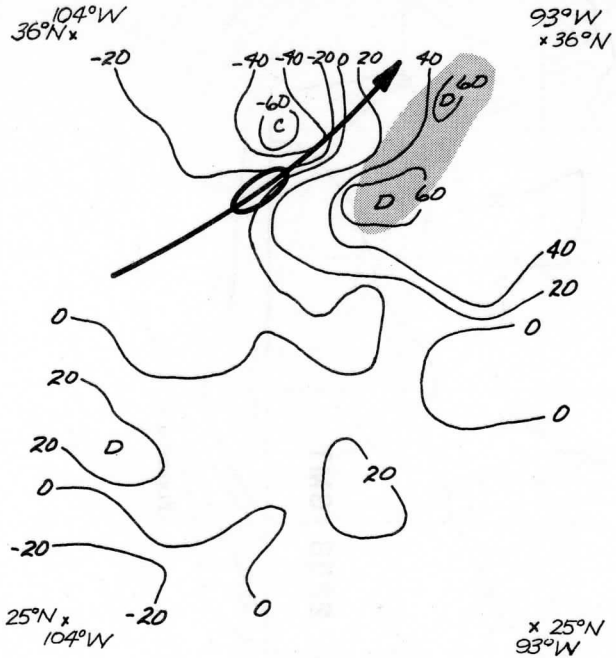

Figure 6a

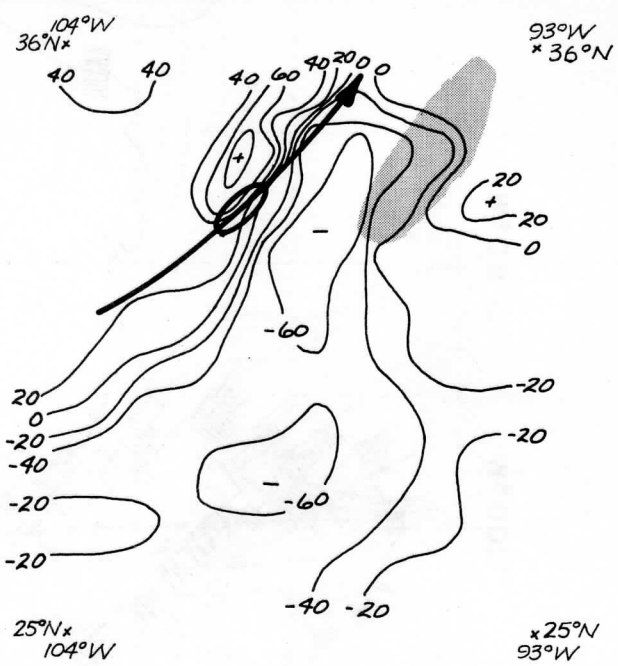

Figure 6b

300mb HORIZONTAL DIVERGENCE (10^{-6}sec^{-1}) 300mb RELATIVE VORTICITY (10^{-6}sec^{-1})

ISOPLETHS OF DIVERGENCE OR RELATIVE VORTICITY

LOCATION OF JET STREAM AXIS

LOCATION OF MAXIMUM WIND SPEEDS

LOCATION OF RADAR ECHO

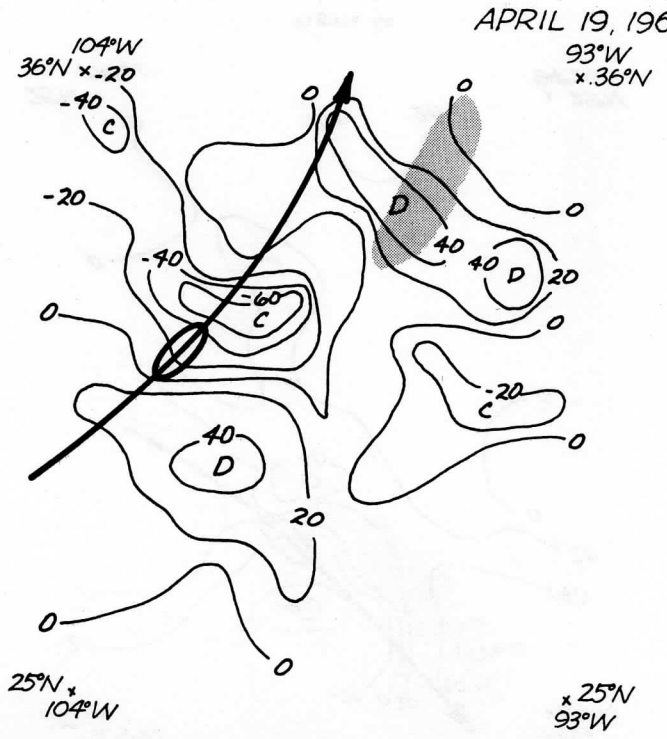

Figure 7a

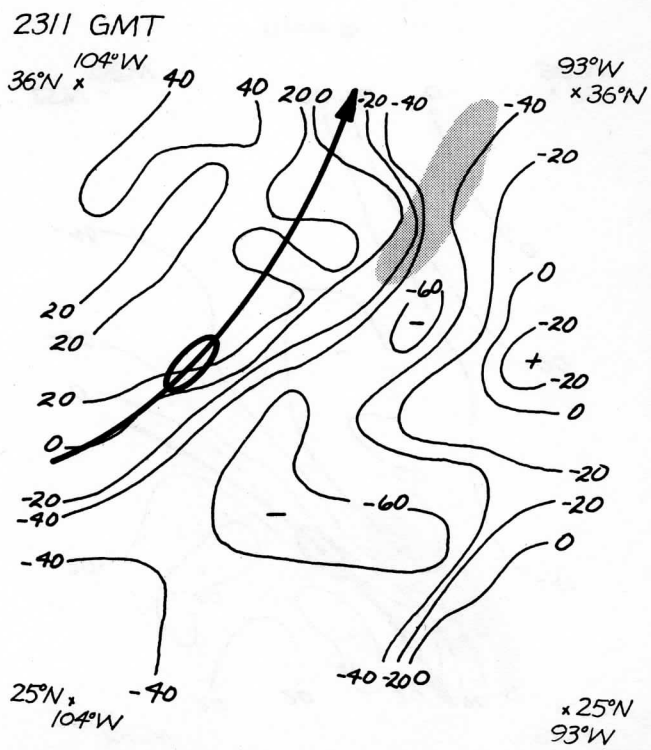

Figure 7b

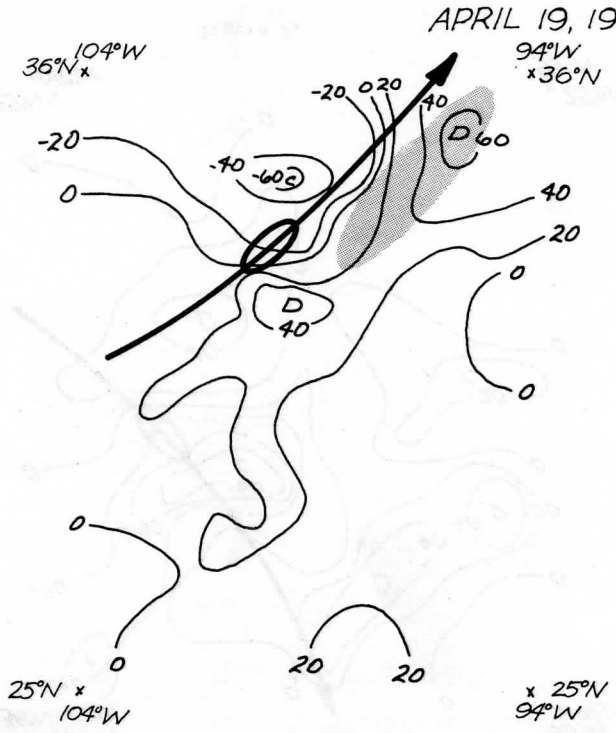

Figure 8a

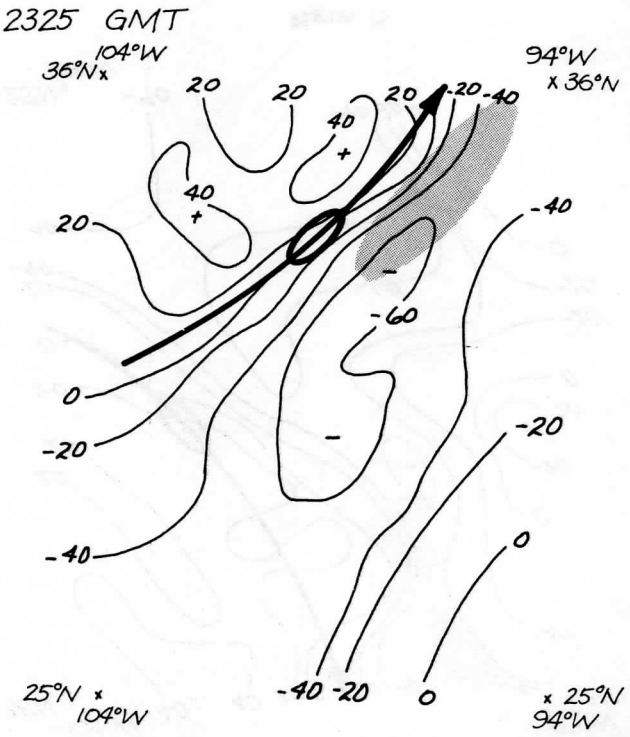

Figure 8b

APRIL 23, 1968 1856 GMT

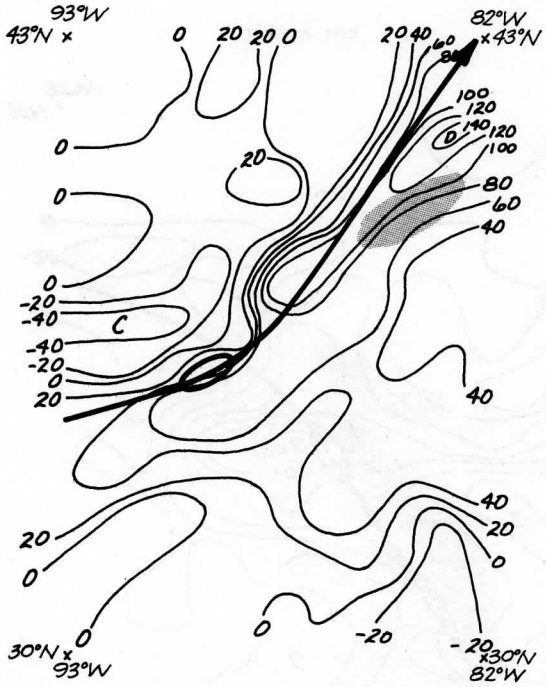

300mb HORIZONTAL DIVERGENCE (10^{-6} sec^{-1})

Figure 9a

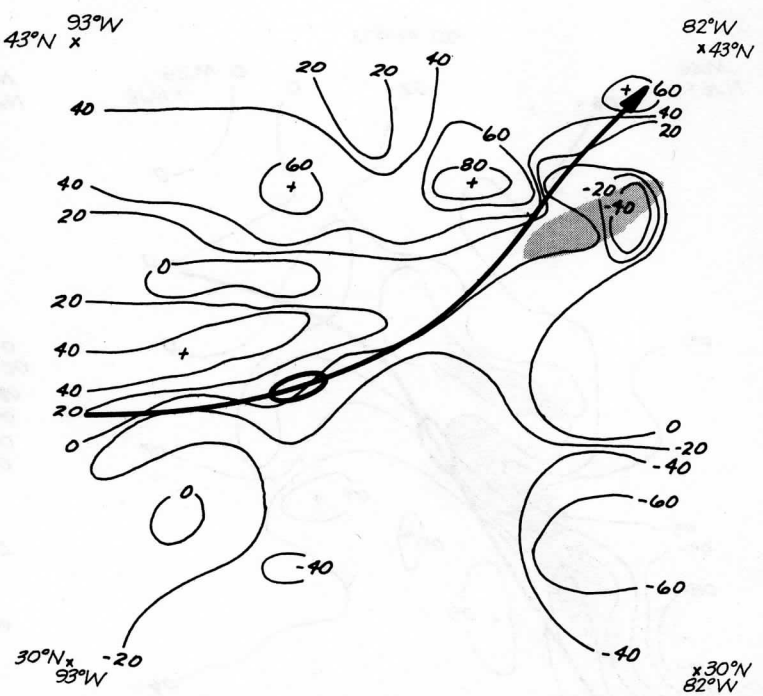

300mb RELATIVE VORTICITY (10^{-6} sec^{-1})

Figure 9b

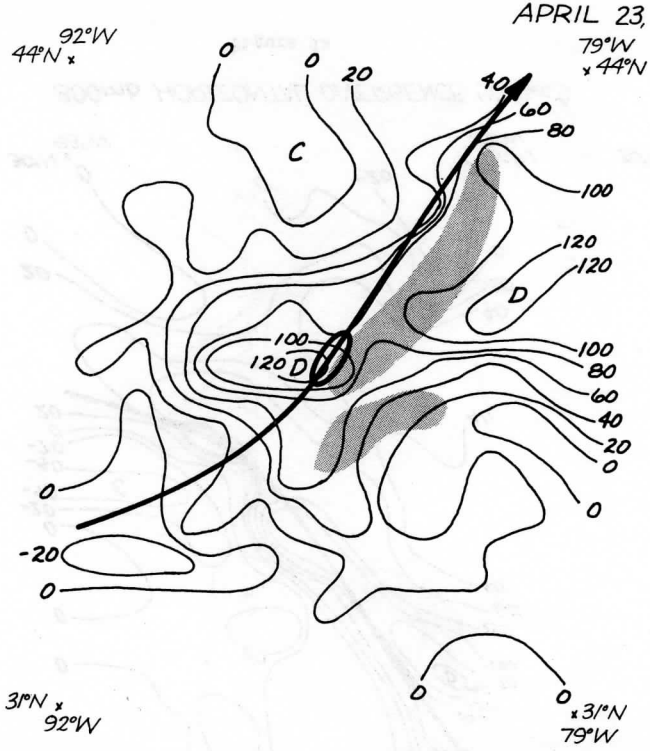

Figure 10a

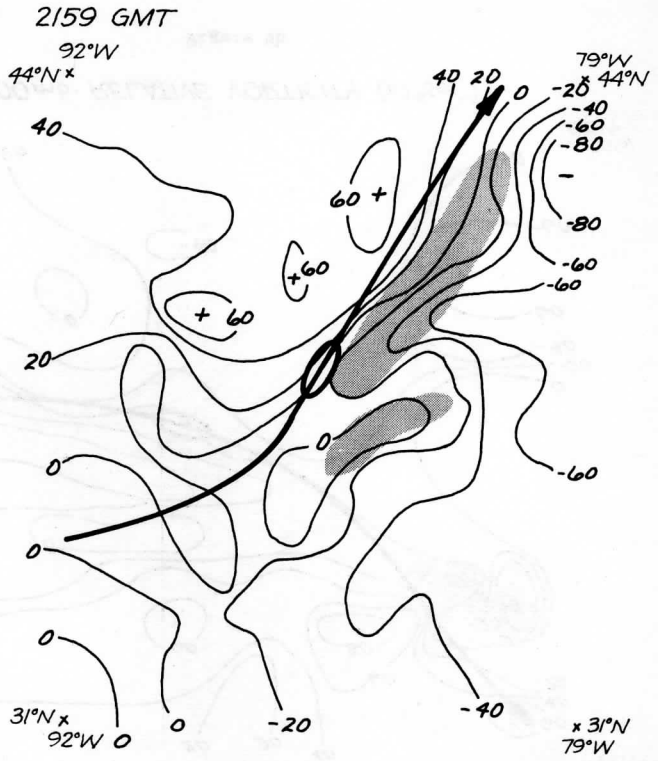

Figure 10b

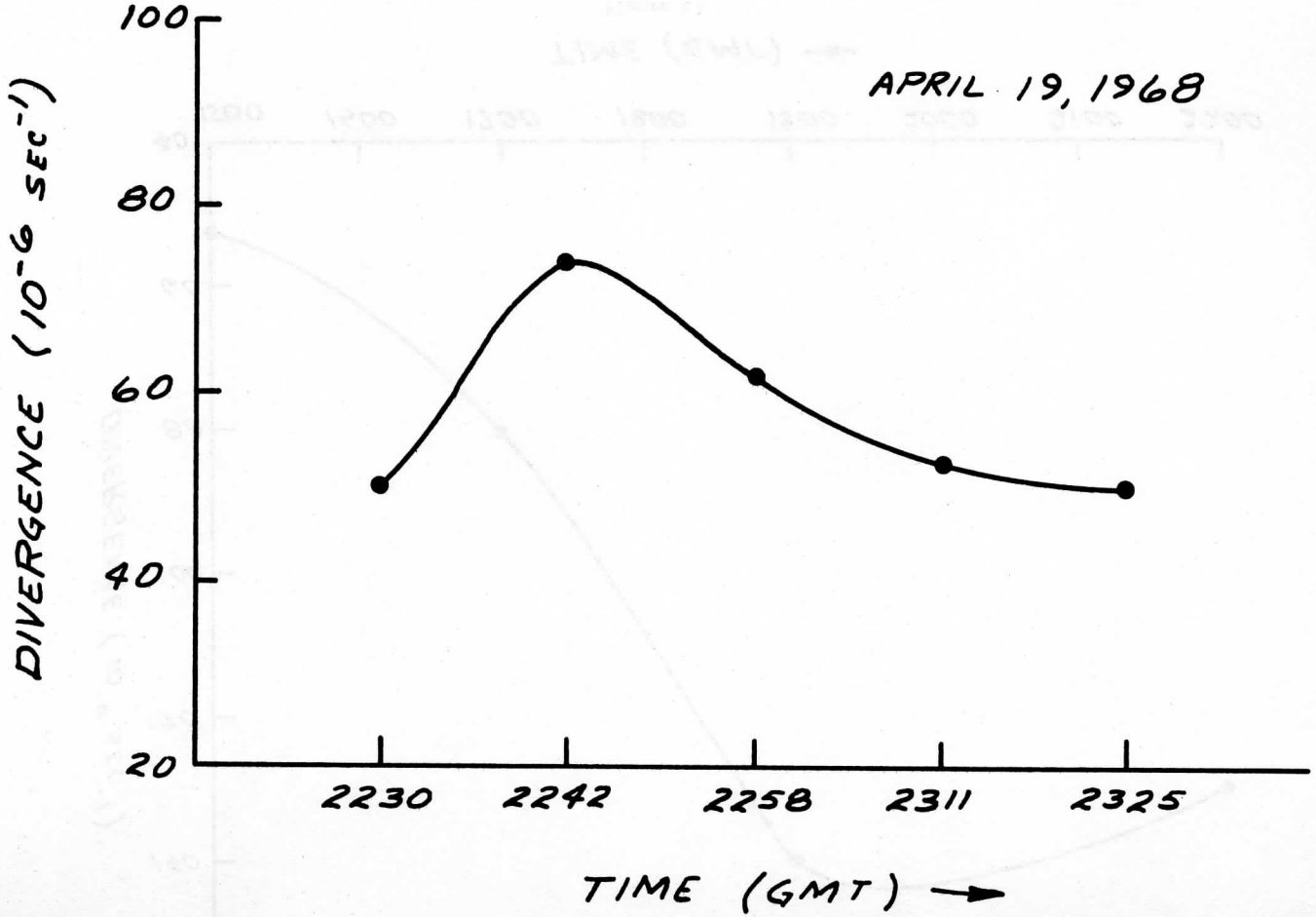
APRIL 19, 1968
DIVERGENCE (10^{-6} SEC^{-1})
100
80
60
40
20
2230
2242
2258
2311
2325
TIME (GMT)

Figure 11

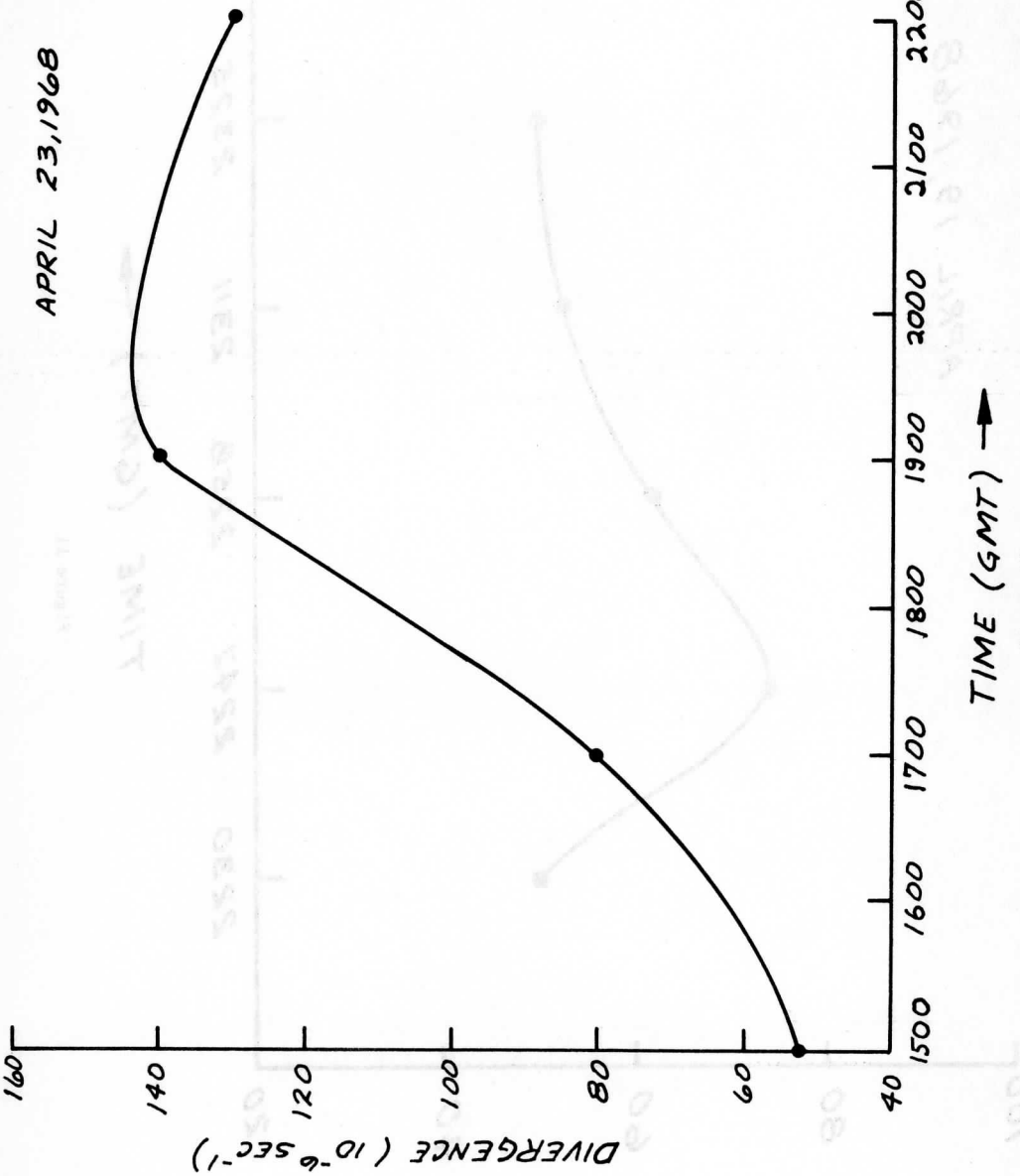
APRIL 23,1968
DIVERGENCE (10^{-6} sec^{-1})
160
140
120
100
80
60
40
1500
1600
1700
1800
1900
2000
2100
2200
TIME (GMT)

Figure 12

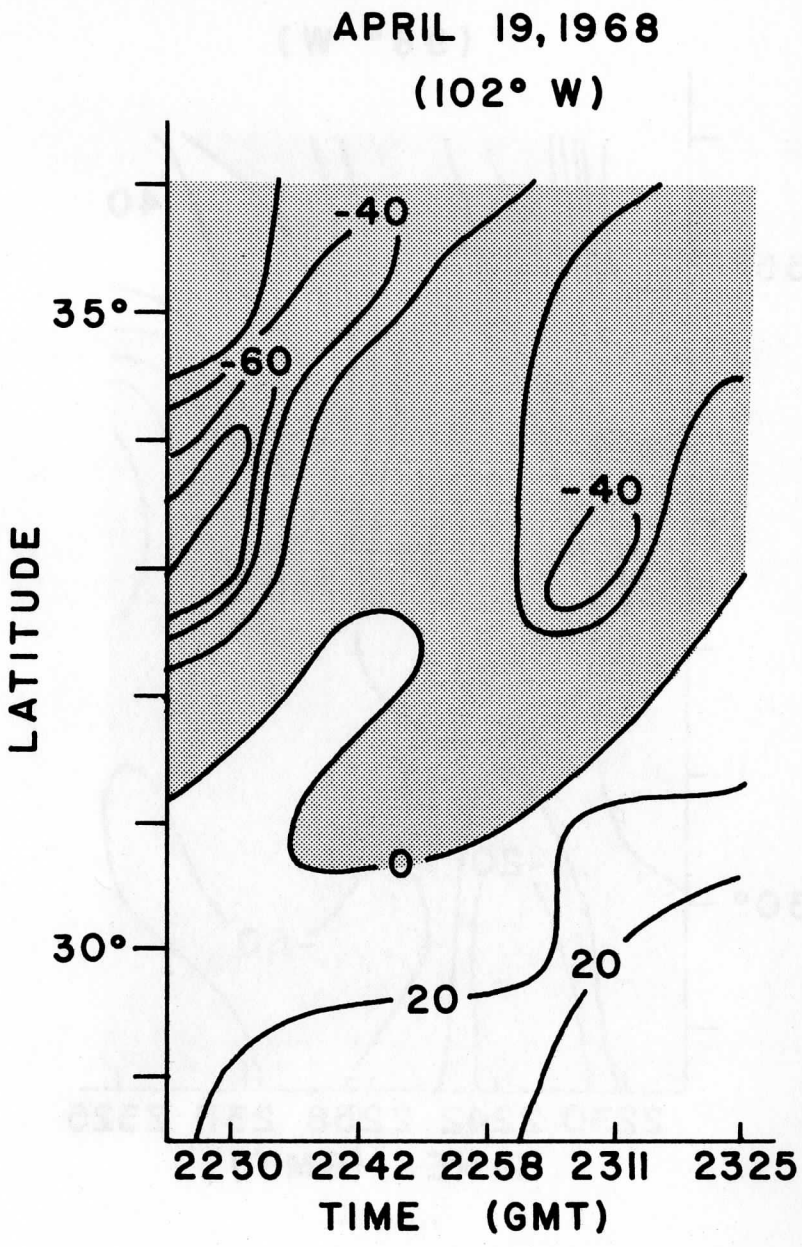
APRIL 19, 1968
(102° W)
-40
-60
-40
0
20
20
35°
30°
LATITUDE
2230
2242
2258
2311
2325
TIME (GMT)

Figure 13

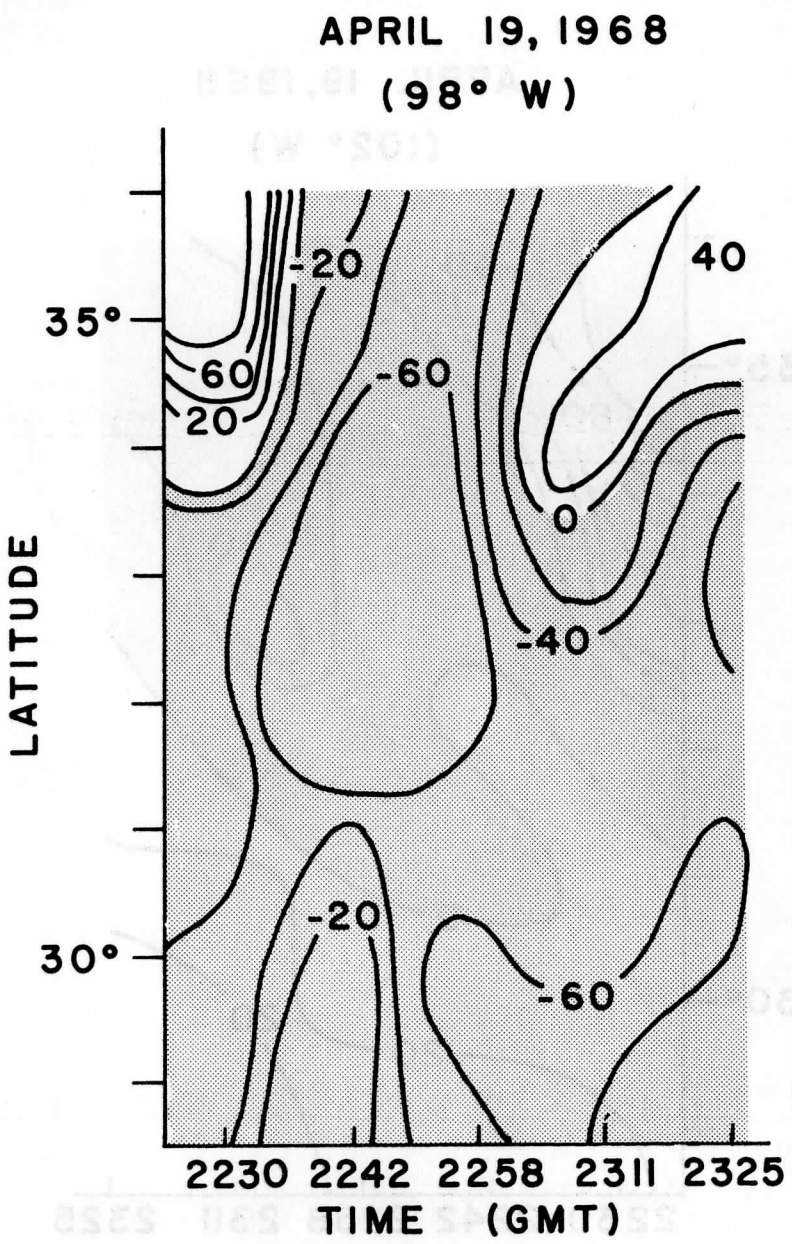
APRIL 19, 1968
(98° W)
LATITUDE
35°
30°
-20
40
60
-60
20
0
-40
-20
-60
2230 2242 2258 2311 2325
TIME (GMT)

Figure 14

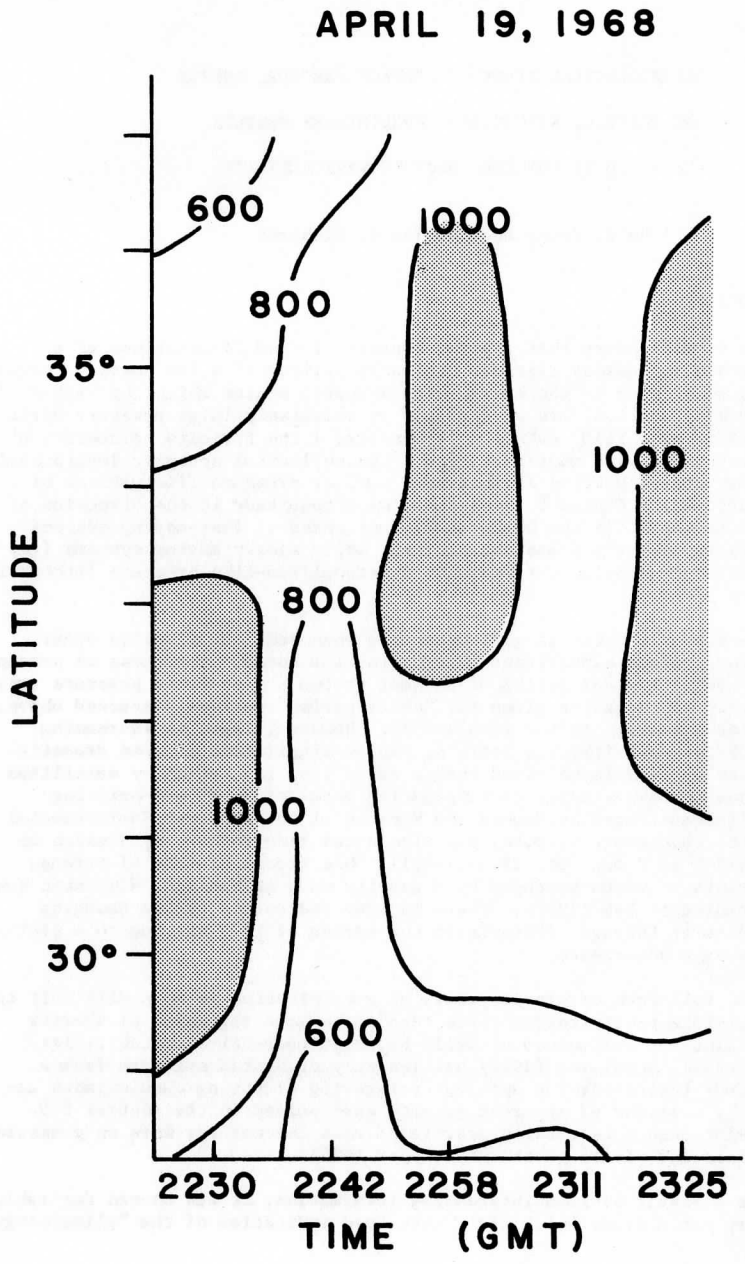
APRIL 19, 1968
600
800
1000
1000
800
1000
600
35°
30°
LATITUDE
2230
2242
2258
2311
2325
TIME (GMT)

Figure 15

A CLIMATOLOGICAL STUDY OF SURFACE PRESSURE EVENTS AT MADISON, WISCONSIN: PRELIMINARY RESULTS RELATING TO POSSIBLE GRAVITY WAVE ACTIVITY

John A. Young and Charles F. Richards

INTRODUCTION

It is well known that typical spectra of wind fluctuations at a given location possess distinct minima at periods of a few hours. Longer periods correspond to the energy-rich synoptic scales which, by virtue of the earth's rotation, are accompanied by relatively large pressure variations of order $\rho(fL)U'$ (where ρ is density, f the Coriolis parameter, U' the fluctuating wind magnitude, and L the horizontal synoptic length scale). The short period motions exhibit much smaller pressure fluctuations of order $\rho(|c-\overline{U}|)U'$ (where $\overline{U}$ is the mean wind magnitude in the direction of propagation and c is the horizontal phase speed). Fast-moving systems ($|c|>>\overline{U}$) represent a transient extreme, while slowly moving systems ($|c|<<\overline{U}$) represent an advective extreme with a Bernoullian-like pressure fluctuation given by $\rho\overline{U}U'$.

Despite the spectral gap, mesoscale phenomena occasionally occur. These can produce significant changes in wind speed, cloudiness or precipitation over a typical period of an hour or two. Associated pressure amplitudes obey the relation given for "short-period" motions discussed above. A prominent example is the squall line. However, there is increasing evidence that gravity wave activity can be significant or even dramatic. For example, time-lapse cloud images taken from geostationary satellites have shown numerous cases of propagating modulations of pre-existing clouds (communicated by Gruber and Winston of the National Environmental Satellite Laboratory of NOAA; see also notes from lecture by Winston on pp. 276-280 in Young, et. al., (1972)). One recent example of strong, non-convective winds produced by a gravity wave at Madison, Wisconsin has been studied by Eom (1972). There is some indication that a damaging wind event at Chicago, Illinois in the spring of 1973 was due to a similar gravity wave occurrence.

The influence of gravity waves on precipitation is more difficult to assess, since precipitation rates tend to be more variable, of shorter time scale, and influenced strongly by moist convective instabilities. Nevertheless, Uccellini (1972) has recently presented evidence from a case study indicating the apparent triggering of strong cumulonimbus activity by a series of apparent gravity wave pulses in the central U.S. This relationship is closely associated with the earlier work on pressure jump lines and severe weather by Tepper (1954).

As a result of such interesting information, it was deemed desirable to carry out a study which would give some indication of the "climatology"

of apparent gravity wave activity. Our starting point is an analysis of 33 "winters" of surface pressure records for Madison, Wisconsin. The study attempts to identify pressure "events" on a meso-time scale which are possibly related to local gravity waves. The advantage of studying this variable arises from its long, continuously recorded trace and its pertinence to divergent, accelerated air flow. We have defined the pressure events as strong, short-term pressure fluctuations with equivalent periods ranging typically between 30 minutes and four hours. In many cases the fluctuations were far from periodic; the "equivalent period" might correspond to twice the time interval for a step-change in pressure. The screening procedure was simple: the barograph traces were examined by eye (by CFR) for qualitatively significant "bumps." These were then classified as "events" if they exceeded .06 inches of mercury (2.0 mb) over two hours.

The basic data consisted of copies of Madison barograph traces for the period January 1940-March 1973. The traces were "five-day" traces during the period 1940-1953 and for 1973; they were "twelve-hour" traces during 1953-1972. Most traces were provided by the National Climate Center, Asheville for the Madison weather station which was located first on the University of Wisconsin campus (1940-1948) and then at Truax Field (1948-1972). The 1973 data was taken from the Meteorology and Space Science Building on the campus. (Comparisons of traces from the latter site with Truax Field traces during the period 1970-73 indicated that the pressure events defined above were identical.) We have confined the data to the "winter" months, December through March. In this way we have attempted to reduce the number of thunderstorms producing "events."

In the remainder of this article we present the results of this preliminary study of the data. Since the time available for the study was limited by changes in professional plans of the investigators, these results are not as complete as they might have been. The next section presents statistics on the occurrences of "events" and some example traces. The third section contains some of the associated synoptic weather information. Possibilities for further research are discussed in the final section.

PRESSURE EVENT STATISTICS FOR THE PERIOD 1940-1973

Sample Traces

Figure 1 gives examples of each of the six different kinds of event traces identified in this study.[1] The percentage of events for each category (out of a total of 290 events) is also indicated. It is seen that events associated with falling surface pressure are most common. The reason for this becomes more apparent when the synoptic data is discussed in the third section. The sudden "step" rises (type D) form only 8% of the events, and in some cases may correspond to a cold front passage.

In some cases, the events occur repeatedly, as though the gravity waves formed an unsteady "train". An example of such a trace is shown in Figure 2.

---

[1] Similar examples and categorizations may be found in Tepper (1954).

Amplitudes

Figure 3 shows a sampling of some interesting pressure traces identified for the period 1940-1950. The event occurring on April 19, 1970 was studied by Eom (1972).

Figure 4 shows the distribution of maximum amplitudes for the 209 events. There is a general decline from the maximum at the cut-off. Secondary maxima and minima do not appear to be statistically significant.

Events by Year

More than one event may occur on a given date, and a sequence of events may be spread over two successive days. Thus we will distinguish between events, event days, and event sequences in the remainder of the text. Presumably each event sequence corresponds to a single synoptic system.

Table 1 lists the dates of all events identified in this study. The number of event days varies strongly from one calendar year to the next. The distribution of event sequences taken from Table 1 is shown in Figure 5. Over the 33 year sample, one very active year (1954) and one completely quiescent year (1969) occurred. Between 2 and 8 event sequences occurred in 85% of the years. Interestingly, the active year (1954) was marked by a surprisingly regular sequence of event days with a typical interval of about one week.

Since a given calendar year contains the end of one winter and the beginning of the next, statistics for a particular year will tend to represent two successive winter seasons. A tally of number of events by individual winter seasons was also performed. The results, not shown here, give a distribution similar to that shown in Figure 5, with a secondary peak at high values (corresponding to the single year of 11 event sequences in Figure 5). The range is between 1 and 15 events per winter season, based on the 33 year sample.

Events by Time of Year

In order to distinguish possible systematic seasonal changes in activity, we have categorized each event sequence by the date of its start. Figure 6 shows the distribution for successive half-month periods during the winter season. The peaks and valleys at successive intervals are of uncertain statistical reliability, but the larger increase during March appears to be real. An immediate suspicion is that March would have increased events because of thunderstorms. However, the partial evidence discussed in the final section of this paper and recent experiences of "wave watchers" at the University suggest that this suspicion may be false.

A similar tally of events by half-month periods (not shown) gave a distribution in close qualitative agreement with that in Figure 6. The primary difference was the stronger increase in late March, indicating that this period is favored by event sequences rather than isolated events.

Events by Time of Day

Since static stability is known to influence the unstable generation and propagation of gravity waves, and since it undergoes diurnal variations near the surface, events were classified by their time of initiation. The results are shown in Figure 7. We see that there appears to be a significant diurnal variation with a maximum in the middle of the night. Interestingly, the intense fall of April 19, 1970 occurred at about 4 a.m. (CST) (Eom, 1972). Secondary maxima are found in the afternoon and evening, as might be expected if the events were influenced by convective activity.

Table 1

EVENT DAYS (month/day). Dates on which thunderstorms occurred (but not necessarily at the time of an event) are in parentheses for the periods 1940-1951 and 1965-1971. Thunderstorm occurrences are unknown for years 1952-1964 and 1972-1973.

1940: 2/9
1941: 1/11 12/25
1942: 1/10 (3/15) 3/16 12/14 (12/26) 12/27
1943: 1/20 1/21 1/22 1/24 (3/15)
1944: 2/22 (2/26) (3/14)
1945: 2/12 2/15 2/20 2/27 3/24 (3/25)
1946: (2/26) (12/27)
1947: 1/14 1/30 3/30
1948: 2/14 2/27 3/10 3/19 3/26
1949: 1/4 1/27 2/14 3/25 (3/31)
1950: (1/25) (3/26)
1951: 1/14 1/31 (2/28) 3/23 3/29 12/6 12/31

1952: 1/14 1/22 3/21 3/22 3/31 12/4
1953: 3/3 3/14 3/23
1954: 1/11 1/16 1/20 1/28 2/3 2/10 2/15 2/24 3/12 3/25 12/29
1955: 1/15 2/20 3/3 3/21 12/3 12/18 12/24
1956: 1/6 1/29 2/17 2/25 3/6 3/10 3/27 12/2
1957: 3/14
1958: 1/21
1959: 1/21 2/10 2/27 3/5
1960: 2/9 3/29 3/30 12/9 12/24
1961: 1/17 2/18 3/6 3/27 12/9 12/11,12 12/16 12/25
1962: 2/13 2/23 3/4 3/11 12/13 12/14
1963: 1/21 1/22 2/1 2/2 3/5 3/12 3/19 12/7 12/23
1964: 1/24 3/2 3/9 3/23 12/25

1965: 1/7 1/17 2/12 3/17 12/24
1966: (3/3) 3/21 3/23 (12/8)
1967: (1/24) 2/1 12/17 (12/20) 12/21
1968: 3/19 12/19 12/22
1969: no cases
1970: 1/25 12/19
1971: (1/3) 2/4 2/19 (2/22) (3/14) 3/15 12/10 12/15 12/30

1972: 1/6 1/16 1/19 2/23 3/2 3/12 3/24 12/28
1973: 3/13 (through 3/31 only)

PRESSURE EVENTS RELATED TO SYNOPTIC DATA FOR THE PERIOD 1940-1948

As utilized in the last section, the surface pressure signature is a primary tool for the initial identification of possible gravity wave activity. However, it is only the first step in a complete study of surface data. The surface wind direction and speed, for example, are of comparable interest because their variations are driven by the pressure gradient fluctuations. Unfortunately, these wind changes were not generally available on a continuous trace basis, although the times of sudden changes are noted in the observer's log. The gravity waves may also produce vertical motions which alter cloudiness or precipitation, which are thus potentially useful observables. However, they also suffer from being generally non-continuous. The precipitation associated with vigorous convection is also frequently associated with pressure and wind fluctuations which could be mistakenly attributed to gravity waves.

As an initial attempt to examine other synoptic data, we have examined reports of hourly averages of variables observed during pressure events at the surface for the period January 1940-December 1948. The one-hour interval was considered to be short enough to resolve most events. An analysis was made of 35 dates.

Thunderstorms

Climatological records indicated that thunderstorms occurred during 5 of the 35 event sequences. Thus, 86% of the sequences were caused by pressure fluctuations not associated with thunderstorms. The dates of pressure events with thunderstorms were (using month/day/year notation): 3/15/43, 2/26/44, 3/14/44, 2/26/46, 12/27/46. Only two thunderstorm events occurred during mid or late March. Thunderstorms then could not account for a March increase in total pressure events for this sample.

Wind Direction

Significant fluctuations in hourly mean wind directions were found in 13 of the 30 non-thunderstorm event sequences. These direction changes were almost equally divided between backing and veering. The predominant initial wind directions were from the NE, N, SE, and SW, with an average direction from the East.

Average Wind Speed

Of the 30 non-thunderstorm sequences, it was found that 7 had hourly average wind speed fluctuations with a range in excess of 5 knots. Also, 4 of the 7 dates experienced wind direction changes (see above). In many cases, the change was only slightly in excess of 5 knots. An event on 3/26/48 was an exception, the average wind speed increasing from 9 to 30 knots in one hour. Thus, typical events did not change the wind speed dramatically, but occasional events could.

Wind Gusts

Seven of 30 non-thunderstorm sequences were associated with wind gusts exceeding 20 knots. These were usually cases where the mean wind was strong; 4 of these 7 cases also experienced average wind speed changes (see above).

Cloud Cover

Of the 30 non-thunderstorm sequences, 9 were associated with changes in percent coverage of the sky by clouds. Only one of these (2/14/48) was associated with a fluctuating average wind direction. Four cases corresponded to clearing skies, 3 to increasing coverage, and 2 to a sequential combination of the two trends.

Precipitation

Ten of the 30 non-thunderstorm sequences were associated with changes in precipitation. Three involved the onset of precipitation, 2 the ending, 3 both the onset and ending, and 4 a change in form (liquid to frozen). Five of these ten sequences occurred when average wind direction changes were also noted.

CONCLUDING REMARKS

The results of this limited study suggest the following:

a) the great majority of pressure events in the winter season are related to gravity wave activity, rather than thunderstorms;

b) these events are often not isolated. They occur on the same date as one or more others;

c) on the average, an event of significant amplitude (2 mb in this study) will occur on one day per winter month in Madison, Wisconsin;

d) on the average, an event with amplitude in excess of 3.5 mb will occur only one day per winter season;

e) late March is the most likely time for an event during the winter season;

f) a marked diurnal cycle is evident, with most likely activity in the middle of the night, and least likely activity during the previous hours;

g) pressure events are often associated with changes in hourly wind vectors, especially when the wind initially has a significant easterly component;

h) most wind speed changes are on the order of 5 knots or less, but a few may be much larger;

i) some pressure events occur when the mean wind is strong and gusty;

j) some non-thunderstorm pressure events are associated with obvious changes in cloudiness, precipitation rate, or precipitation form.

Extensions of this study are needed to verify some of these points. Several alternatives immediately present themselves. First, work with single-station data could be extended. The hourly synoptic data for Madison could be investigated for the entire period and carefully compared with the continuous pressure trace. The study of continuous pressure traces could be extended back to the beginning of such records. Multi-variate statistical analyses could be used to isolate the primary inter-relations, and convective or frontal activity could be screened out. Continuous records of incoming radiation could be analyzed, especially for days of complete coverage by stratiform clouds.

Second, surface events could be analyzed for the areas surrounding Madison from hourly data at synoptic stations. The coherence of activity over meso- or sub-synoptic areas could be determined in this way and the propagation characteristics identified. On a smaller scale, a meso-network of micro-barographs could be very useful for circumventing the problem of spatial aliasing; a pilot project in the Madison area is already being conducted by members of the Meteorology Department. Another potentially rich data source is the records from the Midwest Tornado and Severe Storm observational program (Tepper, et. al., 1954).

Finally, the large-scale environment for the activity could be identified using soundings and upper and surface maps. As noted above, there are indications that surface low pressure centers to the south and west of Madison seemed to accompany those events and produce wind direction changes. This is consistent with the case study of Eom (1972) which showed the waves propagating northeastward from an approaching upper level jet. Such a study could give insight into the generation, propagation, and weather influence of these disturbances.

ACKNOWLEDGMENTS

This research was supported by NOAA Grant 1-36036 to the Space Science and Engineering Center and partially by National Science Foundation Grant GA-38811 to the Department of Meteorology. One of us (C.F.R.) gratefully acknowledges the support of a National Science Foundation Traineeship. Thanks also go to Professor Lyle H. Horn for his interest in this project.

REFERENCES

Eom, J., 1972: "Analysis of the Internal Gravity Wave Occurrence of April 19, 1970 in the Midwest," U. of Wisconsin, M.S. thesis, Dept. of Meteorology, 72 pp.

Tepper, Morris, 1954: "Pressure Jump Lines in Midwestern United States, January-August 1951," Weather Bureau Research Paper No. 37, U.S. Government Printing Office, Washington, D.C.

Uccellini, Louis W., 1972: "A Case Study of Apparent Gravity Wave Initiation of Severe Convective Storms," U. of Wisconsin, M.S. thesis, Department of Meteorology, 70 pp.

Young, J. A., Krishnamurti, T. N., and R. S. Lindzen, 1972: Dynamics of the Tropical Atmosphere (Notes from a Summer Colloquium: Summer 1972), National Center for Atmospheric Research, Boulder, Colorado, 587 pp.

Figure Legends

Figure 1. Examples of traces for each of 6 primary event types. Time interval (abscissa) is 2 hours, pressure interval (ordinate) is 2 mb. Type A: fall followed by no recovery. Type B: fall followed by partial recovery. Type C: fall followed by complete recovery. Type D: rise followed by no recovery. Type E: rise followed by partial recovery. Type F: rise followed by complete recovery. The percentage of events for each category during the years 1940-1973 (total of 209 events) is also indicated. (The example traces were selected from the years 1940-1953 only. They were chosen to illustrate the characteristic signatures, and do not necessarily represent non-thunderstorm events.)

Figure 2. Short-period component of pressure trace for 3/16/65 - 3/17/65 illustrating unsteady "train." Strong long-period fall has been removed by smoothing. Abscissa is marked at 2 hour intervals, ordinate in units of 1.0 mb.

Figure 3. A sampling of 5 non-thunderstorm traces for the years 1940-1950 and the trace of 4/19/70 studied by Eom (1972). Time interval (abscissa) is 2 hours, pressure interval (ordinate) is 2.0 mb. Note distorted scales for case of 4/19/70.

Figure 4. Histogram of number of pressure event amplitudes exceeding 2.0 mb at Madison, Wisconsin for the period Dec. 1940-March 1973.

Figure 5. Histogram of number of pressure event sequences per calendar year at Madison, Wisconsin during 1940-1973. Percentage refers to the 33 year period 1940-1973.

Figure 6. Histogram of date of initiation pressure event sequences for half-month intervals at Madison, Wisconsin during 1940-1973.

Figure 7. Histogram of hour of initiation (CST) pressure events at Madison, Wisconsin during 1940-1973.

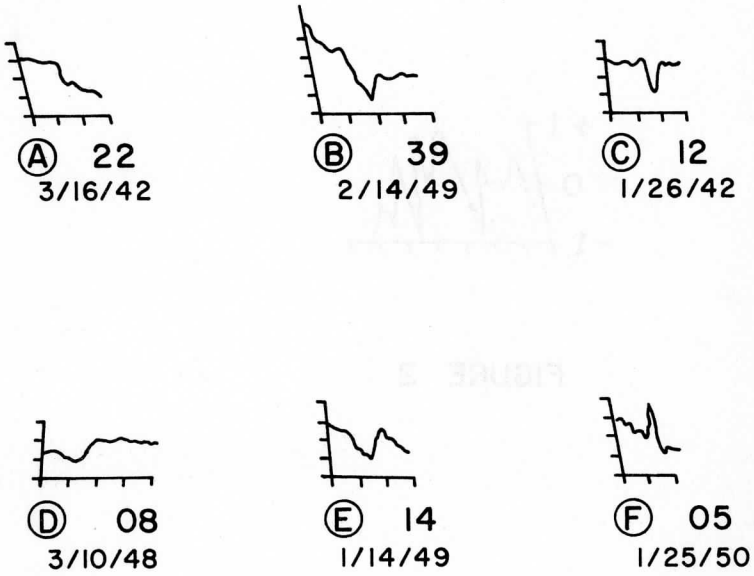

FIGURE 1

FIGURE 2

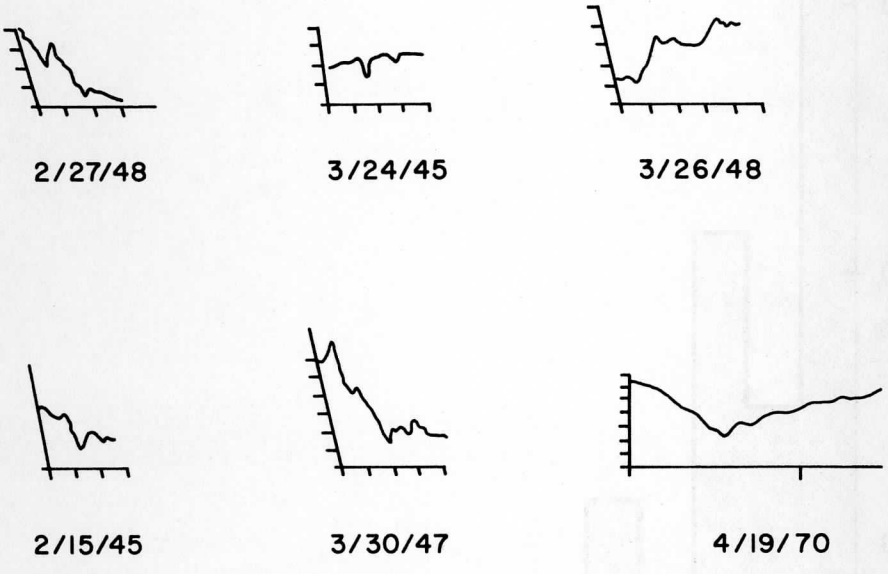

FIGURE 3

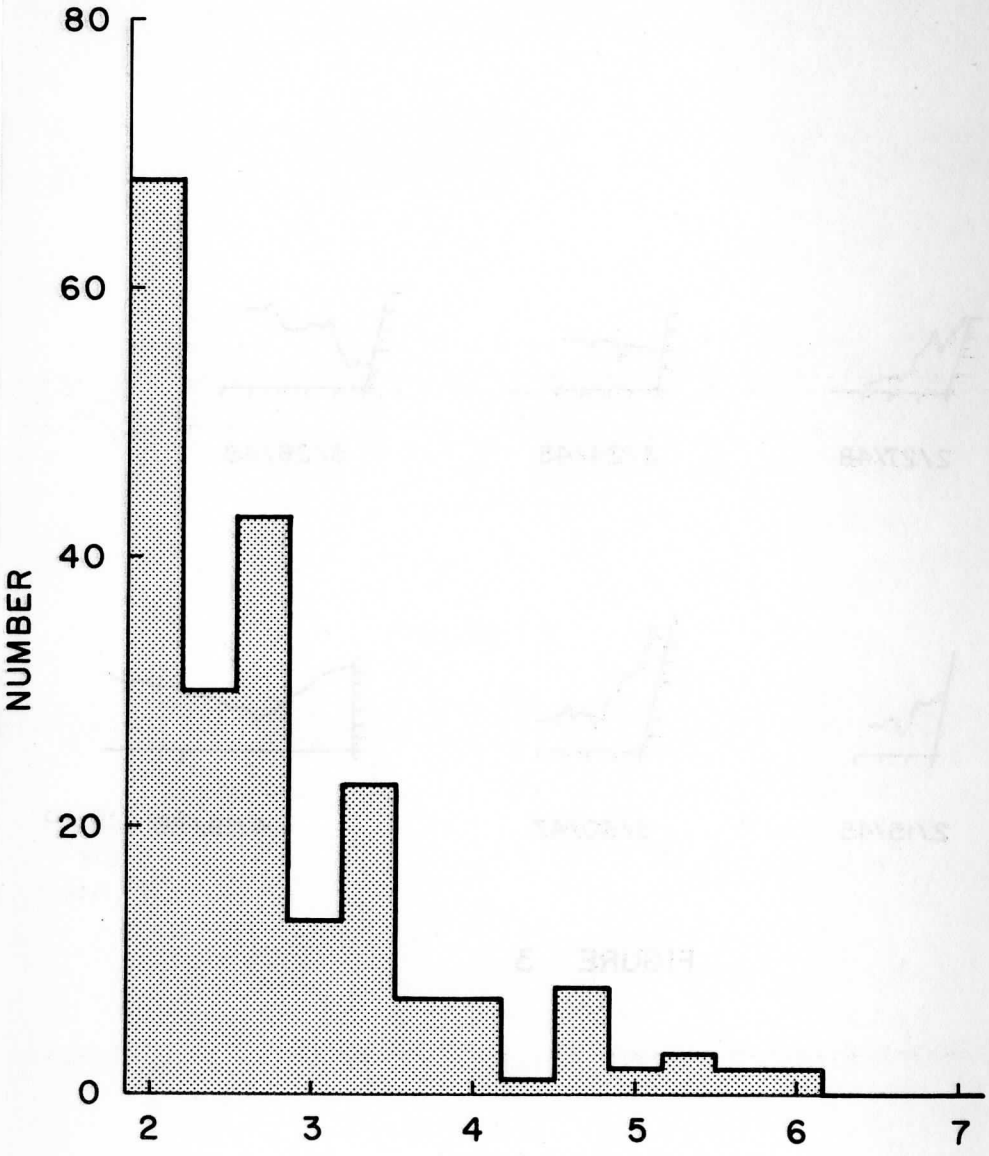

FIGURE 4

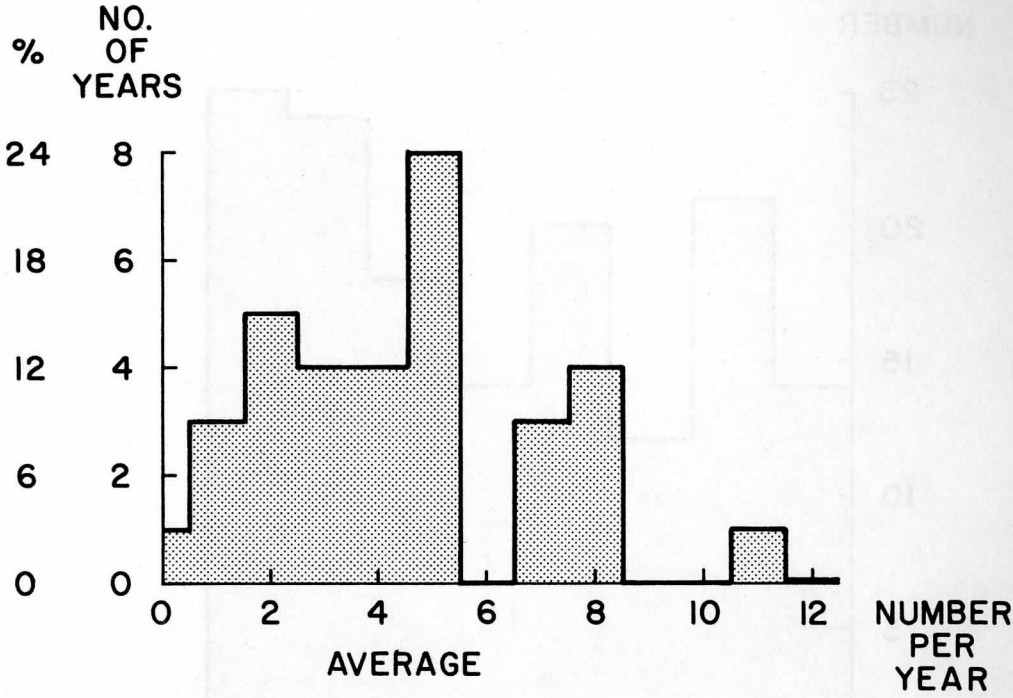
%
NO. OF YEARS
24
18
12
6
0
8
6
4
2
0
0
2
4
6
8
10
12
AVERAGE
NUMBER PER YEAR

FIGURE 5

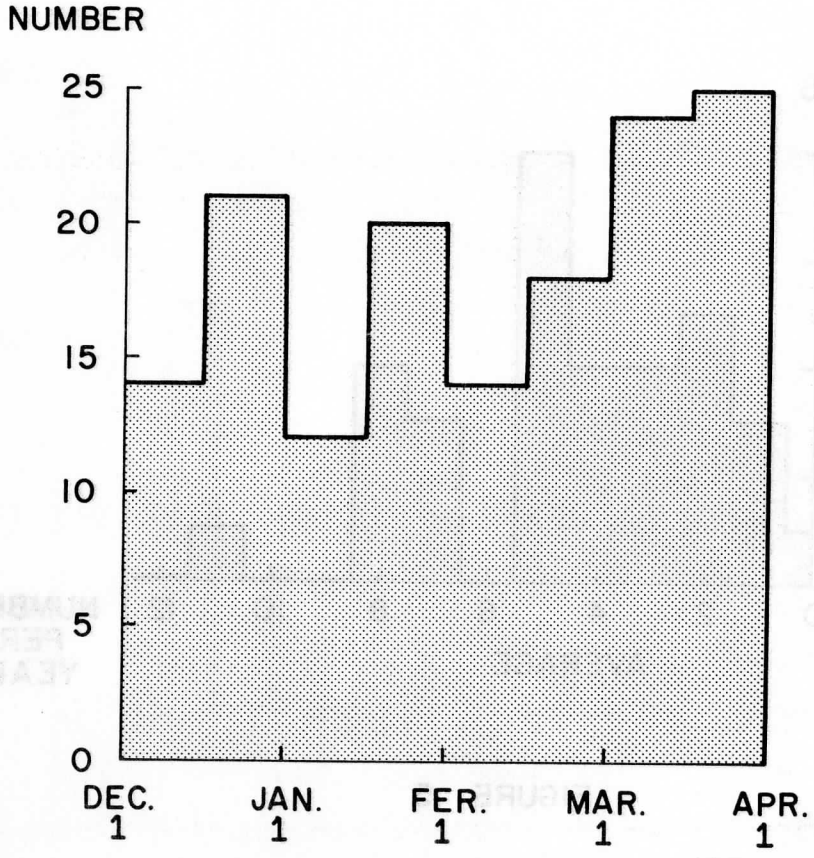

FIGURE 6

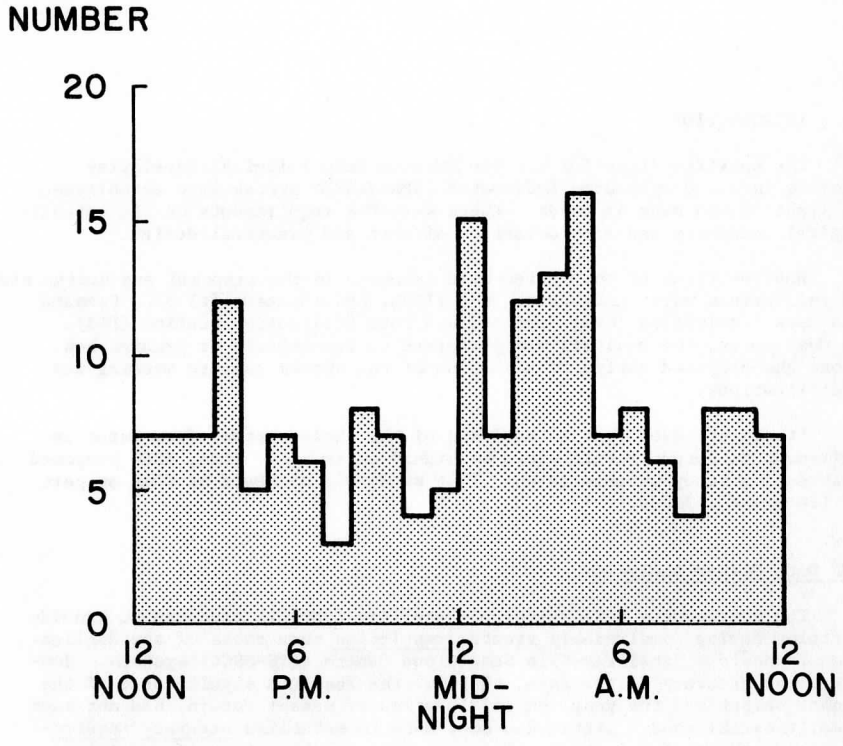

FIGURE 7

SMS DATA SYSTEM ANALYSIS-POSITION: A SUMMARY

Robert J. Parent

I. INTRODUCTION

The specifications for the Synchronous Meteorological Satellite-Visible Infrared Spin Scan Radiometer (SMS-VISSR) system were established in light of two sets of needs. These were the requirements of the meteorological community and considerations of cost and practical design.

Many portions of the system were examined in the proposal and design stages of the various major components, the VISSR, SMS (Spacecraft) S/C, Command and Data Acquisition (CDA) Station, and Data Utilization Station (DUS). In most cases, the analysis was performed to demonstrate or predict how close the proposed design of a section of the system came to meeting its specifications.

It was believed that an analysis of the whole system, from input requirement to output result, would be highly desirable. Thus, SSEC proposed that such a study be undertaken. That study was approved by NOAA as part of its grant 1-36036.

SMS Data System Analysis

The Synchronous Meteorological Satellite (SMS) is expected to provide pictures having considerably greater resolution than those of the Application Technology Satellite-Spin Scan Cloud Camera (ATS-SSCC) systems. However, the accuracy of the data, that is, the absolute significance of the sensor output and the geographical location of sensor return, had not been clearly established. Little had been done to establish accuracy requirements for the system in terms of permissible error content of satellite system output versus various data applications. Such analysis was needed to provide a basis for the development of SMS data processing systems, and for the delineation of possible mandatory modifications to the SMS hardware and software early in the process.

The data system error analysis was generally planned to proceed as outlined below:

a) Define the error categories and specify the permissible error magnitudes of the SMS-VISSR output. These depend on the particular objectives to be met by the data. For example, the acceptable image information from which cloud displacements for wind determination are to be obtained

will differ from the acceptable image information for cloud cover determination. Specifications for image information acceptability, therefore, are considered.

b) Generate a set of system/process chains in which each operation in the system affecting the data is identified and related to the entire system. An attempt has been made to identify all possible error sources in the process chain, although not every link will prove to be a source of error.

c) Estimate the probable error contribution at each link of the process chain, based on the best available information of system design and the state of the art. These errors were then accumulated realistically and compared to the allowable error in the final product. In cases in which it appeared that the probable error might significantly exceed the allowable error, further analysis was performed.

d) Examine the distribution of the allowable error throughout the process chain, recognizing the probable error at each link in the chain allowing the correction or elimination of any excess error at minimum cost. This part of the analysis aided in the identification of the course of action that would insure optimum data utilization and satisfaction of all data requirements.

II. METHOD OF ANALYSIS

Error Categories

There are three basic types of errors:

a) Bias errors (B). Bias errors are caused by many factors (offsets, levels, etc.) that do not change with time or position. If a means for bias measurement is available, then, in many cases, the error reduces to the residual uncertainty inherent in the measurement. In other words, if the offset, position, etc. are known by measurement, the bias may be classified as a departure from some reference or nominal value, but not as an error. Only the uncertainty of measurement is then classified as an error.

b) Systematic errors (S). These are errors which vary with position, time, temperature, etc., but in a predictable way. Again, the variations may be measured and the error reduced to only a measurement error.

c) Random errors (R). This type of error is usually the result of noise, nonsynchronous sampling, unpredictable events, etc. In general, these factors cannot be measured directly or conveniently. The effects of such errors may often be reduced by filtering, integration (smoothing), or averaging processes at appropriate positions in the system.

For each use of the data, however, there is a particular set of allowable errors. Once user requirements have been established, these can be

translated into the accuracy, resolution, stability, etc requirements on the system.

System Characterization

Systems are commonly described in general terms with the aid of a visual display, the block diagram. Additional details concerning the system requirements and performance are given in a set of specifications, usually accompanied by a brief written description of operation.

a) Conventional block diagram

Although a conventional block diagram is a valuable aid in understanding the overall system function and hardware, the diagram does not lend itself well to error analysis. It is difficult to combine blocks to show interaction or isolation, as the case may be, on a functional basis.

b) Function/Process chain

It is usually possible to restructure the system into functions, rather than into devices or components. With the system in this form, one can determine error magnitudes, control capabilities, and measurement accuracy related to the desired parameter.

An ideal function chain should be complete and rigorous, have functional relationships clearly and precisely presented, and be well documented. The chain should serve for all error analyses, regardless of the end use of the system output. Some links in the chain will not contribute error for a particular use. These links can be omitted from the analysis.

The function chain which has been established for the SMS-VISSR Data System is shown in Figure 2-1.

Error Determination or Estimation

Error determination often reduces to error estimation when dealing with a system, such as SMS, in the design and/or testing stage. As design, fabrication, and testing progress, the most realistic current values for performance are used to revise the error budget.

a) Sources of information

The sources of information on which the error values for this analysis were based include: NOAA/NESS SMS Documents; NASA/GSFC SMS Documents; SBRC VISSR Design Reports and Specifications; Philco Ford SMS Design Reports; Westinghouse Design Reports; meeting notes; personal contacts; personal experience. Specific data sources are referenced in the function error presentations.

b) Error information categories

In some cases, the error associated with a function, or resulting from an action will be considered as if it were independent of all other func-

tions. This might be called the raw error. This error may be modified by interaction, control, smoothing, correction, or following functions. An example is nutation error. This error would be intolerable if it were not for a passive nutation damper which reduces the error to a negligible level after a specified period of time. To give a better feel for error sources, the raw error will be indicated. The resultant error will also be given and used in the overall error evaluation.

As previously indicated, errors will be divided into three categories: Bias (B); Systematic (S); Random (R).

Data Referencing

Data sources will be referenced as part of the documentation for each function block.

Error Information Tabulation Format

In an attempt to compactly tabulate and categorize the errors associated with each function in the chain, the form shown in Figures 2-2 through 2-8 is used. Using this format, the function block is reproduced from the function chain, general comments are presented, the sources of error and control associated with the block are tabulated, the magnitude of the Y (perpendicular to scan) and X (along scan) error is shown, and reference sources are given. The errors are given in the most direct units in this tabulation. These units are angles for pointing, linear displacement for positions, time, etc. The goal for this position or pointing analysis is to reduce all errors to a common base which will specify the X and Y coordinates of each pictel in earth coordinates.

III. POSITION ERROR ANALYSIS

Position Accuracy Requirements

In this analysis we specify the position accuracy requirements as those established for the measurement of winds by the Global Atlantic Research Program (GARP). The GARP goal is to measure winds to an accuracy of two knots (± 1 meter/sec). If it can be assumed that the wind velocity is related in a known way to the velocity of certain specific types of tracer clouds in the wind field, then one can measure the wind by measuring the displacement of the clouds during a known time interval.

If one assumes that one frame of VISSR visible data is obtained every 30 minutes, then the displacement of a tracer cloud moving at 1 meter/sec from one frame to the next is 1800 meters. The IGFOV of the VISSR visible channel is 24 μr, which is subtended by approximately 900 meters at the subsatellite point.

Thus, one must be able to measure to one IGFOV relatively between two images if wind determination to 1 meter/sec. is to be made from data in adjacent frames. The goal, then is to have a relative position error of less than one IGFOV (25 μr).

Function Chain for Position Error Analysis

The function chain for position error analysis as developed from the SMS system is given in Figure 2-1. It is organized into three sections:

a) The left hand column forms a continuous chain for the signal. It enables convenient determination of the errors introduced in the VISSR optical and electrical system, the signal conditioning equipment in the S/C, and the communication link to the earth's surface.

b) The middle column, which consists of a much less coherent set of functions, shows the error contributions due to non-optical and non-signal electrical components. Included here are external disturbances, such as axis precession due to solar pressure, orbit inclination, misalignments, etc.

c) The right hand column includes the ground signal data processing and stretched VISSR retransmission functions as well as DUS functions. These functions are generally distinct from those of the first two columns.

Error Tabulation

The function chain of Figure 2-1 is broken down block by block in Figures 2-2 through 2-8. The general approach here is to show the function block, briefly outline the function and main conditions to be considered, list the error sources, then tabulate error magnitudes and type. This is followed by additional remarks and reference to the data source. As noted previously, this tabulation is in the most direct units, angles for pointing, linear displacement for position, etc.

Error Evaluation

Once the errors are tabulated, as in Figures 2-2 through 2-8, the next step in the procedure is to evaluate each of the error components to determine those with significant impact on performance.

In the case of bias and systematic errors, the absolute magnitude may not be the significant factor. If the uncertainty in the magnitude is known, then these types of errors reduce to a residual random error. It is this residual random error that is most significant. Many of the errors have only a random component. These must be considered along with the residual random errors to determine the total random error.

Upon examination of the tabulated errors, it was found that there were only a few individual residual error sources likely to exceed the allowable limits of one IFOV, 25 μr, 2.4 μsec, etc. Of these, a number are compensated for elsewhere in the system. Some examples of error compensation are:

a) The delay in sampling visible channel line elements, in a set of eight, because of sequential time sampling. This is later compensated for in the Synchronizer/Data Buffer (S/DB) in the CDA station.

b) Satellite location errors and attitude errors. These errors may be reduced by the use of landmark techniques in data processing. One of the most serious attitude error factors is precession due to solar pressure.

c) Spin rate changes, particularly after satellite eclipse. This error can be effectively removed in the S/DB at the CDA by proper spin period tracking.

IV. ERROR ANALYSES

A number of questions regarding the significance and interpretation of error values were raised as a result of this study. Specific analyses were made to answer these questions. The analyses evaluate the effect of a given error source, or combination of error sources, on position determination accuracy. They are presented as separate papers in this report. The following is a summary of their contents.

"Wind Errors Resulting from SMS Line Step Errors," L. Sromovsky.

The early specification and quoted value of the absolute line position error of the VISSR scan system was ± 40 μr, which is greater than one IGFOV (25 μr). This error value was based on uncertainty in the scan mirror line step encoder. As expected, the analysis showed the error to be serious. As a result of discussions among Santa Barbara Research Center (SBRC), NOAA and SSEC personnel, a method was devised for testing the line step encoder in a back-to-back mode. This test determined that the error was only ± 3.4 μr, rather than the ± 40 μr originally quoted. With this reduction in absolute error, the scan system error absolute line position error is well within acceptable limits.

"Line Start Errors in the SMS Line-Stretcher Timing System," L. Sromovsky.

The Line-Stretcher Timing System is nominally part of the Synchronizer/Data Buffer located at the CDA station. However, in reality, this subsystem is divided into three portions. One portion is in the SMS, another in the transmission link, and the third is in the S/DB at the CDA station. Thus the subsystem must be treated by considering all portions as a complete system.

Several analyses have been made of the portions and of the whole system based on individual error estimates. However, it was believed necessary to critically examine the bases of the error estimates and their reliability, update the estimates based on recent information, verify the analysis method, and then determine the best RMS line start timing error. The analysis concluded,

> Except for some minor inconsistencies, each major component of the SMS Line-Stretcher Timing System appears to be well defined in terms of its error contribution. Calculation, laboratory tests, computer simulation have been appropriately used to study each component. The estimate presented here, which is based on these analyses, indicates an RMS line start timing error

well below the 0.25 μsec previously specified.

The 0.25 μsec RMS error is quite acceptable.

"Effects of Equal Angle Resampling on Pointing and Cloud Displacement Measurement Accuracy," L. Sromovsky

Equal Angle (EA) resampling of the original Equal Time (ET) sampling of the VISSR video data on board the spacecraft is advantageous to the data user who requires pictorial output. However, there are problems for the user who needs measurements of winds from the motion of tracer clouds. This is due to the fact that the resampling process introduces a periodic variation in apparent position along a scan line which can produce non-random errors in the wind field.

This analysis evaluated the magnitude of the error and indicated the seriousness of its effect on wind determination. The results may be summarized as follows:

> Equal Angle (EA) resampling of S/C Equal Time (ET) samples introduces a relatively small RMS time jitter of approximately 0.3 μsec, resulting in an RMS position error of approximately 0.06 n. mi. at the subsatellite point. However, this error is not random along a scan line, but instead, displays a periodic variation that can lead to false indications of E-W convergence and wind shear.
>
> Equal angle resampling of visible and IR S/C equal time sample produces systematic sawtooth errors in timing (or position) along a line. The phase of this sawtooth error function is random from one line to another, except in the case of visible lines within the same group of eight (8), which have fixed relative phase relationships. The resulting displacement errors of clouds moving parallel to the scan lines have a square wave form along a scan line, and introduce systematic patterns of convergence and wind shear errors. Errors for clouds which also move normal to scan lines are not so systematic and require further analysis to determine what characteristic error patterns might exist.
>
> Preliminary results presented here indicate that EA resampling will not be a major problem in cloud displacement measurements. In practical situations (which need some kind of specification) it is quite probable that the variety of cloud sizes and motions will reduce the resampling error to the equivalent of a random uncorrelated error of 0.3 μsec RMS. This conjecture can be tested by computer simulation if necessary.

"SMS Spin Axis Attitude Error Estimate," E. Smith and D. Phillips.

> The technique used for determining SMS spin axis attitude parameters is similar to the SSEC multiple picture-single landmark approach which has been used with ATS-I and ATS-III since 1970. The basic approach [see "Geosynchronous Satellite Navigation Model," D. Phillips and E. Smith, this report, for the mathematical deri-

vation] requires the identification of a single recognizable landmark throughout a series of SMS image frames (T_1, T_2,...T_n) over a time period which is called t_n. The satellite line coordinate of the landmark is determined in each of the frames. With these measurements a spin axis loci configuration is determined. With three or more of these measurements, a least squares iterative solution of the satellite attitude can be obtained.

The results demonstrate two important facts. First, the error in determining attitude position is virtually invariant under the selection of a landmark location. This is an important operational consideration because the availability of landmarks varies greatly as a function of weather systems (cloudiness). Second, the accuracy of attitude determination is virtually invariant under the spin axis position itself (under normal conditions declination is the critical parameter). This demonstrates that we can safely use the landmark scheme if the spin axis declination has drifted from nominal position.

"The Effect of Parameterization Uncertainties on Wind Measurement," E. Smith and D. Phillips.

In this analysis, all the significant errors and uncertainties are combined to compute the expected position error. This is really the most meaningful analysis of the SMS data system analysis because it presents the probable error in nautical miles in both latitude and longitude directions for the major error components over a range of latitude-longitude combinations referenced to the subsatellite point. The individual errors are then combined to yield total error, both absolute and relative in nautical miles in the latitude and longitude directions at various latitude-longitude combinations.

The general conclusion reached in the analysis is that, within approximately 60° of the subsatellite point, one can expect relative wind measurements to within ± 1.0 meter/second (GARP requirement). The absolute location of the wind field (wind vector placement error) may not be specified as closely, and may depart from true location by as much as five nautical miles. In other words, the wind vector magnitude should be determinable to within ± 1.0 meter per second, but its acutal location may not be known to better than five nautical miles over the area corresponding to 60 degrees from the subsatellite point.

"Geosynchronous Satellite Navigation Model," D. Phillips and E. Smith

This paper is the result of work over a period of time in the general area of geosynchronous satellite navigation problems. The two preceding analyses required the use of the techniques developed in this paper and prompted the formalization of the procedures and their documentation. The paper is included here on its own merits, without further discussion, but with the expectation that those readers interested in the navigation problem will find it useful.

V. SUMMARY AND CONCLUSIONS

The analysis performed on the SMS-VISSR and CDA station combination indicates that potentially significant errors which contribute to pointing error can arise from many parts of the system. However, if the bias and systematic gross errors are known or can be measured, then the individual residual random errors are within reasonable bounds.

If one now adds a third element to the system--the use of landmark techniques in data processing for improved navigation--the pointing errors within 60 degrees of the subsatellite point yield absolute errors in position of less than five nautical miles and relative RMS error of less than 1.0 nautical mile.

If one now considers relative motion of tracer clouds in the determination of winds, then relative cloud position from frame-to-frame can be measured to 1.0 meter/second for frame-to-frame times of 30 minutes. The 1.0 meter/second (2 knots) velocity measurement capability meets the GARP requirement for wind determination.

Thus, it appears that, by using an auxiliary navigation and built-in attitude prediction method such as the landmark program as part of the data processing, the SMS-VISSR system should fulfill position accuracy specifications.

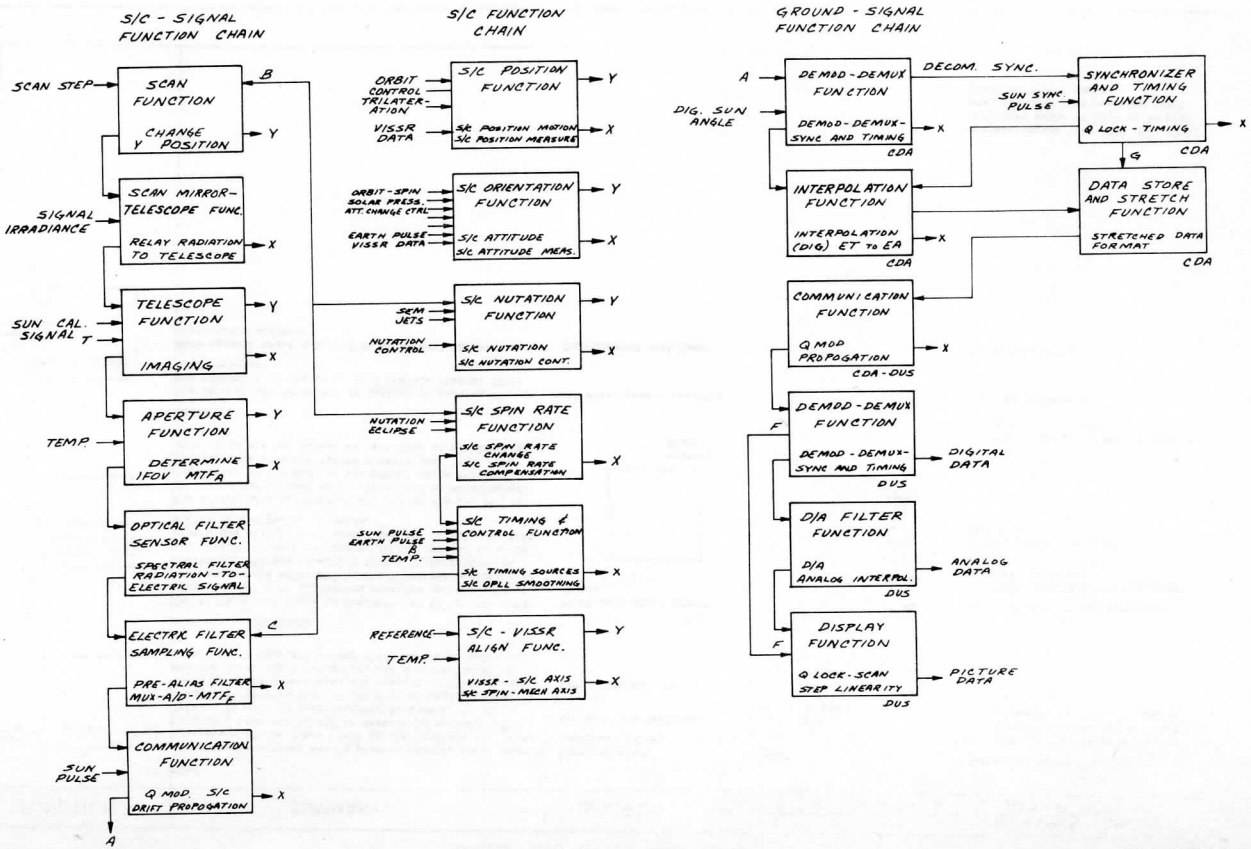
S/C - SIGNAL FUNCTION CHAIN
S/C FUNCTION CHAIN
GROUND - SIGNAL FUNCTION CHAIN
SCAN STEP
SCAN FUNCTION
CHANGE Y POSITION
B
Y
SCAN MIRROR-TELESCOPE FUNC.
SIGNAL IRRADIANCE
RELAY RADIATION TO TELESCOPE
X
TELESCOPE FUNCTION
IMAGING
SUN CAL. SIGNAL
APERTURE FUNCTION
DETERMINE IFOV MTFA
TEMP
OPTICAL FILTER SENSOR FUNC.
SPECTRAL FILTER RADIATION-TO-ELECTRIC SIGNAL
ELECTRK FILTER SAMPLING FUNC.
PRE-ALIAS FILTER MUX-A/D-MTFE
C
COMMUNICATION FUNCTION
SUN PULSE
Q MOD. S/C DRIFT PROPOGATION
A
S/C POSITION FUNCTION
ORBIT CONTROL TRILATER-ATION
VISSR DATA
S/C POSITION MOTION
S/C POSITION MEASURE
S/C ORIENTATION FUNCTION
ORBIT-SPIN
SOLAR PRESS.
ATT. CHANGE CTRL
EARTH PULSE
VISSR DATA
S/C ATTITUDE
S/C ATTITUDE MEAS.
S/C NUTATION FUNCTION
SEM
JETS
NUTATION CONTROL
S/C NUTATION
S/C NUTATION CONT.
S/C SPIN RATE FUNCTION
NUTATION
ECLIPSE
S/C SPIN RATE CHANGE
S/C SPIN RATE COMPENSATION
S/C TIMING & CONTROL FUNCTION
SUN PULSE
EARTH PULSE
B
TEMP.
S/C TIMING SOURCES
S/C DPLL SMOOTHING
S/C - VISSR ALIGN FUNC.
REFERENCE
TEMP.
VISSR - S/C AXIS
S/C SPIN-MECH AXIS
DEMOD-DEMUX FUNCTION
DEMOD-DEMUX-SYNC AND TIMING
CDA
A
DIG. SUN ANGLE
DECOM. SYNC.
SUN SYNC. PULSE
SYNCHRONIZER AND TIMING FUNCTION
Q LOCK-TIMING
G
INTERPOLATION FUNCTION
INTERPOLATION (DIG) ET to EA
DATA STORE AND STRETCH FUNCTION
STRETCHED DATA FORMAT
COMMUNICATION FUNCTION
Q MOD PROPOGATION
CDA-DUS
DEMOD-DEMUX FUNCTION
DEMOD-DEMUX-SYNC AND TIMING
DUS
F
DIGITAL DATA
D/A FILTER FUNCTION
D/A ANALOG INTERPOL.
ANALOG DATA
DISPLAY FUNCTION
Q LOCK-SCAN STEP LINEARITY
PICTURE DATA

FIGURE 2-1

SMS DATA ANALYSIS

FIGURE 2-2
issue page

FUNCTION	SUMMARY	SOURCE	Y B	Y S	Y R	X B	X S	X R	REMARKS AND REFERENCES
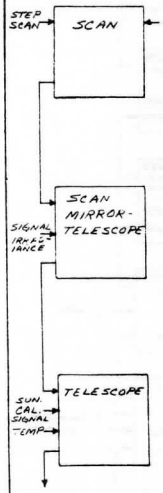	**SCAN** The scanning process should produce exactly equal angular increments of the image field in the latitude (Y) direction each time the mirror is stepped by command. The failure to move in equal angular increments is the result of imperfections in the digital angle encoder on the mirror shaft, stiction and run-out in the bearings and the servo-amplifier-motor, and noncoincidence of mirror minor axis and mirror shaft center of rotation.	Line position (absolute value) Line-to-line registration Line repeatability		±40* μr ±12 μr rms ±5 μr rms					These are expected values. SBRC, VISSR Design Objective Specifications, Rev.B. dated 17 March 71, Sheets 6 and 17.
	SCAN MIRROR-TELESCOPE The VISSR mirror plane is nominally at 45° to the telescope optical axis in midscan position and the axis of rotation should be at 90° to the telescope optical axis. The mirror mid-scan position is set by definition as that which yields a 90° change in the optical axis, to within one visible scan line. The associated line scan number is designated mid-scan. The mirror axis of rotation may not be exactly 90° to the telescope optical axis. This type of misalignment results in an E-W skew as the mirror scans N-S; the optical axis does not follow a meridional line. The scan lines are not tilted by this type of misalignment.	Pivot axis misalignment (skew) 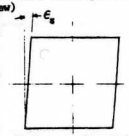					±1.28 mr (skew) ϵ_s ~500 μr 2σ IPOV		No rotation of frame-skew only. SBRC, Quarterly Report, Sept.70 Vol. 2, p. 6-21. Displacement E-W in 20° N-S Scan
	TELESCOPE The axis of the telescope is defined as passing through the mid point of the array of 8 visible channel fiber optic apertures. Misalignment might result from mechanical stresses or temperature effects.	Axis Misalignment (static) Misalignment with Temp.							SBRC, Quarterly Report, Sept.70 Vol. 2, p. 6-19 Zero by definition. To be determined.

*Communication from SBRC, May 1973, indicates value of ±3.4 μr as probable absolute line position error based on actual tests.

SMS DATA ANALYSIS

FIGURE 2-3
issue page

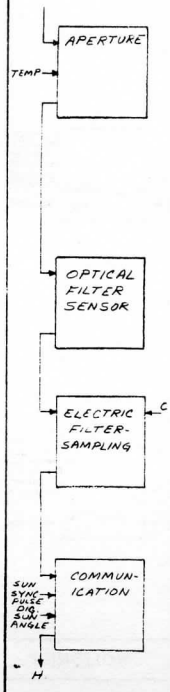

FUNCTION	SUMMARY	SOURCE	Y B	Y S	Y R	X B	X S	X R	REMARKS AND REFERENCES
APERTURE	**APERTURE** The apertures for the visible channels are formed by the ends of 8 fiber optics which terminate in the prime image plane. The center of the array defines the optical axis.	**Alignment of center of array**							**Zero by definition** **SBRC, Quarterly Report, Sept.70** **Vol. 2, p. 6-19**
	One error source is skew of the array which produces an X displacement from one aperture to the next.	Skew of array 				22 mr ϵ_v			Skew angle 22 mr max. SBRC, Quarterly Report, Sept.70 Vol. 2, pp. 6-19 and 6-20
	An additional error results if individual apertures within array are misaligned.					18 mr			Engineering Model Engineering Model Report, SBRC
	Because aperture is of finite size, field of view not infinitely narrow. Signal due to step irradiance is ramp rather than step. 50% point delayed approximately 1/2 dwell time from beginning of ramp, but coincides with irradiance transition.	Misalignment within array 							To be determined
	Temperature change may cause shift in aperture location. To be determined in test.						±1.8 μr		Engineering Model Engineering Model Report SBRC
		Aperture delay							
		Temperature effects							
OPTICAL FILTER SENSOR	**OPTICAL FILTER-SENSOR** This function, although vital to the signal chain, should not contribute to pointing error.								
ELECTRIC FILTER-SAMPLING	**ELECTRIC FILTER-SAMPLING** Pre-aliasing filter will introduce signal delay which should be constant, hence no frame-to-frame error.	Filter delay				2.0 usec			Approx. filter design not final
	Sampling of visible channels is at fixed rate of 500 kHz regardless of spin rate. Nonsynchronous sampling results in rms jitter of 0.1 usec or 0.05 dwell time at 100 RPM.	Sample time jitter						0.1 μsec	Philco Ford, Design Report C Vol. I, Book 1, p. 2-156
	Sampling of visible channels is sequential and produces effect of skewing 8 IGFOV within one VISSR IR scan line. The channels are sampled in 1.5 usec so maximum shift from channel 1 to 8 is 1.5 usec. Shift from array center is ± 0.75 usec. [Compensated for in Synchronizer/Data Buffer (S/DB) in CDA Station].	Sampling 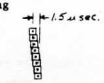					±0.75 usec		Referenced to center of array. Independent of spin rate. Philco Ford, Design Report C Vol. III, pp. 5-15 to 5-19
COMMUN-ICATION	**COMMUNICATION** The communication s-band subcarrier channel used to transmit the sun-sync pulse to the CDA station, adds noise and hence jitter to the pulse leading edge.	Added sun-sync pulse jitter						1.5μs rms	Philco Ford, Design Report C Vol.I, Book 1, pp.2-229 thru 2-234 Philco Ford, SMS-PCC-3452 pp. 3-5 thru 3-7
	The down link can produce bit errors in the digital sun angle word which has the effect of timing error.	Digital sun angle bit error jitter						0.2μs rms	Philco Ford, SMS-PCC-3452 SMS Sun-Pulse Timing Subsystem Analysis, J.H. Huang 1 Oct. 71 pp. ix and 3-21

SMS DATA ANALYSIS

FIGURE 2-4
issue page

FUNCTION	SUMMARY	SOURCE	Y B	Y S	Y P	X P	X S	X P	REMARKS AND REFERENCES
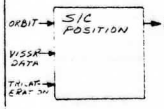	**POSITION** S/C position can be specified by x, y, z, or latitude, longitude and altitude coordinates. For position prediction one also needs to know the derivatives. The position of the spacecraft is not really the important consideration, but rather how closely we can measure and hence specify expected error. Here x, y, z are rectangular coordinates referenced to earth center. Equator in x, y, plane. Position measurement will be done by use of a Trilateration system. Accuracy in orbit sphere coordinates, derivatives and prediction have been estimated. The VISSR data itself will be used to determine position by use of landmarks.	Orbit sphere x, y, z, coordinate error (1σ) Short term 24 hour prediction Orbit sphere $\dot{x}$, $\dot{y}$, $\dot{z}$ velocity error (1σ) Short term 24 hour prediction Landmarks			$\frac{x,y,z}{1\sigma}$ 100m 1000m $\frac{\dot{x},\dot{y},\dot{z}}{1\sigma}$ 0.1 m/min 6 m/min ±0.2 Na.Mi.		0.01 Na.Mi.	±0.5 Na.Mi.	Note that earth sphere x_e, y_e, z_e, coordinate errors will be smaller by ratio of earth and orbit radii. Hughes Aircraft-GSFC Presentation, 22 Feb. 1972 Contract NAS5-21554 Hughes Aircraft-GSFC Presentation, 22 Feb. 1972 Contract NAS5-21554 At subsatellite point E.Smith and D.Phillips, The Effect of Parameterization Uncertainties on Wind Measurement. (Included in this report.)
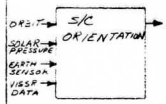	**ORIENTATION** S/C spin axis orientation is influenced by orbit inclination, precession due to solar pressure, action of control jets and motion of mass. Again, the fact that the axis may be shifted or shifting from some nominal reference is not important as long as the actual orientation can be accurately measured. The only error then is that of measurement. One needs to know the axis orientation with respect to a reference system and also the rate of change for prediction. At the present time there is only one axis attitude determining subsystem on the S/C, the earth sensors. The major cause of axis precession will be solar pressure. The rate of precession is a function of the time of year. One indirect method, use of the VISSR data in landmark program will be used. Other methods under consideration include a) Star pattern b) Interferometry	Orientation from earth sensor on S/C Precession rate Maximum Average Minimum VISSR-Landmark Stars Interferometry	0.1°	51 30 7 arc sec/day	0.02° combined YX combined YX			±0.5 Na.Mi.	After ground smoothing over one orbit for bias removal. Bias due to radiance variation. Philco Ford-SMS-PCC-3577, 9 Nov. 71. Drift in arc sec/day Philco Ford-SMS-PCC-3726 1 Dec. 71, p. 2 At subsatellite point. E.Smith and D.Phillips (see above) To be determined To be determined

SMS DATA ANALYSIS

FIGURE 2-5

ISSUE [illegible]

FUNCTION	SUMMARY	SOURCE	Y B	Y S	Y R	X B	X S	X R	REMARKS AND REFERENCES
VISSR, SEM, JETS, CONTROL → S/C NUTATION	**NUTATION** Nutation of S/C spin axis caused mainly by: (a) VISSR scan mirror motion (b) SEM motion (c) Control jets								
	Passive damper with time constant of 2 minutes will reduce nutation to 0.5 arc sec (2.42 ur) in time depending on magnitude of induced nutation. Nutation period ≃ 6 sec.	Normal operation-passive damper control		0.5 arc sec (2.4 μr)			0.5 arc sec (2.4 μr)		Nutation period ≈ 6 seconds Philco Ford-Quarterly Report 1 Oct. 71-31 Dec.71, dated 15 Jan. 72, p. 2-10
	Nutation maxima and time in minutes to damp to 0.5 arc sec. (a) Normal Mirror Scan — Max. Nutation Angle 0.48 arc sec — Time in Min. to Decay to 0.5 arc sec. - - - (b) Mirror Retrace 20X — 13.4 arc sec — 6.58 (c) SEM — 0.6 arc sec — 0.36 (d) Worst Jet Action (Inclination change) — 2.17 degrees — 19.3	Intermittent disturbances and decay times. (see table at left.)							
	Program non-VISSR disturbance around VISSR operation to avoid large nutation errors. Delay new VISSR frame for ≃6.58 minutes after retrace or accept greater nutation.								
VISSR, NUTATION, ECLIPSE → S/C SPIN RATE	**SPIN RATE** Spin period variations fall into two categories: (a) Long term-thruster operation--need not be included in error budget. (b) Short term.								
	Short term spin period changes of significance due to: (a) Scan mirror stepping	Period change in full frame due to scan mirror stepping					0.2 μsec		Philco Ford, SMS-PCC5825, 15 May 1973
	(b) Nutation and sun declination	Nutation and sun declination					∠+0.1 usec		For 0.5 arc sec nutation and max. sun declination Philco Ford-Design Report C Vol.I, Book 2, p. 4-28
	(c) Solar eclipse--Temp. change of S/C	Period change ΔTsp in usec in 30 min. from time t* after leaving eclipse 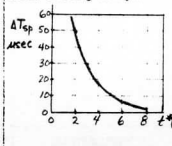					2.4 μsec (t*=8 hrs)		Warm up time constant, 2= 2 hrs. ΔTsp in 30 min.,8 hrs. out of eclipse. (Max. eclipse case). Philco Ford, Design Report C Vol.I, Book 2 pp. 4-26, 4-27
	Average spin period over 8 visible lines can be measured at CDA station from synchronizer data to within 0.05 usec.	Avg. spin period over 8 visible lines						0.05 μsec	Westinghouse, S/DB Design Plan Oct. 71, p. 2-70

SMS DATA ANALYSIS

FIGURE 2-6
issue page

FUNCTION	SUMMARY	SOURCE	Y B	Y S	Y R	X B	X S	X R	REMARKS AND REFERENCES
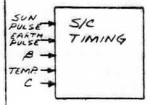	**S/C TIMING** There are three basic timing sources in S/C. (a) 14 MHz bit rate clock also divided down to 3.5 MHz for sun pulse to word zero decom sync time measure, and to 500 kHz for VISSR video sampling. (b) Spin clock locked to sun or earth pulses which divides S/C rotation into a fixed number of intervals independent of spin rate. (c) Conditioned sun pulse (sun-sync pulse). Errors (a) Bit rate clock--stability--short term (linetime) Long term stability not an error source since osc.at CDA station locked to osc. in S/C with phase lock loop.	Short term stability (line time)					0.25 usec	Short term--within a line. Westinghouse, Sync./Data Buffer Design Plan, Oct.71, p.2-63
	(b) Quantization error of sun-sync pulse leading edge to word zero decom sync interval using 3.5 MHz clock.	Quantization					0.08 usec	Philco Ford-SMS-PCC-3452 1 Oct. 71, p.3-19
	(c) Sun-sync pulse leading edge jitter due to noise and level selection.	Sun-sync pulse jitter					1.0 usec	Philco Ford-Design Report C Vol.III, p. 4-4
	A note on spin clock: The spin clock has a resolution of approximately o.2° and absolute accuracy of only ± 0.5°. It is used in VISSR system timing to initiate start of video data multiplexing and decom sync, but not line start timing. Line start timing established at CDA station.							
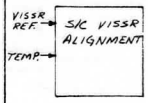	**S/C VISSR ALIGNMENT** Three S/C VISSR alignment error sources exist. (a) VISSR optical axis to VISSR external reference alignment mirror.	VISSR to reference Latitude shift Skew		±0.01 mr			±0.01 mr	Skew only--no rotation SBRC, VISSR Quarterly Report Sept. 70, Vol.2, p. 6-21
	(b) VISSR reference to S/C principal axis	VISSR reference to S/C principal axis Latitude shift Skew		0.1°			0.1°	Worst case. To be measured after assembly. In flight accuracy not known. Philco-Ford-SMS-PCC-3577, 9 Nov71
	(c) S/C spin to S/C principal axis	S/C spin to principal axis Latitude shift Skew		0.12°			0.12°	Estimated. Accuracy of determination from measurement to be established. Philco Ford-SMS-PCC-3577 9 Nov.71.
	Final values will have to be deduced from in orbit operation. Long term data analysis required. Accuracy capability to be determined.							

SMS DATA ANALYSIS

FIGURE 2-7
issue page

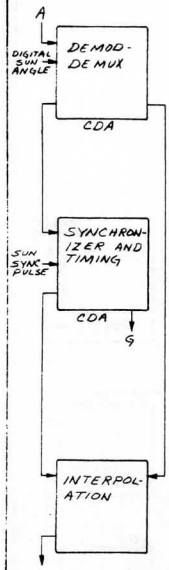

FUNCTION	SUMMARY	SOURCE	Y B	Y S	Y R	X B	X S	X R	REMARKS AND REFERENCES
	DEMOD-DEMUX								
	The signal is demodulated and then demultiplexed from timing supplied by a bit rate locked oscillator and sync provided in the bit stream.	Bit timing							Westinghouse-S/DB Design Plan.
	The bit rate locked loop provides the bit timing and also a 3.5 MHz signal by division which is locked to the 3.5 MHz in the S/C which was used to determine the digital sun angle.	3.5 MHz clock							
	Digital sun angle transmitted as 8LSB of equivalent 22 bit word.	Digital sun-angle quantization timing error						0.08 usec	Westinghouse-S/DB Design Plan, Oct. 71, p. 2-16
	SYNCHRONIZER AND TIMING								
	Receives sun-sync pulse, decom-sync and 3.5 MHz clock. Measures interval between ground sun-sync and decom-sync. compares with digital sun angle from S/C. Phase lock loop drives to equal sun angles and phases to sun-sync pulse. Output from synchronizer provides equal angle (EA) sampling. Also provides other timing to strobe stretched data out of storage.								
	Smoothing provided by phase-lock-loop (PLL) reduces regenerated sun pulse jitter to less than 0.25 usec.	Regenerated sun pulse jitter						0.25 usec	During normal VISSR scan. Westinghouse-S/DB Design Plan Plan, Oct. 71, p. 3-6
	Line start produced by proper B delay from regenerated sun pulse.	Line start jitter						0.25 usec	During normal VISSR scan Westinghouse-S/DB Design Plan, Oct. 71, p. 3-6
	INTERPOLATION								
	Digital interpolation is performed on the equal time (ET) data from the S/C and then resampled at equal angle (EA) independent of spin rate. Contemplated interpolation methods will provide augmentation of data by generation of linearly interpolated value midway between original values. Resampling at EA now done by choosing nearest sample.								
	This procedure produces effective time jitter in samples from ET samples 1 usec apart.	Resampling time jitter						0.3 usec	rms jitter due to resampling Westinghouse, S/DB Design Plan, Oct. 71, p. 2-26
	Another phenomena that results from resampling when the periods for ET and EA sampling are not equal, and original samples must be omitted or repeated, is a beat at the difference frequency. This can cause varying time and apparent position modulation across a scan line. The max. modulation amplitude can reach 1 usec. The effect may produce an artificial wave motion in position.	Resampling time modulation						±1.0 usec	For augmented sampling (1 usec interval).
	Further analysis by L. Sromovsky, SSEC, shows the error due to all sources in the interpolation process to be well within acceptable limits.							0.3 usec	L. Sromovsky, Effects of Equal Angle Resampling on Pointing and Cloud Displacement Accuracy (Included in this report).

SMS DATA ANALYSIS

FIGURE 2-8
issue page

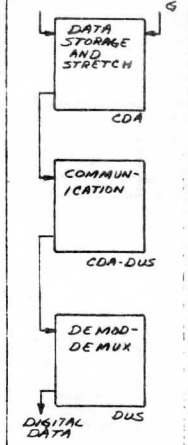

FUNCTION	SUMMARY	SOURCE	Y B	Y S	Y R	X B	X S	X R	REMARKS AND REFERENCES
DATA STORAGE AND STRETCH	**DATA STORAGE AND STRETCH** Data from 8 visible channels routed to 8 buffers during line scan and then strobed out between scans at lower rate (stretched) for retransmission to DUS via SMS. Line sync and other documentation included. No additional timing error should be introduced by this function.								
COMMUNICATION	**COMMUNICATION** Noise and random delays may be added in the transmission process. Estimated jitter due to propogation.	Time jitter due to propogation.						0.2 usec	
DEMOD-DEMUX	**DEMOD - DEMUX** Bit carrier is phase-locked and signal demodulated to produce bit stream. Demultiplexer sorts out channels and delivers digital data.	Timing jitter							To be determined.

WIND ERRORS RESULTING FROM SMS LINE STEP ERRORS

L. A. Sromovsky

INTRODUCTION

If SMS specifications (SBRC, VISSR Design Objective Specifications, Rev. B, 17 March 1971, sheets 16 and 17) are truly descriptive of actual line step errors, wind determinations made from SMS image data can contain errors in the North-South wind component which greatly exceed the GATE requirement of ±1.5 m/sec. In addition, the line step error component, responsible for the large displacement error, is non-random in nature and cannot be removed by local spatial averaging. Thus, it appears essential either to measure this non-random component for each line step position or to determine by some other means that the actual non-random stepping error is within acceptable limits. The alternative method could be encoder-encoder comparisons. And there is reason to believe that the encoder performance is much better than that indicated by the specifications. (1)

STEPPING ERRORS ALLOWED BY SPECIFICATIONS

The line step error specifications are:

a) absolute value of line position: ±40μr (1)

b) frame to frame line repeatability: ±5μr RMS

The second error is approximately 0.2 IFOV (visible) and is a tolerable error level for wind determinations. The first error is approximately 1.6 IFOV (visible) and is by far the largest single error in the SMS system. However, its precise effect on displacement measurements depends strongly on its variation with line number. A diagram of one possible type of line step behavior is presented in Figure 1. Neglecting the 5μr repeatability error, the angular stepping error is the same for all frames. It is shown as a solid line which does not exceed the bounds of ±40μr. The line chosen is only an example of behavior allowed by the specifications and does not represent any measured results.

CLOUD DISPLACEMENT ERRORS RESULTING FROM NON-RANDOM LINE STEP ERRORS

Consider two clouds A and B in two successive SMS image frames. If their line positions are denoted by $L_{A,1}$ and $L_{B,1}$ in the first frame and $L_{A,2}$ and $L_{B,2}$ in the second frame, then the apparent frame to frame N-S displacements of these clouds are given by

$$L_{A,2} - L_{A,1} = \Delta L_{S,A} + \varepsilon(L_{A,2}) - \varepsilon(L_{A,1}) + \Delta L_{C,A}$$

$$L_{B,2} - L_{B,1} = \Delta L_{S,B} + \varepsilon(L_{B,2}) - \varepsilon(L_{B,1}) + \Delta L_{C,B}$$

Here ΔL_S is the displacement caused by motion of the earth in the satellite coordinate frame (removable by proper navigation techniques), ΔL_C is the true cloud displacement relative to the earth's surface, and $\varepsilon(L)$ is the absolute line step error at line L (Figure 1).

The relative frame to frame displacement error depends on the combined total of cloud and earth motion in the data frame as well as on the local slope of the line step error curve. Two extreme cases are shown in the diagram (Figure 1). The A cloud displacement error is approximately 80μr, while the B cloud displacement error is approximately 5μr. For a 30 minute interval between frames, and for clouds near the subsatellite point, this leads to velocity errors (in the N-S component) of 2.9 m/sec and 0.4 m/sec respectively. The first example is considerably outside the error range of ±1.5 m/sec acceptable for GATE.

Not only is this line step error a possible source of large displacement errors but, in addition, the errors produced cover entire latitude bands. They are thus not removable by simple (local) averaging techniques. The systematic errors can result in bands of false convergence and divergence which, because the errors depend on apparent earth motion in the frame, have a diurnal variation and a dependence on the magnitude of the N-S wind component.

RECOMMENDATIONS

To permit reliable and accurate cloud displacement measurements (and inferred winds) from SMS image data, more information about line step errors is required. An investigation to answer this sequence of questions is recommended:

(1) Is the absolute line step error as large as that allowed by specifications, or is it negligible? According to Gary Barnett of SBRC, it is possible that absolute encoder accuracy is as good as frame to frame repeatability (≃ 5μr).

(2) If the absolute (non-random) stepping error is not negligible, what is the approximate error power spectrum (with line number as the frequency variable)? If it is possible to determine that existing errors have periods (in line number) much greater than the maximum target motion within the frame, then there is no likelihood of serious relative displacement error.

(3) If the absolute error in stepping, as shown by the error power spectrum, is at high line frequencies, what is the absolute angular position of each of the 1821 steps?

The first two questions probably can be answered easily by measuring the signal output of the redundant VISSR encoder while the primary encoder is used for stepping. By comparing the two encoders (which are mounted facing each other) in this way, it should be possible to detect absolute error differences between them. It should also be possible to obtain ap-

proximate estimates for the characteristic magnitudes and line frequencies of the errors, should they turn out to be significant. (1) If the errors are large and of high frequency, it is then necessary to measure by other means the precise (within ± 5μr) angular position of each of the 1821 steps.

---

(1) This test, originally suggested by Gary Barnett of Santa Barbara Research Center, was subsequently made by SBRC. The test results (Kenneth A. Shamordola, "VISSR Scan Mirror Encoder Back-to-Back Accuracy Test," Santa Barbara Research Center, Goleta, California, May 1973) show an RMS angular difference of approximately one arc sec. This suggests that the absolute accuracy of a single encoder is within 0.707 arc sec RMS (≈ 3.4 μ radians) which is more than 10 times better than the original specification of ±40μ radians. Thus, wind accuracy will not be degraded by absolute line step errors.

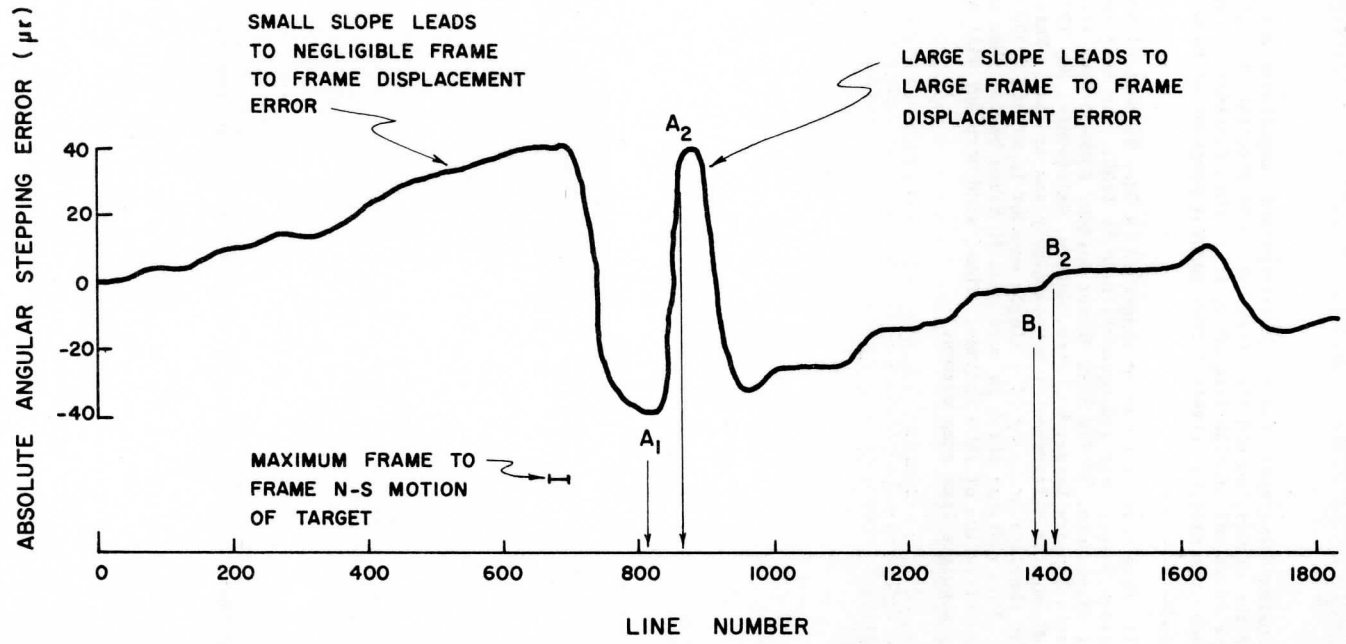

Figure 1

An example of line step error behavior allowed by SMS specifications. Line positions of example cloud targets are indicated by A_1 and B_1 in frame 1 and A_2 and B_2 in frame 2.

LINE START ERRORS IN THE SMS LINE-STRETCHER TIMING SYSTEM

L. A. Sromovsky

1. INTRODUCTION

Current estimates of SMS Line-Stretcher timing errors indicate that line start timing is sufficiently precise (less than 0.25 μsec RMS error) to cause no significant problems in cloud displacement measurements. However, the extreme importance of line start timing requires a critical review of current error estimates to establish their reliability. This paper, which must rely to a large extent on work done by Philco-Ford and Westinghouse, is a partial fulfillment of that requirement.

Except for some minor inconsistencies, each major component of the SMS Line-Stretcher Timing System appears to be well defined in terms of its error contribution. Calculation, laboratory tests, and computer simulation have been appropriately used to study each component. The most recent estimate based on these analyses indicates an RMS line start timing error well below the 0.25 μsec previously specified.

2. TIMING SYSTEM OPERATION

The SMS Line-Stretcher timing system is diagrammed in Figure 1. All timing information is derived from the output of the sun sensor on board the spacecraft, producing one trapezoidal pulse per SMS rotation. The signal conditioner detects the time location of the leading edge of this pulse and creates two new pulses to specify it. These are an analog sun pulse, transmitted to the ground and used for coarse tuning of the Command and Data Acquisition (CDA) Phase Lock Loop and a sun synch pulse, used to turn on a spacecraft (S/C) 3.5 MHz counter. At a later time determined by the S/C spin clock, a DECOM SYNC pulse turns off the S/C counter and is simultaneously transmitted to the CDA station. The contents of the S/C 3.5 MHz counter are transmitted to the ground as the S/C DIGITAL SUN PULSE. This contains the 8 LSB (Least Significant Bits) of the number of 3.5 MHz clock pulses during the time interval between the SUN SYNC PULSE and DECOM SYNC PULSE.

In similar fashion, the time interval between the smoothed SUN SYNC PULSE output of the CDA DPLL (Digital Phase Lock Loop) and receipt of the DECOM SYNC PULSE is measured by a CDA 3.5 MHz counter. The difference between this CDA DIGITAL SUN PULSE and the S/C DIGITAL SUN PULSE is the error signal used to provide phase and frequency corrections to the DPLL. The parameters A and B are adjustable and control the loop bandwidth.

The basic DPLL clock frequency depends on spin rate since it is adjusted to produce a constant number of counts per SMS rotation. (At 100 RPM the synthesizer frequency is 5.2416 MHz). The SUN ANGLE COUNTER (SAC) counts up to M = 3144960 at a rate determined by the synthesizer frequency and then recycles. The DPLL smoothed sun sync pulse output occurs when the SAC reaches zero. This pulse turns on the 3.5 MHz CDA counter and also determines line start timing.

The DPLL output is a smoothed SUN SYNC pulse which is aligned to the mean leading edge of a sequence of sun sensor pulses. In addition to reducing the time jitter of the sun sensor output by averaging, the DPLL must also track variations in spin rate which occur during forward mirror stepping, retrace, and after eclipse. Because low RMS noise and accurate spin rate tracking (low bias noise) are somewhat contradictory requirements, optimum choices of the loop parameters A and B must be made for each situation.

3. SMS LINE STRETCHER TIMING ERRORS

Three factors affect the timing error in the DPLL output: (1) noise in the sun sensor and signal conditioner electronics; (2) errors in communicating the sun pulse location to the CDA station; and (3) limitations in DPLL performance.

1. Sun Sensor and Signal Conditioner Errors

A functional diagram of this system is presented in Figure 2. Operation of the system can be described best by quoting from Vol I, Book 2, Phase C Design Report, Philco Ford, 30 June 1971 (p. 14-3):

> The sun sensor consists of a light sensitive diode which is illuminated by the sun once per spacecraft revolution. The width and amplitude of the output current pulse are functions of the angle of the sun with respect to the spacecraft longitudinal axis. A preamplifier located in the sun sensor assembly converts the current pulse to a voltage pulse. This is accomplished at the sun sensor in order to minimize the effects of the noise picked up by the sun sensor to Attitude Determination and Control (ADAC) electronics wiring, and the equivalent input noise of the various amplifiers located in the signal conditioner assembly. The bandpass filter serves the dual purpose of reducing the signal noise bandwidth and eliminating the effect of preamplifier offset voltage drift. The peak signal voltage detector output, when divided in half, establishes a switching reference for the sun sync and sun angle comparators.
>
> The leading edge of the sun sync comparator output pulse establishes a precise spin period reference while the width of the sun angle comparator output pulse is proportional to the

spacecraft-to-sun angle. The effects of sun sensor thermal change are eliminated by the use of a peak detector for establishing threshold reference.

The time location of the 50% point of the sun sensor signal corresponds to the SUN-SYNC PULSE output of the threshold detector. The time jitter in the SUN SYNC PULSE is equal to the combined SUN SENSOR signal noise and threshold reference noise divided by the slope of the sun pulse at the 50% point (all quantities measured at the threshold detector input). Using a worst case slope of 2.4 mV/μsec and a requirement of 1/3 μsec RMS time jitter, Philco-Ford established a total noise budget of 678 μV at the threshold detector. Combining the effects of sun sensor noise, preamp noise, bandpass filter noise, peak detector and low-pass filter noise, threshold detector noise, spacecraft harness noise, and gain variation (some quantities measured and some estimated), they concluded that the system noise would not exceed the specified budget. Philco Ford also conducted laboratory tests on the sun sensor signal conditioner and preamplifier circuits using a simulated sun sensor input pulse. Results showed a probable RMS time jitter of 0.330 μsec and a worst case RMS jitter of 0.38 μsec (Philco-Ford, Phase C Design Report, Book 2, Vol.I, 30 June 1971, p. 14-17). A later SMS Error Budget up-date (Philco Ford, SMS-PCC-3577, 14 February 1972), indicated an RMS time jitter of 0.343 μsec and a DC offset error of 0.0292 μsec.

2. Communication Errors

The information which must be communicated to the CDA station DPLL is the time difference between the S/C SUN SYNC pulse and the DPLL output. The actual difference is between two digital 3.5 MHz counters, one on the S/C and one at the CDA station (see Figure 1), both turned off by the DECOM SYNC pulse. Errors produced in communicating this difference are:

(a) Quantization Errors: These result from the measurement of continuous time variables in discrete units [(1/3.5 MHz) = 0.286 μsec]. The combined counting error of S/C and CDA sun angle counters was computed by both Westinghouse and Philco-Ford, under what appear to be identical assumptions. However, Westinghouse (Synchronizer Data Buffer [S/DB] Design Plan, Oct. 1971, p. 2-61) derives an RMS counting error of 0.117 μsec, while Philco-Ford (TM #204, SMS-PCC-3452, SMS SUN-PULSE TIMING SUBSYSTEM ANALYSIS, J. Y. Huang, Oct. 1971, p. 3-19) obtains an RMS counting error of 0.202 μsec. At present, information to explain this difference is not available. It should be noted that a later Philco-Ford update of the SMS error budget (SMS-PCC-3577, 14 February 1972) maintains the 0.2 μsec RMS counting error.

(b) Frequency Errors: These arise if the S/C and CDA station 3.5 MHz clocks do not have precisely the same period. Westinghouse (S/DB Design Plan, Oct. 71, p. 2-61 and 2-62) allocated 0.3 μsec RMS timing error to this source. They estimated equal contributions from short term drift of the S/C oscillator and from CDA tracking loop errors

(the CDA oscillator is locked to the S/C oscillator by a PLL). The Philco-Ford group does not explicitly include frequency errors in its timing error analysis. They state no reason for this omission.

(c) Bit Errors: In the S/C - CDA station transmission link, bit detection errors can cause an effective timing jitter in the digital sun pulse. The RMS value of this jitter depends on the number of bits in the data word and the probability (p) that one bit of data is erroneously detected. Huang (SMS-PCC-3452) found the RMS timing error to be $\sqrt{p}$ x 59.6 μsec. With a bit detection error probability of 10^{-5}, the resultant RMS timing error turns out to be 0.188 sec. Incredibly, Westinghouse finds a linear dependence on p and estimates an RMS timing error of 0.042 μsec for $p = 10^{-3}$.

Using the largest estimates for each of these sources, we may estimate an RMS communication timing error of $[0.2^2 + 0.3^2 + 0.19^2]^{1/2} = 0.408$ μsec. A later Philco-Ford update of the SMS Error Budget uses $[0.2^2 + 0.19^2]^{1/2} = 0.276$ μsec for the total RMS communication error.

3. Limitations in DPLL Performance

The basic task of the DPLL (Digital Phase-Lock Loop) is to track the real variations in spin rate (signal) and, at the same time, to smooth the false variations due to sun pulse time jitter (noise). The primary sources by signal variations can be summarized as (N. Furomato, "Inputs to Line-Stretcher Timing System", SMS-PCC-1669; May 20, 1971):

(a) Thermally Induced Moment of Inertia Change Due to Eclipse. Two hours after eclipse the differential spin period change is 30 μsec per frame. This change decays exponentially in time with a two hour time constant. The change is less than 1 μsec ten hours out of eclipse.

(b) Stepping of an Unbalanced Scan Mirror. This causes S/C moment of inertia changes during each frame and results in a continuous spin rate change (linear in time) during normal scanning. This is followed by an equal but opposite net change during retrace. Estimates for the peak to peak variation during a frame span the range from 0.25 μsec (SMS-PCC-1669, May 1971) to 4.5 μsec (SMS-PCC-3452, Oct. 1971), depending on the assumed scan mirror imbalance. (Actually the 4.65 μsec estimate appears to be an error.) The most recent estimate (SMS-PCC-3577, Feb. 1972) is 2.33 μsec, assuming a dynamic imbalance of 7.08 lb-in^2.

(c) Nutation Due to Scan Mirror Stepping. Even if the scan mirror is balanced, reaction torque produced during scan mirror stepping causes the S/C spin axis to wobble (nutate). This causes an apparent periodic variation in spin period which is, nevertheless, considered as signal because both the sun sensor and the VISSR are similarly affected, that is, nutation causes no apparent change in the angle between sun sensor and VISSR look directions. Under steady state assumptions, continuous mirror motion instead of the actual step and stop motion, the apparent spin period variation is periodic. It has

an amplitude of 0.06 μsec (0.52 μsec during a two minute retrace) and a period of six seconds. Although the nutational transient was considered to be a possible source of significant error (Westinghouse, S/DB Design Plan, Oct. 1971, P 2-71), attitude motion simulation tests by Philco-Ford (Phase C Design Report, Book 2, Vol. I, p. 4-18, 30 June 1971) have shown this not to be the case.

Since the DPLL is based on digital operations during tracking, computer simulation of the system can be considered a meaningful test of its performance. Both Westinghouse and Philco-Ford conducted simulation tests of the DPLL. General results of these tests are presented in Table 1. Except for the noted difference in spin rate variation, both groups used the same signal input discussed in this section. They both used a random noise of approximately 1.1 μsec superimposed on the DPLL signal input. Not surprisingly, the determined values of RMS noise in the DPLL output are also quite similar.

There are a number of DPLL performance characteristics which are not revealed in Table 1. Among these, the following might be significant:

(i) The loop cannot track periodic variations resulting from nutation because of their high frequency relative to the natural frequency of the loop. This currently does not represent any serious problem because the peak timing drift due to nutation is only 0.06 μsec. However, any increase in nutation induced errors could be serious because the loop is powerless to reduce them.

(ii) In the presence of small loop frequency errors, timing error linearly increases with time until a phase correction is required. This results in a sawtooth pattern of timing error, with a peak to peak amplitude of approximately 0.2 μsec and a period ranging from 10 to 100 input pulses per cycle. This "limit cycle" oscillation could result in frame to frame displacement errors which are periodic in scan line and have peak errors as large as 0.4 μsec (leading to a 0.2 knot E-W velocity error for 30 minute frame interval). Although this error is quite small in magnitude, for a given pair of frames it can be constant over a wide latitude band (70 km to 700 km) and completely immune to the averaging of displacement measurements of cloud elements within the band. Thus, it could interfere with determinations of small velocity, large scale motions.

The simulation tests verify the linear mathematical analysis of the loop made by Huang (SMS-PCC-3452). The loop reduces random input RMS jitter by a factor 0.2 and introduces a peak quantization error of 0.1 μsec. It cannot track nutational variations, resulting in a peak error of 0.06 μsec.

Table 1. DPLL PERFORMANCE

TESTING GROUP	SIGNAL INPUT	RMS NOISE INPUT	RMS NOISE OUTPUT	BIAS ERROR (1 FRAME)	TIMING DRIFT (1 FRAME)
Westinghouse[1]	Nutation + 0.25 μsec/frame spin period change	1.1 μsec	0.24 μsec	0.104	N.A.
Philco-Ford[2]	Nutation + 4.67 μsec/frame spin period change	1.05 μsec	0.25 μsec	0.1 μsec[4]	0.7 μsec (peak-to-peak)[3]

NOTES: (1) S/DB DESIGN PLAN, Oct. 1971, p. 2-70

(2) "SMS SUN-PULSE TIMING SUBSYSTEM ANALYSIS", J. Y. HUANG, SMS-PCC-3452, Oct. 1971, p. ix

(3) This applies only to the first frame after acquisition of the DPLL. The drift drops to 0.35 μsec or less in the second and succeeding frames.

(4) This requires changing the DPLL bandwidth during retrace.

4. LINE START TIMING ERROR SUMMARY

Table 2 summarizes the contributions of all error sources previously discussed and the resulting error in the DPLL output sun pulses. The peak value stated is approximately equivalent to 4σ value (The RMS error is approximately one fourth of the peak). The net error is probably somewhat conservative. It is slightly larger than the more recent Philco-Ford estimate of 0.57 μsec peak (SMS-PCC-3577, Feb. 7 72) because it includes frequency errors. It is smaller than Huang's first estimate of 1.16 μsec peak because a smaller and more recent value is used for the RMS jitter in the sun pulse signal conditioner output.

The line start time contains an additional source of error. This is the quantization error in the earth angle counter which counts the 24 bit β value and defines the angular delay between the scan synch pulse and the start of earth view sampling. Since this count is made at the VCO frequency (twice the synthesizer frequency), the unit of time is approximately 0.096 μsec. The peak and RMS errors from this source are thus 0.05 μsec and 0.03 μsec respectively. These are insignificant errors. Thus, it appears that the RMS jitter in line start timing should be well within the 0.25 μsec specified.

The significance of the systematic displacement error, resulting from the limit cycle oscillation of the DPLL, depends on user requirements for highly accurate measurements of large scale E-W motions. However, even if better than 0.2 knot accuracy is required, averaging over several frame pairs should be justifiable for this scale. Averaging should also be effective in reducing the displacement errors since the limit cycle oscillations will have phases that are random from frame to frame.

Table 2. SUN PULSE TIMING ERROR SUMMARY

INPUT ERRORS

S/C SUN SYNC PULSE RMS jitter	0.343 μsec
Communication Errors (RMS)	
Quantization Error	0.20 μsec
S/C to CDA transmission link ($P_E=10^{-5}$)	0.19 μsec
Frequency errors in 3.5 MHz clocks	0.30 μsec
Total RMS jitter input to DPLL	0.532 μsec

OUTPUT SUN PULSE ERRORS

RMS Jitter out = (σout/σin) 0.532 = 0.106 μsec
4σ jitter = 0.425 μsec
DPLL Quantization (Peak Value) = 0.1 μsec
S/C Nutational Motion (Peak Value) = 0.06 μsec (not tracked by DPLL)

Total Timing Error (Peak Value) = 0.69 μsec

The probability that the timing error of any one of the smoothed pulses in a picture frame exceeding 0.69 μsec is approximately 0.10.

EFFECTS OF EQUAL ANGLE RESAMPLING ON POINTING AND CLOUD DISPLACEMENT MEASUREMENT ACCURACY

L. A. Sromovsky

INTRODUCTION

Equal Angle (EA) resampling of S/C Equal Time (ET) samples introduces a relatively small RMS time jitter of approximately 0.3 μsec. This results in an RMS position error of approximately 0.06 n. mi. at the subsatellite point. However, this error is not random along a scan line but, instead, displays a periodic variation that can lead to false indications of E-W convergence and wind shear.

A major portion of this document is devoted to the precise mathematical description of the error patterns produced by the EA resampling, thus providing a basis for computer simulation and analysis. A hand calculation of a sixteen line error field is included as an example of errors that can result in the measured displacements of small clouds that move parallel to scan lines. This example represents a worst case situation. Large clouds and clouds with variable N-S motions would not show such distinctive error patterns because of their inherent error averaging characteristics.

Preliminary results presented here indicate that EA resampling will not be a major problem in cloud displacement measurements. In practical situations, which need some kind of specification, it is probable that the variety of cloud sizes and motions will reduce the resampling error to the equivalent of a random uncorrelated error of 0.3 μsec RMS. This conjecture can be tested by computer simulation if necessary. If it is found to be erroneous, a suggested method can be employed to reduce the resampling error to acceptable levels.

I. SYSTEM OPERATION (Figure 1)

1) S/C Video Sampling and Transmission

1.1) Time between samples = τ_{ET}, determined by S/C 14 MHz bit rate clock divided down to 500 kHz, independent of spin rate.

1.2) Start of video sampling is determined by Earth Angles Generator and, ultimately, by the S/C Spin Clock which has a resolution of 0.2° and an absolute angular accuracy of 0.5°.

2) Command and Data Acquisition Station (CDA) Interpolation

2.1) At CDA interpolated samples are inserted midway between original S/C samples.

2.2) The interpolated samples are formed from linear combinations of the adjacent two or adjacent four original samples.

2.3) The time spacing between adjacent members of this augmented set of samples is $\frac{1}{2}\tau_{ET}$.

3) CDA Equal Angle (EA) Resampling

3.1) The timing of EA resampling is controlled by the CDA (Phase Locked Loop) PLL which is locked to the smoothed S/C spin rate.

3.2) The nominal time between adjacent equal angle samples = τ_{EA}. This is obtained by dividing the S/C spin period into a fixed number of angular increments, thus depending on spin rate.

3.3) The start of EA resampling is determined by the sun synch pulse output of the CDA PLL shifted by the Earth Sun angle. Timing accuracy at 100 RPM is approximately 0.30μ sec (≃ 3μ radians).

3.4) Whenever the EA clock calls for an EA sample, the actual sample selected from the augmented set is the sample which occurs nearest in time to the EA request.

3.5) The selected samples are subsequently treated as equal angle samples although their actual time locations can differ from the nominal EA time by as much as $\frac{1}{4}\tau_{ET}$. This leads to a systematic timing, or, equivalently, positional error in the EA samples.

II. DERIVATION OF EA TIMING ERROR

1) Definitions

τ_{ET} = time between S/C Equal Time (ET) samples

$\frac{1}{2}\tau_{ET}$ = time between AUGMENTED ET samples

τ_{EA} = time between EA sample requests

t_{ET}^{K} = the time location of the kth sample of the augmented ET set

t_{EA}^{L} = the time at which the Lth EA sample is requested

K_L denotes the sample of the augmented ET set which is chosen as the Lth EA sample

t_s^L = the time location of the sample selected as the Lth EA sample

$\phi_{ET} = t_{EA}^{o} - t_{ET}^{o}$, the time interval between the EA start time and the ET start time.

INT(X) = the largest integer $\leq$ X

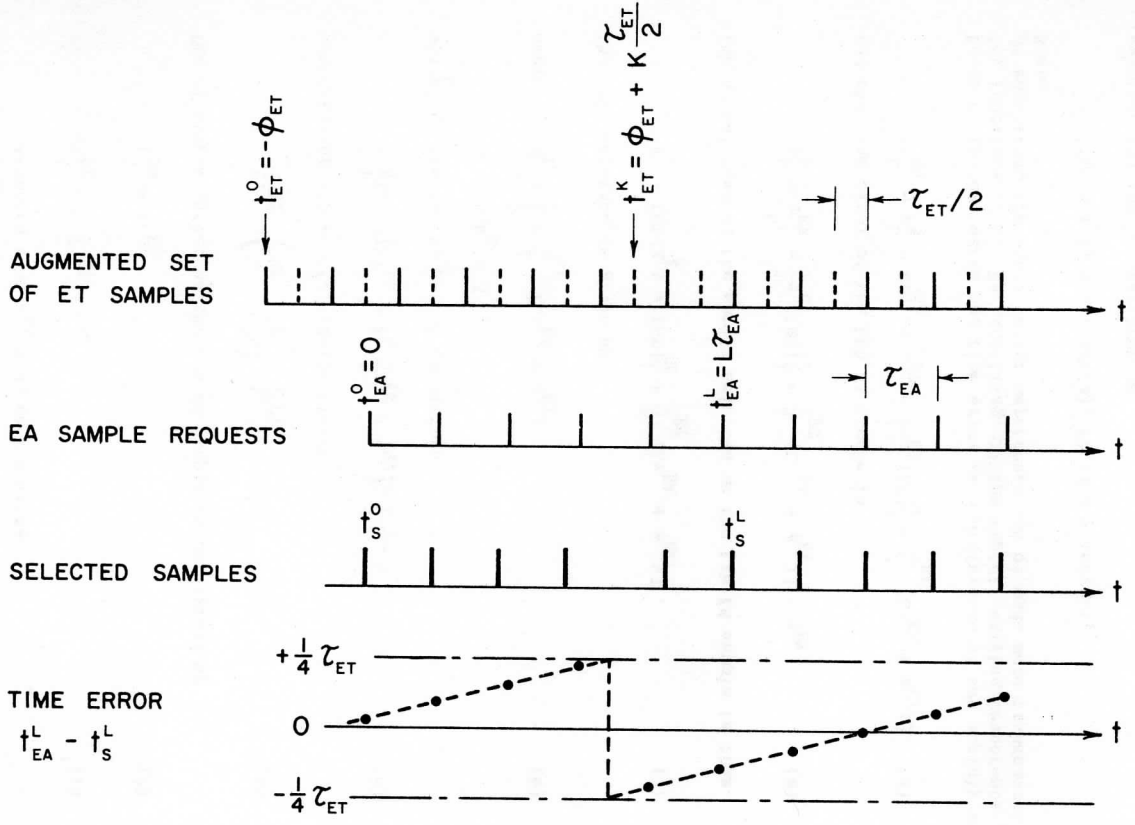

Figure 1

Resampling Systame Operation

2) Derivation

Assuming that $t_{EA} = 0$, we can write

$$t_{ET}^{K} = K\frac{1}{2}\tau_{ET} - \tau_{ET} \tag{1}$$

$$t_{EA}^{L} = L\tau_{EA} \tag{2}$$

The ET sample chosen as the Lth EA sample is determined by

$$-\frac{1}{4}\tau_{ET} < \left(t_{EA}^{L} - t_{ET}^{K_L}\right) \leq \frac{1}{4}\tau_{ET} \tag{3}$$

Substituting (1) and (2) in (3) yields

$$-\frac{1}{4}\tau_{ET} < \left(L\tau_{EA} - K_L\frac{1}{2}\tau_{ET} + \phi_{ET}\right) \leq \frac{1}{4}\tau_{ET}\ , \tag{4}$$

which reduces to the set of conditions

$$X_L - 1 \leq K_L < X_L\ ,$$

where $$X_L = \frac{1}{2} + \frac{2}{\tau_{ET}}(L\tau_{EA} + \phi_{ET}) \tag{6}$$

The only solution is given by

$$K_L = \mathrm{INT}(X_L) = \mathrm{INT}\left[\frac{1}{2} + \frac{2}{\tau_{ET}}(L\tau_{EA} + \phi_{ET})\right]\ . \tag{7}$$

The actual time of the sample selected as the Lth EA sample is thus

$$t_S^L = t_{ET}^{K_L} = \frac{1}{2}\tau_{ET}\mathrm{INT}\left[\frac{1}{2} + \frac{2}{\tau_{ET}}(L\tau_{EA} + \phi_{ET})\right] - \phi_{ET} \tag{8}$$

and the time error of the Lth EA sample is

$$t_{EA}^L - t_S^L = L\tau_{EA} + \phi_{ET} - \frac{1}{2}\tau_{ET}\mathrm{INT}\left[\frac{1}{2} + \frac{2}{\tau_{ET}}(L\tau_{EA} + \phi_{ET})\right]. \tag{9}$$

Equation (9) expresses the time error as a difference of two rapidly varying functinns of L. By cancelling off the rapidly varying components of each term, the actual error dependence can be made more transparent. Since

$$\mathrm{INT}(A + I) = I + \mathrm{INT}(A),\ \forall A \text{ if } I = \text{integer},$$

equation (9) can be rewritten as

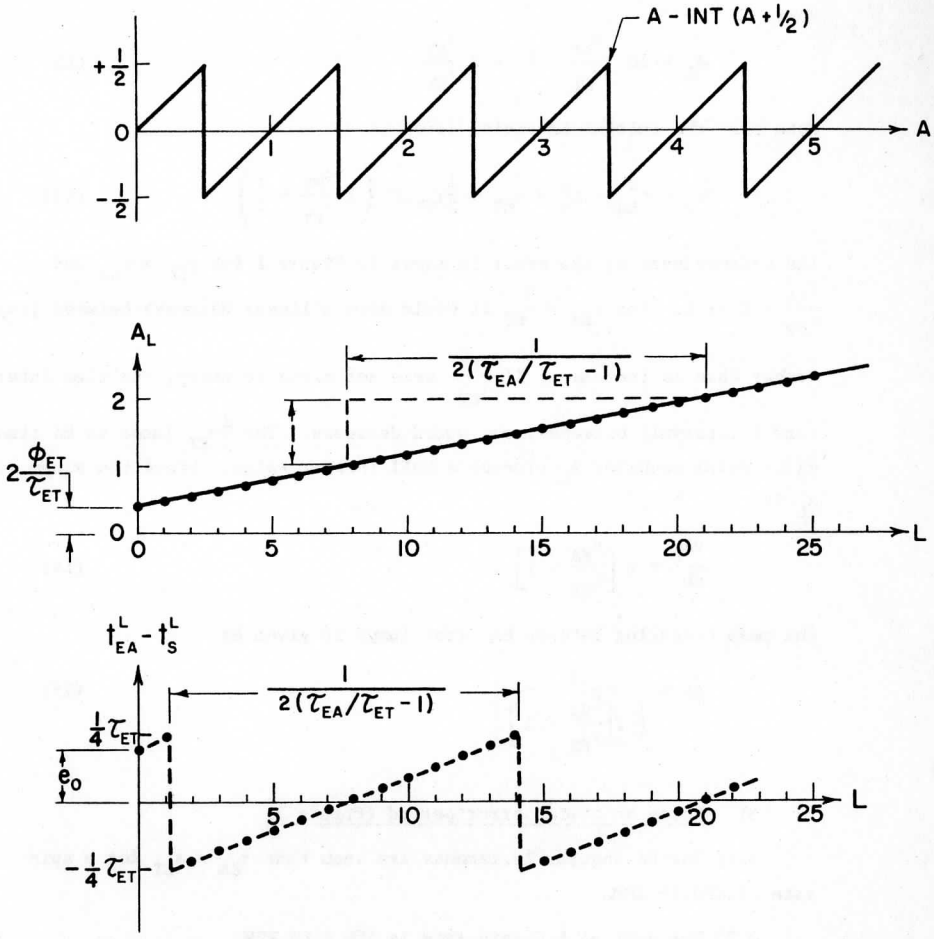

Figure 2

EA Timing Error

$$t^{L}_{EA} - t^{L}_{S} = \frac{1}{2}\tau_{ET}[A_L - INT(A_L + \tfrac{1}{2})] \ , \tag{11}$$

where

$$A_L = 2L \ \frac{\tau_{EA}}{\tau_{ET}} - 1 \ + 2 \ \frac{\phi_{ET}}{\tau_{ET}} \ . \tag{12}$$

Note that the initial EA timing error is

$$e_o = t^{o}_{EA} - t^{o}_{S} = \phi_{ET} - \frac{1}{2}\tau_{ET} INT\left(2 \ \frac{\phi_{ET}}{\tau_{ET}} + \frac{1}{2}\right) \tag{13}$$

The L-dependence of the error is shown in Figure 2 for $\tau_{EA} > \tau_{ET}$ and $\frac{\tau_{EA}}{\tau_{ET}} - 1 \ll 1$. For $\tau_{EA} < \tau_{ET}$ it would show a linear decrease between jumps rather than an increase. If $\frac{\tau_{EA}}{\tau_{ET}}$ were not close to unity, the time interval (and L interval) between jumps would decrease. The $\frac{1}{2}\tau_{ET}$ jumps in EA time error occur whenever A_L crosses a half integer value. Since the slope of A_L is

$$\frac{dA_L}{dL} = 2\left[\frac{\tau_{EA}}{\tau_{ET}} - 1\right] \ , \tag{14}$$

the mean L-spacing between EA error jumps is given by

$$\Delta L = \left| \frac{1}{2\left[\frac{\tau_{EA}}{\tau_{ET}} - 1\right]} \right| . \tag{15}$$

3) Notes on timing error period (Figure 3)

3.1) The EA angular increments are such that $\tau_{EA} = \tau_{ET}$ for a spin rate of 100.16 RPM.

3.2) The nominal S/C spin rate is 100 ± 10 RPM.

3.3) In terms of spin rate w, equation (16) can be written as

$$\Delta L = \frac{w}{2|w_o - w|} \ , \tag{16}$$

where w_o = 100.16 RPM.

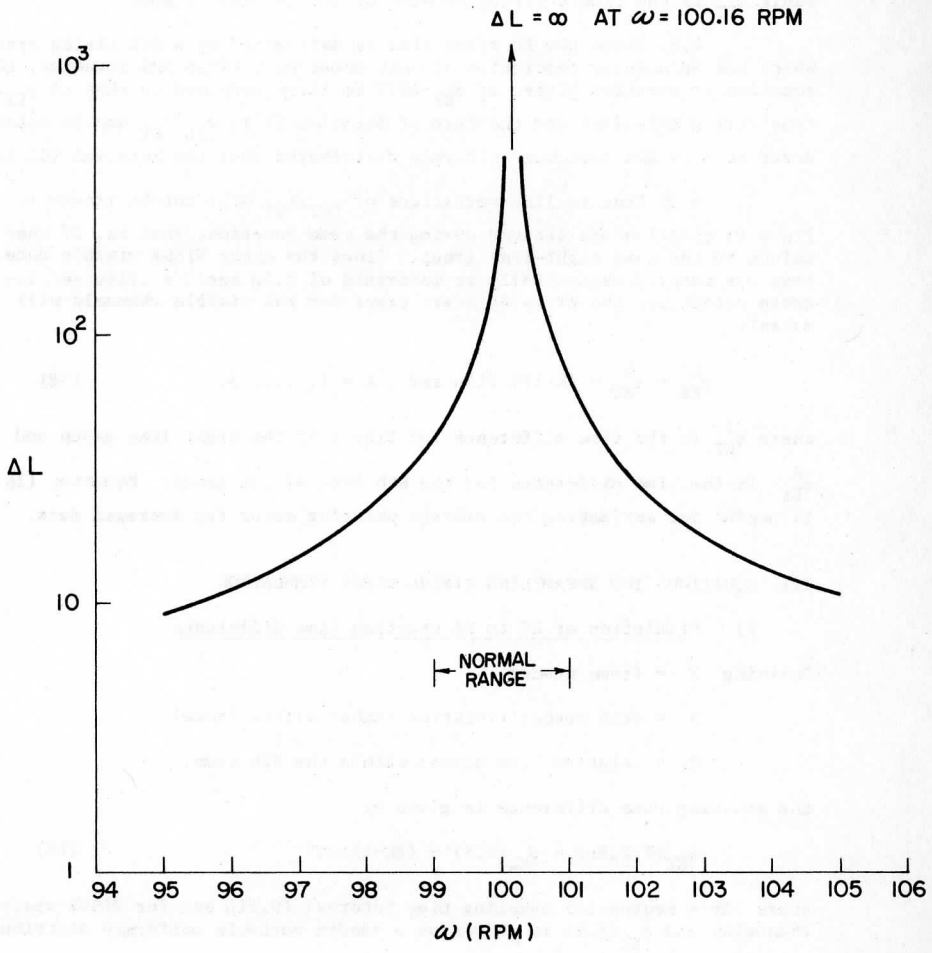

Figure 3

Timing error period as a function of spin rate

4) Notes on initial timing error

4.1) The initial timing error can be written as

$$e_o = \frac{1}{2}\tau_{ET}\left[2\frac{\phi_{ET}}{\tau_{ET}} - \mathrm{INT}\left(2\frac{\phi_{ET}}{\tau_{ET}} + \frac{1}{2}\right)\right], \tag{17}$$

where ϕ_{ET} is the time interval between ET and EA start times.

4.2) Since the ET start time is determined by a S/C timing system, which has an angular resolution of only about 0.2° of an SMS rotation, the rotation to rotation jitter of ϕ_{ET} will be large compared to that of τ_{ET}. Considering this fact and the form of equation (17), ϕ_{ET}/τ_{ET} may be considered as a random variable uniformly distributed over the interval (0, 1/2).

4.3) Line to line variations of ϕ_{ET}/τ_{ET} will not be random if the lines in question are scanned during the same rotation, that is, if they belong to the same eight-line group. Since the eight VISSR visible detectors are sampled sequentially at intervals of 1.5μ sec/7 ≃ .214μ sec between detectors, the ET to EA start times for the visible channels will satisfy

$$\phi_{ET}^{K} = \phi_{ET}^{1} - (K-1)0.214\mu \text{ sec}, \quad K = 1, \ldots, 8, \tag{18}$$

where ϕ_{ET}^{1} is the time difference for line 1 of the eight line group and ϕ_{ET}^{K} is the time difference for the Kth line of the group. Equation (18) is useful for estimating the average pointing error for averaged data.

III. EQUATIONS FOR RESAMPLING TIMING ERROR SIMULATION

1) Simulation of ET to EA starting time difference

Defining F = frame number

S = scan number (rotation number within frame)

RL = relative line number within the Sth scan,

the starting time difference is given by

$$\phi_{ET}(F,S,RL) = \phi_{ET}(F,S) - (RL-1)\Delta\tau, \tag{19}$$

where $\Delta\tau$ = sequential sampling time interval (0.21μ sec for VISSR visible channels) and $\phi_{ET}(F,S)$ is chosen as a random variable uniformly distributed over the interval $(0, \frac{1}{2}\tau_{ET})$.

2) Simulating the time location of each EA sample

According to equation (8), the actual time of the Lth EA sample of the Fth frame, Sth scan and RLth line within the Sth scan is

$$t_s^L(F,S,RL) = \frac{1}{2}\tau_{ET}\,INT\left(\frac{1}{2} + \frac{2}{\tau_{ET}}\left[L\tau_{EA} + \phi_{ET}(F,S,RL)\right] - \phi_{ET}(F,S,RL)\right) \qquad (20)$$

where $\phi_{ET}(F,S,RL)$ is given by equation (19).

3) Simulation of the EA timing error

According to equation (11), the difference between the EA request time and the actual time of the selected sample is given by

$$e_L(F,S,RL) = [t_{EA}^L - t_s^L]_{F,S,RL} = \frac{1}{2}\tau_{ET}\left[A_L(F,S,RL) - INT[A_L(F,S,RL) + \frac{1}{2}]\right] \qquad (21)$$

where

$$A_L(F,S,RL) = 2L\left[\frac{\tau_{EA}}{\tau_{ET}}\right] + 2\,\frac{1}{\tau_{ET}}\,\phi_{ET}(F,S,RL)\ , \qquad (22)$$

and, as before, $\phi_{ET}(F,S,RL)$ is given by equation (19).

4) Conversion to errors in angle

If T is the satellite spin period, then the angular pointing error δ_L can be obtained from the timing error e_L according to

$$\delta_L = 2\pi\frac{e_L}{T} \qquad (23)$$

IV. DISPLACEMENT ERRORS

1) Small Clouds (displacement error of two elements)

Consider two different EA samples located at (F,S,RL,L) and (F',S',RL',L') respectively. Since no data averaging is involved, it is sufficient to consider only the coordinates (F,L) and (F',L'). The inferred relative time displacement is given by

$$t_{EA}^{L',F'} - t_{EA}^{L,F} = t_S^{L',F'} - t_S^{L,F} + [e_{L'}(F') - e_L(F)] \qquad (24)$$

where $t_s^{L',F'} - t_s^{L,F}$ is the actual relative time displacement of the selected samples and $[e_{L'}(F') - e_L(F)]$ is the displacement error. Making use of equation (22) the displacement error can be written as

$$[e_{L'}(F') - e_L(F)] = \frac{1}{2}\tau_{ET}[Y + INT(B) - INT(B+Y)], \tag{25}$$

where

$$Y = 2(L'-L)\left[\frac{\tau_{EA}}{\tau_{ET}} - 1\right] + \frac{2}{\tau_{ET}}[(\phi_{ET}(F'') - \phi_{ET}(F)], \tag{26}$$

$$B = 2L\left(\frac{\tau_{EA}}{\tau_{ET}} - 1\right) + \frac{2}{\tau_{ET}}\phi_{ET}(F) + \frac{1}{2}\ .$$

For fixed Y (same L'-L difference), the displacement error [e'-e] is a square wave function of the variable B (or L). Defining

$$Y = Y_I + Y_F \quad \text{where } Y_I = INT(Y), \tag{27}$$

we find

$$[e'-e] = \frac{1}{2}\tau_{ET}[Y_F + INT(B) - INT(B+Y_F)] \tag{28}$$

which satisfies the square wave conditions

$$[e'-e] = \frac{1}{2}\tau_{ET}Y_F \quad \text{for } N \leq B \leq N + 1 - Y_F \tag{29}$$

$$[e'-e] = \frac{1}{2}\tau_{ET}(Y_F-1) \quad \text{for } N-Y_F \leq B < N$$

This function is displayed in Figure 4. Note that the total variation of the displacement error ($[e'-e]_{max} - [e'-e]_{min}$), is independent of Y_F and equal to $\frac{1}{2}\tau_{ET}$. Note also that the L-period of the square wave cycles is given by equation (15) or (16). The L-distance corresponding to Y_F is just the product of Y_F and the L-period.

For fixed B (equivalent to fixed L), [e'-e] is a sawtooth function of the variable Y. If we define

$$B = B_F + B_I\ , \quad \text{where } B_I = INT(B), \tag{30}$$

then the displacement error can be expressed as

$$[e'-e] = \frac{1}{2}\tau_{ET}[Y - INT(B_F+Y)]\ . \tag{31}$$

Since L is assumed fixed and $(\tau_{EA}/\tau_{ET}-1)$ is assumed positive, Y is an increasing function of L' (actually L'-L). The L'-L period of the sawtooth is given by equation (15) or (16), and the total error range $[e'-e]_{max} - [e'-e]_{min}$ is independent of B_F and equal to $\frac{1}{2}\tau_{ET}$. The function is displayed

in Figure 5. The L' (or L'-L) distance corresponding to B_F is obtained, of course, by the multiplication of B_F and the L'-L period.

2) An example of a small cloud error field

2.1) Assumed conditions: $\Delta L = 100$ (equivalent to w = 100.56 RPM); Relative Navigation of the two frames is accomplished by the alighment of relative line 3 of scan 2 of frame 1 with relative line 1 of scan 1 of frame 2. Longitude shifts need not be considered. Relative cloud displacements, measured in units of EA elements, are small compared to ΔL (this allows Y of equation (26) to be assumed constant along a line) and parallel to scan lines (this is required to insure a unique error field). Basic time intervals are $\tau_{ET} = 2.0\mu$ sec and $\Delta\tau = 0.214\mu$ sec.

2.2) Calculation summary: The calculation of the square wave error parameters is displayed in Table 1 for a sixteen (16) line swath. For each of the four scans (rotations) a starting time is chosen at random. The remaining starting times are determined from equation (19). Given the values of Y_F it is possible to construct appropriate square wave error plots as a function of B, shown in Figure 6. From the B(L=0) values (indicated by arrows in Figure 6) and the fact that one unit of B corresponds to 100 units of L, the displacement error, as a function of element position along a line, can be found for each line. The results are displayed as an array in Figure 7. Each unit represents 0.10 μsec relative time location error, or $\simeq 1\mu$ radian, or $\simeq$ 0.025 n. mi at the subsatellite point. The largest displacement error for this example is 8 x 0.025 n. mi. = 0.2 n. mi. For a frame interval of 30 minutes this would result in a wind error of 0.4 knots or 0.2 m/sec (at the subsatellite point). The displacements shown are the amounts by which the apparent displacements exceed the actual displacements.

The wind vector error field corresponding to Figure 7 is shown in Figure 8. Recall that all these results apply only to clouds which do not move perpendicular to scan lines. Although it is possible to calculate displacement errors for such motions, the error field can no longer be specified uniquely by line and element. A third dimension, specifying the extent of perpendicular motions, would be required. For a frame interval of 30 minutes, the largest vector corresponds to an error of 0.2 m/sec and the shortest to an error of 0.05 m/sec.

The wind error patterns of Figure 8 lead to similar patterns of horizontal convergence (parallel to the scan direction) and wind shear (perpendicular to the scan direction). These patterns are shown in Figure 9. If adjacent wind error vectors (along a line) are pointing toward each other, the convergence is taken as positive (+). If adjacent wind error vectors on neighboring lines show an increase to the right with increasing line number, the shear is taken as positive (+). Typical values of convergence are near 0.5 knots (0.25 m/sec) relative velocity. The typical wind shear magnitude is near 0.5 knots/line.

3) Effects of resampling errors on large cloud displacements

The measurement of large cloud displacements is, in essence, the measure-

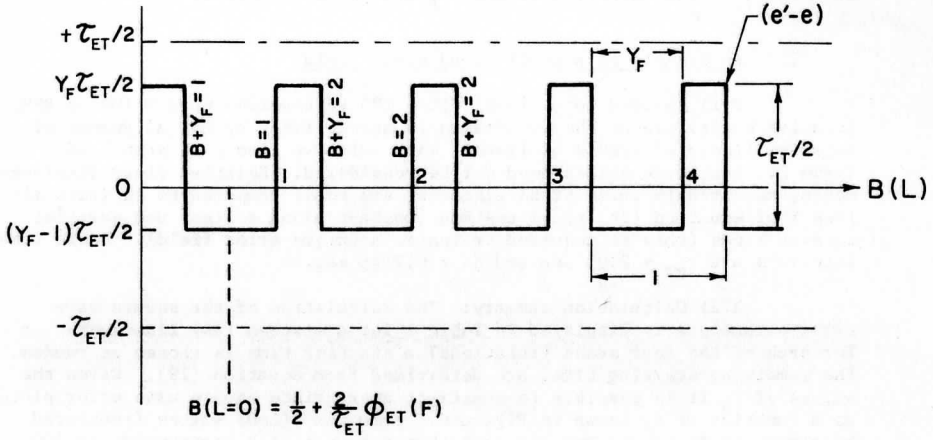

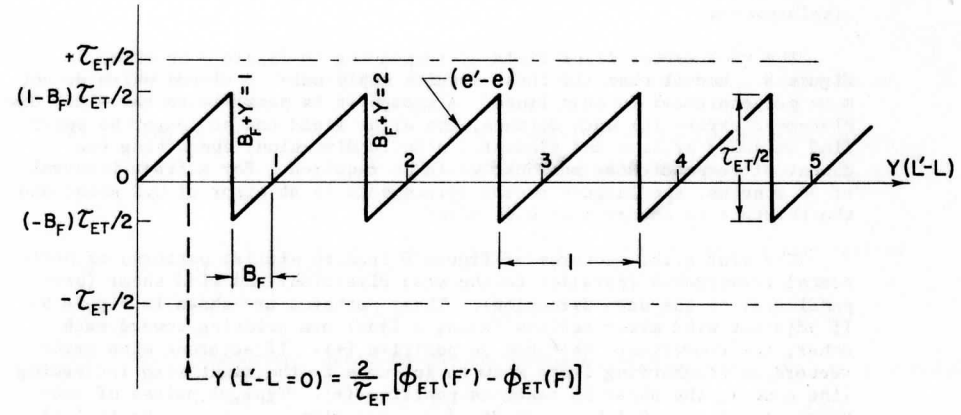

Figure 5

Displacement errors as a function of (L'-L) for a fixed B

Table 1. Sample timing error calculation.

	FRAME 2			FRAME 1							
LINE	S'	RL'	ϕ'_{ET} μsec	S	RL	ϕ_{ET} μsec	$\frac{\phi_{ET} - \phi_{ET}}{\tau_{ET}/2}$	Y_F	Y_F-1	B(L=0)	B(L=0) - INT(B(L=0))
1	1	1	1.500	2	3	1.300	0.20	0.20	-.80	1.80	0.80
2		2	1.286		4	1.086	0.20	0.20	-.80	1.59	0.59
3		3	1.072		5	0.872	0.20	0.20	-.80	1.37	0.37
4		4	0.858		6	0.658	0.20	0.20	-.80	1.16	0.16
5		5	0.642		7	0.442	0.20	0.20	-.80	0.94	0.94
6		6	0.428		8	0.228	0.20	0.20	-.80	0.73	0.73
7		7	0.214	3	1	1.800	-1.59	0.41	-.59	2.30	0.30
8		8	0.000		2	1.586	-1.59	0.41	-.59	2.09	0.09
9	2	1	2.200		3	1.372	0.83	0.83	-.17	1.87	0.87
10		2	1.986		4	1.158	0.83	0.83	-.17	1.66	0.66
11		3	1.772		5	0.942	0.83	0.83	-.17	1.44	0.44
12		4	1.558		6	0.728	0.83	0.83	-.17	1.23	0.23
13		5	1.342		7	0.514	0.83	0.83	-.17	1.01	0.01
14		6	1.128		8	0.300	0.83	0.83	-.17	1.80	0.80
15		7	0.914	4	1	1.514	-0.60	0.40	-.60	2.01	0.01
16		8	0.700		2	1.300	-0.60	0.40	-.60	2.80	0.80

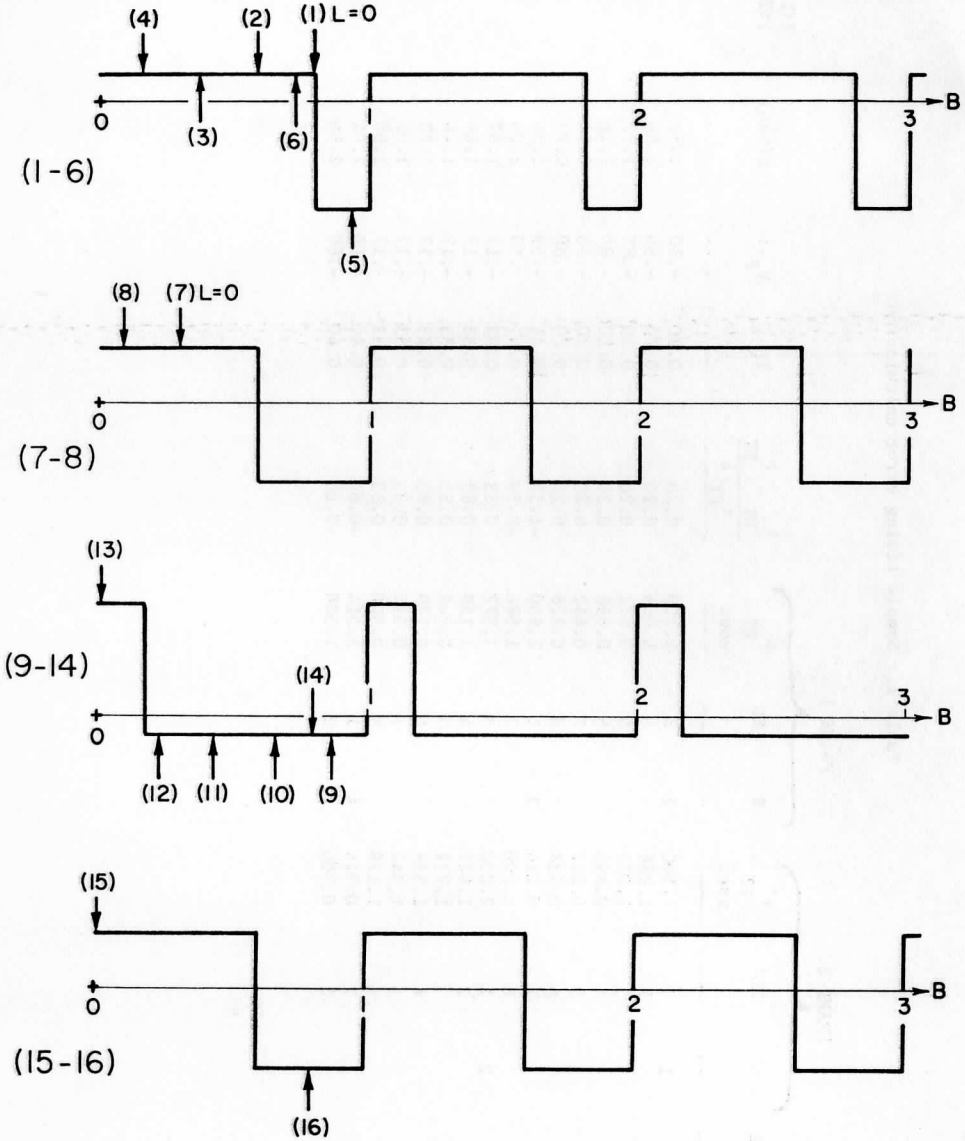

Figure 6

Error waveforms used in example calculations

ELEMENT

LINE	0					50					100					150					200					250
1	-8	-8	.2	.2	.2	.2	.2	.2	.2	.2	-8	-8	.2	.2	.2	.2	.2	.2	.2	.2	-8	-8	.2	.2	.2	
2	2	2	-8	-8	2	2	2	2	2	2	2	2	-8	-8	2	2	2	2	2	2	2	2	-8	-8	2	
3	2	2	2	2	-8	-8	2	2	2	2	2	2	2	2	-8	-8	2	2	2	2	2	2	2	2	-8	
4	2	2	2	2	2	2	-8	-8	2	2	2	2	2	2	2	2	-8	-8	2	2	2	2	2	2	2	
5	-8	2	2	2	2	2	2	2	2	-8	-8	2	2	2	2	2	2	2	2	-8	-8	2	2	2	2	
6	2	-8	-8	2	2	2	2	2	2	2	2	-8	-8	2	2	2	2	2	2	2	2	-8	-8	2	2	
7	4	4	4	-6	-6	-6	-6	4	4	4	4	4	4	-6	-6	-6	-6	4	4	4	4	4	4	-6	-6	
8	4	4	4	4	4	-6	-6	-6	-6	4	4	4	4	4	4	-6	-6	-6	-6	4	4	4	4	4	4	
9	-2	8	8	-2	-2	-2	-2	-2	-2	-2	-2	8	8	-2	-2	-2	-2	-2	-2	-2	-2	8	8	-2	-2	
10	-2	-2	-2	8	8	-2	-2	-2	-2	-2	-2	-2	-2	9	9	-2	-2	-2	-2	-2	-2	-2	-2	8	8	
11	-2	-2	-2	-2	-2	-2	9	-2	-2	-2	-2	-2	-2	-2	-2	-2	8	-2	-2	-2	-2	-2	-2	-2	-2	
12	-2	-2	-2	-2	-2	-2	-2	-2	8	8	-2	-2	-2	-2	-2	-2	-2	-2	8	-2	-2	-2	-2	-2	-2	
13	8	8	-2	-2	-2	-2	-2	-2	-2	-2	8	8	-2	-2	-2	-2	-2	-2	-2	-2	8	8	-2	-2	-2	
14	-2	-2	8	8	-2	-2	-2	-2	-2	-2	-2	-2	8	8	-2	-2	-2	-2	-2	-2	-2	-2	8	8	-2	
15	4	4	4	4	4	4	-6	-6	-6	-6	4	4	4	4	4	4	-6	-6	-6	-6	4	4	4	4	4	
16	-6	-6	4	4	4	4	4	4	-6	-6	-6	-6	4	4	4	4	4	4	-6	-6	-6	-6	4	4	4	

Figure 7. Displacement Error Field

1 unit = 0.10 μsec or 1μ radian or 0.025 n. mi.

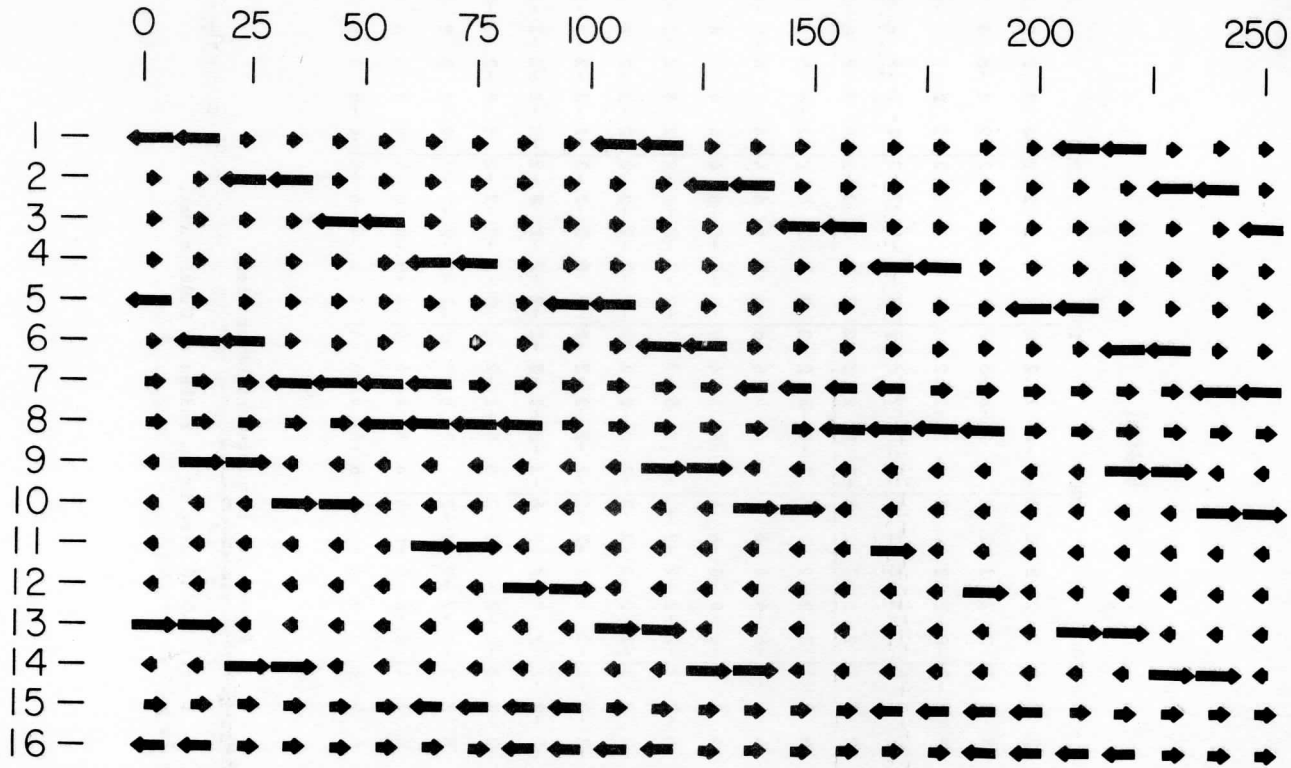

Figure 8
Wind vector field. The longest vector corresponds to a wind error of 0.2 m/sec. for a 30 minute frame interval.

	-0	-25	-50	-75	-100	-125	-150	-175	-200	-225	-250
1-	0 - 0 0 0 0 0 0 + 0 - 0 0 0 0 0 0 0 + 0 - 0 0										
2 -	0 + 0 - 0 0 0 0 0 0 0 + 0 - 0 0 0 0 0 0 0 + 0 -										
3-	0 0 0 + 0 - 0 0 0 0 0 0 0 + 0 - 0 0 0 0 0 0 0 +										
4-	0 0 0 0 0 + 0 - 0 0 0 0 0 0 0 + 0 - 0 0 0 0 0 0										
5-	- 0 0 0 0 0 0 0 + 0 - 0 0 0 0 0 0 0 + 0 - 0 0 0										
6-	+ 0 - 0 0 0 0 0 0 0 + 0 - 0 0 0 0 0 0 0 + 0 - 0										
7-	0 0 + 0 0 0 - 0 0 0 0 0 + 0 0 0 - 0 0 0 0 0 + 0										
8-	0 0 0 0 + 0 0 0 - 0 0 0 0 0 + 0 0 0 - 0 0 0 0 0										
9-	- 0 + 0 0 0 0 0 0 0 - 0 + 0 0 0 0 0 0 0 - 0 +										
10-	0 0 - 0 + 0 0 0 0 0 0 0 - 0 + 0 0 0 0 0 0 0 - 0										
11-	0 0 0 0 - 0 + 0 0 0 0 0 0 0 - + 0 0 0 0 0 0 0 0										
12-	0 0 0 0 0 - 0 + 0 0 0 0 0 0 0 - + 0 0 0 0 0 0 0										
13-	0 + 0 0 0 0 0 - 0 + 0 0 0 0 0 0 - 0 + 0 0 0 0 0										
14-	0 - 0 + 0 0 0 0 0 0 - 0 + 0 0 0 0 0 0 0 - 0 + 0										
15-	0 0 0 0 0 + 0 0 - 0 0 0 0 + 0 0 - 0 0 0 0 0 0 0										
16-	0 - 0 0 0 0 + 0 0 - 0 0 0 0 + 0 0 - 0 0 0 0 0 0										

CONVERGENCE ERROR FIELD

	-0	-25	-50	-75	-100	-125	-150	-175	-200	-225	-250
1-	+ + - - 0 0 0 0 0 0 + + - - 0 0 0 0 0 0 + + - - 0										
2-	0 0 + + - - 0 0 0 0 0 0 0 + + - - 0 0 0 0 0 0 + + -										
3-	0 0 0 0 + + - - 0 0 0 0 0 0 0 + + - - 0 0 0 0 0 0 +										
4-	- 0 0 0 0 0 + + 0 - - 0 0 0 0 0 0 + + 0 - - 0 0 0 0										
5-	+ - - 0 0 0 0 0 0 + + - - 0 0 0 0 0 0 + + - - 0 0										
6-	0 + + - - - - 0 0 0 0 + + - - - - - 0 0 0 0 + + - -										
7-	0 0 0 + + 0 0 - - 0 0 0 0 0 + + 0 0 - - 0 0 0 0 + +										
8-	- + + - - + + + + - - + + - - + + + + - - + + - -										
9-	0 - - + + 0 0 0 0 0 0 - - + + 0 0 0 0 0 0 - - + +										
10-	0 0 0 - - 0 + + 0 0 0 0 0 0 - - 0 + 0 0 0 0 0 0 - -										
11-	0 0 0 0 0 0 0 - - + + 0 0 0 0 0 0 0 - 0 + 0 0 0 0 0 0										
12-	+ + 0 0 0 0 0 0 0 - - + + 0 0 0 0 0 0 0 - 0 + + 0 0										
13-	- - + + 0 0 0 0 0 0 0 - - + + 0 0 0 0 0 0 0 - - + +										
14-	+ + - - + + - - - - - - + - - + + - - - - - + + - -										
15-	- - 0 0 0 0 + + 0 0 - - 0 0 0 0 + + 0 0 - - 0 0 0										

WIND SHEAR ERROR FIELD

Figure 9

ment of the mean displacement of a group of elements. As a result, considerable averaging of resampling displacement errors can occur. Although exact determination of the mean displacement error depends on the line-element locations corresponding to the cloud in question, there are two general characteristics of error averaging. These are:

(i) averaging displacements along a line is relatively ineffective in reducing displacement error unless the averaging length is $\geq \Delta L$ (the error cycle period). This is due to the slow variation of displacement error with L:

(ii) averaging displacements of elements on different lines is effective because of the random starting time for each scan (rotation) and the skewed sampling of the eight lines within each scan.

As an example of averaging characteristics, consider the average displacement error of four-line element averages. Using the single line results presented in Figure 7, the four line results are found to be those displayed in Figure 10. Note that the displacement error magnitude is considerably reduced overall compared to the individual line errors. Averaging more than four lines would show an even greater error reduction. Similar reductions appear in the convergence error and wind shear errors.

V. POSSIBILITIES FOR IMPROVEMENTS

All calculations made in the previous sections assumed that there is no timing error introduced by the interpolation process. Since there is actually no measurement made at the midpoint of the ET sampling interval, this assumption is not strictly correct. In fact, if the prealiasing filter bandpass were large compared to the original sampling frequency, the midpoint interpolated samples could often be in error by as much as $\frac{1}{2}\tau_{ET}$. This would result in an EA resampling error as large as τ_{ET}, and would be no improvement over resampling without interpolation. The specific timing error for this case would depend on two parameters: (1) the phase between the cloud edge and the original sampling positions and (2) the phase between the original sampling and the EA sampling.

In the case of the SMS VISSR, the original sampling is sufficiently frequent, relative to the prealiasing bandpass, to determine cloud edge locations to within 0.05 IFOV (or $\simeq$ 0.1 μsec). This would be true regardless of the sampling phase relative to the cloud edge. As indicated in Figure 11, which is taken from the Philco Ford Design Report C, Vol. I, Book 1, p. 2-157, this is possible because the finite detector aperture and the prealiasing filter spread the system response to the cloud edge over several samples (the 10% to 90% rise time is near 3.0 μsec).

In principle, then, it is possible to construct interpolated samples with an RMS time jitter of 0.1 sec within each interval between two original samples. This holds true for any number of interpolations within an interval, although nothing is gained by interpolating at intervals smaller than the 0.1 μsec jitter. It is quite clear from these considerations that

ELEMENT

LINES AVERAGED	0			50		100			150		200			250
(1-4)	$-\frac{1}{2}$	$-\frac{1}{2}$	$-\frac{1}{2}$	$-\frac{1}{2}$	2	$-\frac{1}{2}$	$-\frac{1}{2}$	$-\frac{1}{2}$	$-\frac{1}{2}$	2	$-\frac{1}{2}$	$-\frac{1}{2}$	$-\frac{1}{2}$	
(5-8)	$\frac{1}{2}$	$\frac{1}{2}$	$\frac{1}{2}$	-2	$\frac{1}{2}$	$\frac{1}{2}$	$\frac{1}{2}$	$\frac{1}{2}$	-2	$\frac{1}{2}$	$\frac{1}{2}$	$\frac{1}{2}$	$\frac{1}{2}$	
(9-12)	-2	$\frac{1}{2}$	$\frac{1}{2}$	$\frac{1}{2}$	$\frac{1}{2}$	-2	$\frac{1}{2}$	$\frac{1}{2}$	$\frac{1}{2}$	$\frac{1}{2}$	-2	$\frac{1}{2}$	$\frac{1}{2}$	
(13-16)	1	$3\frac{1}{2}$	1	$-1\frac{1}{2}$	-4	1	$3\frac{1}{2}$	1	$-1\frac{1}{2}$	-4	1	$3\frac{1}{2}$	1	

Figure 10. 1 unit = 0.10 μsec or 1 μ radian or 0.025 n. mi.

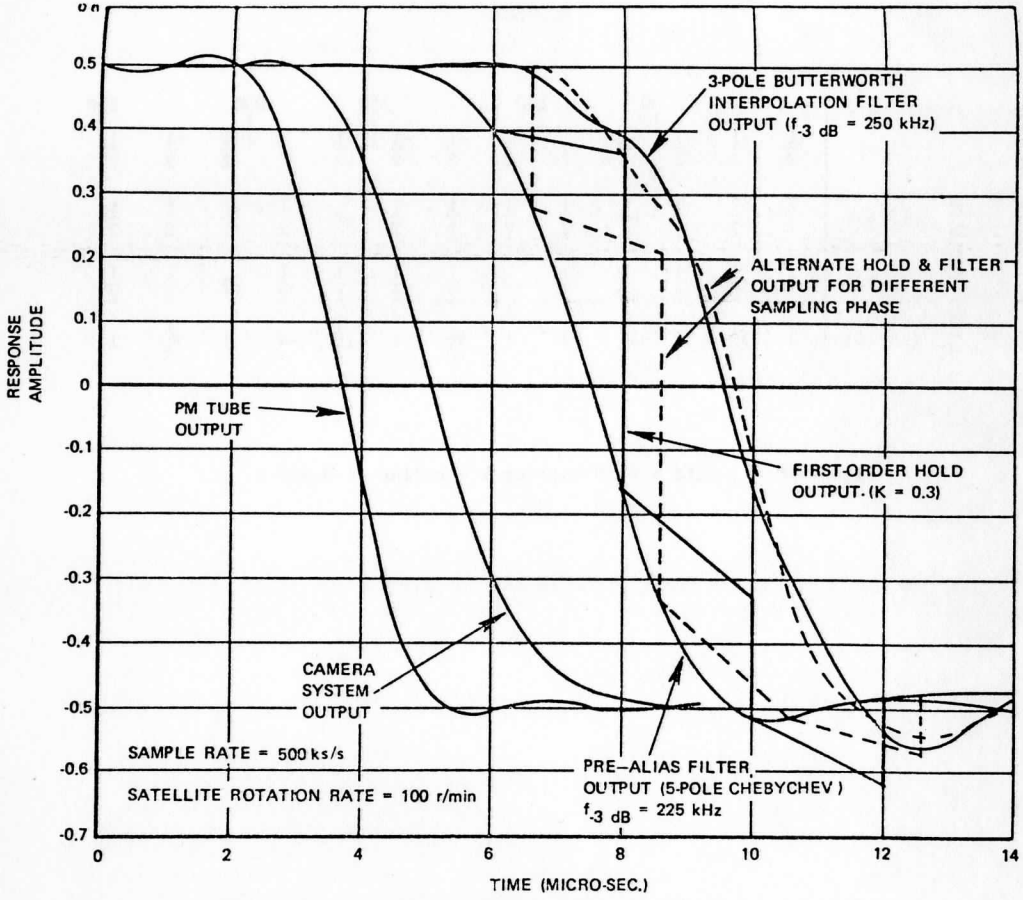

Figure 11. System Response to Image Step Function, Showing Edge Jitter Due to Sampling

midpoint interpolation will come very close to halving the EA resampling error $\frac{1}{2}\tau_{EA}$ = 1.0 μsec >> 0.1 μsec jitter. This is true even for linear interpolation of the non-linearly digitized S/C signal, as demonstrated by a Westinghouse group (S/DB Design Plan, Oct. 71, p. 2-29, 2-33.) Figure 12 summarizes their results for a simulated cloud edge input. They found peak to peak timing errors in the 50% point of 1.6 μsec and 0.8 μsec for the original and midpoint interpolated sets respectively, although their results are somewhat suspicious (the first error is almost certainly 2.0 μsec, not 1.6 μsec).

If three samples were interpolated between each two original samples, the EA resampling error could be reduced to $1/4\ \tau_{ET} \simeq 0.5$ sec peak to peak plus 0.1 μsec RMS jitter, neglecting the errors of linear interpolation of non-linear signals. The actual improvement could be determined easily by a computer simulation similar to that done by Westinghouse.

VI. EA RESAMPLING OF IR DATA

The pointing errors introduced by resampling the IR S/C samples have the same form as that produced by resampling the visible data. However, there are two important differences:

(1) there is no line to line error correlation, that is, the starting time is random for each IR line and

(2) the value of $\frac{1}{2}\tau_{ET}$ is 4.0 μsec instead of 1.0 μsec.

Thus, the peak to peak timing error due to IR resampling is four times that of the visible channels, although this represents a smaller fraction of the IFOV, ≃ 1/4 IFOV instead of ≃ 1/2 IFOV.

VII. SUMMARY AND RECOMMENDATIONS

1) Summary

Equal angle resampling of visible and IR S/C equal time samples produces systematic sawtooth errors in timing (or position) along a line. The phase of this sawtooth error function is random from one line to another, except in the case of visible lines within the same group of eight, which have fixed relative phase relationships. The resulting displacement errors of clouds moving parallel to the scan lines have a square wave form along a scan line and introduce systematic patterns of convergence and wind shear errors. Errors for clouds which also move normal to scan lines are not so systematic and require further analysis to determine the characteristic error patterns that might exist.

Several of the simplest error parameters for the SMS visible and IR resampling are summarized in Table 2. The period of the error waves is not shown since it strongly depends on spin rate (see equations (15) and (16) and Figure 3). The effectiveness of data averaging in reducing displacement errors is not shown because of its complicated dependence on the samples averaged. (For general behavior see section IV (3).)

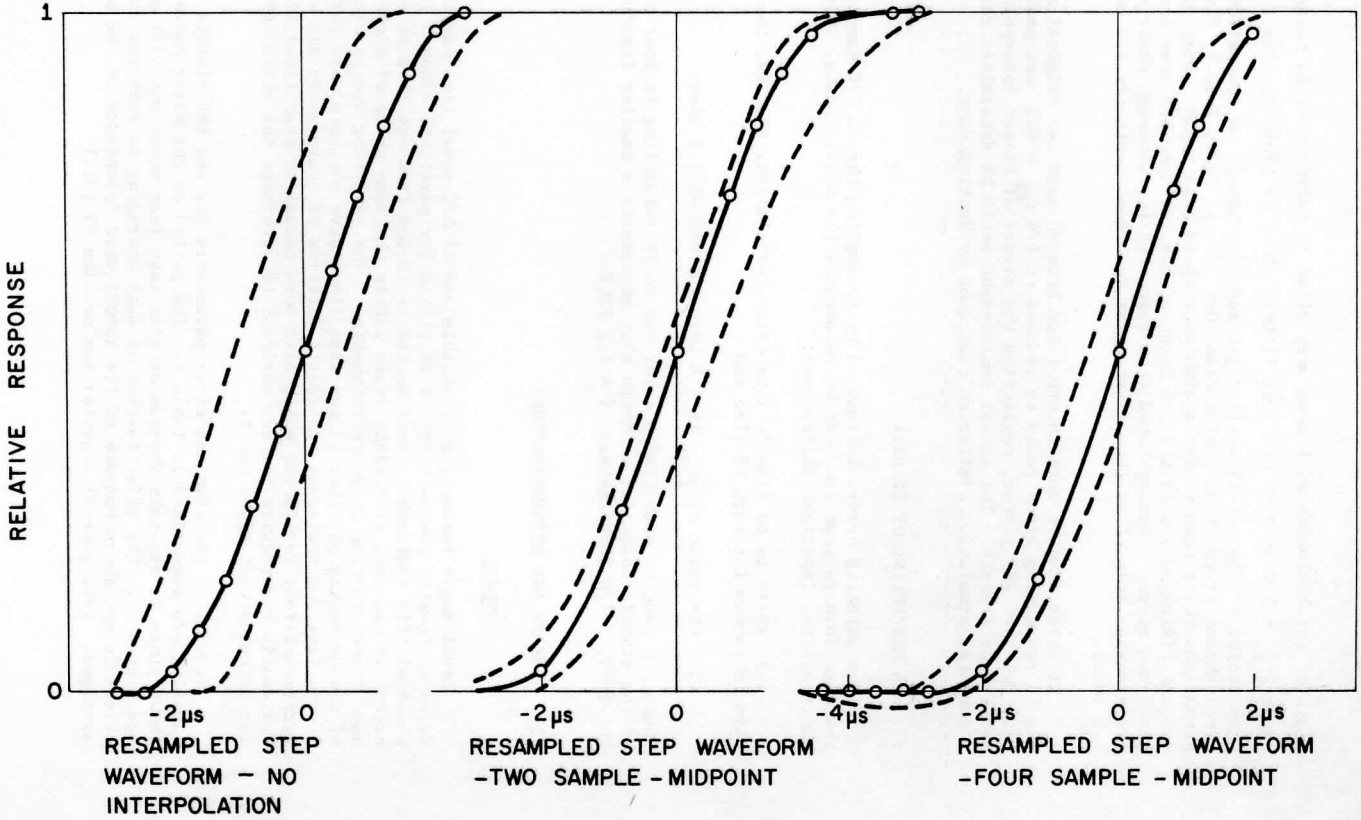

Figure 12

The dashed lines indicate the bounds of the time jitter introduced by resampling

2) Recommendations

2.1) Construct computer simulation to assess the error pattern effects under realistic conditions: clouds moving varying amounts parallel and normal to scan lines and clouds having a variety of sizes.

2.2) Test the effectiveness of double midpoint interpolation (three samples between each original pair), as a means to reduce resampling timing error. It might be necessary to recommend this approach if the results of (2.1) indicate that present errors are not tolerable.

Table 2. Gross characteristics of resampling errors.

	Peak-to-Peak	Maximum (Absolute)	RMS[1]
Position Error (Sawtooth Along Scan)			
Visible (1/2n.mi. x 1/2n.mi.)	1.0 μsec 0.25 n.mi.[2]	0.5 μsec 0.125 n.mi.	0.29 μsec 0.007 n.mi.
IR Window (4n.mi. x 2n.mi.)	4.0 μsec 1.0 n.mi.	2.0 μsec 0.5 n.mi.	1.16 μsec 0.28 n.mi.
Displacement Error (Square Wave Along Scan)			
Clouds moving parallel to scan direction			
Visible (1/2n.mi. x 1/2n.mi.)	1.0 μsec 0.25 n.mi. 0.5 knots[3]	1.0 μsec 0.25 n.mi. 0.5 knots	0.58 μsec 0.14 n.mi. 0.28 knots
IR Window (4n.mi. x 2n.mi.)	4.0 μsec 1.0 n.mi. 2.0 knots	4.0 μsec 1.0 n.mi. 2.0 knots	2.32 μsec 0.56 n.mi. 1.12 knots

Notes 1. RMS values are obtained by averaging over all possible ET to EA starting time differences; RMS errors along a line can in general be different from these averages.

2. Errors in n. mi. are for the subsatellite point only.

3. Velocity errors are based on a frame to frame interval of 30 minutes.

SMS SPIN AXIS ATTITUDE ERROR ESTIMATE

Eric Smith and Dennis Phillips

The technique used for determining SMS spin axis attitude parameters is similar to the multiple picture-single landmark approach which has been used with ATS-I and ATS-III since 1970. The basic approach was developed at the Space Science and Engineering Center of the University of Wisconsin-Madison. It requires the identification of a single recognizable landmark throughout a series of SMS image frames (T_1, T_2, ..., T_n) over a time period t_n.(1) The satellite line coordinate of the landmark is determined in each of the frames. Using these measurements, a spin loci configuration is determined. With three or more of these measurements, a least squares iterative solution of the satellite attitude can be obtained.

The dynamic relationship between a geosynchronous satellite coordinate system and an earth centered coordinate system consists of well known euclidian transforms which are periodic and continuous in time.(1) Thus, the essential source of error in deriving an attitude solution results from random scatter in the loci configuration which, in turn, is derived from the landmark position measurements themselves. With a well behaved system, multiple measurements enable a reduction of the scatter of the attitude loci. Accordingly, since longer time intervals increase the number of available landmark measurements, the accuracy of the attitude solution is maximized by incorporating a sufficiently long time period. We have found that five to seven landmark measurements, distributed uniformly over a three hour period, generate a stable solution. Shorter time periods tend toward high variance in solutions, dependent on the number of landmarks and their location. Longer time periods, however, do not contribute toward significant improvement.

For this study we used seven measurements from seven picture frames spaced 30 minutes apart over a three hour period (T_n start time = 12:00). Three landmark locations were chosen for investigation, as seen in Figure 1. These locations were artificially generated by the satellite-earth coordinate transform model under a representative set of orbital and model parameters. (1) The first location is ideally located at the sub-satellite point; the second is 30 degrees to the north in latitude and 30 degrees to the east in longitude from the SSP: the third is 60 degrees to the north and 60 degrees to the east. This selection of landmark positions is sufficient to examine one quadrant of the earth's visible surface; the other three quadrants would exhibit similar results, although orbital effects would slightly affect symmetry. The earth to satellite transform was used to generate a satellite line coordinate for each of the seven picture start times

(T_1 = 12:00, T_2 = 12:30, T_3 = 13:00, T_4 = 13:30, T_5 = 14:00, T_6 = 14:30, T_7 = 15:00) at each of the three landmark locations under six different attitude parameterizations. The attitude parameters (Declination, Right Ascension) chosen for the calculations are listed at the bottom of Figure 1.

The resultant transforms generated data which could be used as perfect measurements to recompute the six attitude positions for each of the three landmark sequences. An error estimate of attitude determination could then be calculated by applying scatter to the artificial landmark positions before reentering the measurements into the attitude computation equations. The scatter applied to the measurements was representative of scatter that would be found in an operational system.

Based on actual experience with landmark data in ATS-I and ATS-III imagery, we feel that landmark recognition to $\pm$ 2 scan lines can be achieved by the use of video displayed time sequences. In considering the SMS system, which has four times the visible spatial resolution, we assumed that $\pm$ 2 scan line landmark recognition is obtainable.

For the purposes of the study, the landmark line position scatter was allowed up to $\pm$ 5 scan lines. Figure 2 shows the results of the experiment. The results for each landmark are represented separately. The abscissa of each graph indicates the absolute value of allowable scan line measurement error running from perfect measurements zero (0) to five. The ordinate indicates the bounds of the standard deviation of the computed error values from the six known attitude positions, which we call pointing uncertainty.

The results demonstrate two important facts. First, the error in determining attitude position is virtually invariant under the selection of a landmark location. This is an important operational consideration because the availability of landmarks varies greatly as a function of weather systems (cloudiness). Secondly, the accuracy of attitude determination is virtually invariant under the spin axis position itself; under normal conditions declination is the critical parameter. This demonstrates that we can safely use the landmark scheme if the spin axis declination has drifted from nominal position.

The attitude determination accuracy is, therefore, only a function of the random scatter introduced in making landmark measurements. Using $\pm$ 2.5 lines as a conservative estimate of landmark measurement scatter, we judge, from the graphs, that the accuracy of the attitude determination system has a pointing uncertainty of 15 arc seconds. With better landmark recognition schemes (two dimensional image matching systems), attitude determination can be improved up to an uncertainty of only five arc seconds.

REFERENCE

(1) Phillips, Dennis, and Eric Smith. Geosynchronous Satellite Navigation Model, this report.

LANDMARK POSITIONS

1. EQ, 60°W
2. 30°N,30°W
3. 60°N, 0°W

ATTITUDE	DECLINATION	RIGHT ASCENSION
1	90°	90°
2	89°	90°
3	88°	90°
4	87°	90°
5	89°	135°
6	87°	135°

Figure 1

ATTITUDE ERROR

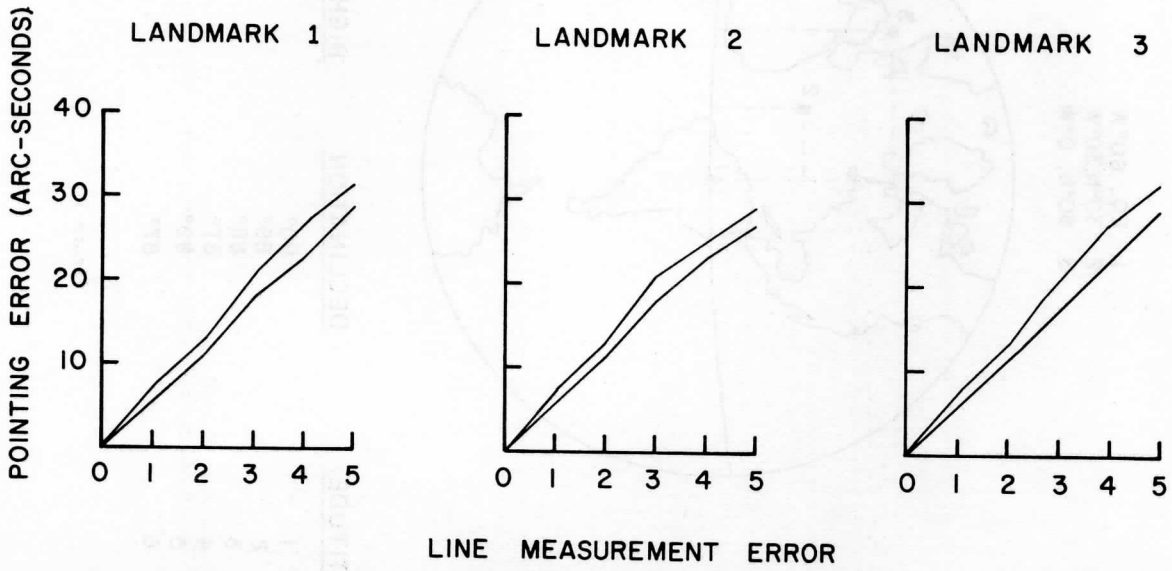

Figure 2

THE EFFECT OF PARAMETERIZATION UNCERTAINTIES ON WIND MEASUREMENTS

Eric Smith and Dennis Phillips

The location uncertainty of an SMS image sample in an earth located reference system is a function of a number of system parameters and of the dynamic satellite-earth relationship. The accuracy of a model transforming a satellite coordinate to an earth reference system is strictly a function of the uncertainties in the parameterization of the model used to generate the transform.(1) For this study, nine components affecting the satellite-earth transform functions were considered. Table 1 indicates the nine components and the range of uncertainty expected for each parameter. Notice that, for the purposes of the study, the line step error was treated over two different ranges: once at a contract specification uncertainty and again with a Philco Ford estimate. Furthermore, the element position errors were treated as a single parameter, with the range of uncertainty set to the summation of the various element jitter terms.

The errors in this analysis were categorized in two different ways according to their effect on the accuracy of wind measurements. The accuracy of frame to frame alignment treated as relative error, while the accuracy with which an earth reference system is tied to one specific image frame has been treated as absolute error. The relative error has the immediate undesirable effect of biasing wind measurements. The absolute error in a particular frame only causes the wind measurement to be misplaced with respect to earth location. With this categorization of errors, it has been found that bias error, which is consistent in a frame to frame sense, has little effect on relative error. However the effect of bias error, in an absolute sense, can be somewhat significant. Random error is not repeated in a frame to frame sense and has the same effect on both relative error and on absolute error. All the parameters used in the model are categorized according to whether they cause bias error or random error (see Table 1).

Bias error is a differential with respect to time, whereas random error exhibits fixed variance at any point in time. Figure 1 illustrates the effect of bias error manifesting itself in a frame to frame sense, defined as relative error. On frame T_1, the point represented by a small square is incorrectly identified by the transform as the point represented by a small circle. By definition this initial misidentification is referred to as absolute error at T_1. A portion of this error was generated by bias parameters in the transform. On frame T_2, the point represented by a small square (same point as in

frame T_1) is incorrectly identified by the transform as the point represented by a small triangle. The point represented by a small circle would correspond to the equivalent misidentification that was made by the transform for frame T_1. In this manner the bias error made, in a frame to frame reference, is represented by the distance from the small circle to the small triangle. This relative portion of the transform error is independent of the absolute portion of the transform error on individual frames. It is this bias which skews all wind measurements made from time sequenced images. The absolute error only affects the placement of the measurements in an earth reference system.

To study the effects of parameter uncertainties, satellite image coordinates were transformed to an earth frame of reference as the various model parameters varied over their range of uncertainty. The minimum and maximum values of the range of coordinate transformations were converted to nautical miles and used as error bounds. Tables 2 and 3 show some of the experimental results. Table 2 lists the errors treating each parameter individually in the model. Table 3 lists the errors when all parameter uncertainties were combined during the transform process.

Three satellite coordinate points were chosen to illustrate the results for Table 2. These points correspond to the following earth locations (subsatellite point is 0°N, 60°W):

Location 1: Sub-satellite point (0°N, 60°W)
Location 2: 30°N, 30°W
Location 3: 60°N, 0°W

The range of errors is given in nautical miles, divided into a North-South component (latitude) and an East-West component (longitude). Both the absolute error and the relative error terms are indicated. The relative errors exist with respect to a 30 minute interval between image frames.

As is seen in Table 2, the relative errors generated by each parameter individually, for locations 1 and 2, are all less than one nautical mile. An exception is the line step error at its specification uncertainty. If Philco Ford's value is used, the error is within a tolerable level. Although the third location exhibits larger error terms, it should be noted that this location is 75° from the SSP. Normally, the usable data from geosynchronous satellite images is limited to a region within 60° of the SSP (a geosynchronous satellite views 81° from the SSP). The random error type parameters cause an absolute error equal to their relative error. This can be seen in Table 2.

Under the absolute error columns, it is seen that the major source of positional error is due to uncertainties in the spin axis parameters and in the spin scan camera alignment to the principal axis. However,

uncertainties in these terms translate into very small relative errors. The effect of not selecting the proper level in the atmosphere during the transform is shown to be virtually insignificant up to 60° from the SSP. Also, the expected orbit uncertainty (this assumes a successful Range-Range Rate satellite tracking system) causes virtually insignificant errors during the transform, as does the nominal spin rate uncertainty.

Table 3 shows the combined maximum effects of both the bias error and the random error on the relative error and the absolute error of image frames. The effect of bias error on the relative error is in general much smaller than its effect on the absolute error. However, as might be expected, the effect of the random error has the same magnitude, in a frame to frame sense, as it has in an individual frame.

Figure 2 illustrates the effect of relative error on wind measurements made between two images frames having a 30 minute time interval. The contours (meters per second) designate regions in which wind measurements would be skewed up to the indicated velocity. These boundaries are encouraging. Wind measurements can be made up to approximately 60 degrees from the SSP without incurring biases in the measurements greater than a meter per second (GARP requirement). It should be noted that the relative error effects are smaller for a wider swath in the longitude direction than in the latitude direction. This is true because the effect on the relative alignment of the camera sweep is considerably less than the effect of the camera stepping. The outer boundary in Figure 2 outlines the region around the SSP for which absolute error (wind vector placement error) can be expected to be less than six nautical miles.

REFERENCE

(1) Phillips, Dennis, and Eric Smith. Geosynchronous Satellite Navigation Model, this report.

Expected Uncertainties

Parameter	Uncertainty
Line Step (Random)	
a. Expected Performance	±5 μr
b. Specification	±40 μr
Element Increment (Random)	
a. Line Start Synchronizing Error	±8 μr
b. Equal Angle Resampling	±4 μr
c. Communication Jitter, Electronic Filters, Clock Timing	±12 μr
d. Total	±24 μr
Spin Rate (Random)	±.05 sec
Orbit Position (Bias) Expected Performance From Tri-lateration System (Experimental)	±100 m
Spin Axis Attitude (Bias) Assuming landmark technique with 2.5 line measurement error	15 arc-seconds
Spin Axis Precession (Bias) Determined after launch (Should be determinate to higher accuracy)	±10 arc-seconds/day ±1° direction
Nutation (Random) Expected performance after ≃ 2 minute damping cycle (6 second period) - no phase information	.5 arc-seconds
Camera Misalignment (Bias) Determined after launch	
a. Pitch	±.05 mr
b. Yaw	±.05 mr
c. Roll	±.05 mr
Atmospheric Level - Cloud Height (Bias) Refraction component of error is ≃ 5 ft.	±5 miles

Table 1

Errors By Individual Parameters (Nautical Miles)

Parameter	Location	Absolute Error		Relative Error	
		Lat.	Long.	Lat.	Long.
Line Step (expected) ±5 μr	1	.097	.001	.097	.001
	2	.126	.042	.126	.042
	3	.512	.868	.512	.868
Line Step (specification) ±40 μr	1	.772	.012	.772	.012
	2	1.011	.331	1.011	.331
	3	4.067	6.857	4.067	6.857
Element Increment ±24 μr	1	.007	.463	.007	.463
	2	.047	.602	.047	.602
	3	.739	2.424	.739	2.424
Spin Rate ±.05 μsec	1	0	0	0	0
	2	0	0	0	0
	3	0	.001	0	.001
Orbit (Inclination, Eccentricity, Period, Longitudinal Drift ±100 meters position	1	.037	.059	.005	.003
	2	.069	.077	.009	.004
	3	.303	.545	.2	.343
Spin Axis Attitude (Declination, Right Ascension) 15 arc-seconds	1	2.516	.038	.176	.001
	2	2.863	1.128	.209	.081
	3	11.146	19.558	1.022	1.757
Spin Axis Precession ±10 arc-seconds/day ±1° direction	1	.578	.008	.186	.001
	2	.643	.249	.296	.073
	3	2.387	4.092	1.286	2.183
Spin Axis Nutation .5 arc-seconds	1	.084	.002	.084	.002
	2	.096	.038	.096	.038
	3	.371	.652	.371	.652
East-West Position (β,$\dot{\beta}$)	1				
	2	(Included in Element Increment)			
	3				
Camera Misalignment (Pitch, Yaw, Roll) ±.05 mr	1	1.958	.981	.003	.001
	2	2.741	1.776	.005	.002
	3	13.555	14.146	.133	.224
Atmospheric Level and Atmospheric Refraction ±5 miles	1	.004	0	.002	0
	2	.320	.362	.03	.003
	3	2.027	3.866	.235	.434

Table 2

Combined Errors (Nautical Miles)

Relative

Location		Bias Error		Random Error	
		Latitude	Longitude	Latitude	Longitude
Eq.	60°W	.357	.009	.188	.466
10°N	50°W	.379	.014	.193	.482
20°N	40°W	.422	.047	.217	.547
30°N	30°W	.496	.151	.269	.681
40°N	20°W	.633	.381	.375	.946
50°N	10°W	.935	.975	.625	1.558
60°W	0°W	2.141	3.639	1.631	3.972
10°N	60°W	.373	.022	.190	.469
20°N	60°W	.409	.034	.202	.475
30°N	60°W	.472	.044	.228	.484
40°N	60°W	.577	.052	.273	.494
50°N	60°W	.766	.058	.356	.506
60°N	60°W	1.154	.064	.529	.518
Eq.	50°W	.363	.01	.188	.477
Eq.	40°W	.371	.011	.189	.514
Eq.	30°W	.382	.012	.191	.583
Eq.	20°W	.394	.014	.96	.704
Eq.	10°W	.408	.019	.201	.922
Eq.	0°W	.426	.027	.209	1.363

Absolute

Location		Bias		Random	
		Latitude	Longitude	Latitude	Longitude
Eq.	60°W	4.111	1.086	.188	.466
30°N	30°W	4.951	3.236	.269	.681
60°N	0°W	20.068	6.713	1.671	3.972

Table 3

ABSOLUTE AND RELATIVE ERROR

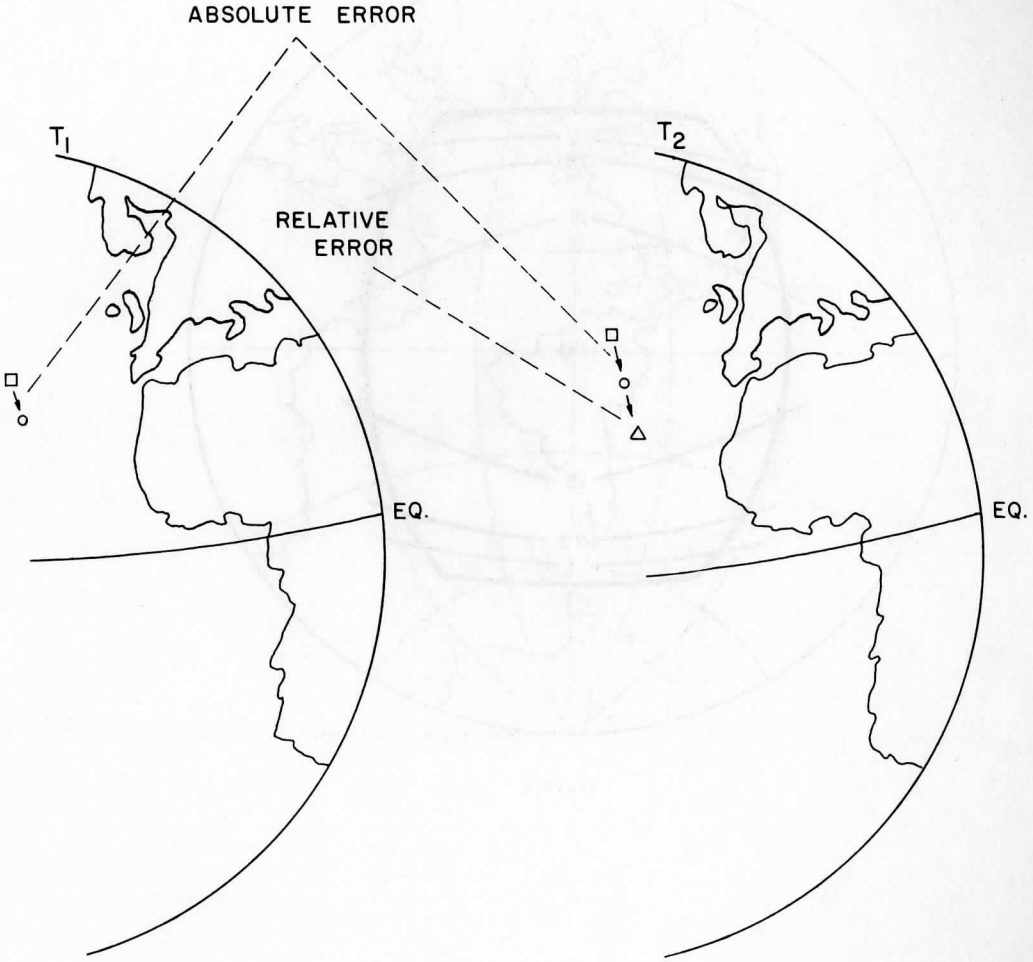

Figure 1

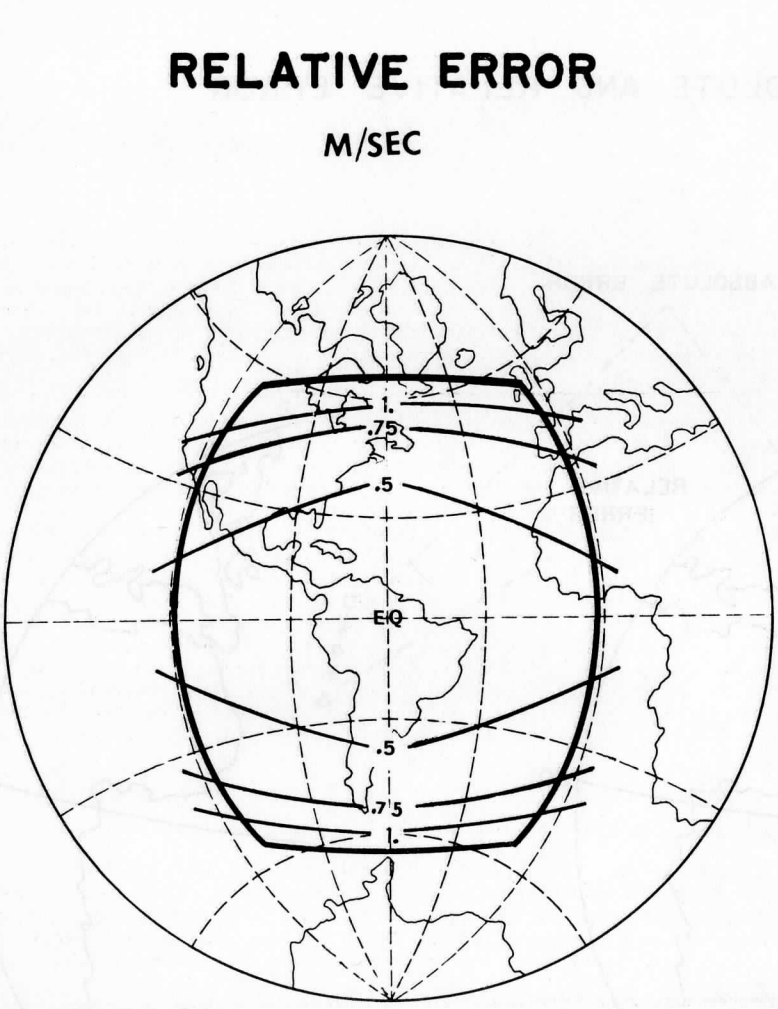

Figure 2

GEOSYNCHRONOUS SATELLITE NAVIGATION MODEL

D. Phillips and E. Smith

I. INTRODUCTION

The transformation of radiance values from an image frame position of a near geosynchronous satellite to an earth reference system requires a model to account for a number of individual satellite parameters necessary to form the complete transformation. Such a model, developed at the Space Science and Engineering Center of the University of Wisconsin-Madison, can handle sequences of image frames from ATS and SMS satellites over extended time periods.

Spacecraft attitude determination uses a time sequence of landmark references. This technique is immediately adaptable to any spin stabilized satellite. The primary focus of the SSEC-developed model is the geometric transformation from a nominal satellite coordinate system to an earth reference system, varying as a continuous function of time, to account for the dynamical effects of the satellite's orbit and attitude. Describing the vagaries incurred in transforming frame sweep coordinates (line-element) of the data imagery to the nominal satellite coordinate system has been of secondary consideration. This is due to the fact that the vagaries are relatively time stable. Also, the cataloging of these errors lies in the area of satellite instrumentation. Parameters have been included in the model on the grounds that they could be measured or inferred and that their inclusion would improve the accuracy of the transformation to an earth reference system. Table 1 lists the parameters considered in the model. Figure 2 illustrates these parameters in a satellite-earth relationship.

II. ORBIT PARAMETERS

Modeling the transformation from the nominal satellite coordinate system to the earth coordinate system involves two essential dynamical aspects of the satellite: the satellite's orbit and its attitude. It is assumed that orbit parameters of the satellite are independently available from the imagery and that they are available in the following form:

1. orbit inclination,
2. orbit period,
3. longitudinal position and time of southern equator excursion,
4. orbit eccentricity,
5. time and height of an orbit apogee.

The orbit position vector in earth coordinates is given by $\vec{S}(t)$ in equation (1).

$$\vec{S}(t) = \begin{pmatrix} x(t) \\ y(t) \\ z(t) \end{pmatrix} = \begin{Vmatrix} \cos(EQC) & -\sin(EQC) & 0 \\ \sin(EQC) & \cos(EQC) & 0 \\ 0 & 0 & 1 \end{Vmatrix} \cdot$$

$$\begin{Vmatrix} \cos(2\cdot\pi\cdot(t-t_{eqc})/P_e) & \sin(2\cdot\pi\cdot(t-t_{eqc})/P_e) & 0 \\ -\sin(2\cdot\pi\cdot(t-t_{eqc})/P_e) & \cos(2\cdot\pi\cdot(t-t_{eqc})/P_e) & 0 \\ 0 & 0 & 1 \end{Vmatrix} \cdot$$

$$\begin{Vmatrix} 1 & 0 & 0 \\ 0 & \cos(I) & \sin(I) \\ 0 & -\sin(I) & \cos(I) \end{Vmatrix} \cdot \begin{Vmatrix} H(t)\cdot\cos(2\cdot\pi\cdot(t-t_{eqc})/P_s) \\ H(t)\cdot\sin(2\cdot\pi\cdot(t-t_{eqc})/P_s) \\ 0 \end{Vmatrix} \quad (1)$$

where EQC = Longitude of satellite's position during an equatorial crossing (southward)

t_{eqs} = Inclination of the orbital plane with respect to the equatorial plane

H(t) = Height of satellite at time t

P_s = Orbital period

P_e = Length of celestial day

and

$$H(t) = (H_{max} - e\cdot H_{max})/(1+e\cdot\cos(t-t_{min})\cdot 2\cdot /P_s)) \quad (2)$$

where e = Orbital eccentricity

H_{max} = Maximum height of satellite

H_{min} = Minimum height of satellite

t_{min} = Time of minimum height

III. ATTITUDE DETERMINATION

A prime motivation for developing this model was to compute spin axis coordinates (attitude) with the use of orbit parameters and a set of n landmark measurements from the image data. We define the spin axis with two parameters and one camera reference as seen in Figure 3.

D = Declination
RA = Right Ascension
PC = Orthogonal Reference (Picture Center Line)

The orbit parameters enable the translation of landmark measurements $\vec{K}_i$ and their corresponding step angles ψ_i to a relationship between the spin axis and the celestial sphere. $\vec{K}_i$ and ψ_i are given by:

$$\vec{K}_i = \begin{pmatrix} r_i \cdot \cos\theta_i \cos\lambda_i \\ r_i \cdot \cos\theta_i \sin\lambda_i \\ r_i \cdot \sin\theta_i \end{pmatrix} \tag{3}$$

where r_i = Radius of oblate sphere at landmark i

θ_i = Latitude of landmark i

λ_i = Longitude of landmark i

and

$$\psi_i = R \cdot (L_i - PC) \tag{4}$$

where R = Radians per scan line

L_i = Image line coordinate

The position of the satellite in space is found for the time a landmark is viewed by the spin scan camera. The vectors from the center of the earth to the landmark and the satellite are rotated in a celestial coordinate system according to the time the landmark was scanned. The vector from the satellite to the landmark is then found in celestial coordinates by subtracting the two resultant vectors. The vector is normalized to a unit pointing vector. This yields a celestial coordinate unit vector C_i for each landmark measurement defined as follows:

$$\vec{C}_i = (C_x, C_y, C_z)_i \tag{5}$$

where

$$\vec{C}_i = \begin{pmatrix} \cos((t-t_o)/P_s) & -\sin((t-t_o)/P_s) & 0 \\ \sin((t-t_o)/P_s) & \cos((t-t_o)/P_s) & 0 \\ 0 & 0 & 1 \end{pmatrix}$$

$$(\vec{K}_i - \vec{S}(t))/||\vec{K}_i - \vec{S}(t)|| \tag{6}$$

The angle between the spin axis and the pointing vector C_i is determined by the step angle ψ_i corresponding to the scan line at which the landmark occurred. This angle and pointing vector (determined by the landmark and the satellite's position) determine a circular loci of points on the celestial sphere, illustrated in Figure 4. The spin axis is necessarily restricted to this loci, within the limit of the available landmark measurements and the accuracy of the satellite's orbit.

Two landmark measurements determine an attitude position at the intersection of the circular loci on the celestial sphere. To determine which

of the two intersections represents the satellite's attitude, we must know that the true spin axis position is the closest to the north pole of the celestial sphere. If there are more than two measurements, a least square procedure must be used to obtain a best fit of the attitude position. The least square procedure minimizes the sums of squares of differences between the cosines of step angles (of the camera from the spin axis of the satellite) and the cosines between the celestial pointing vectors (determined by a landmark and the satellite's position) and the unit vector representing the spin axis position. The expression is given in equation (7).

$$g(\alpha,\delta,\phi) = \sum_{i=1}^{n}\left((\sin\alpha,\cos\alpha\cdot\cos\delta,\cos\alpha\cdot\sin\delta)\cdot(C_x,C_y,C_z)_i - \cos(\psi_i+\phi)\right)^2 \quad (7)$$

This solution can be found by steepest descent to where partials $\partial g/\partial\alpha$, $\partial g/\partial\delta$, $\partial g/\partial\phi$ are sufficiently close to 0. The iteration technique uses a steepest descent method with a convergence criteria dependent on the step size. Thus,

$$\begin{aligned}\partial g/\partial\alpha = {} & \sum_{i=1}^{n}(C_x)^2\cdot\cos\alpha\cdot\sin\alpha + \sum_{i=1}^{n}(C_x\cdot C_y)\cdot\cos\delta\cdot(2\cdot\cos\alpha^2-1) \\ & + \sum_{i=1}^{n}(C_x\cdot C_z)\cdot(2\cdot\cos\alpha^2-1)\cdot\sin\delta - \sum_{i=1}^{n}(C_y)^2\cdot\cos\alpha\cdot\sin\alpha\cdot\cos\delta^2 \\ & - \sum_{i=1}^{n}(C_y\cdot C_z)\cdot 2\cdot\sin\alpha\cdot\cos\alpha\cdot\sin\delta\cdot\cos\delta - \sum_{i=1}^{n}(C_z)^2\cdot\sin\alpha\cdot\cos\alpha\cdot\sin\delta^2 \\ & - \sum_{i=1}^{n}(C_x\cdot\cos\psi_i)\cdot\cos\alpha\cdot\cos\phi + \sum_{i=1}^{n}(C_x\cdot\sin\psi_i)\cdot\cos\alpha\cdot\sin\phi \\ & + \sum_{i=1}^{n}(C_y\cdot\cos\psi_i)\cdot\sin\alpha\cdot\cos\delta\cdot\cos\phi - \sum_{i=1}^{n}(C_y\cdot\sin\psi_i)\cdot\sin\alpha\cdot\cos\delta\cdot\sin\phi \\ & + \sum_{i=1}^{n}(C_z\cdot\cos\psi_i)\cdot\sin\alpha\cdot\sin\delta\cdot\cos\phi - \sum_{i=1}^{n}(C_z\cdot\sin\psi_i)\cdot\sin\alpha\cdot\sin\delta\cdot\sin\phi \end{aligned} \quad (8)$$

$$\begin{aligned}\partial g/\partial\delta = {} & -\sum_{i=1}^{n}(C_x\cdot C_y)\cdot\cos\alpha\cdot\sin\alpha\cdot\sin\delta + \sum_{i=1}^{n}(C_x\cdot C_z)\cdot\sin\alpha\cdot\cos\alpha\cdot\cos\delta \\ & - \sum_{i=1}^{n}(C_y)^2\cdot\cos\alpha^2\cdot\cos\delta\cdot\sin\delta + \sum_{i=1}^{n}(C_y\cdot C_z)\cdot\cos\alpha^2\cdot(2\cdot\cos\delta^2-1) \\ & + \sum_{i=1}^{n}(C_z)^2\cdot\cos\alpha^2\cdot\sin\delta\cdot\cos\delta + \sum_{i=1}^{n}(C_y\cdot\cos\psi_i)\cdot\cos\alpha\cdot\sin\delta\cdot\cos\phi \\ & - \sum_{i=1}^{n}(C_y\cdot\sin\psi_i)\cdot\cos\alpha\cdot\sin\delta\cdot\sin\phi - \sum_{i=1}^{n}(C_z\cdot\cos\psi_i)\cdot\cos\alpha\cdot\cos\delta\cdot\cos\phi \\ & + \sum_{i=1}^{n}(C_z\cdot\sin\psi_i)\cdot\cos\alpha\cdot\cos\delta\cdot\sin\phi \end{aligned} \quad (9)$$

$$\partial g/\partial\phi = \sum_{i=1}^{n}(C_x\cos\psi_i)\cdot\sin\alpha\cdot\sin\phi + \sum_{i=1}^{n}(C_x-\sin\psi_i)\cdot\sin\alpha\cdot\cos\phi$$

$$+ \sum_{i=1}^{n}(C_y\cdot\cos\psi_i)\cdot\cos\alpha\cdot\cos\delta\cdot\sin\phi + \sum_{i=1}^{n}(C_y\cdot\sin\psi_i)\cdot\cos\alpha\cdot\cos\delta\cdot\cos\phi$$

$$+ \sum_{i=1}^{n}(C_z\cdot\cos\psi_i)\cdot\cos\alpha\cdot\sin\delta\cdot\sin\phi + \sum_{i=1}^{n}(C_z\cdot\sin\psi_i)\cdot\cos\alpha\cdot\sin\delta\cdot\cos\phi$$

$$- \sum_{i=1}^{n}(\cos\psi_i)^2\cdot\sin\phi\cdot\cos\phi + \sum_{i=1}^{n}(\sin\psi_i)^2\cdot\sin\phi\cdot\cos\phi$$

$$+ \sum_{i=1}^{n}(\sin\psi_i\cdot\cos\psi_i)\cdot(2\cdot\sin\phi^2-1) \qquad (10)$$

Because the step number (picture center line), at which the spin scan camera is perpendicular to the spin axis of the satellite, is not necessarily known, a parameter corresponding to this step number PC has been incorporated into the model. This makes finding the spin axis position a three parameter problem. We solve for D, RA, PC from the three angles

$$D = \text{asin}(\cos\tilde{\alpha}\cdot\sin\tilde{\delta}) \qquad (11)$$

$$RA = \text{atan}(\cos\alpha\cdot\cos\delta/\sin\alpha) \qquad (12)$$

$$PC = PC_n-(\tilde{\phi}-\pi/2)/R_\ell \qquad (13)$$

where $\tilde{\alpha}$, $\tilde{\delta}$, and $\tilde{\phi}$ are the respective values of α, δ, and ϕ after the last iteration and PC_n is the nominal picture center line.

IV. NOMINAL SATELLITE COORDINATE SYSTEM

The nominal satellite coordinate system is determined by the spin axis pointing vector and the position of the earth in each scan line. The z axis coincides with the spin axis of the satellite. The x axis is perpendicular to the earth. The y axis completes a right handed coordinate system, as illustrated in Figure 5. The position of the earth in each line sweep determines the x, y coordinates of the pointing vector of each sample on that line. Hence, a transformation from the raw image frame coordinates to the satellite's nominal reference frame is needed.

In transforming from the satellite's raw image frame to the satellite's nominal reference frame, it is thus necessary to measure the earth position in each scan line. In the model, the deviation of the earth from its nominal position is determined from landmarks measurements. Any deviation from the nominal position can be approximated as a linear function of time. For this reason, a regression line is fitted to the residuals obtained from measured landmark sample positions and their positions in the nominal frame of reference. The y intercept of the regression line is referred to as β at time t_o and the slope of the line is referred to as $\dot{\beta}$ as seen in Figure 6. The equations for deriving the regression line follow.

Let $\gamma(t) = \beta + \dot{\beta}t$ (14)

where γ = Drift in radians from frame center.

Minimize the expression

$$\sum_{i=1}^{n}(\beta_i-\beta-\dot{\beta}t_i)^2 \quad (15)$$

where PICTIM = Frame start time

n = Number of landmarks

$$\beta_i = R_e(E_i^{\gamma o} - E_i^m) \qquad \text{where } \gamma_o = 0 \quad (16)$$

$$t_i = \text{PICTIM} + \omega_i[L_i+(E_i\cdot A_e)/(T_e\cdot 360)] \quad (17)$$

Using the following sums,

$$S_\gamma = \sum_{i=1}^{n} \gamma_i \quad (18)$$

$$S_{\gamma t} = \sum_{i=1}^{n} \gamma_i t_i \quad (19)$$

$$S_t = \sum_{i=1}^{n} t_i \quad (20)$$

$$S_{t^2} = \sum_{i=1}^{n} t_i^2 \quad (21)$$

solve for β and $\dot{\beta}$

$$\beta = (S_{t^2}S_\gamma - S_t S_{\gamma t})/(nS_{t^2} - S_t^2) \quad (22)$$

$$\dot{\beta} = (nS_{\gamma t} - S_\gamma S_t)/(nS_{t^2} - S_t^2) \quad (23)$$

V. SATELLITE-EARTH COORDINATE TRANSFORMATION

We desire a transform f such that

$$f(L,E) = (\theta,\lambda) \quad (24)$$

and $$f^{-1}(\theta,\lambda) = (L,E) \quad (25)$$

where L = Line (satellite coordinate)

E = Element (satellite coordinate)

θ = Latitude (earth coordinate)

λ = Longitude (earth coordinate)

The ability to transform to an earth frame of reference (θ,λ) from satellite imagery coordinates (L,E) results from the ability to transform vectors in the satellite's nominal coordinate system to an earth reference frame and vice versa (see Figure 7). The transformation is a rigid Euclidean rotation and displacement. The displacement vector from the earth's reference frame to the satellite's nominal coordinate system is determined by the satellite's position at that particular time in the earth's reference frame. The third column of the rotational matrix is the pointing vector of the spin axis in the earth's frame of reference, given in equations (26) and (27).

$$\overrightarrow{SPAX}(t) = \begin{Vmatrix} \cos[(t-t_o)\cdot 2\pi/P_e] & \sin[(t-t_o)\cdot 2\pi/P_e] & 0 \\ -\sin[(t-t_o)\cdot 2\pi/P_e] & \cos[(t-t_o)\cdot 2\pi/P_e] & 0 \\ 0 & 0 & 1 \end{Vmatrix} \cdot \begin{Vmatrix} \cos D & \cos RA \\ \cos D & \sin RA \\ \sin D & 0 \end{Vmatrix} \quad (26)$$

$$\overrightarrow{AROT}_3(t) = \overrightarrow{SPAX}(t) \quad (27)$$

where D = Declination of satellite spin axis

RA = Right Ascension of satellite spin axis

$\overrightarrow{SPAX}(t)$ is assumed to have been adjusted for precession and nutation by the respective equations (28) and (29)

$$\overrightarrow{SPAX}(t) = \overrightarrow{SPAX}(t)\cdot\cos[P_{rate}\cdot(t-t_o)] + P_{dir}\cdot\sin[P_{rate}\cdot(t-t_o)] \quad (28)$$

where P_{rate} = Precession Rate

P_{dir} = Precession Direction

and $\overrightarrow{SPAX}(t) = \overrightarrow{SPAX}(t)\cdot\cos[N_{mag}] + N_{dir}\cdot\sin[N_{mag}]$ (29)

where N_{mag} = Nutation Magnitude at time t

N_{dir} = Nutation Direction at time t

The first column of the rotational matrix is perpendicular to the third column and lies in the same plane as the spin axis pointing vector and the satellite position vector:

$$\overrightarrow{AROT}_1(t) = \frac{\dfrac{\vec{S}(t)}{||\vec{S}(t)||} - \dfrac{\vec{S}(t)}{||\vec{S}(t)||}\cdot\overrightarrow{SPAX}(t)\cdot\overrightarrow{SPAX}(t)}{\left|\left|\dfrac{\vec{S}(t)}{||\vec{S}(t)||} - \dfrac{\vec{S}(t)}{||\vec{S}(t)||}\cdot\overrightarrow{SPAX}(t)\cdot\overrightarrow{SPAX}(t)\right|\right|} \quad (30)$$

The second column is a cross product of the third and first columns, resulting in an orthogonal rotational matrix.

$$\overrightarrow{AROT}_2(t) = \overrightarrow{AROT}_3(t) \times \overrightarrow{AROT}_1(t) \quad (31)$$

The rotational matrix and displacement vector enable a conversion of vectors from an earth reference frame to the nominal satellite reference system.

$$\text{AROT}(t) = \begin{pmatrix} \overrightarrow{\text{AROT}}_1(t) \\ \overrightarrow{\text{AROT}}_2(t) \\ \overrightarrow{\text{AROT}}_3(t) \end{pmatrix} \tag{32}$$

In transforming from the image frame coordinates to the nominal satellite reference system, an adjustment has to be made for misalignment between the camera axis and the spacecraft spin axis. This is done with a rotational matrix defined in terms of the three angles of misalignment (ζ, η, κ) given by equation (33).

$$\text{ROT} = \begin{Bmatrix} (\cos\kappa \cdot \cos\zeta) & 0 & (\sin\eta \cdot \sin\kappa \cdot \cos\zeta + \cos\eta \cdot \sin\zeta) \\ (-\sin\kappa) & 0 & (\sin\eta \cdot \cos\kappa) \\ (\cos\kappa \cdot \sin\zeta) & 0 & (\cos\eta \cdot \cos\zeta - \sin\eta \cdot \sin\kappa \cdot \sin\zeta) \end{Bmatrix} \tag{33}$$

where ζ = Pitch misalignment (North-South displacement)

η = Yaw misalignment (Total skew effect)

κ = Roll misalignment (East-West displacement)

The Euler angles of this rotation are referred to as roll, pitch and yaw. This rotation actually accounts for two effects: (1) the misalignment of the camera axis from the principle axis of the satellite and (2) the misalignment of the principle axis from the span axis of the satellite. Both misalignments can be modeled as one effect. The values of these parameters are expected to remain constant over long time periods and will be extractable from the imagery data.

VI. SATELLITE TO EARTH - $(\theta,\lambda) = f(L,E)$

The background has been sufficiently explained to permit a detailed examination of the transformation from satellite image coordinates to earth latitude and longitude coordinates. First a pointing vector, $\vec{V}_s(t)$, is found in nominal satellite coordinates, with adjustment for principle axis anomolies

$$\vec{V}_s(t) = \begin{pmatrix} \cos E & \sin E & 0 \\ -\sin E & \cos E & 0 \\ 0 & 0 & 1 \end{pmatrix} \cdot \begin{pmatrix} \text{ROT} \end{pmatrix} \cdot \begin{pmatrix} \cos L \\ 0 \\ -\sin L \end{pmatrix} \tag{34}$$

Next, $\vec{V}_s(t)$ is rotated into a pointing vector $\vec{V}_e(t)$ in earth coordinates.

$$\vec{V}_e(t) = (\text{AROT}(t))^{-1} \cdot \vec{V}_s(t) \tag{35}$$

where

$$\begin{pmatrix} x'(t) \\ y'(t) \\ z'(t) \end{pmatrix} = \vec{V}_e(t) \tag{36}$$

and

$$\begin{pmatrix} x(t) \\ y(t) \\ z(t) \end{pmatrix} = \vec{S}(t) \tag{37}$$

The pointing vector $\vec{V}_e(t)$ is extended to an intersection with an oblate sphere, representing the earth's surface at the proper atmospheric level with the parameter d in equation (38).

$$1 = \frac{[x(t)-d\cdot x'(t)]^2 + [y(t)-d\cdot y'(t)]^2}{a^2} + \frac{[z(t)-d\cdot z'(t)]^2}{b^2} \tag{38}$$

where a = Equatorial radius of earth

b = Polar radius of earth

This intersection determines an earth coordinate vector EC(t):

$$\vec{EC}(t) = [EC_x(t), EC_y(t), EC_z(t)] = \vec{S}(t) - d_1\cdot\vec{V}_e(t) \tag{39}$$

where d_1 (the smallest root of equation (39)) is the distance from the satellite to the intersection with the earth's surface at that atmospheric level. A correction for atmospheric refraction can be made by the following three steps:

1. Determine the intersection of the pointing vector $\vec{V}_e(t)$ with the appropriate oblate sphere at the top of the atmosphere.

2. Perturbate the pointing vector by the refraction angle determined from Snell's principles of refraction.

3. Solve for a new pointing vector $\vec{V}_e(t)$ and then proceed to determine the earth coordinate vector $\vec{EC}(t)$.

The final step solves for θ and λ.

$$\theta = \text{atan}(EC_z/\sqrt{EC_x^2 + EC_y^2} \tag{40}$$

$$\lambda = \text{atan}(EC_y/EC_x) \tag{41}$$

This completes the satellite image coordinate (L,E) transformation to earth coordinates (θ,λ).

VII. EARTH TO SATELLITE - (L,E) = $f(\theta,\lambda)$

The transformation from earth coordinates to satellite image coordinates is easier. First an earth coordinate vector is generated.

$$\overline{EC}(t) = \begin{pmatrix} r(\theta) \cdot \cos\theta \cdot \cos\lambda \\ r(\theta) \cdot \cos\theta \cdot \sin\lambda \\ r(\theta) \cdot \sin\theta \end{pmatrix} \tag{42}$$

where $r(\theta)$ = Radius of oblate sphere at the specified atmospheric level at latitude θ

The vector from the earth's surface to the satellite is given by equation (43).

$$\vec{W}(t) = [\vec{EC}(t) - \vec{S}(t)] \tag{43}$$

Normalize this vector to a pointing vector $\vec{V}_e(t)$ in earth coordinates,

$$\vec{V}_e(t) = \vec{W}(t) / \left|\left| W(t) \right|\right| \tag{44}$$

Note that an atmospheric refraction correction can be applied in an inverse manner, as before.

Rotate $\vec{V}_e(t)$ into a pointing vector in satellite coordinates

$$\vec{V}_s(t) = [AROT(t)] \cdot \vec{V}_e(t) \tag{45}$$

where

$$\begin{pmatrix} x''(t) \\ y''(t) \\ z''(t) \end{pmatrix} = \vec{V}_s(t) \tag{46}$$

The final step solves for L and E corrected for principle axis anomolies

$$L = PC - \left(\text{asin}[z''(t)/\sqrt{ROT_{3,1}^2 + ROT_{3,3}^2}] - \text{atan}(ROT_{3,1}/ROT_{3,3})\right) R_\ell \tag{47}$$

$$E = PE - \Big(\text{atan}[(ROT_{2,1} \cdot CL + ROT_{2,3} \cdot SL)/(ROT_{1,1} \cdot CL + ROT_{1,3} \cdot SL)] - \text{atan}[y''(t)/x''(t)]\Big)/R_e \tag{48}$$

where PC = Picture Center Line

PE = Picture Center Element

$$SL = \frac{z''(t)}{\sqrt{ROT_{3,1}^2 + ROT_{3,3}^2}}$$

$$CL = \sqrt{1 - SL^2}$$

The transformation from earth to satellite coordinates requires an iterative procedure because t is not known exactly for the earth coordinate (θ,λ). Thus, $\vec{S}(t)$ and AROT(t) are not known. Five iterations are sufficient to converge to the proper t. The picture start time is used as an initial guess. This completes the model's ability to achieve satellite imagery coordinates (L,E) from earth reference coordinates (θ,λ).

VIII. IMAGE FRAME COORDINATES IRREGULARITIES

The irregularities involved in registering image data in the time dependent coordinate system of the satellite's camera sweep across the earth's surface have been ignored in the model. These irregularities result from electronic timing errors, signal sampling errors, and sun pulse detection errors during the data acquisition process. However, as has been explained, any steady linear shear of the picture, with respect to the earth, is modeled with an initial value and slope term. Finally, the spin rate and angular sample resolution are included in the model, thereby completing the set of parameters needed to describe the sweep coordinate of the imagery frame.

The scan line step coordinates in the imagery frame are dependent upon camera step measurements, with respect to the principle axis, made before launch. Any non-repeatable stepping irregularities from one image frame to another, or post-launch line stepping distortions within the same frame are not considered in this model. However, frame coordinate irregularities can be easily implemented in such a model by using camera step-sweep increment lookup tables.

IX. CONCLUSION

The geosynchronous satellite navigation model was developed for its applications to the data handling of time sequenced satellite images. The model has predictive capabilities since the dynamic relationships it describes are stable with respect to time. Thus, the model parameters, which achieve an earth reference in the data imagery, need not be restricted to the time interval of available landmark measurements. The model is adaptable to an operational system.

TABLE 1

Model Parameters

1. Frame Definition (see Figure 1)

   A_e = Angular Sweep-Elements
   T_e = Total Elements in Frame
   $R_e = A_e/T_e$ = Radians per Element
   A_ℓ = Angular Breadth-Lines
   T_ℓ = Total Lines in Frame
   $R_\ell = A_\ell/T_\ell$ = Radians per Line

2. Spin Rate

   a. ω_I = Initial Spin Rate
   b. ω_F = Final Spin Rate
   c. Spin Rate at Line i = $\omega_i = (\omega_I-(\omega_I-\omega_F)\cdot(L_i/T_\ell))/3600000$

3. Orbit

   a. Inclination
   b. Eccentricity
   c. Period
   d. Longitudinal Drift

4. Satellite Spin Axis

   a. Attitude
      1. Declination
      2. Right Ascension
      3. Picture Center Line
         (Spin Axis Orthogonality Reference)
   b. Spin Axis Precession
   c. Spin Axis Nutation

5. Earth Element Positioning (λ)

   a. Position at t_o = β
   b. Drift Rate = β

6. Camera Mount Misalignment from Projected Spin Axis

   a. Pitch
   b. Yaw
   c. Roll

7. Atmosphere

   a. Refraction
   b. Cloud Height

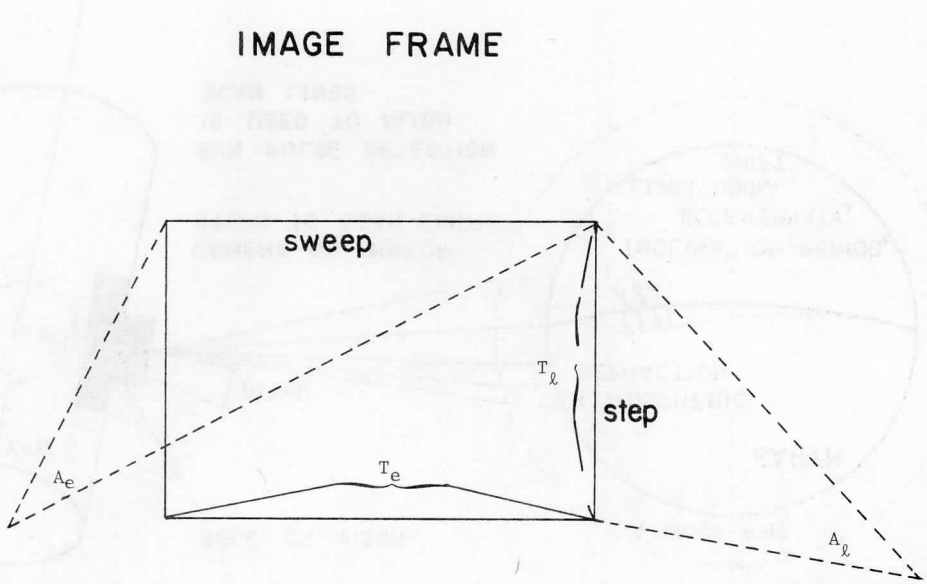

Figure 1

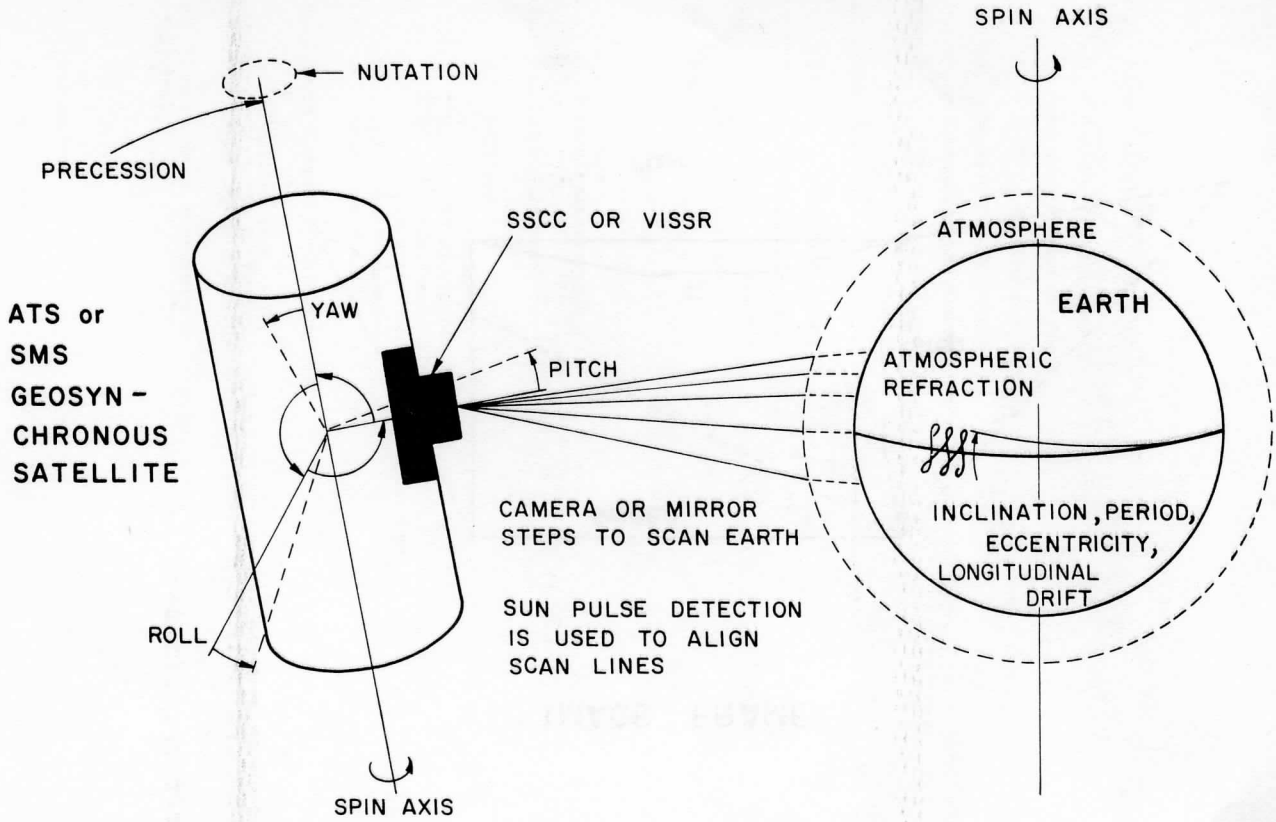
SPIN AXIS
NUTATION
PRECESSION
SSCC OR VISSR
ATMOSPHERE
EARTH
ATS or
SMS
GEOSYN-
CHRONOUS
SATELLITE
YAW
PITCH
ATMOSPHERIC
REFRACTION
CAMERA OR MIRROR
STEPS TO SCAN EARTH
INCLINATION, PERIOD,
ECCENTRICITY,
LONGITUDINAL
DRIFT
SUN PULSE DETECTION
IS USED TO ALIGN
SCAN LINES
ROLL
SPIN AXIS
(NOMINAL SPIN RATE = 100 RPM)

Figure 2

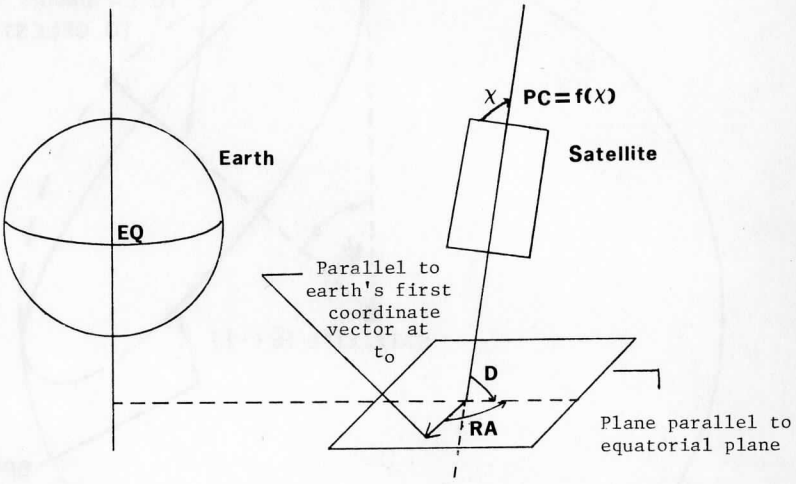
Satellite Spin Axis
Earth
EQ
χ
PC=f(χ)
Satellite
Parallel to
earth's first
coordinate
vector at
t_o
D
RA
Plane parallel to
equatorial plane

Figure 3

Attitude Determination using Landmark Measurements

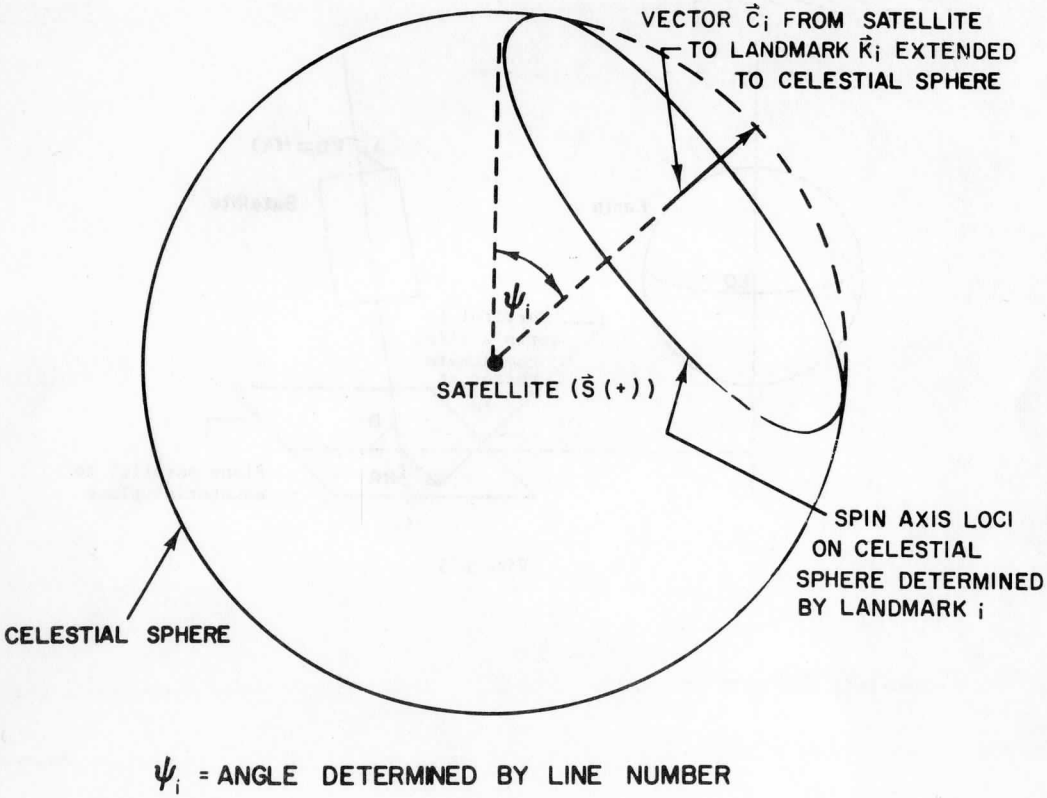

Figure 4

NOMINAL SATELLITE COORDINATE SYSTEM

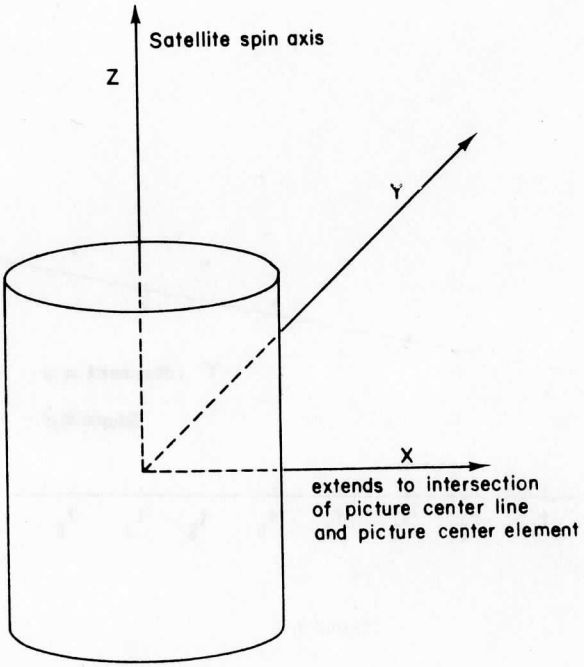

Figure 5

Beta and Beta-Dot Calculation

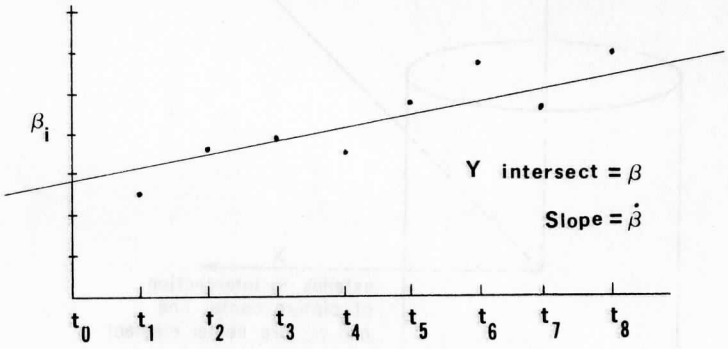

Figure 6

SATELLITE – EARTH TRANSFORM

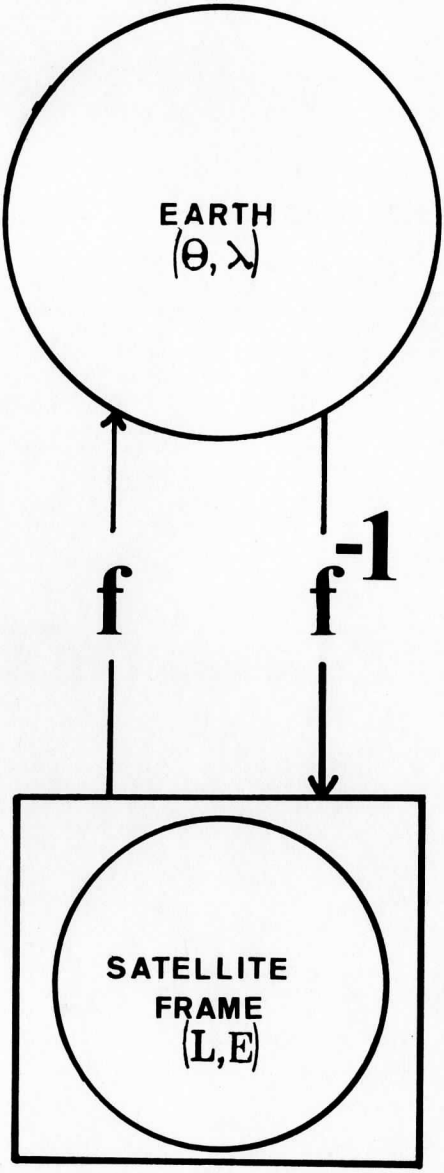

Figure 7

REPORTS AVAILABLE FROM

THE UNIVERSITY OF WISCONSIN PRESS, BOX 1379, MADISON, WISCONSIN 53701

(continued from inside back cover)

97040. Teleconferencing in Wisconsin. 240 pages. 1971. $10.00

97041. Measurements from Satellite Platforms: Annual Scientific Report on NAS5-11542, 1970-71. 270 pages. 1972. $10.00

97042. Experiments in Medical Communications via the ATS-1 Satellite. 136 pages. 1972. $7.50

97043. Specifications for a Vertical Temperature and Moisture Sounder for the Synchronous Meteorological Satellites. 82 pages. 1972. $5.00

97044. Scientific Requirements of Sea Surface Measurements for the GARP Tropical Experiment. 18 pages. 1972. $2.50

97045. Studies of the Atmosphere Using Aerospace Probings: Annual Report, 1971, Vol. II: Application Studies. 104 pages. 1972. $5.00

97046. Multidisciplinary Studies of the Social, Economic, and Political Impact Resulting from Recent Advances in Satellite Meteorology: An Interim Report, Vol. 3. 252 pages. 1972. $10.00

97047. Multidisciplinary Studies of the Social, Economic, and Political Impact Resulting from Recent Advances in Satellite Meteorology: An Interim Report, Vol. 4. 199 pages. 1972. $10.00

97048. Satellite Teleconferencing: An Annotated Bibliography. 130 pages. 1972. $7.50

97049. Measurements from Satellite Platforms: Annual Scientific Report on NAS5-11542, 1971-72. 228 pages. 1972. $7.50

97050. Synchronous Meteorological Satellite Sounder Specification: Final Report Under NASA Contract NAS5-21607. 73 pages. $5.00

97051. Multidisciplinary Studies of the Social, Economic, and Political Impact Resulting from Recent Advances in Satellite Meteorology: An Interim Report, Vol. 5. 290 pages. 1973. $10.00

97052. Measurements from Satellite Platforms: Annual Scientific Report on NAS5-21798, 1972-73. 331 pages. 1974. $10.00

97053. Visual Channel Data Analysis for Synchronous Meteorological Satellite. Scientific Report on NOAA/NESS Grant NG-26-72/ 252 pages. 1974. $7.50

97054 Studies of the Atmosphere Using Aerospace Probes: Annual Report, 1973. 272 pages. 1974. $7.50.

REPORTS AVAILABLE FROM

THE UNIVERSITY OF WISCONSIN PRESS, BOX 1379, MADISON, WISCONSIN 53701

97024. Studies in Atmospheric Energetics Based on Aerospace Probings: Annual Report, 1966. 129 pages. 1967. $5.00

97026. Studies in Atmospheric Energetics Based on Aerospace Probings: Annual Report, 1968. 162 pages. 1969. $5.00

97027. Radiation Experiment in the Vicinity of Barbados: Final Report, NSF Grant Ga. 12603. 100 pages. 1970. $5.00

97028. The Study of Radiation in a Tropical Atmosphere: Final Report. 100 pages. 1970. $5.00

97029. The Educational and Social Uses of Communications Satellites: A Bibliography. 42 pages. 1970. $3.50

97030. Measurements from Satellite Platforms: Annual Scientific Report on NAS5-11542, 1968-69. 388 pages. 1970. $10.00

97031. A Pilot Study on the Application of Geosynchronous Meteorological Satellite Data to Very Short Range Terminal Forecasting. 113 pages. 1970. $5.00

97032. Studies of the Atmosphere Using Aerospace Probings: Annual Report, 1969. 243 pages. 1970. $7.50

97033. Teleconferencing: A Bibliography. 1971. $3.50

97034. Legal and Political Aspects of Satellite Telecommunication: An Annotated Bibliography. 126 pages. 1971. $7.50

97035. Multidisciplinary Studies of the Social, Economic, and Political Impact Resulting from Recent Advances in Satellite Meteorology: An Interim Report, Vol. 1. 459 pages. 1971. $15.00

97036. Multidisciplinary Studies of the Social, Economic, and Political Impact Resulting from Recent Advances in Satellite Meteorology: An Interim Report, Vol. 2. 431 pages. 1971. $15.00

97037. Measurements from Satellite Platforms: Annual Scientific Report on NAS5-11542, 1969-70. 180 pages. 1971. $7.50

97038. Studies of the Atmosphere Using Aerospace Probings: Annual Report, 1970. 69 pages. 1971. $5.00

97039. Legal Aspects of Satellite Teleconferencing. 213 pages. 1971. $7.50